THE UNIVERSITY OF QUEENSLAND

AUSTRALIA

Interfacial structure of polymers near a surface: a molecular dynamics study

Ravi Chandra Dutta

Master's in chemical engineering

A thesis submitted for the degree of Doctor of Philosophy at

The University of Queensland in 2019

School of Chemical Engineering

Abstract

The efficient separation of gases is a subject of considerable interest due to economic and environmental threats associated with air pollution, and is an imperative to meet energy demands of the world. Membrane based gas separation is considered as an efficient, productive, readily scalable, and environmentally friendly process that can operate in a continuous fashion. The recent advances have shifted towards the development of mixed matrix membranes (MMM), due to the challenges with the current spectrum of polymeric and inorganic membranes. MMMs have been commonly prepared by incorporating inorganic fillers such as zeolites or metal organic frameworks in a continuous polymer matrix. However, the success of MMMs depends greatly on the screening and selection of suitable polymer matrix, inorganic filler and interaction between them. Though the past decade has witnessed substantial progress in both the fundamental and application aspects of MMMs in gas separation, interface problems such as the formation of non-selective voids, rigidified polymer and pore blockage due to poor interaction between the polymer and inorganic filler are still challenging. Hence, understanding and minimising interfacial barriers between the polymer and the inorganic filler are critical to the design and optimisation of MMMs; however, trial and error experimentation is required to address these non-ideal interface issues. On the other hand, atomistic simulations have become an important tool in the screening and selection of suitable materials in MMMs. The present thesis aims to develop a fundamental knowledge of the polymer structure near a surface, and thus facilitate the design of MMMs, especially for gas-separation.

Firstly, the morphology of the polyimide (PI) polymer membrane is characterized by exploring the volume-temperature relations, distribution of free volume elements in the polymer and available free volume analysis. Then, the separation performance of a PI membrane in pure gas conditions is investigated. Gas sorption isotherms were extracted via a two-step methodology considering the dynamics and structural transitions in the polymer matrix upon gas sorption using a combination of equilibrium molecular dynamics (EMD) in the constant pressure ensemble and grand canonical Monte Carlo simulations. The gas transport behavior in the polymer membrane is evaluated by extracting Maxwell-Stefan diffusivities, and found to be consistent with experimental evidence.

Further, the separation performance of a polymer membrane in mixed gas conditions is investigated by considering an equimolar mixture of CO_2 and CH_4 in a fluorinated PI polymer membrane. Significant swelling of the polymer in the presence of CO_2 is found, as a result of which the predictions of traditional models such as ideal adsorption solution theory and dual mode sorption for mixed gases in mixed gas conditions are inaccurate, particularly for CH_4. The Onsager coefficients indicate that in mixed gas conditions finite correlations exist between the diffusing species in the polymer membrane. Further, the swollen membrane is diffusive selective for CH_4 at high pressures in mixtures due to availability of large pores, in contrast to pure gas conditions where the membrane is diffusive selective for CO_2 over CH_4 at all pressures. Analysis of membrane behavior under practical conditions using EMD-based transport coefficients shows that while the CO_2/CH_4 perm-selectivity increases with increase in pressure based on pure component data, the trend is opposite for mixture data. Thus, the commonly used approach of screening membrane materials based on pure component data can be misleading, as it overlooks the correlation effects arising from the presence of other species in the mixture.

Subsequently, the structure of the PI in the vicinity MFI-zeolite, and its CO_2/CH_4 transport properties is investigated. It was found that incorporation of MFI zeolite into PI results in the formation of a densified polymer layer near the surface, having thickness around 1.2 nm, contradicting empirical suggestions of an approximately 1-micron thick interface between the polymer and filler. This interfacial region offers extra resistance to gas diffusion, which increases with kinetic diameter. Consequently, significant increase in CO_2/CH_4 selectivity as well as gas permeability is observed in the PI-MFI composite membrane compared to the pure PI polymer membrane, which is correlated with the high selectivity of the rigidified interfacial layer in the polymer. Thus, while enhancing transport resistance, the rigidified layer can be beneficial to membrane selectivity.

Finally, the structure of a PI in the vicinity of the ZIF-8 surface is investigated. It is seen that incorporation of ZIF-8 into PI results in formation of sub-nanometer voids as defects near the polymer-filler interface. We then identified an ionic liquid (BMIM-BF_4) which has favorable interactions with both ZIF-8 as well as polymer to achieve a defect-free interface, thus exhibiting superior gas separation performance compare to the pure polymer membrane.

In summary, this thesis has developed a nanoscale understanding of polymer structure near a surface for the information necessary to design MMMs. This investigation also includes strategies to minimise the interfacial defects such as nano-scale voids to achieve separation performances surpassing the Robeson upper bound limit in MMM membranes.

Declaration by author

This thesis *is composed of my original work, and contains* no material previously published or written by another person except where due reference has been made in the text. I have clearly stated the contribution by others to jointly-authored works that I have included in my thesis.

I have clearly stated the contribution of others to my thesis as a whole, including statistical assistance, survey design, data analysis, significant technical procedures, professional editorial advice, financial support and any other original research work used or reported in my thesis. The content of my thesis is the result of work I have carried out since the commencement of my higher degree by research candidature and does not include a substantial part of work that has been submitted *to qualify for the award of any* other degree or diploma in any university or other tertiary institution. I have clearly stated which parts of my thesis, if any, have been submitted to qualify for another award.

I acknowledge that an electronic copy of my thesis must be lodged with the University Library and, subject to the policy and procedures of The University of Queensland, the thesis be made available for research and study in accordance with the Copyright Act 1968 unless a period of embargo has been approved by the Dean of the Graduate School.

I acknowledge that copyright of all material contained in my thesis resides with the copyright holder(s) of that material. Where appropriate I have obtained copyright permission from the copyright holder to reproduce material in this thesis and have sought permission from co-authors for any jointly authored works included in the thesis.

Publications included in this thesis

1. Ravi C. Dutta and SK. Bhatia, Transport diffusion of light gases in polyethylene using atomistic simulations, *Langmuir*, 33, 936 (2017)

2. Ravi C. Dutta and SK. Bhatia, Structure and gas transport at the polymer–zeolite Interface: Insights from molecular dynamics simulations, *ACS Appl. Mater. Interfaces*,10, 5992 (2018).

3. Ravi C. Dutta and SK. Bhatia, Interfacial barriers to gas transport in zeolites: distinguishing internal and external resistances, *Phys. Chem. Chem. Phys.*, 20, 26386 (2018)

4. Ravi C. Dutta and SK. Bhatia, Interfacial barriers to gas transport: probing solid-gas interfaces at the atomistic level, *Mol.Simul.,* DOI:10.1080/08927022.2019.1635694 (2019)

5. Ravi C. Dutta and SK. Bhatia, Atomistic Investigation of Mixed-Gas Separation in a Fluorinated Polyimide Membrane, *ACS Appl. Polym. Mater.,* 16,1359 (2019)

Submitted manuscripts included in this thesis

No manuscripts submitted for publication.

Other publications during candidature

Peer-reviewed papers

Ravi C. Dutta and SK. Bhatia, Transport diffusion of light gases in polyethylene using atomistic simulations, *Langmuir,* 33, 936 (2017)

Ravi C. Dutta and SK. Bhatia, Structure and gas transport at the polymer–zeolite Interface: Insights from molecular dynamics simulations, *ACS Appl. Mater. Interfaces*, 10, 5992 (2018).

Ravi C. Dutta and SK. Bhatia, Interfacial barriers to gas transport in zeolites: distinguishing internal and external resistances, *Phys. Chem. Chem. Phys.*, 20, 26386 (2018)

Ravi C. Dutta and SK. Bhatia, Atomistic Investigation of Mixed-Gas Separation in a Fluorinated Polyimide Membrane, *ACS Appl. Polym. Mater.*, 16,1359 (2019)

Ravi C. Dutta and SK. Bhatia, Interfacial barriers to gas transport: probing solid-gas interfaces at the atomistic level, *Mol.Simul.,* DOI:10.1080/08927022.2019.1635694 (2019)

Conference abstracts

Ravi C. Dutta and SK. Bhatia, Mixed Gas Adsorption in Polyimides: Insights from Molecular Dynamics Simulations, 13th International Conference on the Fundamentals of Adsorption, Cairns, Australia, May 2019.

Ravi C. Dutta and SK. Bhatia, Gas Transport at the Polymer-Zeolite Interface Using Atomistic Simulations, AIChE Annual Meeting, Pittsburg, USA, Nov 2018.

Contributions by others to the thesis

Contributions were made by Prof. Suresh Kumar Bhatia in concept, analysis, interpretation, drafting, and writing in the advisory capacity.

Statement of parts of the thesis submitted to qualify for the award of another degree

No works submitted towards another degree have been included in this thesis.

Research Involving Human or Animal Subjects

No animal or human subjects were involved in this research.

Acknowledgements

Firstly, I would like to express my sincere gratitude to my principal advisor Prof. Suresh Kumar Bhatia for his continuous support, patience, motivation, and immense knowledge. His guidance helped me in all the time of research and writing of this thesis. His willingness to give his time so generously has been very much appreciated. I could not have imagined having a better mentor for my Ph.D. I would like to also thank my co-advisor Dr. Timothy Nicholson, for his support.

Besides my advisory team, I would like to thank my thesis committee members: A/Prof. Greg Birkett and A/Prof. Simon Smart for their time, insightful comments and encouragement. Also, I would like to thank A/Prof. Greg for giving me an opportunity as a tutor. My special thanks are extended to the staff of post-graduate team at the school of chemical engineering, especially to Siu and June, for their great support during my initial days at UQ.

My sincere thanks to Prof. Jayanth Kumar Singh at IIT Kanpur for his constant support and encouragement.

I am grateful to Mrs. Rajya Lakshmi, who have provided me moral and emotional support throughout this journey and my life in general.

I thank all my friends for the stimulating discussions, and for all the fun we have had in the last three years. My special thanks to Dr. Rohit, Dr. Gloria, Dr. Piyali, Dr. Kaustav, Dr. Qinglan, Dr. Pawarisa and Dr. Nur for their unconditional love towards me. My special words of gratitude to Dr. Lang Liu, Dr. Srinivas Varanasi and Dr. Ashok Nanjundanan for all their personal and professional help that they have extended to me throughout.

To Goutham, Prhashanna, PB and Monika: you should know that your support and encouragement is worth more than what I can express on paper.

I am extremely grateful to my parents for their love, support and the sacrifices they have made for me. I am also thankful to Nalini for always believing, encouraging and being there for me. My special thanks to the best people of my life: Sitaamma, Dr. Sravan, Shashidhar, Ram Charan, Harsha and Madhuri. Last but not the least, I am very thankful to Pranav Karthikeya for his great support.

Financial support

This research was supported by The University of Queensland International Scholarship.

Keywords

Mixed matrix membranes, organic-inorganic interface, gas separation, Maxwell-Stefan formalism, molecular dynamics, Monte Carlo simulations, transport diffusion, zeolites, MOFs, interfacial resistance

Australian and New Zealand Standard Research Classifications (ANZSRC)

ANZSRC code: 090404, Membrane and Separation Technologies, 100%

Fields of Research (FoR) Classification

FoR code: 0904, Chemical Engineering, 100%

Table of Contents

List of Figures

List of Tables

List of Abbreviations

EMD: Equilibrium Molecular Dynamics

GCMC: Grand Canonical Monte Carlo

MMM: mixed matrix membrane

PI: polyimide

PEI: polyetherimide

PIM: polymers of intrinsic micro porosity

TR: thermally rearranged

PE: polyethylene

BPDA-APB: biphenyltetracarboxylic dianhydride and 1,3-bis(4-aminophenoxy) benzene

6FDA-durene: 4,4′-hexafluoroisopropylidene diphthalic anhydride, 2,3,5,6-tetramethyl-1,4-phenylenediamine

PMP: poly 4-methyl-2-pentyne

MSD: mean square displacement

IAST: ideal adsorbed solution theory

PSD: pore size distribution

FFV: fractional free volume

FVE: fractional volume elements

DMS: dual-mode sorption

IL: ionic liquid

DFT: density functional theory.

Chapter 1 Introduction

1.1 Background

Efficient separation of fluid mixtures into their constituents is critical to the performance of a range of industrial applications including adsorption, molecular-sieving, catalysis, sensing, electro chemical storage, drug delivery and ion-exchange.[1-3] Membranes permit selective mass transport driven by concentration or chemical potential gradient, and have become pervasive with the advantages of modularity, scalability, compactness and high energy efficiency.[3] Fluid transport across a membrane, depending on the properties of the fluid as well as the membrane, can be described through Knudsen-diffusion, molecular sieving or solution-diffusion mechanism, as shown in Figure. 1.1.

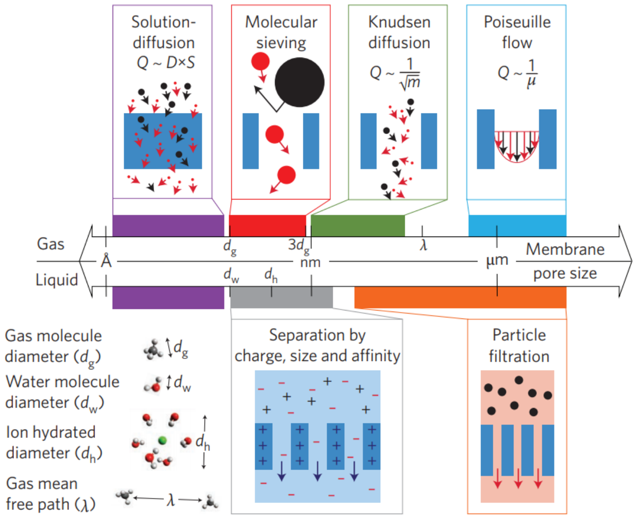

Figure 1-1:Length-scale dependence of membrane transport mechanisms. Relative scales of gas and water molecules, hydrated ions and gas mean free path are depicted on bottom. Q, flux; D, diffusivity; S, sorption coefficient; m, molecular mass; μ, viscosity. Adapted by permission from ref [2], Copyright 2017.

In a dense, non-porous membrane, solution-diffusion mechanism provides a convenient framework to describe the gas transport, where the fluid molecules at high pressure condition are adsorbed onto the surface of the membrane in the feed side. Subsequently gas molecules diffuse across the membrane based on the difference in thermodynamic activities (concentration gradient and pressure gradient), and gas molecules are desorbed in the low pressure side or permeate phase of the membrane.

1.2 Membrane performance

The separation performance of a membrane for any given gas pair is characterized by permeability and selectivity. The permeability coefficient (P_i) is the product of gas flux (N_i) and membrane thickness (δ), divided by the pressure difference (Δp_i) across the membrane, following:

$$P_i = \frac{N_i.\delta}{\Delta p_i} \tag{1-1}$$

Further, membrane selectivity for a given gas pair ($\alpha_{i/j}$) is the ratio of permeability coefficients of the two gases, following:

$$\alpha_{i/j} = \frac{P_i}{P_j} \tag{1-2}$$

The higher is the permeability the lower will be the required membrane area to treat a given amount of gas leading to low capital costs. Further, the higher the selectivity the higher will be the has purity in the product. Thus, membranes that demonstrate high permeability as well as high selectivity are desirable. In addition, membranes should be defect-free in large scale, with high thermal, chemical, and mechanical stabilities.

1.3 Membrane types

Membranes are classified into polymeric and inorganic membranes, depending on the type of material used to prepare them.

Polymer membranes: Polymer membranes are used commercially to separate important gas mixtures, owing to their excellent processability, easy scale-up, reproducibility for large scale production, low cost of fabrication and feasibility in various modules.[4-6] Polymeric membranes are normally robust and exhibited promising results in gas separation; however, a trade-off relation between the permeability and selectivity is observed for most of the polymer membrane materials,[7, 8] as shown in Figure 1.2. This trade-off relation indicating an increase in permeability of a polymer to gas *i*, P_i, leads to decrease in selectivity of the polymer for gas *i* over gas *j*, $\alpha_{i/j}$, following:[7, 9]

$$\alpha_{i,j} = \beta_{i,j} P_i^{-\lambda_{i,j}} \tag{1-3}$$

where $\lambda_{i,j}$ and $\beta_{i,j}$ are empirical parameters depend on the gas pair. The values for these parameters of many common gas pairs has been reported in the literature.[8-10] Freeman developed a theory to understand this upper bound relation in polymer materials and suggested that simultaneous increase in backbone stiffness and interchain separation can lead to a membrane with high permeability as well as high selectivity.[9] Over the last decade, much effort has been devoted to modify the existing polymer materials including polymer backbone structure modification,[6, 11] as well as develop new polymer materials such as polymers of intrinsic microporosity (PIMs),[12] thermally rearranged (TR) polymers[13, 14] to achieve high permeability as well as high selectivity; however, the success is modest. This has created much interest in the development of alternative membrane materials.

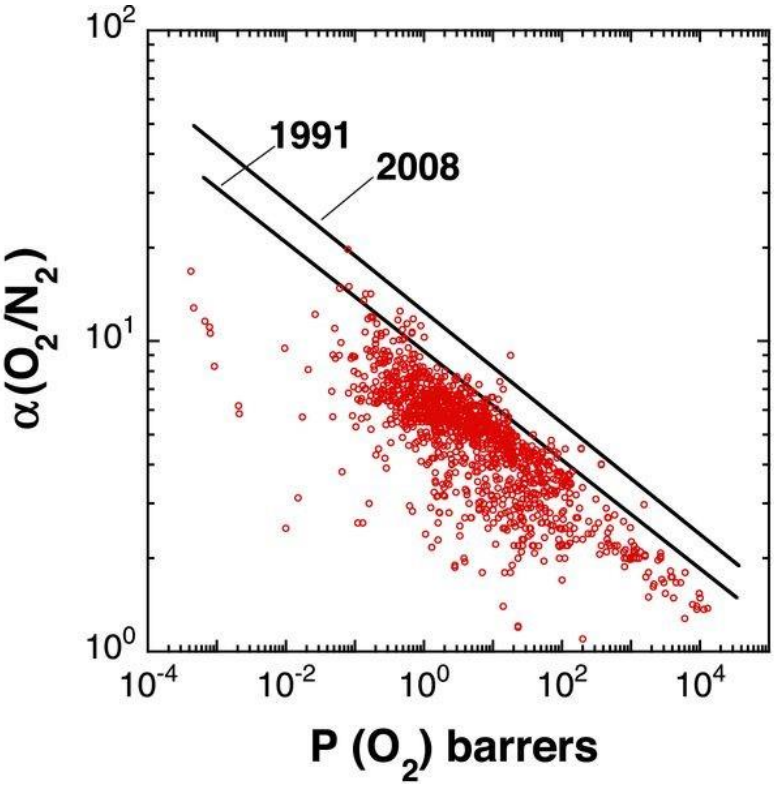

Figure 1-2:Upper bound correlation for O_2/N_2 separation in polymeric membranes. Taken from ref [7,15].

Inorganic membranes: Inorganic membrane materials are well-defined crystalline materials with ordered structures, high porosity, *excellent thermal and chemical stabilities*. These membrane materials can perform well above the permeability/selectivity trade-off.[16-19] Recent progress in the syntheses of nonporous solids, has given rise to an impressive array of new structures, such as metal organic and zeolitic imidazole framework materials (MOFs and ZIFs respectively), which are considered potentially attractive for technological exploitation for gas separation. The future directions for these new membrane materials are very promising, primarily because of the enormous chemical flexibility of their base structures. However, it is still difficult and expensive to fabricate large membranes due to their fragile structure. Therefore, polymeric membranes are still attractive but alternate approaches that can enhance their gas separation characteristics well above the Robeson upper-bound are needed. This leads to the development of Mixed-matrix membranes (MMM).

Mixed-matrix membranes: MMMs comprise fillers of nanoscale size blended with polymer. The bulk phase is typically a polymer and the dispersed phase represents the inorganic particles. These fillers can be of conventional materials such as zeolites, carbon nanotubes (CNTs), or advanced materials such as MOFs, metal–organic polyhedral (MOP) porous aromatic frameworks (PAFs), covalent organic frameworks (COFs) and graphene, as shown Figure 1.3. By combining the advantages of each material: for instance, the flexibility and processability of polymers, and the selectivity and thermal stability of the inorganic fillers, MMMs have the potential to achieve higher selectivity as well as higher permeability relative to existing polymeric membranes.

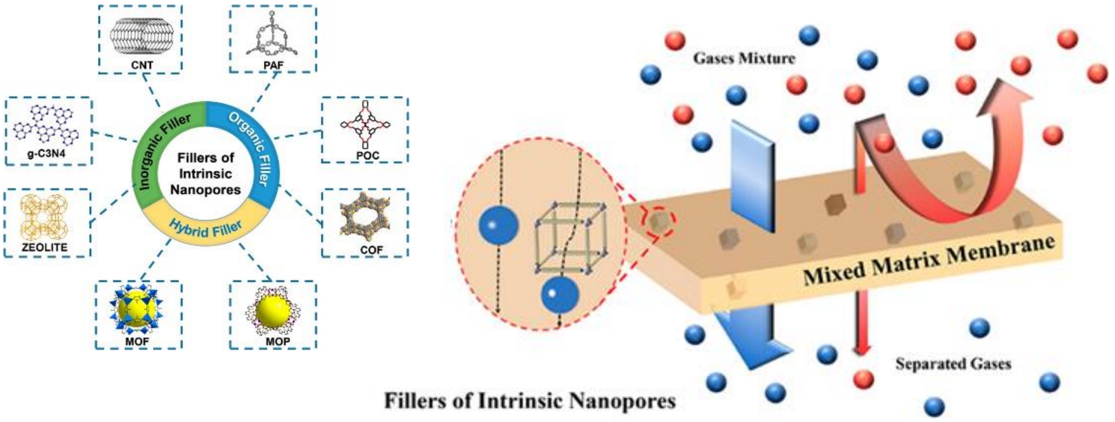

Figure 1-3: Schematic representation of MMM. Reprinted with permission from ref [20]. Copyright 2019 American Chemical Society.

1.4 Challenges

Although MMMs present an attractive approach to develop a membrane with high permeability as well as high selectivity, the ultimate success of these advanced membranes depends on material selection and interface defect elimination. The polymer–filler interface can be of four types, depending on the nature of interaction between the constituents, as highlighted in Figure 1.4. First is an ideal interface with properties nearly similar to those of the bulk polymer, which arises when polymer–filler and polymer–polymer interactions are comparable, leading to a homogenous polymer–filler blend. Second, when the polymer–filler interaction is weaker than the polymer–polymer interaction, net repulsion between the polymer and filler occurs, leading to the formation of nonselective interfacial voids around the filler or “sieve in a cage” configuration. Such a MMM results in higher permeability with reduction in selectivity, as the gas molecules take the least resistance path offered by the voids.[21] Furthermore, these voids can affect the mechanical integrity of the membrane. The third is the formation of a rigidified layer of polymer at the interface because of the attractive interaction between the polymer and filler promoted by a stronger polymer–filler interaction compared with the polymer–polymer interaction. This polymer in the rigidified layer has a more restricted chain motion than that in the bulk, which reduces gas permeability. This results in reduction in both permeability and selectivity.[22] The last is plugged sieves, in which the surface pores of the zeolites have been partially blocked by the polymer. This leads to reduction in the gas permeability in the composite system.[23] Thus, the nature of the polymer–filler interface can strongly affect the overall membrane performance. In addition, poor dispersion of the inorganic filler contributes to its agglomeration in the polymer matrix.[24] This deteriorates the properties of membrane, particularly when dealing with high loading compositions of inorganic filler. Thus, understanding and minimizing interfacial barriers between the polymer and the inorganic filler are therefore critical to the design and optimization of such membranes. Therefore, a nanoscale understanding of polymer structure near a surface is necessary to develop a defect free MMM that demonstrates high permeability as well as high selectivity.

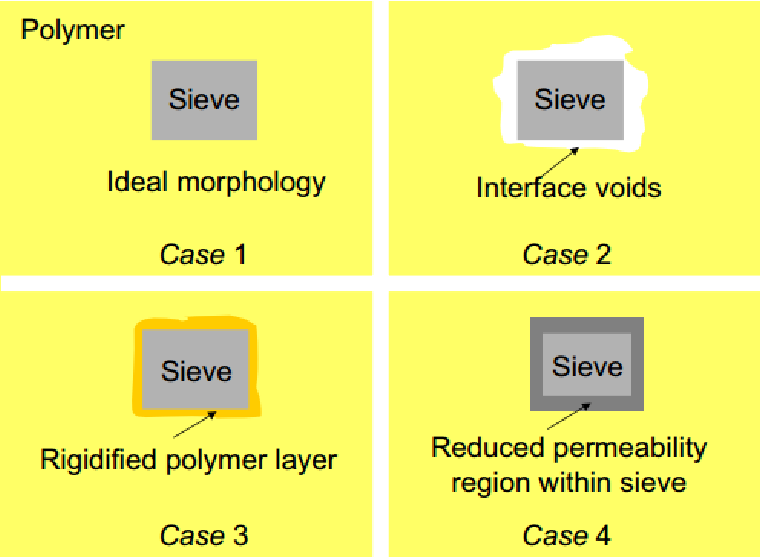

Figure 1-4: Schematic representation of interfacial defects in MMM. Reprinted with permission from ref [20].

1.5 Objectives

This thesis aims to develop a nanoscale understanding of polymer structure near a surface for the information necessary to design advanced membrane-based gas separation technologies such as MMMs. This investigation also includes strategies to minimise the interfacial defects such as nano-scale voids/ polymer rigidification to achieve MMM separation performance surpassing the Robeson upper bound limit.

This thesis has the following objectives:

- Determine single component gas separation characteristics of neat polymer membranes including sorption isotherms, considering polymer structural transitions upon gas sorption.

- Determine multi-component gas transport characteristics in the neat polymer membrane including sorption isotherms, considering polymer structural transitions upon gas sorption.
- Develop an EMD-based simulation method to determine the interfacial as well as internal transport resistance for gases in inorganic membrane materials (fillers). Screening and selection of appropriate combination of polymer and filler for a given gas pair.
- Fundamental understanding of polymer-surface interactions to capture the structure-property relationships of interfacial layers at the nanoscale, by employing force field based atomistic modelling techniques.
- Determine the pure component separation performance of a MMM having a homogenous polymer-filler blend using EMD simulations.

1.6 Structure of the thesis

This thesis is arranged into individual chapters that address the research objectives presented in section 1.5, as summarized below:

Chapter 1. Introduction

The practical significance of conducting this research highlighting the challenges with the current spectrum of membrane materials is discussed in this chapter. Further, the objectives and structure of the present thesis are included in this chapter.

Chapter 2. Literature Review

In this chapter, we discuss the state-of-the-art experimental and simulation techniques employed to understand the polymer-inorganic interfaces and associated challenges highlighting the earlier works.

Chapter 3. Computational Model and Methodology

In chapter 3, computational models used to describe the polymer, inorganic filler and polymer-filler hybrid systems are discussed. Further, methodology implemented to extract the gas diffusion and solubility coefficients are presented.

Chapter 4. Pure component Gas Transport in a Polymer Membrane

In this chapter, we investigate the gas sorption and transport characteristics of a neat polymer membrane in pure gas conditions. Firstly, polymer structure is characterized by extracting the polymer structure-property relations. Further, the gas sorption isotherms are extracted using a two-step methodology combining grand canonical Monte Carlo simulations (GCMC) coupled with NPT (constant number of particles, pressure, and temperature) equilibrium molecular dynamics (EMD) simulations. In addition, we extracted Maxwell-Stefan diffusivities of the gases in pure gas conditions in a neat polymer membrane.

Chapter 5. Multi-component Gas Transport in a Polymer Membranes

In this chapter, we investigate the gas separation characteristics of a fluorinated polyimide polymer membrane in mixed gas conditions by considering an equimolar mixture of CO_2 and CH_4. In addition, the membrane performance in practical scenarios is predicted by solving the Maxwell-Stefan equations for a given membrane thickness and driving force, from the simulation based microscopic diffusivities and sorption characteristics.

Chapter 6. Gas Transport in Filler Materials

In this chapter, contributions of internal and external barriers to the permeation of methane in different classes of zeolites are determined. Furthermore, the effect of the presence of dense external media such as polymer on gas permeation in the zeolites is explored.

Chapter 7. Structure and Gas Transport at the Polymer-Zeolite Interface

In this chapter, we explore the microscopic structure of the polymer at the polymer–MFI zeolite interface and its influence on the gas transport in a model MMM system in detail through EMD simulations. Furthermore, an insight into the gas diffusion at the interface (rigidified region) between the polymer and filler is explored and presented.

Chapter 8. Interfacial Engineering of Polyimide-ZIF8 Mixed Matrix Membrane

In this chapter, the structure of 6FDA-durene polyimide polymer near a zeolitic imidazolate framework (ZIF-8) surface is investigated. In addition, the strategies to promote the interface compatibility between the polymer and filler is presented.

Chapter 9. Conclusions and Perspectives

This chapter summarizes the major findings from this investigation. The possible future investigations based on this study are also recommended in this chapter.

1.7 References

1. Kärger, J.; Ruthven, D. M.; Theodorou, D. N., *Diffusion in Nanoporous Materials*. Wiley-VCH Verlag & Co. KGaA: Boschstr. 12, 69469 Weinheim, Germany, 2012; Vol. 1.

2. Wang, L.; Boutilier, M. S. H.; Kidambi, P. R.; Jang, D.; Hadjiconstantinou, N. G.; Karnik, R., Fundamental transport mechanisms, fabrication and potential applications of nanoporous atomically thin membranes. *Nat. Nanotechnol.* **2017,** *12,* 509.

3. Baker, R. W., Future Directions of Membrane Gas Separation Technology. *Ind. Eng. Chem. Res.* **2002,** *41* (6), 1393-1411.

4. Favre, E., 2.6 Polymeric Membranes for Gas Separation. In *Comprehensive Membrane Science and Engineering (Second Edition)*, Drioli, E.; Giorno, L.; Fontananova, E., Eds. Elsevier: Oxford, 2017; pp 124-175.

5. *Polymeric Gas Separation Membranes*. 1 ed.; CRC Press: Boca Raton,FL,USA 1994.

6. *Materials Science of Membranes for Gas and Vapor Separation*. John Wiley & Sons, Ltd: The Atrium, Southern Gate, Chichester,West Sussex PO198SQ, England, 2006.

7. Robeson, L. M., The upper bound revisited. *J. Membr. Sci.* **2008,** *320* (1), 390-400.

8. Robeson, L. M., Correlation of separation factor versus permeability for polymeric membranes. *J. Membr. Sci.* **1991,** *62* (2), 165-185.

9. Freeman, B. D., Basis of Permeability/Selectivity Tradeoff Relations in Polymeric Gas Separation Membranes. *Macromolecules* **1999,** *32* (2), 375-380.

10. Robeson, L. M.; Burgoyne, W. F.; Langsam, M.; Savoca, A. C.; Tien, C. F., High performance polymers for membrane separation. *Polymer* **1994,** *35* (23), 4970-4978.

11. Li, X.; Singh, R. P.; Dudeck, K. W.; Berchtold, K. A.; Benicewicz, B. C., Influence of polybenzimidazole main chain structure on H2/CO2 separation at elevated temperatures. *J. Membr. Sci.* **2014,** *461*, 59-68.

12. Budd, P. M.; Elabas, E. S.; Ghanem, B. S.; Makhseed, S.; McKeown, N. B.; Msayib, K. J.; Tattershall, C. E.; Wang, D., Solution-Processed, Organophilic Membrane Derived from a Polymer of Intrinsic Microporosity. *Adv. Mater.* **2004,** *16* (5), 456-459.

13. Moon, J. D.; Bridge, A. T.; D'Ambra, C.; Freeman, B. D.; Paul, D. R., Gas separation properties of polybenzimidazole/thermally-rearranged polymer blends. *J. Membr. Sci.* **2019,** *582*, 182-193.

14. Park, H. B.; Jung, C. H.; Lee, Y. M.; Hill, A. J.; Pas, S. J.; Mudie, S. T.; Van Wagner, E.; Freeman, B. D.; Cookson, D. J., Polymers with Cavities Tuned for Fast Selective Transport of Small Molecules and Ions. *Science* **2007,** *318* (5848), 254-258.

15. Park, H. B.; Kamcev, J.; Robeson, L. M.; Elimelech, M.; Freeman, B. D., Maximizing the right stuff: The trade-off between membrane permeability and selectivity. *Science* **2017,** *356* (6343), eaab0530.

16. Kumar, R.; Koros, W. J., 110th Anniversary: High Performance Carbon Molecular Sieve Membrane Resistance to Aggressive Feed Stream Contaminants. *Ind. Eng. Chem. Res.* **2019,** *58* (16), 6740-6746.

17. Singh, A.; Koros, W. J., Significance of Entropic Selectivity for Advanced Gas Separation Membranes. *Ind. Eng. Chem. Res.* **1996,** *35* (4), 1231-1234.

18. Koros, W. J.; Zhang, C., Materials for next-generation molecularly selective synthetic membranes. *Nature Materials* **2017,** *16*, 289.

19. Rungta, M.; Zhang, C.; Koros, W. J.; Xu, L., Membrane-based ethylene/ethane separation: The upper bound and beyond. *AIChE J.* **2013,** *59* (9), 3475-3489.

20. Wang, Y.; Wang, X.; Guan, J.; Yang, L.; Ren, Y.; Nasir, N.; Wu, H.; Chen, Z.; Jiang, Z., 110th Anniversary: Mixed Matrix Membranes with Fillers of Intrinsic Nanopores for Gas Separation. *Ind. Eng. Chem. Res.* **2019,** *58* (19), 7706-7724.

21. Husain, S.; Koros, W. J., Mixed matrix hollow fiber membranes made with modified HSSZ-13 zeolite in polyetherimide polymer matrix for gas separation. *J. Membr. Sci.* **2007,** *288* (1), 195-207.

22. Li, Y.; Chung, T.-S.; Cao, C.; Kulprathipanja, S., The effects of polymer chain rigidification, zeolite pore size and pore blockage on polyethersulfone (PES)-zeolite A mixed matrix membranes. *J. Membr. Sci.* **2005,** *260* (1), 45-55.

23. Ding, X.; Li, X.; Zhao, H.; Wang, R.; Zhao, R.; Li, H.; Zhang, Y., Partial pore blockage and polymer chain rigidification phenomena in PEO/ZIF-8 mixed matrix membranes synthesized by in situ polymerization. *Chinese Journal of Chemical Engineering* **2018,** *26* (3), 501-508.

24. Fang, M.; Wu, C.; Yang, Z.; Wang, T.; Xia, Y.; Li, J., ZIF-8/PDMS mixed matrix membranes for propane/nitrogen mixture separation: Experimental result and permeation model validation. *J. Membr. Sci.* **2015,** *474*, 103-113.

Chapter 2 Literature Review

The content of this chapter is published as:

Ravi C. Dutta and SK. Bhatia, Interfacial barriers to gas transport: probing solid-gas interfaces at the atomistic level, *Mol.Simul.,* DOI:10.1080/08927022.2019.1635694 (2019)

Contributor	Statement of contribution
Ravi C Dutta	Wrote the paper (80%)
Suresh K. Bhatia	Wrote the paper (20%)

The past decade has witnessed substantial both theoretical and experimental progress in the selection aspects of Mixed matrix membrane (MMM) materials for a given application by considering fundamental intrinsic material properties of the individual phases. On the other hand, interface-related problems such as the formation of nonselective voids, rigidified polymers, and pore blockage are still challenging. Although the polymer–filler interface occupies only a small fraction of the membrane volume, it appears to affect the MMM performance significantly. Thus, understanding and minimizing interfacial barriers between the polymer and the inorganic filler are critical to the design and optimization of such membranes. Consequently there is a growing need to develop techniques for characterizing the interfacial structure of polymers near a surface and elucidate the underlying mechanisms. In this chapter, a brief summary of the major findings in the development MMMs for gas separation highlighting the various interfacial defects in MMMs is provided. In addition, we also present a brief review on the nature of interfacial barriers and their contribution to gas transport in inorganic filler materials such as CNTs and zeolites.

2.1 Experimental investigations

MMMs have been extensively investigated over the past few years to realize high performance for gas separation, as theoretically demonstrated by Koros et al.[1] However, most experimental investigations fail to manifest the separation performance that transcends the permeability-selectivity trade-off, which is attributed to non-ideal interfacial morphology of the polymer that significantly deteriorates membrane performance.[2, 3] While much effort has been devoted to the experimental design and fabrication of defect free MMMs for gas transport in the literature, success has been modest. Nair et al.[4] fabricated a defect free MMM comprising sub-micrometer size ZIF-90 and polyimide (PI), demonstrating superior separation performance for CO_2 over CH_4. Kim et al.[5] successfully synthesized a defect free MCM-48 silica/polysulfone MMM and reported an increase in gas permeability resulting from increase in both solubility and diffusivity without sacrificing selectivity. Merkel et al.[6] found that inclusion of nonporous, nanoscale, fumed silica particles in glassy amorphous poly 4-methyl-2-pentyne (PMP), enhances both membrane permeability and selectivity for n-butane over methane, as shown in Figure 2-1. This is attributed to the disruption of polymer chain packing induced by silica particles, leading to an increase in free volume.

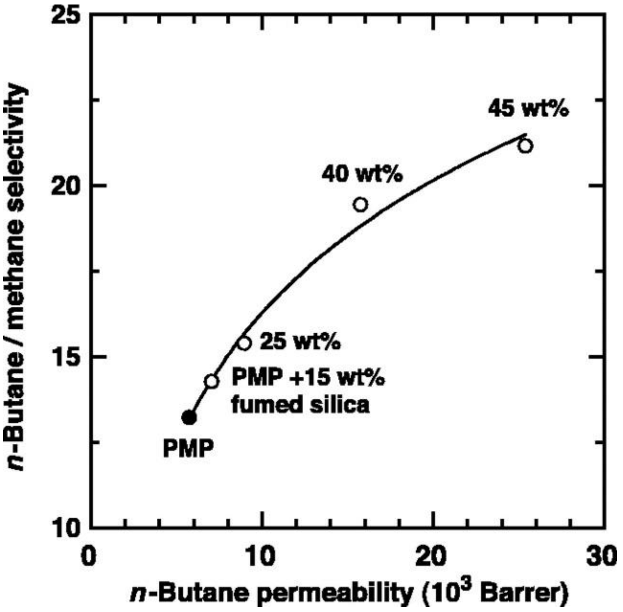

Figure 2-1: The effect of fumed silica content on n-butane permeability and n-butane/methane selectivity of glassy PMP. These data were acquired at 25°C from mixtures composed of 98 mole % methane and 2 mole %n-butane at a feed pressure of 11.2 atm and a permeate pressure of 1 atm. From ref. [6]. Reprinted with permission from AAAS.

On the other hand, several investigations have reported the presence of interfacial defects in MMMs,[7-9] and proposed methods to improve the polymer-filler compatibility. A review highlighting major challenges in MMMs and the strategies to tackle these problems has been discussed by Dong et al.[10] In addition, the progress and opportunities in the area of MMMs has been discussed in detail in several review articles.[11-15] In this section, we will highlight various types of non-ideal interfacial morphology of the polymer that exits in MMMs and its influence on gas transport characteristics, as depicted in Figure 2-2.

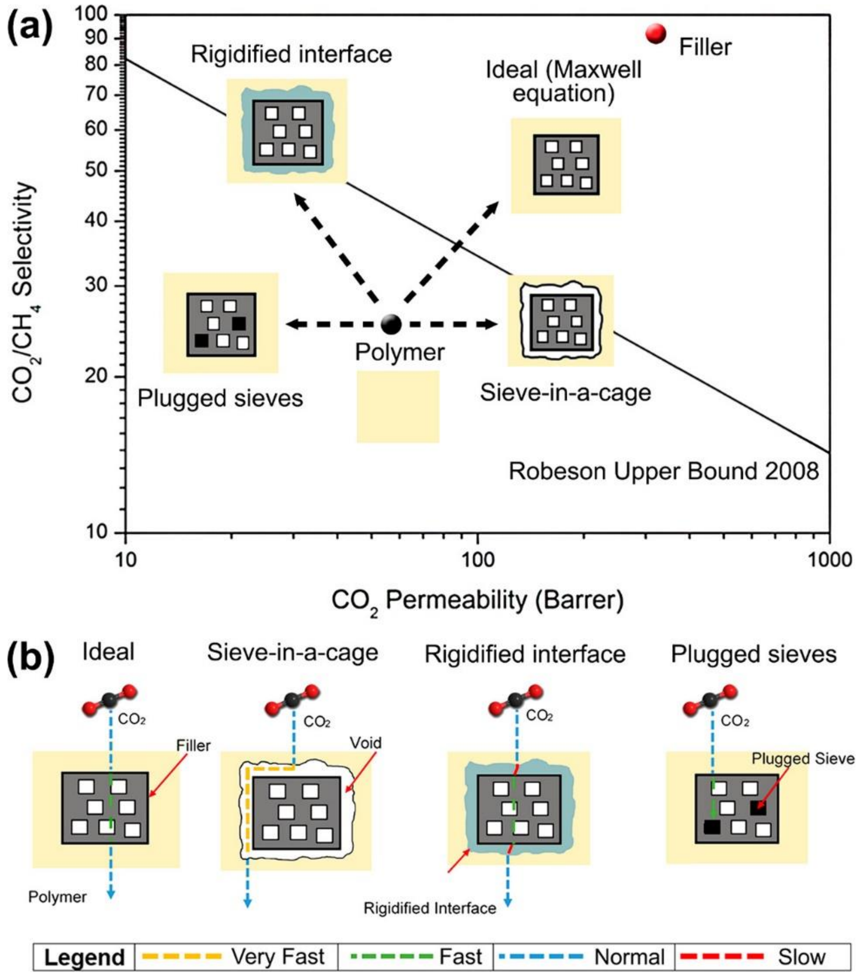

Figure 2-2: (a) Impact of ideal (following prediction from Maxwell Equation) and nonideal morphologies on the performances of composite membranes, and (b) Signature CO_2 transport profiles of various interfacial morphologies of composite membranes. The normal profile refers to the diffusivity of CO_2 molecules in the polymer phase. Reprinted with permission from ref. [12]. Copyright 2018 American Chemical Society

2.1.1 Polymer rigidification

The formation of a rigidified layer of polymer at the interface is due to the attractive interaction between the polymer and filler promoted by a stronger polymer–filler interaction compared with the polymer–polymer interaction. The gas transport in the rigidified polymer region is distinctively different as compared to that in the bulk polymer. This can be attributed to reduced fractional free volume as well as restricted chain motion of the polymer in the interfacial region. This leads to a decrease in the diffusivity as well as sorption of the gas molecules and thus lowers the gas permeability. The gas permeability in this rigidified interface can be up to an order of magnitude smaller than that of the corresponding neat polymer membrane.[16] Such a reduction has a great effect on the separation performance of a MMM especially at high filler loadings. Further, the intensity of rigidification determines overall membrane performance. For instance, the reduction in permeability of the gases in the rigidified interface can potentially compensate for increase in gas diffusivity through the filler, leading to an overall reduction in the membrane. Several experimental investigations have reported a decrease in gas permeability by the inclusion of filler in a polymer matrix compared to that of corresponding neat polymer membrane.[17-25] On the other hand, the perm-selectivity can increase or remain the same depending on the available free volume in the rigidified region as well as size of the fluid molecules. For example, around 20% reduction in the permeability for N_2 and O_2, while 60% for CO_2 and H_2 in MMM compared to the corresponding neat polymer membrane, leading to an increase in selectivity of CO_2/N_2 and H_2/CH_4 has been reported.[22] However, the direct experimental characterization of the rigidified region and determining the gas transport properties in this region is still challenging. Thus, indirect methods such as calculation of glass transition temperature in the MMM are used, as shown in Figure 2-3.

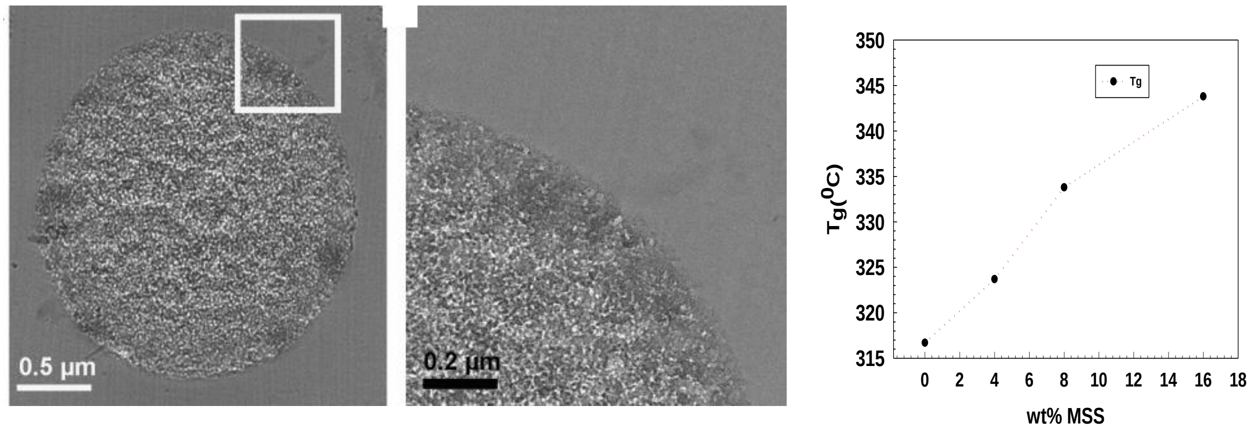

Figure 2-3:TEM images of a calcined meso porous silica surface within PI phase, and (b) variation of glass transition (Tg) temperature with filler loading. Reprinted from ref. [19]. Copyright 2011, with permission from Elsevier.

2.1.2 Sieve-in-a-cage (Leaky) Interface

The sieve-in-a-cage type morphology at the interface is essentially as a result of weak polymer–filler interaction compared to the polymer–polymer interaction, net repulsion between the polymer and filler occurs, leading to the formation of nonselective interfacial voids around the filler or “sieve in a cage” configuration. This resulting in a region of high free volume between the polymer matrix and filler and such a MMM results in higher permeability with reduction in selectivity, as the gas molecules take the least resistance path offered by the voids. For example, a sharp increase in CO_2 permeability and decrease in perm-selectivity of CO_2 over CH_4 compared to that of Maxwell model predictions with inclusion of zeolite 4A in Matrimid polymer has been reported.[26] This is attributed to leakage of gas molecules along the nanometric interface. Koros et al. characterized "sieve in a cage" morphology of the polymer in a MMM system having zeolite 4A dispersed in Ultem polymer through microscopic images, indicating voids at the interface, as shown in Figure 2-4.[27] In addition, the amount of dispersing agent used to cast the membrane can result in voids at the interface. For example, MMMs prepared with a dispersing agent toluene of concentration less than 64 wt.% were found to be defect-free, while membranes prepared with toluene concentration greater than 64 wt.% resulted in MMMs having voids at the interface. [28]

In addition, agglomeration of filler particles that results in the formation of the sieve-in-a-cage morphology. The shape of the filler deviates when they agglomerate, resulting in a wide particle size distribution, leading to a weak interaction with the polymer. A decrease in gas permeability occurs with the inclusion zeolite-13X and zeolite-4A zeolites in PES polymer.[22] This can be attributed to the presence of rigidified polymer at the interface. However, at higher loadings, a sharp increase in gas permeability with increase in filler loading has been reported. This is possibly due to the agglomeration of the filler particles in the membrane that lead to the formation of non-selective voids. A similar observation has been made in a MMM having zeolites particles dispersed in PDMS polymer.[29]

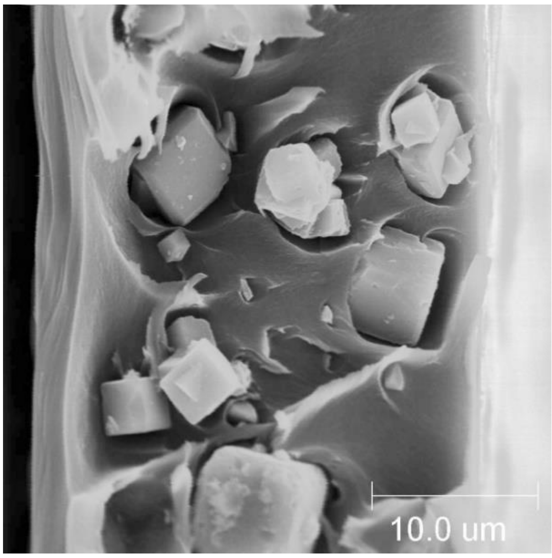

Figure 2-4: Non-selective voids in MMM comprised of zeolite 4A dispersed in Ultem. Adapted with permission from [27]. Copyright, 2007, Wiley.

2.1.3 Plugged sieves

In contrast to the leaky interface, plugged sieves emerge because of inaccessible surface pores of the fillers. This is predominantly due to the partially/complete blockage of the surface pores by the flexible polymer chains. In addition, the surface pores of fillers materials are also blocked by the solvents used in the preparation of MMM, or contaminants that can be present in the feed gas. If the surface pores are completely not accessible, the gas molecules are unable to diffuse through the pores of the filler and the fillers behave like nonporous material. In this case, the membrane selectivity is not enhanced if the fillers do not alter the interfacial structure of the polymer. On the other hand, when the pores are partially available, a decrease in gas permeability in MMM as compared to when the surface pores are completely blocked. In addition, depending on the fluid size, the membrane perm- selectivity can also be affected by the partial plugging of pores.

Further, the nature of the polymer also plays a significant role in determining the interfacial morphology of polymer in MMMs. For instance, the plugged sieve morphology are found to be more prominent when MMMs are prepared with rubbery polymers rather than glassy polymers. As demonstrated by Bae and Long,[30] MMMs prepared by encapsulating Mg_2(dobdc) filler in rubbery polymers such as cross-linked polyethylene oxide (XLPEO) and poly dimethyl siloxane (PDMS), result in a decrease in gas permeability with little increase perm-selectivity. On the other hand, MMMs prepared by encapsulating Mg_2(dobdc) filler in a glassy PI polymer, result in an increase in gas permeability as well as perm-selectivity, in line with theoretical calculations, as shown in Figure 2-5. This difference is attributed to the high mobility of the rubbery polymer chains even at room temperature, resulting in partial/complete pore blockage of filler

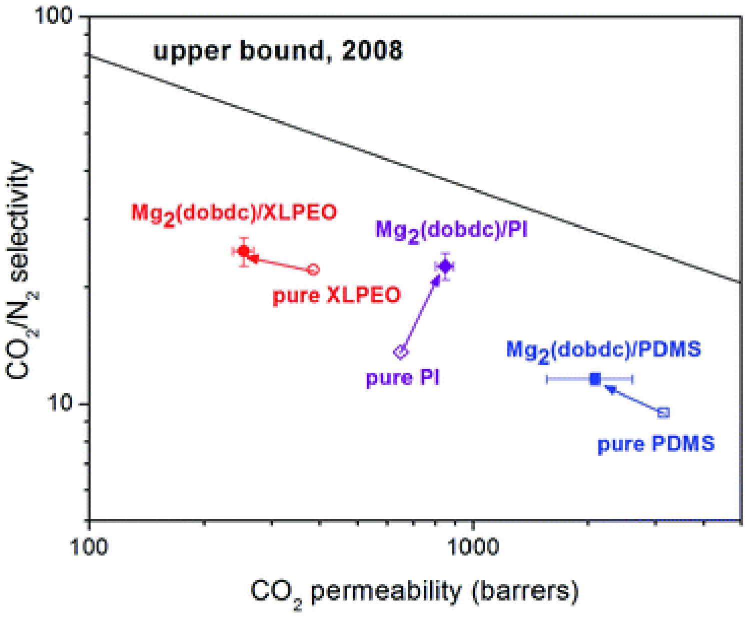

Figure 2-5: Pure component CO_2 and N_2 permeation properties of membranes measured at 2 bar upstream pressure and 25 °C. The Mg_2(dobdc) loadings in composite membranes are 20, 10, and 10 wt% for PDMS, XLPEO and PI, respectively. Reproduced from ref. [30] with permission from The Royal Society of Chemistry.

2.1.4 Strategies to improve the interface

Several strategies to promote the interfacial compatibility between the polymer and inorganic filler are proposed. These strategies include the manipulation of filler surface or polymer backbone by grafting functional groups, or modification filler geometry. Various experimental methods to manipulate the filler surface and/or polymer backbone has been discussed in detail in a recent review.[12, 31] Further, an effective way to obtain well dispersed MOF and restrain agglomeration is by employing "one-pot synthesis" technique,[32] that takes the advantage of using the same solvent for MOF synthesis as well as membrane-casting. In addition, removing water, solvents and other contaminants, which can plug the pores of the filler is considered as a mitigation strategy to avoid the plugged sieves interfacial morphology. Alternatively, surface pores on the filler can be protected using silane coupling agents, that can form covalent bonds on both ends (one end to polymer, while other to the filler).[33] Further, this also helps to avoid sieve-in-a-cage interfacial morphology.[34] However, proper selection of the silane coupling agent is necessary to achieve a defect-free interface, as the poor selection of silane coupling agents can result in non-ideal morphologies such as polymer rigidification and formation of non-selective voids at the interface.[35, 36] Further, inclusion of third phase such as using additional dispersion agent or interface agents such as ionic liquids (ILs) have also been investigated.[37-39]

Among these methods, us of room temperature ionic liquids (ILs) that serve as wetting agent between the filler and polymer shows a great potential due to their unique properties including good intrinsic CO_2 solubility. In addition, stable dispersion of inorganic fillers can be achieved in the presence of ILs due to the strong steric repulsions of the ILs on the ion functionalized filler surface.[40] Lin et al. [41] observed improved gas separation performance when a MMM was fabricated with IL decorated HKUST-1 in PI, as the ILs are successful in restricting the formation of nonselective interfacial voids. Vu et al. [42] successfully fabricated a MMM having micron-sized ZIF-67 coated with a thin layer of IL dispersed in PI polymer, leading to a significant improvement in CO_2/CH_4 gas separation performance, as depicted in Figure 2-6. However, lack of cost-effective ILs demonstrating diverse functionalities for MMM is still challenging.

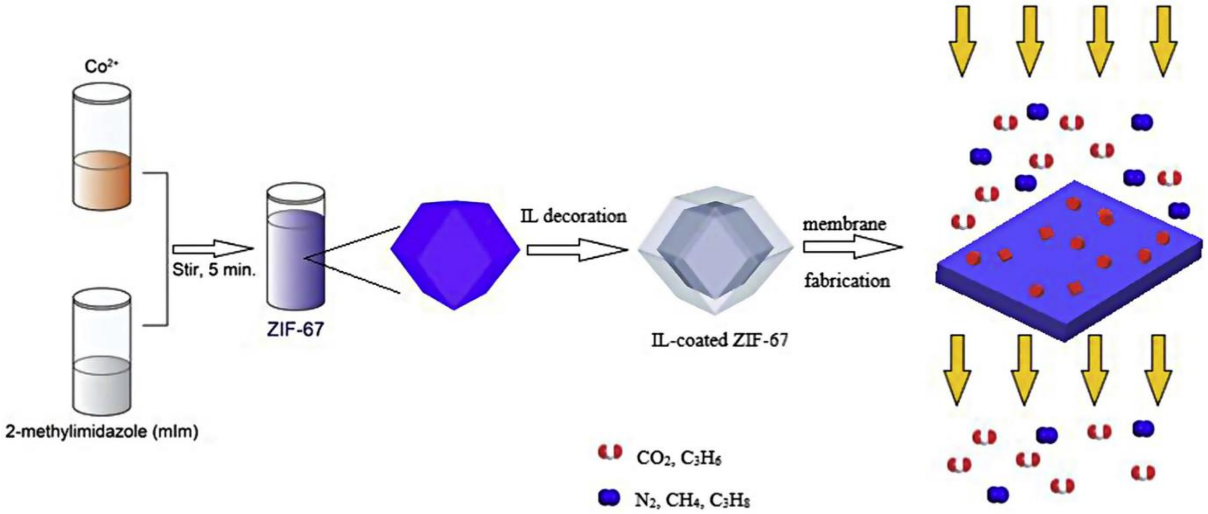

Figure 2-6: Schematic illustration of synthesis process of MMM having micron-sized ZIF-67 coated with a thin layer of IL dispersed in PI. Reprinted from ref. [42]. Copyright 2019, with permission from Elsevier.

2.1.5 Interface characterization techniques:

The polymer near the surface is expected to exhibit significantly different chain and segmental dynamics due to steric hindrance and polymer/nanoparticle (NP) interactions. Ding et al. quantitatively characterize the interface in the carbon nanotube– polycarbonate composite system by direct observation through scanning electron microscope.[43] However, this technique is inapplicable to other particle shapes. In addition, sophisticated techniques such as small-angle neutron scattering (SANS) is employed to probe the structure of polymer-grafted NP and free polymer chains and found that a completely immobilized polymer layer of thickness near the interface.[44] Nevertheless, these investigations demonstrated the existence of a wide distribution of segmental relaxation rates in the interfacial regions. In contrary, Holt et al., by employing advanced techniques such as broadband dielectric spectroscopy (BDS) and small-angle X-ray scattering (SAXS), found that the segmental mobility of the polymer interfacial layer is slower than the bulk polymer by 2 orders of magnitude.[45] Further, interfacial layer thickness in polymer nano-composites is found to be in the range of 1.3 to 5 nm,[45-47] and is independent of the NP concertation in the system, as depicted in Figure 2-7.[45] Thus, current understanding of the structure of the intrinsic interfacial region is incomplete. Indirect measurements such as field emission scanning microscopes (FESEM),[5] positron annihilation lifetime spectroscopy (PALS)[48] and differential scanning calorimetry (DSC)[49] are therefore used. Further, the effect of filler size, shape and loading on the structure of the polymer at the interface and thus gas separation performance is not clear and requires trial and error experimentation.

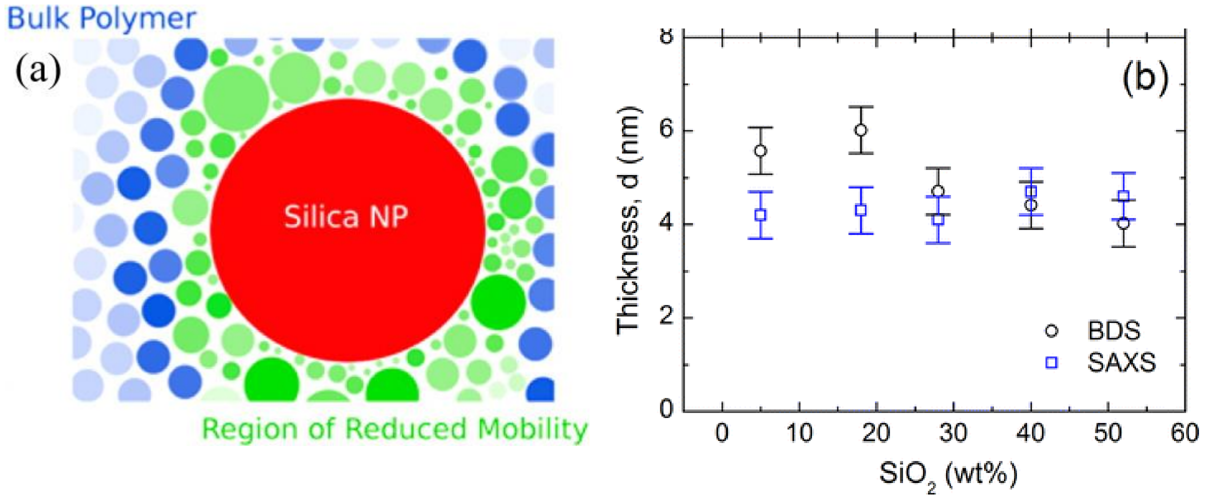

Figure 2-7: (a) Schematic illustration of interface between the polymer and filler in polymer composite materials and (b) calculated interfacial polymer thickness surrounding the silica nanoparticles from different experimental techniques. Reprinted with permission ref. [45]. Copyright 2014 American Chemical Society.

2.2 Modelling investigations:

Tremendous effort has been made in the past to develop models to quantify the effectiveness of a filler in MMMs. Such attempts were aimed to assist the screening and selection of filler particles and to identify the optimum filler loadings to obtain the best gas separation performance.[50] A review highlighting the major models and their advantages as well as limitations have been discussed in-detail by Monsalve-Bravo et al.[51] In this section, a brief summary of the major models are provided. The performance of an ideal MMM can be predicted through one of the earliest models, the Maxwell model,[52] following:

$$P_m = P_c\left[\frac{P_f + 2P_c - 2\phi_f(P_c - P_f)}{P_f + 2P_c + \phi_f(P_c - P_f)}\right] \tag{2-1}$$

where ϕ_f is volume fraction of the filler, P_m, P_c, and P_f are permeabilities in the MMM, filler and continuous phases, respectively. However, recent work has shown that Maxwell model predictions are accurate only at small filler loading below about 20% by volume.[53] Further, the Bruggeman model,[54] based on the dielectric permeability can predict the performance of an ideal MMM accurately even at higher filler loadings. Good agreement between the experimentally observed performance of a MMM comprising of carbon molecular sieve in a glassy polymer with predictions of Maxwell as well as Bruggeman models has been reported.[55, 56] However, the effect of filler size and shape are not accounted in these models. Further, Lewis-Nielsen[57] and Pal[58] models have been developed considering the effect of filler size and shape on gas permeability. However, all these models assume an ideal interface between the filler and polymer. More often than not, the interface morphology of the polymer near a filler is likely to be non-ideal. Several modifications have been proposed to account the non-ideal morphologies of the polymer including rigidified polymer layer,[33, 59, 60] interfacial voids[2, 61, 62] and pore blockage, [26] as shown in Figure 2-8. The popular models for permeation in non-ideal mixed-matrix membranes is provided in Table 2-1. Nevertheless, they disregard effect of isotherm nonlinearity and particle size of the filler.

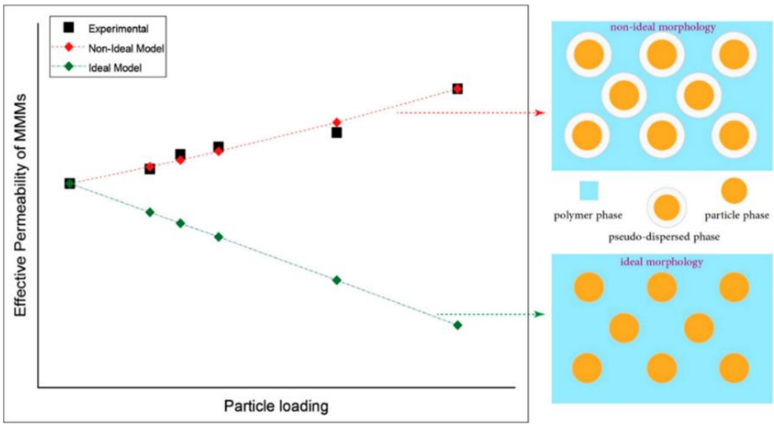

Figure 2-8: Concept of ideal and nonideal permeation predictive models. Reprinted with permission from ref. [63]. Copyright 2019 American Chemical Society.

Table 2-1: Summary of popular models for permeation in non-ideal MMMs. Here, P and ϕ denote the permeability and volume fraction, respectively. The superscripts/subscripts f,c,i,m and g denote filler phase, continuous phase, interface, MMM and combined filler phase and interface of the composite. Adapted from ref. [51]

Model	Key equations	Reference
Felske model	$P_m = P_c\left[\dfrac{2(1-\phi_{gc})+(1+2\phi_{gc})(\eta/\gamma)}{(2+\phi_{gc})+(1-\phi_{gc})(\eta/\gamma)}\right]$	64
	$P_m = P_c\left[\dfrac{P_g+2P_c-2\phi_{gc}(P_c-P_g)}{P_g+2P_c+\phi_{gc}(P_c-P_g)}\right]$	33

PTP Maxwell model	$P_g = P_i \left[\frac{P_f + 2P_i - 2\phi_{fi}(P_i - P_f)}{P_f + 2P_i + \phi_{fi}(P_i - P_f)} \right]$	
PTP Bruggeman model	$\left[\frac{P_m}{P_c} \right]^{\frac{1}{3}} \left[\frac{(P_g/P_c) - 1}{(P_g/P_c) - (P_m/P_c)} \right] = \left[1 - \phi_{gc} \right]^{-1}$	62
	$\left[\frac{P_g}{P_i} \right]^{\frac{1}{3}} \left[\frac{(P_f/P_i) - 1}{(P_f/P_i) - (P_g/P_i)} \right] = \left[1 - \phi_{fi} \right]^{-1}$	
PTP Chiew-Glandt	$P_m = P_c \left[\frac{1 + 2\beta_{gc}\phi_{gc} + (\kappa_2^{gc} - 3\beta_{gc}^2)\phi_{gc}^2}{1 - \beta_{gc}\phi_{gc}} \right]$	65
	$P_g = P_i \left[\frac{1 + 2\beta_{fi}\phi_{fi} + (\kappa_2^{fi} - 3\beta_{fi}^2)\phi_{fi}^2}{1 - \beta_{fi}\phi_{fi}} \right]$	

Permeation models in Table 2-1 are commonly used in conjunction with experimental data to fit the polymer-filler interface properties. Thus, the interfacial properties are empirically fixed while the gas permeability is calculated upon error minimization between the experimental permeabilities and the model predictions, by assuming the mean filler particle size is known. These empirical fits often lead to a wide range distribution of interfacial thickness ranging from 20 nm to 1 micron between the polymer and filler.[63, 65] Furthermore, the gas transport characteristics in the interfacial region such as gas permeability are necessary for accurate prediction of MMM performance, whose experimental values are not accessible through existing techniques. On the other hand, MD simulations has become powerful tool to investigate the structure of polymer near an inorganic surface.

2.3 Atomistic simulations:

Beside experimental studies, atomistic simulations have been successfully employed to investigate the structure of polymer as well as filler materials and gas transport properties of these materials. This section provides a brief overview of gas transport in inorganic filler materials such as CNTs and zeolites, emphasizing the interfacial barriers and their contribution to overall gas transport. Further, investigations on gas sorption, transport in neat polymer membrane materials are highlighted. In addition, major attempts to understand the polymer structure near an inorganic particle as well as behavior of nanocomposites through atomistic simulations are discussed.

2.3.1 Gas transport in filler materials:

Mass transport resistance that include both intra-crystalline and interfacial resistances, determines the diffusive transport in porous inorganic materials. The drag exerted by the pore network of the membrane on the gas molecules contributes to intra-crystalline resistance, while the interfacial resistance includes entrance and exit barriers that arise from potential energy differences between activated states in the vicinity of the phase boundary due to symmetry breaking at the interface. These interfacial barriers can be distinguished as external fluid phase resistance and internal interfacial barriers. *External fluid phase resistance* exists on the gas side of the phase boundary, and is experienced by gas molecules entering the pore network, in the external boundary layer; on the other hand, *internal interfacial barriers* exist on the solid side of the crystal surface and are due to the asymmetric potential experienced by the gas molecules inside the crystal but near the phase boundary.

For long, intra-crystalline resistance has been extensively explored using atomistic simulations through MD simulations in an infinite long crystal, following the Einstein's relation,[66] and interest in the contribution from interfacial barriers to the mass transport is relatively recent. The past decade has witnessed substantial progress in understanding the role of interfacial barriers in mass transport both theoretically and experimentally. Recent advances in nanotechnology offer attractive routes for increasing the efficiency of such processes by decreasing system as well as feature size, thereby reducing transport resistance. However, with decrease in system size the governing resistance for transport in nanomaterials shifts from that of intra-crystalline transport, to that of interfacial transport, which limits the efficiency achievable. As a consequence, there is a growing need to develop techniques for characterizing the interfacial transport, and elucidate the underlying mechanisms.

The intra-crystalline transport is known to be an activated process, and the temperature as well as loading-dependence of the diffusion coefficients can be determined directly by applying these techniques. Far less studied is the interfacial resistance, associated with interfacial barriers that arise from the potential energy differences between activated states in the vicinity of the phase boundary due to symmetry breaking at the interface. Figure 2-9 schematically illustrates the potential energy landscape for a diffusing molecule in the surface region, [67] where the potential energy well inside the crystal is considerably lower than outside due to the attractive van der Waals forces.

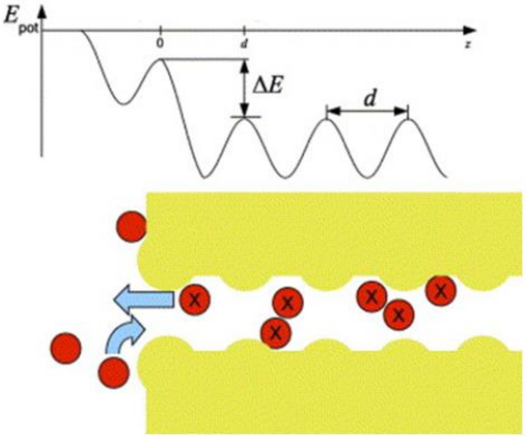

Figure 2-9: Schematic of the potential energy landscape of molecules in the surface region of zeolite crystals. Here, d is the site-to-site distance, and ΔE the desorption barrier. Reprinted from ref [67]. Copyright 2006 with permission from Elsevier.

For sufficiently long ideal crystals, the influence of these interfacial barriers can be negligible, and separation characteristics of both polymer and inorganic membranes have been evaluated based on based on intra-crystalline resistance. [66, 68-70] Recent progress in the syntheses of nanoporous solids, has given rise to an impressive array of new structures, such as MOFs and ZIFs, which are considered potentially attractive for technological exploitation for gas separation. The future directions for these new membrane materials are very promising, primarily because of the enormous chemical flexibility of their base structures. However, to make their membranes commercially feasible for large scale industrial separations, ultra-thin membranes have been synthesized by reducing the thickness, and thereby lowering the driving force required for a given flux.[71, 72] In these upcoming class of extremely thin and highly oriented nanoporous membranes[71-73] and mixed matrix membranes (MMM) with nanosize fillers, [74, 75] interfacial barriers can be significant and detrimental to separation kinetics.

Interfacial barriers can be distinguished as external interfacial barriers and internal interfacial barriers. The external interfacial barriers exist on the fluid side of the phase boundary, while internal interfacial barriers exist on the solid side of the phase boundary. Thus, the interfacial resistance ($R_{interface}$), is the *excess* resistance due to presence of interfaces at the ends (i.e. finite adsorbent/membrane size), include contributions of both internal ($R_{internal}$) and external ($R_{external}$) interfacial resistances, and can be written as:

$$R_{interface} = R_{internal} + R_{external} \tag{2-2}$$

Further, the total transport resistance (R_{sys}), comprising interfacial and intra-crystalline resistances (R_{intra}), follows a resistance in series model as depicted in Figure 2-10:

$$R_{sys} = R_{interface} + R_{intra} \tag{2-3}$$

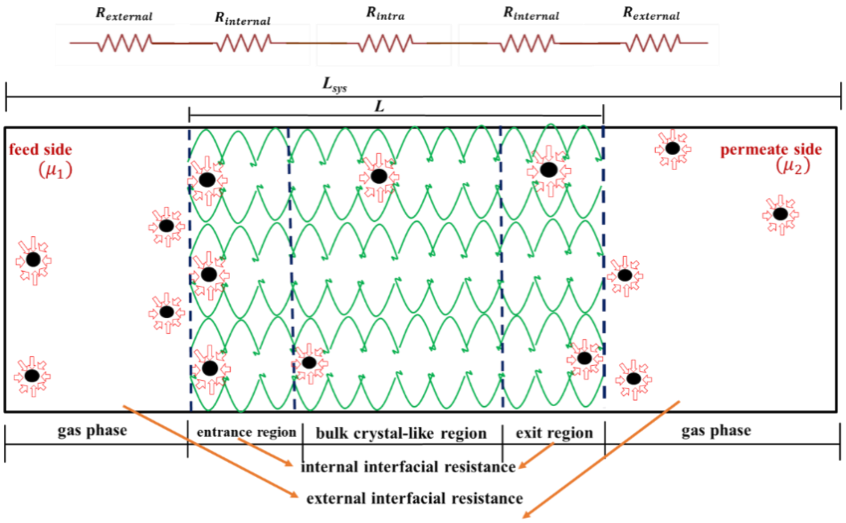

Figure 2-10: Illustration of various types of interfacial barriers in a nanoporous membrane.

Typically, interfacial barriers slow down the overall transport rate; however, they are not necessarily undesirable[76] and may be useful to alter the surface properties of nanoporous membrane materials. [77, 78] The origin and nature of these barriers are as follows:

External interfacial barriers: External interfacial barriers exist on the fluid side of the phase boundary and are due to the difficulties experienced by fluid molecules to reach the entrance of the pore from the bulk fluid phase. It is well known that flow near a surface has two components: direct flux and surface flow.[79] The fluid molecules that enter directly from the bulk phase into the adsorbent or membrane contribute to the direct flux, and must overcome the viscous resistance and diffusion (in the case of a mixture) resistance when they move from the distant bulk reservoir to enter the pore network. On the other hand, the fluid molecules that first adsorb onto the surface and then move toward the pore rim contribute to the surface flow, and these fluid molecules experience curved streamline bending effect near the surface. These two resistances together contribute to the external fluid phase resistance and determine the rate of molecular exchange at the interface.[79, 80]

Internal interfacial barriers: Fluid molecules must overcome the thermodynamic adsorption/desorption barriers due to the strong entropic and enthalpic changes near the phase boundary to enter into the pore network.[80-82] Such internal interfacial barriers exist on the solid side of the crystal and are coupled with effects of the asymmetric potential experienced by the fluid molecules inside the crystal but near the phase boundary, as shown in Figure 2-10. Further source of these barriers includes grain boundaries and internal defects, due to which the gas molecules must detour to reach the outer surface. In addition, the surrounding medium, such as a dense polymer can influence these barriers significantly. Further, there exist, entrance-exit resistance that can be induced by diffusion in systems such as CNTs and one-dimensional zeolites as well as structural defects such as pore narrowing at the surface with partial or total pore blockages; such interfacial defects can result in large and even dominant contribution to interfacial resistance when present.[83] These barriers are independent of the magnitude and direction of the diffusion.[84]

A significant amount of work, both experimental and computational, on the nature of interfacial barriers in nanoporous membranes has been reported in recent years. [81, 83, 85-89] The existence of interfacial barriers was considered as one of the possible explanation for the remarkable discrepancy between intra-crystalline diffusivities measured directly using PFG-NMR and macroscopic uptake/release measurements.[90] Interfacial barriers that exist on the surface have been found to be significant and larger than the intra-crystalline resistance for cyclohexane transport in silicalite particles of size 0.2 μm or smaller.[91] Using a frequency response technique, Teixeira et al. found experimentally that cyclohexane sorption in MFI zeolite is controlled by a combination of internal diffusional resistance and surface resistance.[85, 92] Between these, the former is dominant in large crystals, with increasing contribution from surface resistance as the crystal size is reduced, and the latter becomes dominant when the crystal size is below 0.1 μm. In addition, surface barriers are found to be asymmetric in nature, with different rate-controlling mechanisms for entering and exiting surface pores. This is attributed to the extra length required for desorbing molecules within porous materials, which can be directly related to the surface structure.

Further, nanoporous crystals typically deviate from the ideal structure, exhibiting structural defects such as grain boundaries and intergrowths, which influence interfacial resistance. Kärger and co-workers [83, 87, 93, 94] developed a microkinetic model of surface resistance, considering that only a small fraction of surface pores are accessible for a fluid to enter/exit, whose predictions closely fit experimentally observed results for short-chain alkanes in Zn(tbip)-MOFs. The presence of physical surface pore blockages is described as a possible mechanism for surface resistance to diffusion in nanoporous materials. [87] In MFI-type zeolite, it was proposed that most of the surface pores exhibit blockages, with only a very small fraction allowing transport through the surface. Such blockages are proposed to be surface structure dependent, with the fraction of blocked pores expected to be independent of particle size.[85] Furthermore, with the aid of advanced micro-imaging techniques, [95] uptake and release rates by single crystals can be determined. Interfacial barriers in different crystals from the same sample are found to vary by more than an order of magnitude in zeolites as well as MOFs, which is explained by diversity in the crystal structure.[93, 96] The interfacial barriers are more pronounced and are found to be rate limiting in single crystals. Therefore, while the intra-crystallite diffusivity may be expected to be independent of crystal size, this is not necessarily true for the surface resistance.

While the current imaging techniques [97-99] allow characterization of e structural defects such as pore blockage, crystal intergrowth *etc.*, the experimental manifestation of surface termination and the presence of sub-nanometer surface defects is still challenging. Further, the exact nature and contributions of these interfacial barriers to overall transport remained beyond direct experimental assessment. The experimental challenges in determining diffusion coefficients in nanoporous materials have been discussed in detail by Kärger. [100, 101] On the other hand, atomistic simulation can provide molecular level details of the transport mechanisms that cannot be viewed directly in experiments, and are becoming an indispensable tool. Here, we review the nature of interfacial barriers and their contribution to fluid transport in nanoporous membranes such as CNTs and zeolites, evidenced in simulations.

<u>Simulation techniques to extract interfacial barriers:</u> Non-equilibrium molecular dynamics [80, 88, 102-107] as well as equilibrium molecular dynamics [67, 82, 89] simulations have been successfully employed to investigate interfacial barriers in nanoporous crystals and membranes, and their relative importance in gas transport. In general, these methods use a system such as that in Figure 2-10, with an external gas phase on both sides of a finite crystal or membrane and determine transport resistance by measuring the molar flux or diffusivity. The transport resistance (R) can be related to the molar flux (j) of a fluid, based on the commonly adopted irreversible thermodynamic description of the transport:[108]

$$j = \frac{D_o \rho}{k_B T}(-\nabla \mu) \tag{2-4}$$

where D_o is corrected diffusivity, ρ is the adsorbed gas density, k_B is Boltzmann constant and T is temperature. For sufficiently small chemical potential gradient across a membrane of length L and cross-sectional area A_c, for which the chemical potential can be considered to be uniform, transport resistance can be defined as:

$$R = \frac{(-\Delta \mu)/k_B T}{A_c j} = \frac{L}{A_c D_o \rho} \tag{2-5}$$

Application of this definition of transport resistance to both the total system and intra-crystalline resistances, highlighted in eq (2-3), provides

$$R_{interface} = \frac{L_{sys}}{A_{sys}\rho_{sys}D_{o,sys}} - \frac{L}{A_c\rho D_{o,\infty}} \tag{2-6}$$

where, L_{sys} is the total length of the system including the solid adsorbent/membrane of length L and external gas phase, as indicated in Figure 2-10, A_{sys} is the cross-sectional area of the simulation box (which may be larger than that of the solid adsorbent, A_c), ρ_{sys} is the density in the whole system, ρ is the adsorbate density in the solid, and $D_{o,\infty}$ is the corrected diffusivity in the infinitely large sold at the same density ρ. Thus,

$$R_{intra} = \frac{L}{A_c\rho D_{o,\infty}} \tag{2-7}$$

represents the intra-crystalline resistance of the solid adsorbent or membrane if it were to have the same diffusivity ($D_{o,\infty}$) as an infinitely large crystal/membrane. We note that use of fugacity or pressure difference rather than chemical potential difference as the driving force, which is a matter of convenience, does not influence the results in terms of governing mechanisms. In this section, we outline the simulation procedures that have been used to evaluate the interfacial resistance, and to decompose it into the associated internal and external contributions.

Non-equilibrium molecular dynamics (NEMD): The interfacial resistance in a nanoporous membrane can be determined through NEMD simulations, by imposing an external force on to the fluid molecules, thereby simulating a chemical potential/pressure gradient across the membrane.[80, 102, 103] The system attains a steady state flux at which the external force is equivalent to the sum of internal and interfacial chemical potential drops required to achieve the flux. The corrected diffusion coefficient (D_o) of fluid molecules in the finite membrane can readily from the net flux (j), following:[102]

$$D_o = \frac{jk_BT}{\rho\Gamma_{ext}} \tag{2-8}$$

where Γ_{ext} is the applied external force, k_B is the Boltzmann constant, T is temperature and ρ is fluid density in the system. We note that diffusivities computed using eq (2-8) based on a force in accordance with a small chemical potential gradient are in good agreement with predictions of EMD simulations.[102] Further, based on knowledge of intra-crystalline diffusivity that can be obtained for an infinite membrane at a given pressure and temperature, the total interfacial resistance can be estimated following eq (2-6). Liu et al.[80, 102] estimated the interfacial resistance in CNT membranes, considering the external interfacial resistance is negligible, for which eq (2-6) reduces to:

$$R_{interface} = \frac{L}{A_c \rho}\left(\frac{1}{D_o} - \frac{1}{D_{o,\infty}}\right) \tag{2-9}$$

where, D_o is the corrected diffusion coefficient in the finite membrane.

Dual control volume grand canonical molecular dynamics (DCV-GCMD): DCV-GCMD is a hybrid simulation technique that combines grand canonical Monte Carlo (GCMC) and molecular dynamics (MD) simulations to model nonequilibrium systems,[109] and is extensively used to evaluate individual contributions of resistance associated with entrance, intra-crystalline transport, and exit steps.[84, 107, 110-113] In this method, the simulation box is divided into two control volumes (CV), designated CV1 and CV2, and these CVs are separated by a transport region as shown in Figure 2-11. To create a concentration gradient across a membrane, chemical potentials in the two CVs are maintained at chosen fixed values by inserting and deleting molecules in each CV through GCMC simulations. The molecules are allowed to move from one CV to another through the transport region using MD simulations. The intra-crystalline resistance can be extracted using eqs (2-4) and (2-5) when both CVs are filled with membrane and determining the net flux by counting the number of molecules crossing a given surface. Further, entrance interfacial resistance (including external and internal interfacial barriers) can be extracted by determining the net flux across the membrane when only CV2 is filled with membrane and CV1 is maintained at a higher chemical potential than CV2 [84]. Similarly, exit resistance can be determined using the above procedure when CV2 is maintained at a higher chemical potential than CV1. However, DCV-GCMD simulations are computationally expensive even for extremely thin membranes. Further, DCV-GCMD simulations must be performed for conditions in which the net streaming velocity of the fluid molecules is small compared to the typical molecular thermal velocity, and hence performing reliable DCV-GCMD simulations is computationally challenging [113].

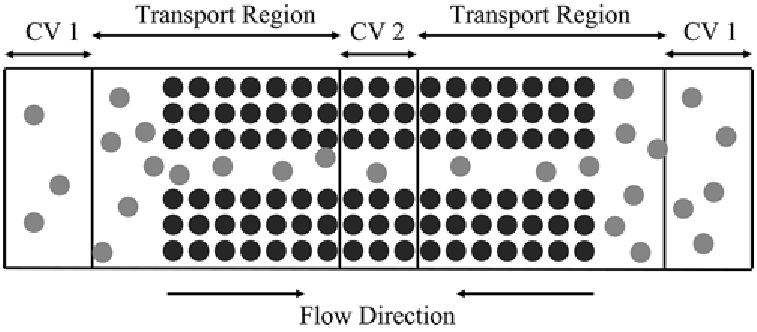

Figure 2-11: Schematic illustration of DCV-GCMD simulation system. Zeolite crystal atoms are shown in black, and adsorbate atoms in gray. Reprinted with permission from ref [113]. Copyright 2005 American Chemical Society.

Local equilibrium flux method (LEFM): It has been proposed that the mass transfer resistance associated with molecules entering and leaving pores at the gas−solid interface of a nanoporous membrane can be estimated without directly measuring the net steady flux, by employing the LEFM method. [77, 88, 113] The net flux (j_{feed}), in the LEFM method, is estimated by the difference of the one-way equilibrium flux (j_{eq}), at different chemical potentials, following:

$$j_{feed} \cong j_{eq}(\mu_{feed}) - j_{eq}(\mu_{surface}) \tag{2-10}$$

where μ_{feed} and $\mu_{surface}$ represents the fluid chemical potential on the feed side and on the membrane surface, respectively. This method assumes that change in fluid concentration in the boundary layer in the solid due to the internal interfacial resistance is small. The interfacial resistance ($R_{interface}$) in a nanoporous membrane can be estimated using the one-way flux values together with the adsorption isotherm and transport diffusivity in an infinite crystal through EMD simulations, following:

$$\frac{R_{interface}}{R_{intra}} = \frac{D_{o,\infty}(c_{feed})}{\alpha L}\frac{c}{p} \tag{2-11}$$

where $\frac{dj_{eq}}{dP} \cong \alpha$. Once, pressure dependence of one-way equilibrium flux is known, interfacial resistance at any given conditions as well as membrane thickness can be predicted without performing any additional simulations and hence LEFM simulations, as opposed to DCV-GCMD simulations, are not computationally expensive. However, it is not clear to what resistance the resulting interfacial resistance corresponds, as only the flux due to chemical potential difference between the gas phase and that at the surface is only considered. Thus, it does not include the contribution of internal interfacial barriers, found to be significant in zeolite membranes, and likely corresponds to an external resistance.

EMD simulations: The contributions of external and internal interfacial barriers to gas transport in nanoporous membranes have been investigated by employing EMD simulations.[82] The internal interfacial barriers ($R_{internal}$) in a membrane can be determined, considering a finite system of length L and surface area A_c, as depicted in Figure 2-12. The intra-crystalline and internal interfacial resistances for this system, follow a resistance in series model, leading to [89]:

$$R_{internal} + R_{intra} = \frac{L}{\rho . D_o A_c} \tag{2-12}$$

where ρ is the gas density and D_o is the collective diffusivity inside the membrane. This D_o can be computed through a collective coordinate n, defined as

$$dn = \sum_{i \in memb(t)} \frac{dz_i}{L} \tag{2-13}$$

where dz_i is displacement of gas molecule i in the z direction during time dt. The coordinate n executes a random walk due to the entry and exit of molecules from the membrane, which comprises an open system. Consequently, for sufficiently long times the mean square displacement of n obeys the Einstein relation, following

$$D_n = \frac{< n^2(t) >}{2t} \tag{2-14}$$

where D_n is the collective diffusion coefficient and can be related to D_o, following:

$$D_o = \frac{D_n.L}{\rho.A_c} = \frac{D_n L^2}{< N_{mol} >} \tag{2-15}$$

where $<N_{mol}>$ is the ensemble averaged number of gas molecules inside a membrane.

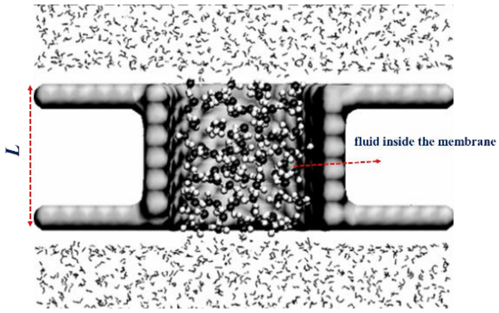

Figure 2-12: Schematic representation of a finite membrane of length L, highlighting the fluid molecules that contribute to the collective coordinate (n). Reprinted figure with permission from ref [114]. Copyright 2004 by the American Physical Society.

Further, the contribution of intra-crystalline resistance (R_{intra}) can be determined by computing the corrected diffusion coefficient ($D_{o,\infty}$) of all adsorbed fluid molecules of density ρ in an infinite long crystal, following eq (2-7). Combining eqs (2-7) and (2-12) provides:

$$\left\{\frac{1}{\rho.D_o}\right\} = \left\{\frac{1}{\rho.D_{o,\infty}}\right\} + \left\{\frac{A_c R_{internal}}{L}\right\} \tag{2-16}$$

The quantitative value of internal interfacial resistance can be determined from the slope of the plot of $\frac{1}{\rho.D_o}$ *vs.* $\frac{1}{L}$, based on the linear relation in eq (2-16).

In addition, the overall system resistance including the membrane region and surrounding bulk gas regions can be determined from the overall diffusivity of the system, following:

$$R_{sys} = \frac{L_{sys}}{A_c \rho_{sys} D_{o,sys}} \tag{2-17}$$

where, $D_{o,\,sys}$ is the corrected diffusivity considering all adsorbed fluid molecules (of density ρ_{sys}) in a system of length L_{sys}. Further, the external interfacial barriers can be determined by subtracting the internal transport resistance from the overall resistance of the system, following:

$$R_{external} = \frac{L_{sys}}{A_c \rho_{sys}.D_{o,sys}} - \frac{L}{A_c \rho.D_o} \tag{2-18}$$

Evidence of interfacial barriers in nanoporous membranes: The smoothness of the pore surface, framework density, crystal defects and molecular size as well as thermodynamic state of the fluid have been identified as the most important influencing factors of interfacial barriers.[102, 115-117] Due to the significant contribution of interfacial barriers, [80-83, 88, 118] interpretation of fluid transport in membrane materials based on intra-crystalline resistance without knowledge of interfacial barriers can be misleading. In this section, we review the factors that influence these interfacial barriers, and relative importance of interfacial barriers to fluid transport in zeolite and CNT membranes, as many possible applications for these materials have been foreseen, [119-121] primarily related to their potential as membranes for gas separation.[71, 122, 123] Zeolite membranes have shown interesting separation characteristics, such as the separation of hydrocarbon isomers, or the separation of strongly adsorbed components from weakly adsorbed ones.[124, 125] On the other hand, CNT membranes are most promising candidates as next-generation membrane materials owing to their exceptional electrical, thermal, and mechanical properties[126, 127] and hold promise of extraordinary fast transport due to their smooth energy landscape.[128]

Internal interfacial barriers: Internal interfacial barriers strongly depend on the atomistic scale roughness of the surface and can significantly hinder fluid transport in nanocrystals. The intra-crystalline resistance associated with smooth surfaces will be much smaller compared to that for rough surfaces, due to the nearly specular nature of the collisions when the surface is smooth [128]. As a result, it is possible that the contributions of interfacial barriers to the overall resistance of a membrane to gas transport are much more important. The transport diffusivity of methane in finite carbon nanotubes is reduced by more than 2 orders of magnitude [102], and up to an order of magnitude in ideal zeolites [88] as This can be attributed to smooth nature of the pore surface in CNTs, due to the small inter-atomic spacing of 1.42 Å in sp^2 bonding carbons. In addition, the contribution of these interfacial barriers to the overall transport resistance varies with size of the fluid molecule as well as available pore size in the membrane network. The interfacial barriers are expected to increase with increase in molecular size of the fluid molecules as the fluid molecule experience strong confining effects of the pore walls when the molecular size of the fluid molecules and available pore size in the membrane are comparable, leading to an increase in interfacial barrier. Glavatskiy et al. reported an increase in interfacial barriers that exist at the entrance for CO_2 and CH_4 with decrease in CNT radius, and these approach an infinite value when CNT radius the size of adsorbate molecule are comparable.[81] In addition, pore shape [70] and tortuosity [129] can influence the gas diffusivity and hence interfacial barriers. Further, the interfacial barriers to gas transport in these nanoporous membranes can be significantly higher in the presence of dense external media such as a polymer, requiring detailed investigation.

It has been found that interfacial barriers can extend to more than 50 nm inside CNT membranes,[102] due to low Maxwell reflection coefficient of fluids in a CNT where wall collisions are nearly specular, leading to long correlation lengths inside a CNT. In addition, the exothermic nature of the adsorption process results in heat release when fluid molecules enter a membrane, leading to a temperature gradient near the interface in the entrance and exit regions, evident in recent NEMD simulations.[80, 102] The inability of a membrane to dissipate this heat sufficiently rapidly results in an additional transport barrier. Thus, it is possible that fluid transport in these materials can be controlled by both mass and heat transfer resistances, depending on the inherent characteristics of the membrane material and is an area that needs further attention.

External interfacial barriers: The difficulties experienced by the fluid molecules to reach the pore mouth including the soft matter interactions between fluid molecules and the crystal surface are accounted in external interfacial barriers and are found to be significant especially in CNTs. [80, 88, 102] These external interfacial barriers are confined to a region up to a nanometer from the surface near the phase boundary, as depicted in Figure 2-13 (a).[80] As these barriers are independent of crystal length, the contribution of external barriers to the overall resistance decreases with increase in crystal length.[113] Further, we note that strength of external interfacial barriers can affect the internal interfacial barriers. [80]

The flow entering a nanomaterial comprises a direct flow component and that due to adsorption on the external surface, and the contribution of these to the external interfacial barrier can be accurately captured in a procedure developed by Liu et al.[80] In their NEMD simulations of flow of methane through CNTs supported by flanges at ambient temperature, the interfacial barriers to mass transport are decomposed into that on the external flange surface (on which adsorption occurs) and a direct flow component, and it is found that the surface flow rate accounts for up to 90% of the overall flow rate. Thus, barriers associated with external surface flow contribute significantly to external interfacial barriers. The factors that influence the surface flow such as surface adsorption affinity, can therefore be used to manipulate the strength of the external interfacial barrier. For example, a decrease in the external interfacial barrier with increase in flange area and with decrease in flange adsorption affinity for the fluid is reported, as shown in Figure 2-13 (b).[80] Thus, the contribution of external interfacial barriers to overall transport can be significant when the flow is too confined or the surface has low affinity for the fluid. However, the interfacial barriers in CNT membranes are generally dominated by internal interfacial barriers including entrance-exit resistance, rather than external interfacial barriers.[80] A similar observation was made in the case of ideal zeolite crystals, where the contribution of these barriers is found to be insignificant.[77, 113, 130] Nevertheless, surface pore blockage or constrictions as well as terminal functional groups can contribute to these barriers significantly, as fluid molecules experience difficulties to locate an open pore on the surface. [76, 77, 131]

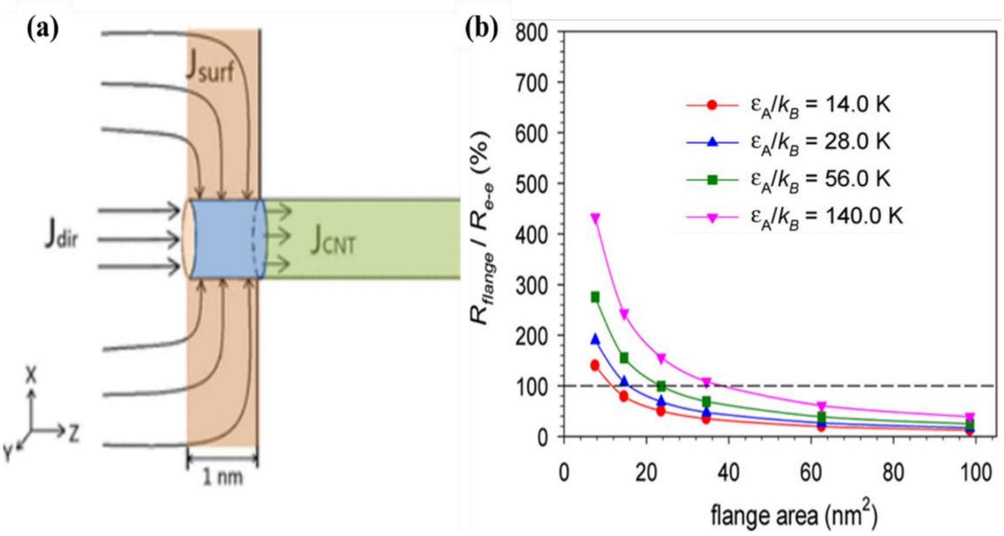

Figure 2-13: (a) Decomposition of the flow rate into surface and direct components. The flange resistances, entrance resistance, and the internal resistance are defined over the light orange, blue, and the green regions, respectively, and b) variation of fractional contribution of flange resistance with flange area for different values of adsorption strength of flange at 15 bar and 300 K. Reprinted with permission from ref [80]. Copyright 2018 American Chemical Society.

On the other hand, the interfacial barriers to water transport in CNT membranes are found to be significant, [82, 103] and the physical mechanisms involved in water transport are quite different from gas transport due to presence of hydrogen bonding in water, both outside and inside of CNTs [82, 88]. It is reported that the energy barrier present at the pore entrance plays an important role in water transport through CNTs and intensity of these energy barriers can be assessed through potential of mean force (PMF) analysis [82, 132-134], as shown in Figure 2-14 (a). Further, the influence of nanotube diameter on the entrance and exit effects is explained in terms of entropy contrast between the bulk and confined regions, where water molecules undergo large increase in translational and rotational entropy on entering from the bulk to the CNT interior [82]. In addition, the intensity of such energy barriers is found to decrease with increase in CNT diameter [82]. Further, Zhang et al. [103] assessed the interfacial barriers to water transport in CNTs of various diameters, by performing NEMD simulations on a flexible CNT. The interfacial barriers to water transport in CNTs are found be dominant and 1-2 orders of magnitude higher than the intra-crystalline resistance. The contribution of interfacial barriers to overall resistance remains as high as 92%, in a CNT of length 100 nm, and strategies to minimize these barriers such as using hourglass-shaped pore mouth at the entrance, that can reduce the interfacial resistance by 30%, as shown in Figure 2-14 (b), have been proposed

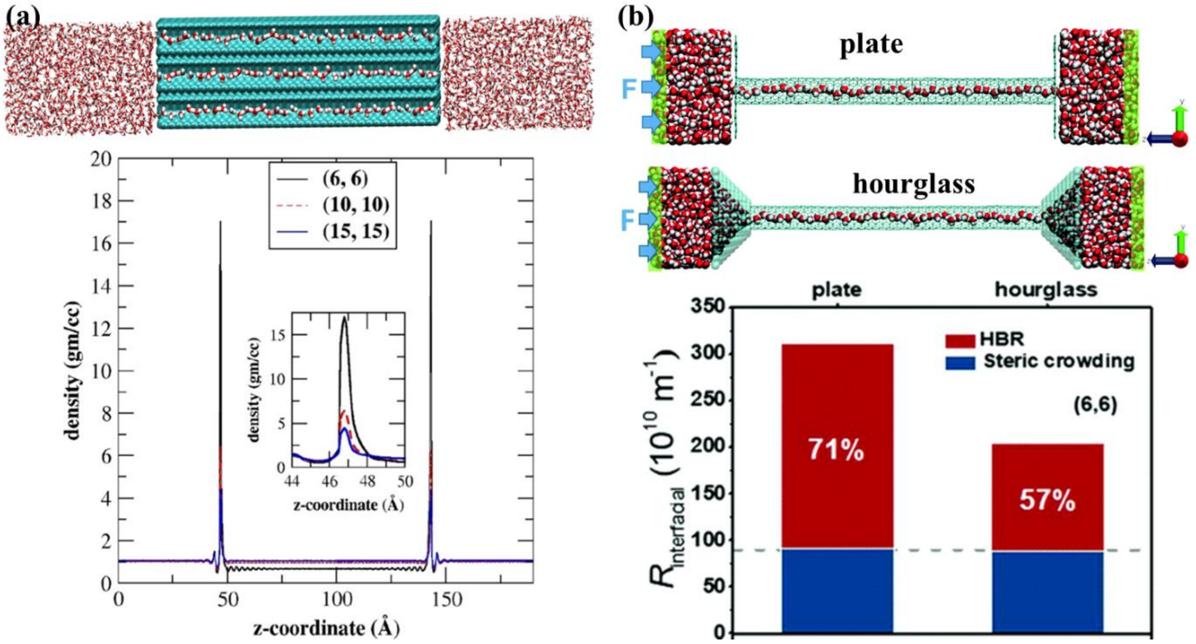

Figure 2-14: Schematic illustration of (a) the mean force experienced by the water molecules at different locations of CNT membrane, and (b) strategies to minimize the external interfacial barriers to water transport in CNT membranes. (a) Reprinted with permission from ref [82]. Copyright 2016 American Chemical Society. (b) Reproduced from ref [103] with permission from The Royal Society of Chemistry.

Effect of structural defects: The presence of structural defects in nanoporous membranes is typically due to uncoordinated lattice or amorphous silica that exists on the surface and/or surface-termination groups that can cause partial or complete blockage of surface pores, restricting entry/exit of fluid molecules [85]. In this case, the fluid molecules must travel an additional distance on the surface, but within the external gas phase, to enter an open pore. This contributes to external fluid phase resistance. On the other hand, fluid molecule must detour within the membrane, to locate an open surface pore, before exit, as depicted in Figure 2-15.[135] This contributes to the internal interfacial barriers. Thus, fluid molecules must experience an additional transport barrier while entering and/or leaving the surface pores when the surface pores are blocked. Teixeria et al. [85] characterized these two processes by employing Teixeira–Qi (T-Q) model, which describes the surface barriers associated with adsorption–desorption due to complete pore blockage successfully and found that energy barriers are asymmetric. The activation energy associated with surface transport (20.8 kJ/mol) is found to be significantly less than that of intra-crystalline diffusion as well as of desorption steps (≈ 54.1 kJ/mol) [85]. Further, the presence of substantial fraction of blocked pores, due to which fluid molecules must detour to locate an open surface pore, as illustrated in Figure 2-15, causing an increase in the diffusional length scale, is considered as a possible mechanism for the commonly observed discrepancies between the macroscopic and microscopic diffusivities in nanoporous materials.[87] Brandani et al.[136] determined the diffusivities of n-alkanes across several length scales in silicalite-1 crystals and observed that smaller diffusivities were likely caused by a longer diffusional path at the same diffusion rate due to complete pore blockage. In this case, the observed self-diffusivity remains constant because it represents the motion of single molecules jumping through the available sites, while the transport diffusivity across the entire particle becomes slower. Further, the additional length does not affect the activation energy, as the transport mechanism remains the same.[86] However, one may expect an increase in activation energy in case of partial pore blockage.

In addition, internal defects such as grain boundaries can act as a source of interfacial barriers [118]. These grain boundaries are formed as a result of crystal imperfections at the interface between two crystallites and are an inevitable feature in polycrystalline materials.[97, 137] A number of experimental investigations reported the existence of grain boundaries in zeolites, [138] MOFs[139] and CNTs.[140] A decrease in ZIF-8 membrane perm-selectivity for several gas pairs due to the presence of grain boundaries is reported. [139] It is reported that polycrystalline ZIF-8 membranes are selective for N_2 over CH_4, while, single crystal ZIF-8 membranes are selective for CH_4 over N_2. This is attributed to the presence of grain boundaries that act as strong sorption sites for N_2.[139] Further, the effect of interfacial barriers on CH_4 and CF_4 permeation due to internal grain boundaries that exist in silicalite-1 crystals has been assessed through DCV-GCMD simulations.[118] The magnitude of interfacial barriers due to grain boundaries is found to be quite substantial, and increases with increase in fluid molecule size as well as adsorption strength. However, incorporating atomic-scale nature of the grain boundaries into the simulation is an additional necessity to capture the interfacial barriers accurately.[118] Further, the existence of grain boundaries in large diameter CNTs is ubiquitous, [140] however their effect on gas transport in CNTs remains to be addressed.

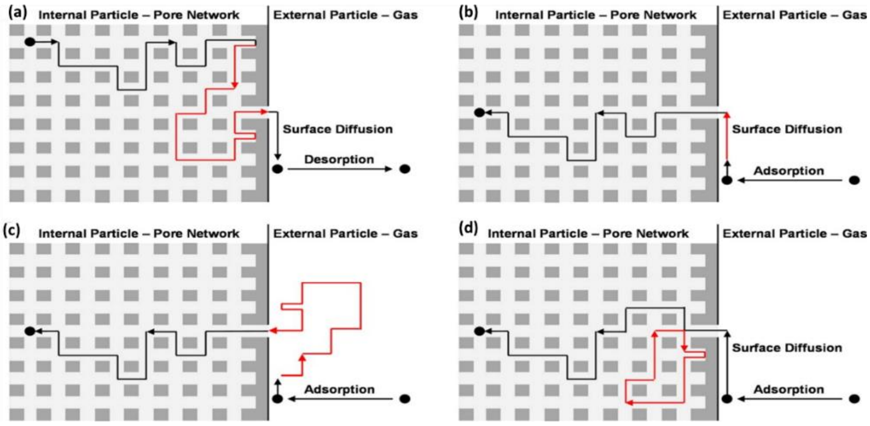

Figure 2-15: Interpretation of kinetic behavior of (a) adsorbate release, and (b) uptake characterized by the T–Q model in silicalite-1 particles with additional diffusional path length depicted in red. The proposed requirement of fixed transport length for uptake would require irrational molecular behavior including either: (c) additional adsorbate movement within the external gas phase, or (d) additional adsorbate movement to find the surface pore opening after just permeating the open surface. Reprinted with permission from ref. [135]. Copyright 2015 American Chemical Society.

Effect of temperature: Diffusion is a temperature activated process following Arrhenius relationship,

$$D = A\exp(-\frac{E_a}{RT}) \tag{2-19}$$

where E_a is activation energy representing the energy required by a fluid molecule to jump from one site to the another, A is the pre-exponential factor, R is universal gas constant and T is temperature. The fluid molecules at higher temperatures possess high kinetic energy, and hence they can easily overcome both internal as well as interfacial barriers at higher temperatures. Thus, the contribution of interfacial barriers to overall transport is found to be significant at lower temperatures, [111, 118] and decreases with increase in temperature. The temperature dependence of corrected diffusivity of methane in CNT membranes of various lengths,[102] evidencing Arrhenius behaviour of diffusivity with temperature. An increase in activation energy of 4.75 kJ/mol for the infinite CNT to about 7 kJ/mol for finite tubes of length 30 nm, is reported. The higher activation energy for finite tubes is indicative of interfacial barriers that are dominant in finite CNT membranes, due to which fluid molecules have to cross an extra barrier. A similar behaviour is also observed in SAS zeolite, where an increase in activation energy for finite SAS zeolites for both CO_2 and CH_4 is reported.

In addition, a decrease in the internal interfacial barrier to methane transport in SAS-type zeolite with increase in temperature, following the Arrhenius type relation, having an activation energy comparable to that of gas diffusivity in an infinite crystal is reported. This suggests an identical elementary mechanism between the intra-crystalline resistance and internal interfacial resistance. On the other hand, the interfacial barrier arising from grain boundaries is found to be significantly vary with temperature; for example, as temperature decreases from 300 to 200K, the interfacial barrier due to grain boundaries increases around 6 times higher than intra-crystalline resistance. [118]

Effect of interfacial barriers on gas sorption: The rate of gas sorption in nanoporous membranes is commonly assumed to be controlled by intra-crystalline resistance,[141] however, it is often strongly influenced or even controlled by interfacial barriers. [91, 142, 143] The effect of interfacial barriers on gas sorption (or desorption) characteristics of nanoporous membrane materials has been highlighted by both theoretical and experimental investigations.[87, 93, 143-145] Good agreement between the adsorption isotherms obtained in an infinitely long AFI crystal and core region (6 Å away from the surface) of a finite crystal,[146] as well as a weak dependency of gas adsorption capacity with the crystal length of finite zeolite crystals, suggesting interfacial barriers are limited to a very narrow region near the gas-solid interface. The resistance associated with gas desorption in an ideal zeolite crystal was satisfactorily explained by Zimmermann et al. [115, 147] through a two-step release mechanism based on free-energy profiles. The fluid molecules have to cross a first barrier (ΔF_{surf}) to enter into the surface adsorption layer from the bulk pore network region, and then a second barrier (ΔF_{gas}), to enter into the bulk gas phase from the surface adsorption layer, before it desorbs. It is found that the contribution of ΔF_{surf} , to overall resistance is significant and can significantly retard gas desorption.[147] This underlines the importance of considering the external boundary layer to accurately predict gas transport in these membranes. In addition, the surface structure may govern the nature of adsorption sites near the surface. For instance, the broken sodalite cages in (011) and (100) in Fujasite surface act as strong adsorption sites for CO_2 compared to the (111) surface;[148]on the other hand, the effect of interfacial barriers that arise from surface modification on H_2 adsorption in silicalite-1 is found to be insignificant.[149] Hence, the interfacial barriers that arise from ideal crystal surfaces on gas sorption characteristics may be small; however, surface barriers due to structural defects can be significant and even control gas sorption rate.[144] Sastre et al. [144] performed MD simulations to investigate the uptake/release behavior of benzene in a finite MFI crystal, and found that sorption kinetics are controlled by the combined effects of surface resistance due to surface pore blockage and intra-crystalline resistance, where adsorption is strongly reduced with increase in pore blockage. Further, the influence of partial surface pore blockage as well as internal defects such as intergrowth effects on sorption kinetics can be significant, and requires attention. [150]

Critical membrane thickness: Based on the above considerations, one may expect that contribution of interfacial barriers to the overall transport decreases with increase in membrane thickness, and thus becoming insignificant for thick enough membranes. The critical membrane thickness (δ_{critical}) below which the contribution of these interfacial barriers to the gas transport is significant is then of interest. [111, 115, 146] This critical membrane thickness, δ_{critical}, is typically taken as the length at which the interfacial resistance is 10-25% of the interfacial resistance, i.e.

$$\frac{R_{interface}}{R_{membrane}} = 1 - \left\{ \frac{D_o}{D_{o,\infty}} \right\} \approx 0.1 - 0.25 \tag{2-20}$$

where D_0 *and* $D_{o,\infty}$ are corrected diffusivities of the fluid molecules in a finite and infinitely long membrane respectively. Newsome et al. report critical membrane thickness values of 2 µm and 0.05 µm for methane permeation at 300 K in CNT and y-oriented silicalite-1 membranes using their LEFM method, respectively. [88, 107] A higher value for δ_{critical} in these cases would be expected, if the calculations were based on interfacial barriers that include internal interfacial barriers. Further, the critical membrane thickness of zeolites depends on the nature of the pore network as well as molecular size of fluid. [115]In addition, critical membrane thickness is dependent on orientation of the membrane [84, 113, 151] as well as operating temperature and pressure. Interfacial barriers typically decrease with increase in temperature as well as pressure, [111] and hence a decreased critical membrane thickness at higher temperature and pressures is expected. For example, a decrease in critical membrane thickness to 100 nm at higher pressure, from around 1000 nm, and 5000 nm, for CH_4 and C_2H_6 respectively, is reported. [115] However, the contribution of interfacial barriers to gas transport for several gases in various ideal zeolite crystals for typical membrane sizes is found to negligible [111, 115]. Nevertheless, defects such as pore blockage/constriction, crystal intergrowth can influence the value of critical membrane thickness, whose effects yet to be explored. On the other hand, interfacial barriers are found to be significant for water transport in CNT membranes.[103] Zhang et al. report critical membrane thickness values of 6-24 µm for water transport in CNT membranes of various diameters. [103] Thus, the critical membrane thickness for water transport in the range of typical membrane sizes and hence the contribution of interfacial barriers to overall transport cannot be overlooked.

2.3.2 Modeling of polymer structures:

Long chain molecules such as polymers with complex topologies and large steric effects, have been extensively investigated through Monte Carlo (MC) as well as Molecular Dynamics (MD) simulations techniques. MC methods offer great flexibility in choosing the random moves by which the system evolves and can achieve equilibration rapidly in complex systems such as dense polymers.

The technical aspects of polymer modeling using MC simulations highlighting the open questions have been reviewed by Kremer et al.[152] Further MC simulations were successfully employed to investigate the polymer structures near a inorganic surface.[153-156] However, the inherent difficulties in attempting moves involving NPs have led to MC simulations being limited to problems in which NPs are rigid and stationary. Further, MC simulations can be time-consuming and inefficient for building long polymer chains.

On the other hand, Molecular dynamics (MD) simulations provide an alternative method to investigate the physical properties of the polymers. Recently, Abbott et al.[157] presented a 3-step algorithm for generating polymer structures that include a compression and relaxation protocol, that can be used further to predict the structural properties of the polymer. Colina et al.[158-161] employed this methodology in conjunction with atomic charge assignment from ab initio calculations, characterized the simulated structure of polymers through the distribution of free volume elements in the polymer, surface areas, structure factors, and gas sorption isotherms.

Further, Molecular transport of small molecules through a variety of polymer structures *via.* diffusion has been studied extensively using atomistic simulations.[162-169] Vegt et al.[166] reported the self-diffusion coefficient by considering single penetrant (CO_2) in PE. Hofmann et al.[170] investigated the transport of small fluid molecules in flexible rubbery polysiloxanes and stiff glassy polyimides and found good agreement between experimental and simulated diffusivities for a number of small molecule penetrants. However, little work has been done to extract the transport diffusivity of gases in polymers. Most studies report self-diffusion coefficients predicted using the Einstein relation, finding them to be in agreement, either quantitatively and/or qualitatively, with experimental measurements. However, to describe molecular transport across a membrane, it is the transport diffusivity that is important, and this can directly be extracted from non-equilibrium molecular dynamics simulations.[171-173] However, this requires very high forces and is also computationally extensive. Recently, an attempt to understand the gas transport characteristics of polymer materials using coarse grained CG-MD simulations has been made. Zhang et al. [174] investigated the gas diffusion using three different polymer models over a wide range of penetrant sizes, temperatures, and monomer densities. They found that slope of the empirical upper bound plot, $\lambda = (d_B/d_A)^2 - 1$, is only valid for polymers that are either supercooled liquids with caged segmental dynamics or glasses and when the penetrant size is approximately half the Kuhn length of the chains, for which the penetrant diffusion is an activated process.

Further, the gas adsorption isotherms in rigid porous materials such as zeolites [175, 176] are well explored. On the other hand, performing reliable simulations to predict sorption isotherms of gases in materials such as polymers that undergo significant structural transition upon gas sorption remains challenging. Gas sorption in polymers is affected by re-distribution of voids[177] (and channels) through two mechanisms associated with dynamics of the polymer. The free volume in the polymer matrix is continuously redistributed randomly either by generation of new voids or by destruction of voids, or by re-distributing the existing voids due to the movements of the one or more segments of the polymer chain and polymer structural transitions such as swelling/plasticization[178, 179] upon sorption. The *in-silico* investigations of gas sorption in polymers considering the structural transition upon gas sorption is relatively recent.[68, 74, 180-186] Velioğlu et al.[185] reproduced the plasticization behavior of various polyimides within an order of magnitude by employing sorption-relaxation cycles. van der Vegt et al.[166] proposed a robust iterative technique which is implicit, and estimates the required external gas pressure for given amount adsorbed, to obtain the sorption isotherms of the gases in glassy polymers. By applying this procedure, Pandiyan et al.[187] studied the sorption and desorption of CO_2, while, Tanis et al.[188] extracted gas sorption isotherms of nitrogen and methane in pure and mixed gas conditions in a variety of fluorinated polyimides and found significant and homogeneous swelling during the sorption. Hölck et al.[189] studied the sorption behavior of gases in a glassy polymer under conditions leading to maximum and no swelling of the polymer, and proposed a model to describe the gas sorption based on linear combination of the corresponding isotherms, that was in agreement with their experimental results. Further, we note that the accuracy of these predictions depends on the adequacy of the forcefield employed to represent the polymer. Further, recent simulations considering the structural transition and redistribution of voids upon gas sorption in 6FDA-bisAPAF polyimide[186] offer a more accurate alternative for the single component case but have yet to be extended for mixtures. Further, to complement experimental investigations, mixture sorption in polymers has been predicted from pure component data,[190] by applying ideal adsorbed solution theory (IAST) [191] that has been reported to be accurate for inorganic membrane materials. However, the validity of the predictions in polymers is unclear due the inherent assumptions on which this theory was developed, such as a rigid host matrix. Additionally, sophisticated techniques such as nonequilibrium thermodynamics of glassy polymers (NET-GP) can be applied to determine the sorption characteristics in a glassy polymer in both pure and mixed gas conditions,[192, 193] however, this model requires the knowledge of volume dilation in the glassy polymer matrix upon gas sorption.

<u>Structure of polymer near a surface:</u> The interfacial structure of polymer near an inorganic surface has been extensively investigated by employing CG [194, 195] as well as fully atomistic MD simulations.[196-199] Typically, the interfacial morphology of the polymer is characterized by computing the density profiles with respect to the position in the simulation box. Further, the interfacial thickness is extracted by measuring the distance required from the surface to reach the average bulk density of

the polymer. In addition, local chain dynamics, radial distribution function and available free volume can be used to characterize the polymer structure in the vicinity of a solid surface.

Eslami et al.[195] characterized the structure of polyamide-6,6 near a graphene surface using CG-MD simulations and reported an interfacial region of thickness ~3.0 nm exists, as shown in Figure 2-16. Further, they also found that the thickness of interfacial region is dependent on length scale of particular property of interest. For instance, the interfacial thickness varies from a minimum value of a few bead diameters to maximum distances as large as 2 times of radius of gyration. The former corresponds to distances up to which the local structural properties such as the density profile of the polymer beads deviate from the corresponding bulk values, while the latter corresponds to distances over which global chain properties, such as end-to-end distance of the polymer are influenced by the interface. Similar investigations have been done to understand the structural and dynamic properties of poly ethylene (PE) through MD simulations near a flat SiO$_2$ surface,[200, 201] spherical NPs [201-203] and C$_{60}$ fullerene.[201, 204-207] The simulation results reveal ordered orientation of PE polymer, forming layers normal to interface. In addition, the interface thickness is found to be independent of the size of the filler particle.[202] Further, clustering of fullerenes has been observed due to which a decrease in polymer density near C$_{60}$ NPs has been reported.

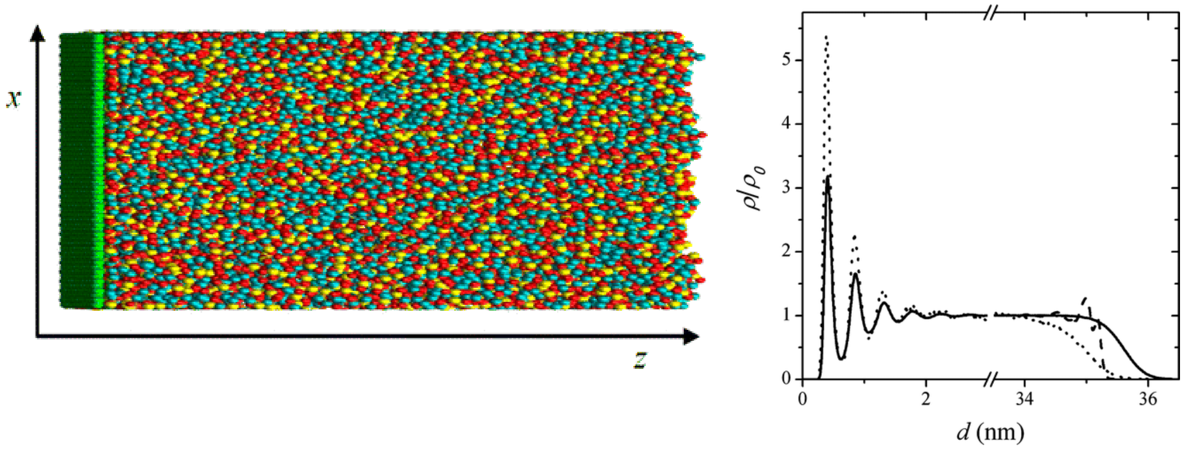

Figure 2-16: Number density profiles for all polymer beads (solid curve) and end beads (dotted curve). The density profiles are normalized by the bulk number density, ρ_0. The dashed curve represents the density profile in the vacuum interphase, calculated with respect to the distance from surface corrugations. Reprinted with permission from Ref. [195] Copyright 2013 American Chemical Society.

Further, the effect of size of NP on the behavior of polymer nanocomposites has been investigated. Emamy et al.[208] found that the interfacial polymer dynamics are less effected with decreasing in NP size. On the other hand, a substantial change in the glass transition temperature in the presence of an extremely small NP has observed, as depicted in Figure 2-17. This is due to a decrease in mean NP spacing with decrease in the particle size at any given NP loading, leading to all polymers being effectively interfacial for sufficiently small NPs, resulting in relatively large shifts in glass transition temperature. Further, the dynamics of NP in polymer nanocomposites has been investigated, and it is found that weakly interacting mixtures of NPs and polymers display two very different classes of behaviour depending on their size.[209] However, most of the above investigations have focused on mechanical and/or thermal properties of the composite materials,[201, 204-210] and gas transport characteristics of these materials are yet to be explored.

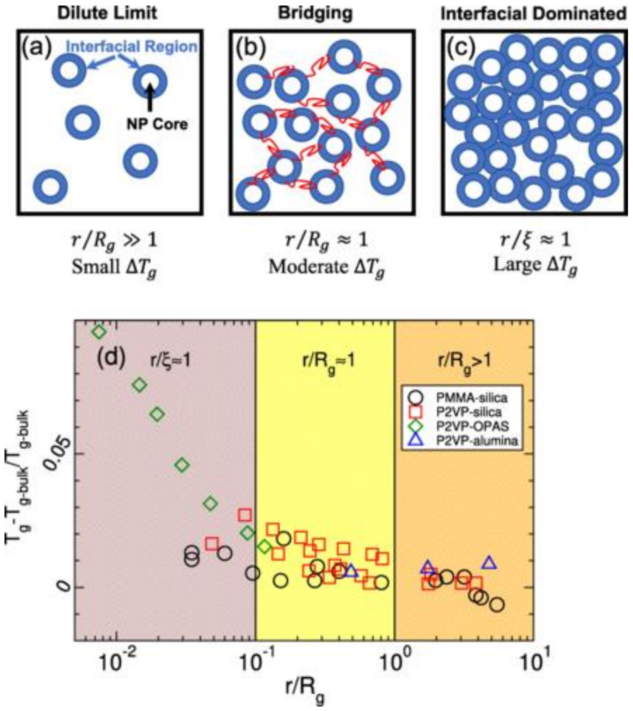

Figure 2-17: Schematics of the different regimes for interfacial effects of the NP. Reprinted figure with permission from ref. [208]. Copyright 2018 by the American Physical Society.

Further, Keskin et al.[211-213] employed atomstic simulations to investigate the gas transport characteristics of neat MOF as well as polymer membrane materials and determined the appropriate combination of MOF/polymer for gas separation by predicting the performance of a composite membrane based on Maxwell model. However, this model assumes ideal interface between filler and polymer, which is often not the case. Recently, Semino et al.[214] investigated the compatibility between MOF surface and PIM-1 polymer using a multi-scale simulation approach by combining Density Functional Theory (DFT) calculations with MD simulations. They found that a micro void region in the vicinity of MOF surface, of 9-15 Å width, exists, as shown in Figure 2-18 (a) and (b). This is in agreement with an experimental finding that the compatibility between the PIM-1 and ZIF-8 is moderate.[215] In addition, it has been found that larger FVEs of 6-7 Å radius and a higher free volume is available in the interfacial region, as shown in Figure 2-18(c). Further, they also developed a CG model that allows the investigation of much larger systems, which can reproduce the salient features of the interface that are in agreement with the findings of atomistic simulations. [216] By applying this methodology they found that poly(vinyl alcohol) polymer penetrates into the open pores of HKUST-1, resulting in surface pore blockage. In addition, Zhang et al.[217] investigated the H_2/CO_2 separation performance of a ZIF-7/ PBI membrane through atomistic simulations and found that H_2 and CO_2 have higher permeabilities in the hybrid membrane than the corresponding neat polymer membrane. Further, an increase in gas solubility with increase in filler loading for both the gases, with a little enhancement in H_2 selectivity over CH_4 has been reported. These investigations highlight the capability of atomistic simulations to predict the interfacial morphology of the polymer near a surface as well as gas transport characteristics in a model MMM. However, the influence of interfacial morphology on gas transport characteristics is yet to be investigated.

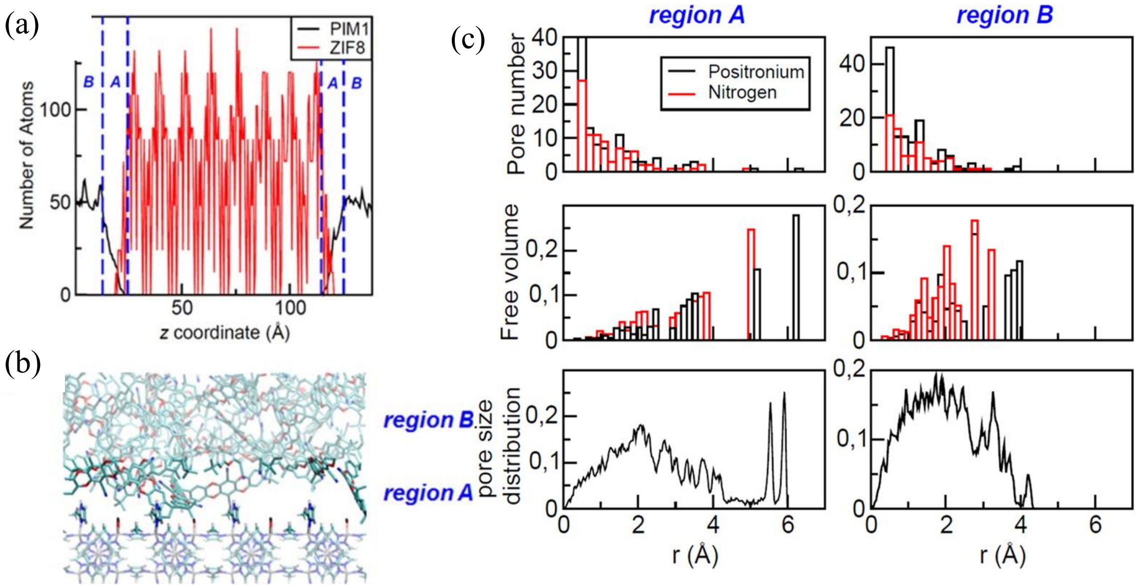

Figure 2-18: (a) Density of polymer (black line) and MOF atoms (red line) as a function of the z coordinate for a representative configuration of PIM-1/rigid ZIF-8 system. The blue dashed lines represent the limits of regions A and B, (b) Snapshot of the interface, where the atoms that belong to region A are opaque, and the rest are transparent, and (c) Histograms for the pore size distribution computed for a representative configuration of PIM-1/rigid ZIF-8 system according to (i) the v_connect methodology for positronium (black) and nitrogen (red) sized probes, weighted by pore number (top) and by free volume fraction (middle) and to (ii) the sphere fitting method (bottom). Reprinted with permission from Ref. [214] Copyright 2016 American Chemical Society.

In conclusion, the issue of the influence of interfacial structure on gas transport remains an open question and a thorough investigation of gas transport near the interface, including the sorption isotherms considering the structural transitions upon gas sorption in detail through EMD simulations, is required to quantitatively understand MMM behaviour and provide information necessary for the in-silico design of MMMs.

2.4 References

1. Zimmerman, C. M.; Singh, A.; Koros, W. J., Tailoring mixed matrix composite membranes for gas separations. *J. Membr. Sci.* **1997,** *137* (1), 145-154.

2. Moore, T. T.; Koros, W. J., Non-ideal effects in organic–inorganic materials for gas separation membranes. *J. Mol. Struct.* **2005,** *739* (1), 87-98.

3. Mahajan, R.; Koros, W. J., Factors Controlling Successful Formation of Mixed-Matrix Gas Separation Materials. *Ind. Eng. Chem. Res* **2000,** *39* (8), 2692-2696.

4. Bae, T.-H.; Lee, J. S.; Qiu, W.; Koros, W. J.; Jones, C. W.; Nair, S., A High-Performance Gas-Separation Membrane Containing Submicrometer-Sized Metal–Organic Framework Crystals. *Angew. Chem* **2010,** *49* (51), 9863-9866.

5. Kim, S.; Marand, E.; Ida, J.; Guliants, V. V., Polysulfone and Mesoporous Molecular Sieve MCM-48 Mixed Matrix Membranes for Gas Separation. *Chem. Mater* **2006,** *18* (5), 1149-1155.

6. Merkel, T. C.; Freeman, B. D.; Spontak, R. J.; He, Z.; Pinnau, I.; Meakin, P.; Hill, A. J., Ultrapermeable, Reverse-Selective Nanocomposite Membranes. *Science* **2002,** *296* (5567), 519-522.

7. Chen, J.-T.; Shih, C.-C.; Fu, Y.-J.; Huang, S.-H.; Hu, C.-C.; Lee, K.-R.; Lai, J.-Y., Zeolite-Filled Porous Mixed Matrix Membranes for Air Separation. *Ind. Eng. Chem. Res* **2014,** *53* (7), 2781-2789.

8. Roilo, D.; Patil, P. N.; Brusa, R. S.; Miotello, A.; Aghion, S.; Ferragut, R.; Checchetto, R., Polymer rigidification in graphene based nanocomposites: Gas barrier effects and free volume reduction. *Polymer* **2017,** *121* (Supplement C), 17-25.

9. Benzaqui, M.; Semino, R.; Menguy, N.; Carn, F.; Kundu, T.; Guigner, J.-M.; McKeown, N. B.; Msayib, K. J.; Carta, M.; Malpass-Evans, R.; Le Guillouzer, C.; Clet, G.; Ramsahye, N. A.; Serre, C.; Maurin, G.; Steunou, N., Toward an Understanding of the Microstructure and Interfacial Properties of PIMs/ZIF-8 Mixed Matrix Membranes. *ACS Appl. Mater. Interfaces* **2016,** *8* (40), 27311-27321.

10. Dong, G.; Li, H.; Chen, V., Challenges and opportunities for mixed-matrix membranes for gas separation. *J. Mater. Chem. A* **2013,** *1* (15), 4610-4630.

11. Galizia, M.; Chi, W. S.; Smith, Z. P.; Merkel, T. C.; Baker, R. W.; Freeman, B. D., 50th Anniversary Perspective: Polymers and Mixed Matrix Membranes for Gas and Vapor Separation: A Review and Prospective Opportunities. *Macromolecules* **2017,** *50* (20), 7809-7843.

12. Chuah, C. Y.; Goh, K.; Yang, Y.; Gong, H.; Li, W.; Karahan, H. E.; Guiver, M. D.; Wang, R.; Bae, T.-H., Harnessing Filler Materials for Enhancing Biogas Separation Membranes. *Chem. Rev.* **2018,** *118* (18), 8655-8769.

13. Zhang, Y.; Sunarso, J.; Liu, S.; Wang, R., Current status and development of membranes for CO2/CH4 separation: A review. *Int J Greenh. Gas Con.* **2013,** *12*, 84-107.

14. Vinoba, M.; Bhagiyalakshmi, M.; Alqaheem, Y.; Alomair, A. A.; Pérez, A.; Rana, M. S., Recent progress of fillers in mixed matrix membranes for CO2 separation: A review. *Sep. Purif. Technol.* **2017,** *188*, 431-450.

15. Rezakazemi, M.; Ebadi Amooghin, A.; Montazer-Rahmati, M. M.; Ismail, A. F.; Matsuura, T., State-of-the-art membrane based CO2 separation using mixed matrix membranes (MMMs): An overview on current status and future directions. *Prog. Polym. Sci.* **2014,** *39* (5), 817-861.

16. Moore, T. T.; Mahajan, R.; Vu, D. Q.; Koros, W. J., Hybrid membrane materials comprising organic polymers with rigid dispersed phases. *AIChE Journal* **2004,** *50* (2), 311-321.

17. Zhang, Y.; Balkus Jr, K. J.; Musselman, I. H.; Ferraris, J. P., Mixed-matrix membranes composed of Matrimid® and mesoporous ZSM-5 nanoparticles. *J. Membr. Sci.* **2008,** *325* (1), 28-39.

18. Chung, T.-S.; Chan, S. S.; Wang, R.; Lu, Z.; He, C., Characterization of permeability and sorption in Matrimid/C60 mixed matrix membranes. *J. Membr. Sci.* **2003,** *211* (1), 91-99.

19. Zornoza, B.; Téllez, C.; Coronas, J., Mixed matrix membranes comprising glassy polymers and dispersed mesoporous silica spheres for gas separation. *J. Membr. Sci.* **2011,** *368* (1), 100-109.

20. Roilo, D.; Patil, P. N.; Brusa, R. S.; Miotello, A.; Aghion, S.; Ferragut, R.; Checchetto, R., Polymer rigidification in graphene based nanocomposites: Gas barrier effects and free volume reduction. *Polymer* **2017,** *121*, 17-25.

21. Li, Y.; Chung, T.-S.; Cao, C.; Kulprathipanja, S., The effects of polymer chain rigidification, zeolite pore size and pore blockage on polyethersulfone (PES)-zeolite A mixed matrix membranes. *J. Membr. Sci.* **2005,** *260* (1), 45-55.

22. Süer, M. G.; Baç, N.; Yilmaz, L., Gas permeation characteristics of polymer-zeolite mixed matrix membranes. *J. Membr. Sci.* **1994,** *91* (1), 77-86.

23. Moore, T. T.; Mahajan, R.; Vu, D. Q.; Koros, W. J., Hybrid membrane materials comprising organic polymers with rigid dispersed phases. *AlChE J.* **2004,** *50* (2), 311-321.

24. Li, Y.; Chung, T.-S.; Cao, C.; Kulprathipanja, S., The effects of polymer chain rigidification, zeolite pore size and pore blockage on polyethersulfone (PES)-zeolite A mixed matrix membranes. *J. Membr. Sci.* **2005,** *260* (1–2), 45-55.

25. Zornoza, B.; Esekhile, O.; Koros, W. J.; Téllez, C.; Coronas, J., Hollow silicalite-1 sphere-polymer mixed matrix membranes for gas separation. *Sep. Purif. Technol.* **2011,** *77* (1), 137-145.

26. Mahajan, R.; Koros, W. J., Mixed matrix membrane materials with glassy polymers. Part 1. *Polymer Engineering & Science* **2002,** *42* (7), 1420-1431.

27. Moore, T. T.; Koros, W. J., Gas sorption in polymers, molecular sieves, and mixed matrix membranes. *J. Appl. Polym. Sci.* **2007,** *104* (6), 4053-4059.

28. Adams, R. T.; Lee, J. S.; Bae, T.-H.; Ward, J. K.; Johnson, J. R.; Jones, C. W.; Nair, S.; Koros, W. J., CO2–CH4 permeation in high zeolite 4A loading mixed matrix membranes. *J. Membr. Sci.* **2011,** *367* (1–2), 197-203.

29. Birgül Tantekin-Ersolmaz, Ş.; Şenorkyan, L.; Kalaonra, N.; Tatlıer, M.; Erdem-Şenatalar, A., n-Pentane/i-pentane separation by using zeolite–PDMS mixed matrix membranes. *J. Membr. Sci.* **2001,** *189* (1), 59-67.

30. Bae, T.-H.; Long, J. R., CO2/N2 separations with mixed-matrix membranes containing Mg2(dobdc) nanocrystals. *Energy Environ. Sci.* **2013,** *6* (12), 3565-3569.

31. Vinh-Thang, H.; Kaliaguine, S., Predictive Models for Mixed-Matrix Membrane Performance: A Review. *Chem. Rev. (Washington, DC, U. S.)* **2013,** *113*, 4980.

32. Seoane, B.; Sebastián, V.; Téllez, C.; Coronas, J., Crystallization in THF: the possibility of one-pot synthesis of mixed matrix membranes containing MOF MIL-68(Al). *CrystEngComm* **2013,** *15* (45), 9483-9490.

33. Li, Y.; Guan, H.-M.; Chung, T.-S.; Kulprathipanja, S., Effects of novel silane modification of zeolite surface on polymer chain rigidification and partial pore blockage in polyethersulfone (PES)–zeolite A mixed matrix membranes. *J. Membr. Sci.* **2006,** *275* (1), 17-28.

34. Ismail, A. F.; Kusworo, T. D.; Mustafa, A., Enhanced gas permeation performance of polyethersulfone mixed matrix hollow fiber membranes using novel Dynasylan Ameo silane agent. *J. Membr. Sci.* **2008,** *319* (1), 306-312.

35. Mahajan, R.; Koros, W. J., Mixed matrix membrane materials with glassy polymers. Part 2. *Polym. Eng. Sci.* **2002,** *42* (7), 1432-1441.

36. Mahajan, R.; Koros, W. J., Mixed matrix membrane materials with glassy polymers. Part 1. *Polym. Eng. Sci.* **2002,** *42* (7), 1420-1431.

37. Karunakaran, M.; Villalobos, L. F.; Kumar, M.; Shevate, R.; Akhtar, F. H.; Peinemann, K. V., Graphene oxide doped ionic liquid ultrathin composite membranes for efficient CO2 capture. *J. Mater. Chem. A,* **2017,** *5* (2), 649-656.

38. Li, H.; Tuo, L.; Yang, K.; Jeong, H.-K.; Dai, Y.; He, G.; Zhao, W., Simultaneous enhancement of mechanical properties and CO2 selectivity of ZIF-8 mixed matrix membranes: Interfacial toughening effect of ionic liquid. *J. Membr. Sci.* **2016,** *511*, 130-142.

39. Hao, L.; Li, P.; Yang, T.; Chung, T.-S., Room temperature ionic liquid/ZIF-8 mixed-matrix membranes for natural gas sweetening and post-combustion CO2 capture. *J. Membr. Sci.* **2013,** *436*, 221-231.

40. Hudiono, Y. C.; Carlisle, T. K.; Bara, J. E.; Zhang, Y.; Gin, D. L.; Noble, R. D., A three-component mixed-matrix membrane with enhanced CO2 separation properties based on zeolites and ionic liquid materials. *J. Membr. Sci.* **2010,** *350* (1), 117-123.

41. Lin, R.; Ge, L.; Diao, H.; Rudolph, V.; Zhu, Z., Ionic Liquids as the MOFs/Polymer Interfacial Binder for Efficient Membrane Separation. *ACS Appl. Mater. Interfaces* **2016,** *8* (46), 32041-32049.

42. Vu, M.-T.; Lin, R.; Diao, H.; Zhu, Z.; Bhatia, S. K.; Smart, S., Effect of ionic liquids (ILs) on MOFs/polymer interfacial enhancement in mixed matrix membranes. *J. Membr. Sci.* **2019,** *587*, 117157.

43. Ding, W.; Eitan, A.; Fisher, F. T.; Chen, X.; Dikin, D. A.; Andrews, R.; Brinson, L. C.; Schadler, L. S.; Ruoff, R. S., Direct Observation of Polymer Sheathing in Carbon Nanotube−Polycarbonate Composites. *Nano Letters* **2003,** *3* (11), 1593-1597.

44. Hore, M. J. A.; Ford, J.; Ohno, K.; Composto, R. J.; Hammouda, B., Direct Measurements of Polymer Brush Conformation Using Small-Angle Neutron Scattering (SANS) from Highly Grafted Iron Oxide Nanoparticles in Homopolymer Melts. *Macromolecules* **2013,** *46* (23), 9341-9348.

45. Holt, A. P.; Griffin, P. J.; Bocharova, V.; Agapov, A. L.; Imel, A. E.; Dadmun, M. D.; Sangoro, J. R.; Sokolov, A. P., Dynamics at the Polymer/Nanoparticle Interface in Poly(2-vinylpyridine)/Silica Nanocomposites. *Macromolecules* **2014,** *47* (5), 1837-1843.

46. Cheng, S.; Carroll, B.; Lu, W.; Fan, F.; Carrillo, J.-M. Y.; Martin, H.; Holt, A. P.; Kang, N.-G.; Bocharova, V.; Mays, J. W.; Sumpter, B. G.; Dadmun, M.; Sokolov, A. P., Interfacial Properties of Polymer Nanocomposites: Role of Chain Rigidity and Dynamic Heterogeneity Length Scale. *Macromolecules* **2017,** *50* (6), 2397-2406.

47. Cheng, S.; Bocharova, V.; Belianinov, A.; Xiong, S.; Kisliuk, A.; Somnath, S.; Holt, A. P.; Ovchinnikova, O. S.; Jesse, S.; Martin, H.; Etampawala, T.; Dadmun, M.; Sokolov, A. P., Unraveling the Mechanism of Nanoscale Mechanical Reinforcement in Glassy Polymer Nanocomposites. *Nano Letters* **2016,** *16* (6), 3630-3637.

48. Galizia, M.; De Angelis, M. G.; Messori, M.; Sarti, G. C., Mass Transport in Hybrid PTMSP/Silica Membranes. *Ind. Eng. Chem. Res* **2014,** *53* (22), 9243-9255.

49. Díaz, K.; Garrido, L.; López-González, M.; del Castillo, L. F.; Riande, E., CO_2 Transport in Polysulfone Membranes Containing Zeolitic Imidazolate Frameworks As Determined by Permeation and PFG NMR Techniques. *Macromolecules* **2010,** *43* (1), 316-325.

50. Dong, G.; Li, H.; Chen, V., Challenges and opportunities for mixed-matrix membranes for gas separation. *J. Mater. Chem. A* **2013,** *1*, 4610.

51. Monsalve-Bravo, G. M.; Bhatia, S. K., Modeling Permeation through Mixed-Matrix Membranes: A Review. *Processes* **2018,** *6* (9), 172.

52. Maxwell, J. C., *A Treatise on Electricity and Magnetism*. Dover Publications: New York, 1954.

53. Monsalve-Bravo, G. M.; Bhatia, S. K., Extending effective medium theory to finite size systems: Theory and simulation for permeation in mixed-matrix membranes. *J. Membr. Sci.* **2017,** *531* (Supplement C), 148-159.

54. Bruggeman, D. A. G., Berechnung verschiedener physikalischer Konstanten von heterogenen Substanzen. I. Dielektrizitätskonstanten und Leitfähigkeiten der Mischkörper aus isotropen Substanzen. *Annalen der Physik* **1935,** *416* (7), 636-664.

55. Vu, D. Q.; Koros, W. J.; Miller, S. J., Mixed matrix membranes using carbon molecular sieves: I. Preparation and experimental results. *J. Membr. Sci.* **2003,** *211* (2), 311-334.

56. Vu, D. Q.; Koros, W. J.; Miller, S. J., Mixed matrix membranes using carbon molecular sieves: II. Modeling permeation behavior. *J. Membr. Sci.* **2003,** *211* (2), 335-348.

57. Lewis, T. B.; Nielsen, L. E., Dynamic mechanical properties of particulate-filled composites. *J. Appl. Polym. Sci.* **1970,** *14* (6), 1449-1471.

58. Pal, R., New Models for Thermal Conductivity of Particulate Composites. *J. Reinf. Plast. Compos.* **2007,** *26* (7), 643-651.

59. Pal, R., Permeation models for mixed matrix membranes. *J. Colloid Interface Sci.* **2008,** *317* (1), 191-198.

60. Felske, J. D., Effective thermal conductivity of composite spheres in a continuous medium with contact resistance. *International Journal of Heat and Mass Transfer* **2004,** *47* (14–16), 3453-3461.

61. Chung, T.-S.; Jiang, L. Y.; Li, Y.; Kulprathipanja, S., Mixed matrix membranes (MMMs) comprising organic polymers with dispersed inorganic fillers for gas separation. *Progress in Polymer Science* **2007,** *32* (4), 483-507.

62. Shariati, A.; Omidkhah, M.; Pedram, M. Z., New permeation models for nanocomposite polymeric membranes filled with nonporous particles. *Chem. Eng. Res. Des.* **2012,** *90* (4), 563-575.

63. Maghami, S.; Sadeghi, M.; Mehrabani-Zeinabad, A.; Zarabadi, M.; Ghalei, B., The Role of Interfacial Morphology in the Gas Transport Behavior of Nanocomposite Membranes: A Mathematical Modeling Approach. *Ind. Eng. Chem. Res* **2019,** *58* (25), 11022-11037.

64. Felske, J. D., Effective thermal conductivity of composite spheres in a continuous medium with contact resistance. *Int. J. Heat Mass Transf* **2004,** *47* (14), 3453-3461.

65. Maghami, S.; Sadeghi, M.; Mehrabani-Zeinabad, A., Recognition of polymer-particle interfacial morphology in mixed matrix membranes through ideal permeation predictive models. *Polym. Test.* **2017,** *63*, 25-37.

66. Sholl, D. S., Understanding Macroscopic Diffusion of Adsorbed Molecules in Crystalline Nanoporous Materials via Atomistic Simulations. *Acc. Chem. Res.* **2006,** *39* (6), 403-411.

67. Gulín-González, J.; Schüring, A.; Fritzsche, S.; Kärger, J.; Vasenkov, S., The influence of the desorption barrier on the transport of molecules through the external surface of nanoporous crystals. *Chem. Phys. Lett.* **2006,** *430* (1), 60-66.

68. Dutta, R. C.; Bhatia, S. K., Transport Diffusion of Light Gases in Polyethylene Using Atomistic Simulations. *Langmuir* **2017,** *33* (4), 936-946.

69. Sanders, E. S.; Koros, W. J., Sorption of CO2, C2H4, N2O and their binary mixtures in poly(methyl methacrylate). *J. Polym. Sci., Part B: Polym. Phys.* **1986,** *24* (1), 175-188.

70. Skoulidas, A. I.; Sholl, D. S., Molecular Dynamics Simulations of Self-Diffusivities, Corrected Diffusivities, and Transport Diffusivities of Light Gases in Four Silica Zeolites To Assess Influences of Pore Shape and Connectivity. *J. Phys. Chem. A* **2003,** *107* (47), 10132-10141.

71. Jeon, M. Y.; Kim, D.; Kumar, P.; Lee, P. S.; Rangnekar, N.; Bai, P.; Shete, M.; Elyassi, B.; Lee, H. S.; Narasimharao, K.; Basahel, S. N.; Al-Thabaiti, S.; Xu, W.; Cho, H. J.; Fetisov, E. O.; Thyagarajan, R.; DeJaco, R. F.; Fan, W.; Mkhoyan, K. A.; Siepmann, J. I.; Tsapatsis, M., Ultra-selective high-flux membranes from directly synthesized zeolite nanosheets. *Nature* **2017,** *543*, 690.

72. Huang, S.; Dakhchoune, M.; Luo, W.; Oveisi, E.; He, G.; Rezaei, M.; Zhao, J.; Alexander, D. T. L.; Züttel, A.; Strano, M. S.; Agrawal, K. V., Single-layer graphene membranes by crack-free transfer for gas mixture separation. *Nat. Commun.* **2018,** *9* (1), 2632.

73. Wang, L.; Boutilier, M. S. H.; Kidambi, P. R.; Jang, D.; Hadjiconstantinou, N. G.; Karnik, R., Fundamental transport mechanisms, fabrication and potential applications of nanoporous atomically thin membranes. *Nat. Nanotechnol.* **2017,** *12*, 509.

74. Dutta, R. C.; Bhatia, S. K., Structure and Gas Transport at the Polymer–Zeolite Interface: Insights from Molecular Dynamics Simulations. *ACS Appl. Mater. Interfaces* **2018,** *10* (6), 5992-6005.

75. Li, T.; Pan, Y.; Peinemann, K.-V.; Lai, Z., Carbon dioxide selective mixed matrix composite membrane containing ZIF-7 nano-fillers. *J. Membr. Sci.* **2013,** *425-426*, 235-242.

76. Hong, M.; Falconer, J. L.; Noble, R. D., Modification of Zeolite Membranes for H2 Separation by Catalytic Cracking of Methyldiethoxysilane. *Ind. Eng. Chem. Res.* **2005,** *44* (11), 4035-4041.

77. Eun Jee, S.; McGaughey, A. J. H.; Sholl, D. S., Molecular simulations of hydrogen and methane permeation through pore mouth modified zeolite membranes. *Mol. Simul.* **2009,** *35* (1-2), 70-78.

78. Chmelik, C.; Varma, A.; Heinke, L.; Shah, D. B.; Kärger, J.; Kremer, F.; Wilczok, U.; Schmidt, W., Effect of Surface Modification on Uptake Rates of Isobutane in MFI Crystals: An Infrared Microscopy Study. *Chem. Mater.* **2007,** *19* (24), 6012-6019.

79. Sun, C.; Boutilier, M. S. H.; Au, H.; Poesio, P.; Bai, B.; Karnik, R.; Hadjiconstantinou, N. G., Mechanisms of Molecular Permeation through Nanoporous Graphene Membranes. *Langmuir* **2014,** *30* (2), 675-682.

80. Liu, L.; Nicholson, D.; Bhatia, S. K., Effects of Flange Adsorption Affinity and Membrane Porosity on Interfacial Resistance in Carbon Nanotube Membranes. *ACS Appl. Mater. Interfaces* **2018,** *10* (40), 34706-34717.

81. Glavatskiy, K. S.; Bhatia, S. K., Effect of pore size on the interfacial resistance of a porous membrane. *J. Membr. Sci.* **2017,** *524* (Supplement C), 738-745.

82. Varanasi, S. R.; Subramanian, Y.; Bhatia, S. K., High Interfacial Barriers at Narrow Carbon Nanotube–Water Interfaces. *Langmuir* **2018,** *34* (27), 8099-8111.

83. Kärger, J., In-depth study of surface resistances in nanoporous materials by microscopic diffusion measurement. *Microporous Mesoporous Mater.* **2014,** *189*, 126-135.

84. Ahunbay, M. G.; Elliott, J. R.; Talu, O., Surface Resistance to Permeation through the Silicalite Single Crystal Membrane: Variation with Permeant. *J. Phys. Chem. B* **2004,** *108* (23), 7801-7808.

85. Teixeira, A. R.; Qi, X.; Chang, C.-C.; Fan, W.; Conner, W. C.; Dauenhauer, P. J., On Asymmetric Surface Barriers in MFI Zeolites Revealed by Frequency Response. *J. Phys. Chem. C* **2014,** *118* (38), 22166-22180.

86. Teixeira, A. R.; Chang, C.-C.; Coogan, T.; Kendall, R.; Fan, W.; Dauenhauer, P. J., Dominance of Surface Barriers in Molecular Transport through Silicalite-1. *J. Phys. Chem. C* **2013,** *117* (48), 25545-25555.

87. Heinke, L.; Kärger, J., Correlating Surface Permeability with Intracrystalline Diffusivity in Nanoporous Solids. *Phys. Rev. Lett.* **2011,** *106* (7), 074501.

88. Newsome, D. A.; Sholl, D. S., Influences of Interfacial Resistances on Gas Transport through Carbon Nanotube Membranes. *Nano Lett.* **2006,** *6* (9), 2150-2153.

89. Dutta, R. C.; Bhatia, S. K., Interfacial barriers to gas transport in zeolites: distinguishing internal and external resistances. *Phys. Chem. Chem. Phys.* **2018,** *20* (41), 26386-26395.

90. Kärger, J.; Caro, J., Interpretation and correlation of zeolitic diffusivities obtained from nuclear magnetic resonance and sorption experiments. *Journal of the Chemical Society, Faraday Transactions 1: Physical Chemistry in Condensed Phases* **1977,** *73* (0), 1363-1376.

91. Gueudré, L.; Jolimaîte, E.; Bats, N.; Dong, W., Diffusion in zeolites: is surface resistance a critical parameter? *Adsorption* **2010,** *16* (1), 17-27.

92. Teixeira, A. R.; Qi, X.; Conner, W. C.; Mountziaris, T. J.; Fan, W.; Dauenhauer, P. J., 2D Surface Structures in Small Zeolite MFI Crystals. *Chem. Mater.* **2015,** *27* (13), 4650-4660.

93. Hibbe, F.; Chmelik, C.; Heinke, L.; Pramanik, S.; Li, J.; Ruthven, D. M.; Tzoulaki, D.; Kärger, J. R., The Nature of Surface Barriers on Nanoporous Solids Explored by Microimaging of Transient Guest Distributions. *J. Am. Chem. Soc.* **2011,** *133*, 2804.

94. Heinke, L.; Tzoulaki, D.; Chmelik, C.; Hibbe, F.; van Baten, J. M.; Lim, H.; Li, J.; Krishna, R.; Kärger, J., Assessing Guest Diffusivities in Porous Hosts from Transient Concentration Profiles. *Phys. Rev. Lett.* **2009,** *102*, 065901.

95. Kärger, J.; Binder, T.; Chmelik, C.; Hibbe, F.; Krautscheid, H.; Krishna, R.; Weitkamp, J., Microimaging of transient guest profiles to monitor mass transfer in nanoporous materials. *Nat. Mater.* **2014,** *13*, 333.

96. Remi, J. C. S.; Lauerer, A.; Chmelik, C.; Vandendael, I.; Terryn, H.; Baron, G. V.; Denayer, J. F. M.; Kärger, J., The role of crystal diversity in understanding mass transfer in nanoporous materials. *Nat. Mater.* **2015,** *15*, 401.

97. Karwacki, L.; Stavitski, E.; Kox, M. H. F.; Kornatowski, J.; Weckhuysen, B. M., Intergrowth Structure of Zeolite Crystals as Determined by Optical and Fluorescence Microscopy of the Template-Removal Process. **2007,** *46* (38), 7228-7231.

98. Mitchell, S.; Michels, N.-L.; Kunze, K.; Pérez-Ramírez, J., Visualization of hierarchically structured zeolite bodies from macro to nano length scales. *Nat. Chem.* **2012,** *4*, 825.

99. Seebacher, C.; Rau, J.; Deeg, F.-W.; Bräuchle, C.; Altmaier, S.; Jäger, R.; Behrens, P., Visualization of Mesostructures and Organic Guest Inclusion in Molecular Sieves with Confocal Microscopy. **2001,** *13* (18), 1374-1377.

100. Kärger, J.; Ruthven, D. M., Diffusion in nanoporous materials: fundamental principles, insights and challenges. *New J. Chem.* **2016,** *40* (5), 4027-4048.

101. Kärger, J., Measurement of Diffusion in Zeolites—A Never Ending Challenge? *Adsorption* **2003,** *9* (1), 29-35.

102. Liu, L.; Nicholson, D.; Bhatia, S. K., Interfacial Resistance and Length-Dependent Transport Diffusivities in Carbon Nanotubes. *J. Phys. Chem. C* **2016,** *120* (46), 26363-26373.

103. Zhang, X.; Zhou, W.; Xu, F.; Wei, M.; Wang, Y., Resistance of water transport in carbon nanotube membranes. *Nanoscale* **2018,** *10* (27), 13242-13249.

104. Arya, G.; Maginn, E. J.; Chang, H.-C., Effect of the Surface Energy Barrier on Sorbate Diffusion in AlPO4-5. *J. Phys. Chem. B* **2001,** *105* (14), 2725-2735.

105. Newsome, D. A.; Sholl, D. S., Predictive Assessment of Surface Resistances in Zeolite Membranes Using Atomically Detailed Models. *J. Phys. Chem. B* **2005,** *109* (15), 7237-7244.

106. Newsome, D. A.; Sholl, D. S., Molecular Dynamics Simulations of Mass Transfer Resistance in Grain Boundaries of Twinned Zeolite Membranes. *J. Phys. Chem. B* **2006,** *110* (45), 22681-22689.

107. Newsome, D. A.; Sholl, D. S., Atomically detailed simulations of surface resistances to transport of CH_4, CF_4, and C_2H_6 through silicalite membranes. *Microporous Mesoporous Mater.* **2008,** *107* (3), 286-295.

108. Mason, E. A.; Malinauskas, A. P.; Evans, R. B., Flow and Diffusion of Gases in Porous Media. *J. Chem. Phys.* **1967,** *46* (8), 3199-3216.

109. Heffelfinger, G. S.; Swol, F. v., Diffusion in Lennard-Jones fluids using dual control volume grand canonical molecular dynamics simulation (DCV-GCMD). **1994,** *100* (10), 7548-7552.

110. Ahunbay, M. G.; Elliott, J. R.; Talu, O., The Diffusion Process of Methane through a Silicalite Single Crystal Membrane. *J. Phys. Chem. B* **2002,** *106* (20), 5163-5168.

111. Arya, G.; Maginn, E. J.; Chang, H.-C., Effect of the Surface Energy Barrier on Sorbate Diffusion in AlPO4-5. *J. Phys. Chem. B* **2001,** *105* (14), 2725-2735.

112. MacElroy, J. M. D.; Boyle, M. J., Nonequilibrium molecular dynamics simulation of a model carbon membrane separation of CH4/H2 mixtures. *Chem. Eng. J.* **1999,** *74* (1), 85-97.

113. Newsome, D. A.; Sholl, D. S., Predictive Assessment of Surface Resistances in Zeolite Membranes Using Atomically Detailed Models. *J. Phys. Chem. B* **2005,** *109* (15), 7237-7244.

114. Zhu, F.; Tajkhorshid, E.; Schulten, K., Collective Diffusion Model for Water Permeation through Microscopic Channels. *Phys. Rev. Lett.* **2004,** *93* (22), 224501.

115. Zimmermann, N. E. R.; Balaji, S. P.; Keil, F. J., Surface Barriers of Hydrocarbon Transport Triggered by Ideal Zeolite Structures. *J. Phys. Chem. C* **2012,** *116* (5), 3677-3683.

116. Sholl, D. S.; Lively, R. P., Defects in Metal–Organic Frameworks: Challenge or Opportunity? *J. Phys. Chem. Lett.* **2015,** *6* (17), 3437-3444.

117. Combariza, A. F.; Sastre, G., Influence of Zeolite Surface in the Sorption of Methane from Molecular Dynamics. *J. Phys. Chem. C* **2011,** *115* (28), 13751-13758.

118. Newsome, D. A.; Sholl, D. S., Molecular Dynamics Simulations of Mass Transfer Resistance in Grain Boundaries of Twinned Zeolite Membranes. *J. Phys. Chem. B* **2006,** *110*, 22681.

119. Horcajada, P.; Chalati, T.; Serre, C.; Gillet, B.; Sebrie, C.; Baati, T.; Eubank, J. F.; Heurtaux, D.; Clayette, P.; Kreuz, C.; Chang, J.-S.; Hwang, Y. K.; Marsaud, V.; Bories, P.-N.; Cynober, L.; Gil, S.; Férey, G.; Couvreur, P.; Gref, R., Porous metal–organic-framework nanoscale carriers as a potential platform for drug delivery and imaging. *Nat. Mater.* **2009,** *9*, 172.

120. Sparreboom, W.; van den Berg, A.; Eijkel, J. C. T., Transport in nanofluidic systems: a review of theory and applications. *New J. Phys.* **2010,** *12* (1), 015004.

121. Das, S.; Dubsky, P.; van den Berg, A.; Eijkel, J. C. T., Concentration Polarization in Translocation of DNA through Nanopores and Nanochannels. *Phys. Rev. Lett.* **2012,** *108* (13), 138101.

122. Majumder, M.; Chopra, N.; Andrews, R.; Hinds, B. J., Enhanced flow in carbon nanotubes. *Nature* **2005,** *438*, 44.

123. Bai, P.; Jeon, M. Y.; Ren, L.; Knight, C.; Deem, M. W.; Tsapatsis, M.; Siepmann, J. I., Discovery of optimal zeolites for challenging separations and chemical transformations using predictive materials modeling. *Nature Communications* **2015,** *6*, 5912.

124. Krishna, R.; Paschek, D., Separation of hydrocarbon mixtures using zeolite membranes: a modelling approach combining molecular simulations with the Maxwell–Stefan theory. *Sep. Purif. Technol.* **2000,** *21* (1), 111-136.

125. Huddersman, K.; Klimczyk, M., Separation of branched hexane isomers using zeolite molecular sieves. **1996,** *42* (2), 405-408.

126. Peng, B.; Locascio, M.; Zapol, P.; Li, S.; Mielke, S. L.; Schatz, G. C.; Espinosa, H. D., Measurements of near-ultimate strength for multiwalled carbon nanotubes and irradiation-induced crosslinking improvements. *Nature Nanotechnology* **2008,** *3*, 626.

127. Wei, B. Q.; Vajtai, R.; Ajayan, P. M., Reliability and current carrying capacity of carbon nanotubes. **2001,** *79* (8), 1172-1174.

128. Bhatia, S. K.; Chen, H.; Sholl, D. S., Comparisons of diffusive and viscous contributions to transport coefficients of light gases in single-walled carbon nanotubes. *Mol. Simul.* **2005,** *31* (9), 643-649.

129. Rincon Bonilla, M.; Bhatia, S. K., Diffusion in Pore Networks: Effective Self-Diffusivity and the Concept of Tortuosity. *J. Phys. Chem. C* **2013,** *117* (7), 3343-3357.

130. Kočiřík, M.; Struve, P.; Fiedler, K.; Bülow, M., A model for the mass-transfer resistance at the surface of zeolite crystals. *J. Chem. Soc., Faraday Trans. 1* **1988,** *84* (9), 3001-3013.

131. Majumder, M.; Chopra, N.; Hinds, B. J., Effect of Tip Functionalization on Transport through Vertically Oriented Carbon Nanotube Membranes. *J. Am. Chem. Soc.* **2005,** *127* (25), 9062-9070.

132. Suk, M. E.; Raghunathan, A. V.; Aluru, N. R., Fast reverse osmosis using boron nitride and carbon nanotubes. **2008,** *92* (13), 133120.

133. Suk, M. E.; Aluru, N. R., Water Transport through Ultrathin Graphene. *J. Phys. Chem. Lett.* **2010,** *1* (10), 1590-1594.

134. Nicholls, W. D.; Borg, M. K.; Lockerby, D. A.; Reese, J. M. J. M.; Nanofluidics, Water transport through (7,7) carbon nanotubes of different lengths using molecular dynamics. **2012,** *12* (1), 257-264.

135. Dauenhauer, P. J., Reply to "Comment on 'On Asymmetric Surface Barriers in MFI Zeolites Revealed by Frequency Response'". *J. Phys. Chem. C* **2015,** *119* (52), 29203-29205.

136. Brandani, S.; Caro, J.; Jobic, H.; Kärger, J.; Krause, C.; Staudt, R., Diffusion of n-alkanes in zeolites: the benefit of observation over different length scales. In *Studies in Surface Science and Catalysis*, Xu, R.; Gao, Z.; Chen, J.; Yan, W., Eds. Elsevier: 2007; Vol. 170, pp 981-987.

137. Karwacki, L.; Kox, M. H. F.; Matthijs de Winter, D. A.; Drury, M. R.; Meeldijk, J. D.; Stavitski, E.; Schmidt, W.; Mertens, M.; Cubillas, P.; John, N.; Chan, A.; Kahn, N.; Bare, S. R.; Anderson, M.; Kornatowski, J.; Weckhuysen, B. M., Morphology-dependent zeolite intergrowth

structures leading to distinct internal and outer-surface molecular diffusion barriers. *Nat. Mater.* **2009,** *8*, 959.

138. Geier, O.; Vasenkov, S.; Lehmann, E.; Kärger, J.; Schemmert, U.; Rakoczy, R. A.; Weitkamp, J., Interference Microscopy Investigation of the Influence of Regular Intergrowth Effects in MFI-Type Zeolites on Molecular Uptake. *J. Phys. Chem. B* **2001,** *105* (42), 10217-10222.

139. Chen, C.; Ozcan, A.; Yazaydin, A. O.; Ladewig, B. P., Gas permeation through single-crystal ZIF-8 membranes. *J. Membr. Sci.* **2019,** *575*, 209-216.

140. Alian, A. R.; Meguid, S. A.; Kundalwal, S. I., Unraveling the influence of grain boundaries on the mechanical properties of polycrystalline carbon nanotubes. *Carbon* **2017,** *125*, 180-188.

141. Kärger, J.; Ruthven, D. M.; Theodorou, D. N., Sorption Kinetics. In *Diffusion in Nanoporous Materials*, Kärger, J.; Ruthven, D. M.; Theodorou, D. N., Eds. Wiley-VCH Verlag GmbH & Co. KGaA: Weinheim, Germany, 2012; Vol. 1.

142. Zhang, L.; Chmelik, C.; van Laak, A. N. C.; Kärger, J.; de Jongh, P. E.; de Jong, K. P., Direct assessment of molecular transport in mordenite: dominance of surface resistances. *Chem. Commun.* **2009,** (42), 6424-6426.

143. Gueudré, L.; Bats, N.; Jolimaître, E., Effect of surface resistance on cyclohexane uptake curves in Silicalite-1 crystals. *Microporous Mesoporous Mater.* **2012,** *147* (1), 310-317.

144. Sastre, G.; Kärger, J.; Ruthven, D. M., Molecular Dynamics Study of Diffusion and Surface Permeation of Benzene in Silicalite. *J. Phys. Chem. C* **2018,** *122* (13), 7217-7225.

145. Ruthven, D. M.; Vidoni, A., ZLC diffusion measurements: Combined effect of surface resistance and internal diffusion. *Chemical Engineering Science* **2012,** *71*, 1-4.

146. Zimmermann, N. E. R.; Smit, B.; Keil, F. J., On the Effects of the External Surface on the Equilibrium Transport in Zeolite Crystals. *J. Phys. Chem. C* **2010,** *114* (1), 300-310.

147. Zimmermann, N. E. R.; Smit, B.; Keil, F. J., Predicting Local Transport Coefficients at Solid–Gas Interfaces. *J. Phys. Chem. C* **2012,** *116* (35), 18878-18883.

148. Crabtree, J. C.; Molinari, M.; Parker, S. C.; Purton, J. A., Simulation of the Adsorption and Transport of CO2 on Faujasite Surfaces. *J. Phys. Chem. C* **2013,** *117* (42), 21778-21787.

149. Kalantzopoulos, G. N.; Policicchio, A.; Maccallini, E.; Krkljus, I.; Ciuchi, F.; Hirscher, M.; Agostino, R. G.; Golemme, G., Resistance to the transport of H2 through the external surface of as-made and modified silicalite-1 (MFI). *Microporous Mesoporous Mater.* **2016,** *220*, 290-297.

150. Vasenkov, S.; Böhlmann, W.; Galvosas, P.; Geier, O.; Liu, H.; Kärger, J., PFG NMR Study of Diffusion in Mfi-Type Zeolites: Evidence of the Existence of Intracrystalline Transport Barriers. *J. Phys. Chem. B* **2001,** *105*, 5922.

151. Ahunbay, M. G.; Elliott, J. R.; Talu, O., Effect of Surface Resistances on the Diffusion of Binary Mixtures in the Silicalite Single Crystal Membrane. *J. Phys. Chem. B* **2005,** *109* (2), 923-929.

152. Kremer, K.; Binder, K., Monte Carlo simulation of lattice models for macromolecules. *Comput. Phys. Rep.* **1988,** *7* (6), 259-310.

153. Jiang, G.; Hore, M. J. A.; Gam, S.; Composto, R. J., Gold Nanorods Dispersed in Homopolymer Films: Optical Properties Controlled by Self-Assembly and Percolation of Nanorods. *ACS Nano* **2012,** *6* (2), 1578-1588.

154. Hore, M. J. A.; Frischknecht, A. L.; Composto, R. J., Nanorod Assemblies in Polymer Films and Their Dispersion-Dependent Optical Properties. *ACS Macro Letters* **2012,** *1* (1), 115-121.

155. Sharaf, M. A.; Mark, J. E., Monte Carlo simulations on the effects of nanoparticles on chain deformations and reinforcement in amorphous polyethylene networks. *Polymer* **2004,** *45* (11), 3943-3952.

156. Dionne, P. J.; Ozisik, R.; Picu, C. R., Structure and Dynamics of Polyethylene Nanocomposites. *Macromolecules* **2005,** *38* (22), 9351-9358.

157. Abbott, L. J.; Colina, C. M., Atomistic Structure Generation and Gas Adsorption Simulations of Microporous Polymer Networks. *Macromolecules* **2011,** *44* (11), 4511-4519.

158. Larsen, G. S.; Lin, P.; Hart, K. E.; Colina, C. M., Molecular Simulations of PIM-1-like Polymers of Intrinsic Microporosity. *Macromolecules* **2011,** *44* (17), 6944-6951.

159. Hart, K. E.; Colina, C. M., Ionomers of Intrinsic Microporosity: In Silico Development of Ionic-Functionalized Gas-Separation Membranes. *Langmuir* **2014,** *30* (40), 12039-12048.

160. Rukmani, S. J.; Liyana-Arachchi, T. P.; Hart, K. E.; Colina, C. M., Ionic-Functionalized Polymers of Intrinsic Microporosity for Gas Separation Applications. *Langmuir* **2018,** *34* (13), 3949-3960.

161. Rukmani, S. J.; Kupgan, G.; Anstine, D. M.; Colina, C. M., A molecular dynamics study of water-soluble polymers: analysis of force fields from atomistic simulations. *Molecular Simulation* **2019,** *45* (4-5), 310-321.

162. Takeuchi, H.; Okazaki, K., Molecular dynamics simulation of diffusion of simple gas molecules in a short chain polymer. *J. Chem. Phys.* **1990,** *92* (9), 5643-5652.

163. Tamai, Y.; Tanaka, H.; Nakanishi, K., Molecular Simulation of Permeation of Small Penetrants through Membranes. 1. Diffusion Coefficients. *Macromolecules* **1994,** *27* (16), 4498-4508.

164. Müller-Plathe, F.; Rogers, S. C.; van Gunsteren, W. F., Computational evidence for anomalous diffusion of small molecules in amorphous polymers. *Chem. Phys. Lett.* **1992,** *199* (3), 237-243.

165. Mozaffari, F.; Eslami, H.; Moghadasi, J., Molecular dynamics simulation of diffusion and permeation of gases in polystyrene. *Polymer* **2010,** *51* (1), 300-307.

166. van der Vegt, N. F. A., Temperature Dependence of Gas Transport in Polymer Melts: Molecular Dynamics Simulations of CO2 in Polyethylene. *Macromolecules* **2000,** *33* (8), 3153-3160.

167. Faure, F.; Rousseau, B.; Lachet, V.; Ungerer, P., Molecular simulation of the solubility and diffusion of carbon dioxide and hydrogen sulfide in polyethylene melts. *Fluid Phase Equilib.* **2007,** *261* (1–2), 168-175.

168. Pant, P. V. K.; Boyd, R. H., Molecular-dynamics simulation of diffusion of small penetrants in polymers. *Macromolecules* **1993,** *26* (4), 679-686.

169. Gestoso, P.; Karayiannis, N. C., Molecular Simulation of the Effect of Temperature and Architecture on Polyethylene Barrier Properties. *J. Phys. Chem. B* **2008,** *112* (18), 5646-5660.

170. Hofmann, D.; Fritz, L.; Ulbrich, J.; Paul, D., Molecular simulation of small molecule diffusion and solution in dense amorphous polysiloxanes and polyimides. *Comput. Theor. Polym. Sci.* **2000,** *10* (5), 419-436.

171. Arya, G.; Chang, H.-C.; Maginn, E. J., A critical comparison of equilibrium, non-equilibrium and boundary-driven molecular dynamics techniques for studying transport in microporous materials. *J. Chem. Phys.* **2001,** *115* (17), 8112-8124.

172. Ford, D. M.; Heffelfinger, G. S., Massively parallel dual control volume grand canonical molecular dynamics with LADERA II. Gradient driven diffusion through polymers. *Mol. Phys.* **1998,** *94* (4), 673-683.

173. Pohl, P. I.; Heffelfinger, G. S., Massively parallel molecular dynamics simulation of gas permeation across porous silica membranes. *J. Membr. Sci.* **1999,** *155* (1), 1-7.

174. Zhang, K.; Meng, D.; Müller-Plathe, F.; Kumar, S. K., Coarse-grained molecular dynamics simulation of activated penetrant transport in glassy polymers. *Soft Matter* **2018,** *14* (3), 440-447.

175. Bhatia, S. K.; Nicholson, D., Adsorption and Diffusion of Methane in Silica Nanopores: A Comparison of Single-Site and Five-Site Models. *J. Phys. Chem. C* **2012,** *116* (3), 2344-2355.

176. Liu, L.; Nicholson, D.; Bhatia, S. K., Impact of H2O on CO2 Separation from Natural Gas: Comparison of Carbon Nanotubes and Disordered Carbon. *J. Phys. Chem. C* **2015,** *119* (1), 407-419.

177. Cozmuta, I.; Blanco, M.; Goddard, W. A., Gas Sorption and Barrier Properties of Polymeric Membranes from Molecular Dynamics and Monte Carlo Simulations. *J. Phys. Chem. B* **2007,** *111* (12), 3151-3166.

178. Visser, T.; Wessling, M., When Do Sorption-Induced Relaxations in Glassy Polymers Set In? *Macromolecules* **2007,** *40* (14), 4992-5000.

179. Bos, A.; Pünt, I. G. M.; Wessling, M.; Strathmann, H., CO2-induced plasticization phenomena in glassy polymers. *J. Membr. Sci.* **1999,** *155* (1), 67-78.

180. Spyriouni, T.; Boulougouris, G. C.; Theodorou, D. N., Prediction of Sorption of CO_2 in Glassy Atactic Polystyrene at Elevated Pressures Through a New Computational Scheme. *Macromolecules* **2009,** *42* (5), 1759-1769.

181. Wang, L.; Zhou, H.; Wang, X.; Mi, J., Modeling Solubility and Interfacial Properties of Carbon Dioxide Dissolved in Polymers. *Ind. Eng. Chem. Res.* **2016,** *55* (4), 1126-1133.

182. Kupgan, G.; Demidov, A. G.; Colina, C. M., Plasticization behavior in polymers of intrinsic microporosity (PIM-1): A simulation study from combined Monte Carlo and molecular dynamics. *J. Membr. Sci.* **2018,** *565*, 95-103.

183. Balçık, M.; Ahunbay, M. G., Prediction of CO2-induced plasticization pressure in polyimides via atomistic simulations. *J. Membr. Sci.* **2018,** *547*, 146-155.

184. Neyertz, S.; Brown, D., Nanosecond-time-scale reversibility of dilation induced by carbon dioxide sorption in glassy polymer membranes. *J. Membr. Sci.* **2016,** *520*, 385-399.

185. Velioğlu, S.; Ahunbay, M. G.; Tantekin-Ersolmaz, S. B., Investigation of CO2-induced plasticization in fluorinated polyimide membranes via molecular simulation. *J. Membr. Sci.* **2012,** *417-418*, 217-227.

186. Velioğlu, S.; Ahunbay, M. G.; Tantekin-Ersolmaz, S. B., An atomistic insight on CO2 plasticization resistance of thermally rearranged 6FDA-bisAPAF. *J. Membr. Sci.* **2018,** *556*, 23-33.

187. Pandiyan, S.; Brown, D.; Neyertz, S.; van der Vegt, N. F. A., Carbon Dioxide Solubility in Three Fluorinated Polyimides Studied by Molecular Dynamics Simulations. *Macromolecules* **2010,** *43* (5), 2605-2621.

188. Tanis, I.; Brown, D.; Neyertz, S.; Heck, R.; Mercier, R.; Vaidya, M.; Ballaguet, J.-P., A comparison of pure and mixed-gas permeation of nitrogen and methane in 6FDA-based polyimides as studied by molecular dynamics simulations. *Comput. Mater. Sci.* **2018,** *141*, 243-253.

189. Hölck, O.; Böhning, M.; Heuchel, M.; Siegert, M. R.; Hofmann, D., Gas sorption isotherms in swelling glassy polymers—Detailed atomistic simulations. *J. Membr. Sci.* **2013,** *428*, 523-532.

190. Lu, W.; Yuan, D.; Sculley, J.; Zhao, D.; Krishna, R.; Zhou, H.-C., Sulfonate-Grafted Porous Polymer Networks for Preferential CO2 Adsorption at Low Pressure. *J. Am. Chem. Soc.* **2011,** *133* (45), 18126-18129.

191. Myers, A. L.; Prausnitz, J. M., Thermodynamics of mixed-gas adsorption. *AlChE J.* **1965,** *11* (1), 121-127.

192. Reijerkerk, S. R.; Nijmeijer, K.; Ribeiro, C. P.; Freeman, B. D.; Wessling, M., On the effects of plasticization in CO2/light gas separation using polymeric solubility selective membranes. *J. Membr. Sci.* **2011,** *367* (1), 33-44.

193. Minelli, M.; Campagnoli, S.; De Angelis, M. G.; Doghieri, F.; Sarti, G. C., Predictive Model for the Solubility of Fluid Mixtures in Glassy Polymers. *Macromolecules* **2011,** *44* (12), 4852-4862.

194. Shengyuan, L.; Michael, C. B.; Florian, M.-P., Role of the interfacial area for structure and dynamics in polymer nanocomposites: molecular dynamics simulations of polystyrene with silica nanoparticles of different shapes. *Mater Res Express.* **2016,** *3* (10), 105301.

195. Eslami, H.; Müller-Plathe, F., How Thick is the Interphase in an Ultrathin Polymer Film? Coarse-Grained Molecular Dynamics Simulations of Polyamide-6,6 on Graphene. *J. Phys. Chem. C* **2013,** *117* (10), 5249-5257.

196. Eslami, H.; Müller-Plathe, F., Structure and Mobility of Nanoconfined Polyamide-6,6 Oligomers: Application of a Molecular Dynamics Technique with Constant Temperature, Surface Area, and Parallel Pressure. *J. Phys. Chem. B* **2009,** *113* (16), 5568-5581.

197. Voyiatzis, E.; Rahimi, M.; Müller-Plathe, F.; Böhm, M. C., How Thick Is the Polymer Interphase in Nanocomposites? Probing It by Local Stress Anisotropy and Gas Solubility. *Macromolecules* **2014,** *47* (22), 7878-7889.

198. Ndoro, T. V. M.; Böhm, M. C.; Müller-Plathe, F., Interface and Interphase Dynamics of Polystyrene Chains near Grafted and Ungrafted Silica Nanoparticles. *Macromolecules* **2012,** *45* (1), 171-179.

199. Eslami, H.; Rahimi, M.; Müller-Plathe, F., Molecular Dynamics Simulation of a Silica Nanoparticle in Oligomeric Poly(methyl methacrylate): A Model System for Studying the Interphase

Thickness in a Polymer–Nanocomposite via Different Properties. *Macromolecules* **2013,** *46* (21), 8680-8692.

200. Mo, Y.-F.; Yang, C.-L.; Xing, Y.-F.; Wang, M.-S.; Ma, X.-G.; Wang, L.-Z., Effects of silica surface on the ordered orientation of polyethylene: A molecular dynamics study. *Appl. Surf Sci.* **2014,** *311*, 273-278.

201. Pandey, Y. N.; Doxastakis, M., Detailed atomistic Monte Carlo simulations of a polymer melt on a solid surface and around a nanoparticle. *J. Chem. Phys.* **2012,** *136* (9), 094901.

202. Brown, D.; Marcadon, V.; Mélé, P.; Albérola, N. D., Effect of Filler Particle Size on the Properties of Model Nanocomposites. *Macromolecules* **2008,** *41* (4), 1499-1511.

203. Brown, D.; Mélé, P.; Marceau, S.; Albérola, N. D., A Molecular Dynamics Study of a Model Nanoparticle Embedded in a Polymer Matrix. *Macromolecules* **2003,** *36* (4), 1395-1406.

204. Yang, H.; Zhao, X. J.; Li, Z. S.; Yan, F. D., Molecular dynamics simulations on crystallization of polyethylene/fullerene nanocomposites. *J. Chem. Phys.* **2009,** *130* (7), 074902.

205. Yang, H.; Zhao, X. J.; Lu, Z. Y.; Yan, F. D., Temperature influence on the crystallization of polyethylene/fullerene nanocomposites: Molecular dynamics simulation. *J. Chem. Phys.* **2009,** *131* (23), 234906.

206. Li, Y., Effect of nano inclusions on the structural and physical properties of polyethylene polymer matrix. *Polymer* **2011,** *52* (10), 2310-2318.

207. Ferdous, S. F.; Sarker, M. F.; Adnan, A., Role of nanoparticle dispersion and filler-matrix interface on the matrix dominated failure of rigid C60-PE nanocomposites: A molecular dynamics simulation study. *Polymer* **2013,** *54* (10), 2565-2576.

208. Emamy, H.; Kumar, S. K.; Starr, F. W., Diminishing Interfacial Effects with Decreasing Nanoparticle Size in Polymer-Nanoparticle Composites. *Phys. Rev. Lett.* **2018,** *121* (20), 207801.

209. Kalathi, J. T.; Yamamoto, U.; Schweizer, K. S.; Grest, G. S.; Kumar, S. K., Nanoparticle Diffusion in Polymer Nanocomposites. *Phys. Rev. Lett.* **2014,** *112* (10), 108301.

210. Gharib-Zahedi, M. R.; Tafazzoli, M.; Böhm, M. C.; Alaghemandi, M., Interfacial thermal transport and structural preferences in carbon nanotube–polyamide-6,6 nanocomposites: how important are chemical functionalization effects? *Phys. Chem. Chem. Phys.* **2015,** *17* (22), 14502-14512.

211. Erucar, I.; Keskin, S., Separation of CO2 Mixtures Using Zn(bdc)(ted)0.5 Membranes and Composites: A Molecular Simulation Study. *J. Phys. Chem. C* **2011,** *115* (28), 13637-13644.

212. Keskin, S., Molecular Simulation Study of CH4/H2 Mixture Separations Using Metal Organic Framework Membranes and Composites. *J. Phys. Chem. C* **2010,** *114* (30), 13047-13054.

213. Keskin, S.; Sholl, D. S., Selecting metal organic frameworks as enabling materials in mixed matrix membranes for high efficiency natural gas purification. *Energy Environ. Sci.* **2010,** *3* (3), 343-351.

214. Semino, R.; Ramsahye, N. A.; Ghoufi, A.; Maurin, G., Microscopic Model of the Metal–Organic Framework/Polymer Interface: A First Step toward Understanding the Compatibility in Mixed Matrix Membranes. *ACS Appl. Mater. Interfaces* **2016,** *8* (1), 809-819.

215. Benzaqui, M.; Semino, R.; Menguy, N.; Carn, F.; Kundu, T.; Guigner, J.-M.; McKeown, N. B.; Msayib, K. J.; Carta, M.; Malpass-Evans, R.; Le Guillouzer, C.; Clet, G.; Ramsahye, N. A.; Serre, C.; Maurin, G.; Steunou, N., Toward an Understanding of the Microstructure and Interfacial Properties of PIMs/ZIF-8 Mixed Matrix Membranes. *ACS Appl. Mater. Interfaces* **2016,** *8* (40), 27311-27321.

216. Semino, R.; Dürholt, J. P.; Schmid, R.; Maurin, G., Multiscale Modeling of the HKUST-1/Poly(vinyl alcohol) Interface: From an Atomistic to a Coarse Graining Approach. *J. Phys. Chem. C* **2017,** *121* (39), 21491-21496.

217. Zhang, L.; Hu, Z.; Jiang, J., Metal–Organic Framework/Polymer Mixed-Matrix Membranes for H2/CO2 Separation: A Fully Atomistic Simulation Study. *J. Phys. Chem. C* **2012,** *116* (36), 19268-19277.

Chapter 3 Computational Model and Methodology

3.1 Model details

In this chapter, we describe the model and the corresponding interaction potential parameters used to represent the polymers as well as gas molecules in the simulations. Further, we also provide the simulations details and the procedure adapted in this investigation to extract the gas diffusion as well as solubility coefficients in the membrane are provided.

3.1.1 Polymer model

Amorphous polyethylene (PE) and polyimide (PI) polymers were considered in this investigation to represent a neat polymer membrane. The polymer chains were generated by following a self-avoiding random walk technique[1] using Packmol.[2] In what follows we describe the model and the corresponding interaction potential parameters used to represent polymers in our simulations.

<u>Polyethylene (PE):</u> The model system is composed of 50 flexible PE chains, each having 78 carbon atoms on the backbone. The non-bonded van der Waals (vdW) interactions were incorporated with united-atom representation, where carbon atoms along with their bonded hydrogen atoms are lumped into single interacting sites with zero charge

$$U_{ij}^{non-bond} = 4\varepsilon_{ij}\left[\left(\frac{\sigma_{ij}}{r_{ij}}\right)^{12} - \left(\frac{\sigma_{ij}}{r_{ij}}\right)^{6}\right] \tag{3-1}$$

where ε_{ij} and σ_{ij} are the energy and length scale parameters of the LJ potential. The methylene (CH_2) and methyl (CH_3) groups are treated as equivalent sites for all bonded interactions, but, not for vdW interactions. Such a united-atom model has been widely used and verified for studying diffusion and melting behaviors of PE polymers. Further, the PE polymer chain is described by a combination of appropriate bonded interactions by considering the constraints for bond length, bond angle and dihedrals of the form:

$$U_{ij}^{bond} = k_b(l-l_o)^2 + k_\theta(\theta-\theta_0)^2 + \sum\nolimits_{n=1,5}(\mathrm{A}_n \cos^{n-1}\phi) \tag{3-2}$$

where k_b and l_o denote the stiffness and equilibrium length of the bond, k_θ and θ_0 denote force constant and equilibrium angle, and A_n, ϕ denote the force constants and torsion angle. The potential forms with corresponding parameters are summarized in Table 3.1.

Table 3-1. Functional Forms and Parameters for the force field of PE.[3-5]

Interaction type	Functional form	Parameters
non-bonded	Lennard-Jones (LJ) 12-6 form $U_{ij}^{non-bond} = 4\varepsilon_{ij}\left[\left(\frac{\sigma_{ij}}{r_{ij}}\right)^{12} - \left(\frac{\sigma_{ij}}{r_{ij}}\right)^{6}\right]$	$\varepsilon_{CH_3} = 0.227 kcal/mol$ $\sigma_{CH_3} = 4.01 Å$ $\varepsilon_{CH_2} = 0.093 kcal/mol$ $\sigma_{CH_2} = 4.01 Å$
bond	harmonic: $E_b = k_b(l - l_o)^2$	$k_b = 419.518 kcal/mol/Å^2$ $l_0 = 1.54 Å$
angle	harmonic: $E_\theta = k_\theta(\theta - \theta_0)^2$	$k_\theta = 62.09 kcal/mol/\deg^2$ $\theta_0 = 114 Å$
dihedral	Multi-harmonic: $E_d = \sum_{n=1,5}(\mathrm{A}_n \cos^{n-1}\phi)$	$A_0 = 1.736 kcal/mol$ $A_1 = 4.500 kcal/mol$ $A_2 = 0.764 kcal/mol$ $A_3 = -7.000 kcal/mol$

Polyimides (PI): PI's are most extensively investigated membrane materials as they exhibit relatively high gas selectivity and permeability. The gas separation characteristics of PI polymer membranes are investigated by considering BPDA-APB (biphenyltetracarboxylic dianhydride and 1,3-bis 4-aminophenoxy benzene) PI. Further, gas separation characteristics of a fluorinated PI, 6FDA-durene (4,4′-hexafluoroisopropylidene diphthalic anhydride, 2,3,5,6-tetramethyl-1,4-phenylenediamine) is also investigated as the presence of $-C(CF_3)_2-$ and a bulky methyl group in the polymer backbone contributes to the reduction of local segmental mobility and inhibits the inter chain packing, resulting in a great amount of free volume and thereby good gas separation performance. The structure of the single PI chain is depicted in Figure 3-1. The model polymer system is composed of 15 flexible PI chains, each having 12 monomers and was generated by following a self-avoiding random walk technique using Packmol.[2]

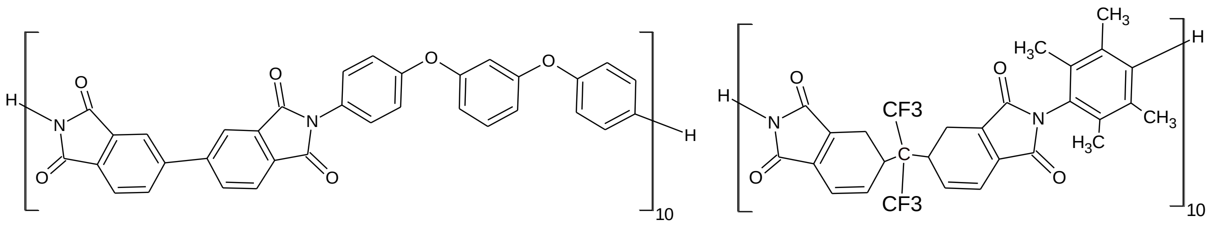

Figure 3-1: Structure of (a) BPDA-APB, and (b) 6FDA-durene polyimide polymer chains.

The polymer chains were described by considering a combination of appropriate bonded and non-bonded interactions with all atom representation, where all the atoms in the system are defined explicitly based on the polymer consistent force field (PCFF).[6] This ab initio force field has been widely used to model the long chain molecules.[7, 8] The non-bonded vdW interactions are incorporated using the 9-6 form of LJ potential:

$$U_{ij}^{non-bond} = \sum_{i,j} 6.75\varepsilon_{ij}\left[\left(\frac{\sigma_{ij}}{r_{ij}}\right)^{9} - \left(\frac{\sigma_{ij}}{r_{ij}}\right)^{6}\right] \tag{3-3}$$

where ε_{ij} and σ_{ij} are the energy and length scale parameters of the LJ potential. Sixth power combining rules[9] were employed to obtain the interaction parameters between the atoms of the polymer. The bonded interactions including bond, angle, dihedral, out of-plane angle and the cross-coupling terms were considered in accordance with PCFF forcefield,

$$\begin{aligned}
U^{bonded} &= \sum_{b}\left[k_2(b-b_0)^2 + k_3(b-b_0)^3 + k_4(b-b_0)^4\right] \\
&+\sum_{a}\left[k_2(\theta-\theta_0)^2 + k_3(\theta-\theta_0)^3 + k_4(\theta-\theta_0)^4\right] \\
&+\sum_{\phi}\left(\left\{k_1\left[1-\cos(\phi-\phi_1^0)\right]\right\} + \left\{k_2\left[1-\cos(2\phi-\phi_2^0)\right]\right\} + \left\{k_3\left[1-\cos(3\phi-\phi_3^0)\right]\right\}\right) \\
&+\sum_{b}\sum_{b'} k(b-b_0)(b'-b'_0) + \sum_{b,\theta} k(b-b_0)(\theta-\theta_0) + \sum_{b,\theta} k(\theta-\theta_0)(\theta'-\theta'_0) + \sum_{\theta,\theta,\psi} k(\theta-\theta_0)(\theta'-\theta'_0)\cos\phi \\
&+\sum_{b,\phi}(b-b_0)\left[k_1\cos\phi + k_2\cos 2\phi + k_3\cos 3\phi\right] + \sum_{\theta,\phi}(\theta-\theta_0)\left[k_1\cos\phi + k_2\cos 2\phi + k_3\cos 3\phi\right] \\
&+\sum_{\chi} k_2\chi^2
\end{aligned} \tag{3-4}$$

3.1.2 Adsorbate models

The 3-site (EPM2) linear model[10] which accounts for the quadrupole of CO_2 explicitly by assigning a point-charge on each atom, was chosen to represent CO_2. N_2, was modelled as a rigid diatomic molecule[11] having negative charge on each nitrogen atom and compensating positive charge at the centre of mass of the molecule. CH_4 was represented by its full atomistic (5-site) model[12] where all the atoms are explicitly included as LJ particles, each carrying a partial charge. All the gas molecules are treated as rigid in the entire simulation. We note that, these gas models were successfully employed to investigate the mixed gas properties in other nonporous membrane materials. The non-bonded vdW interactions between the gas-gas and polymer- gas molecules are incorporated using a 12-6 LJ potential of the form:

$$U_{ij}^{non-bond} = 4\varepsilon_{ij}\left[\left(\frac{\sigma_{ij}}{r_{ij}}\right)^{12} - \left(\frac{\sigma_{ij}}{r_{ij}}\right)^{6}\right] + \frac{q_i q_j}{r_{ij}} \tag{3-5}$$

The potential parameters used to represent gas molecules are given in Table 3.2. The interaction parameters between unlike atoms were obtained through Lorentz−Berthelot rules.

Table 3-2. Lennard–Jones (12-6) parameters, partial charges for the EPM2 CO_2, 5-site CH_4 and 3-site N_2.

Molecule	Atom	$\frac{\varepsilon}{k_b}(K^{-1})$	σ (nm)	q (e)	Ref
Nitrogen (N2)	N_N2	36.4	0.3318	-0.4645	11
	Ncom_N2	0	0	+0.929	
Carbon dioxide (CO_2)	C_CO_2	28.1290	0.2757	0.6512	10
	O_CO_2	80.5071	0.3033	−0.3256	
Methane (CH_4)	C_CH_4	55.0552	0.34	0.66	12
	H_CH_4	7.9011	0.265	-0.165	

3.2 Simulation details:

LAMMPS package[13] was used to perform equilibrium molecular dynamics (EMD) simulations, with periodic boundary conditions imposed in all three dimensions. A Nose′-Hoover thermostat with a damping coefficient of 100-time steps and Berendsen barostat with a damping coefficient of 1000-time steps are used to maintain the temperature and pressure of the system respectively. A cutoff distance of 14 Å was used to truncate short range vdW and electrostatic interactions, while long-range electrostatic interactions were captured by employing the Ewald summation method. Each simulation run comprised an equilibrium run of 10 ns followed by a production run of 40 ns in the NVT ensemble with a time step of 1fs. The results of 10-15 independent runs, each starting from a different initial configuration, were averaged to compute the gas diffusivity. The initial configurations were randomly selected from Grand Canonical Monte Carlo (GCMC) simulations by placing the gas molecules in the polymer matrix based on the sorption isotherm data, and allowing the polymer to swell in the presence of gas molecules for 25 ns in an isobaric ensemble. The error associated with the simulations was determined by computing the standard deviation of the results, obtained by dividing the total simulation run into four equal parts. In the figures to follow the error bars are smaller than symbol size, unless stated otherwise.

3.3 Methodology

3.3.1 Gas sorption isotherms and solubility

Gas sorption characteristics of a polymer membrane were described by extracting sorption isotherms obtained by implementing a two-step procedure, similar to the ‘two-boxes–particle-transfer’ methodology proposed by Hentschke et al.,[14] accounting for structural transition upon gas sorption. In step-1, GCMC simulations were performed using the DL_MONTE/RASPA simulation package[15, 16] considering a rigid polymer matrix where adsorbed gas in phase equilibrium with the ambient gas phase, following

$$\mu^{s}(T,p)=\mu^{g}(T,p) \tag{3-6}$$

where μ^{s} and μ^{g} are chemical potential of the sorbed phase and bulk gas (ambient gas) phase respectively, at constant temperature and pressure. The typical GCMC simulations consisting of insertion, deletion, rotational and translational moves with equal probability were run for approximately 2 x 10^7 steps including the initial equilibration steps of 5 x 10^6.

In the second step, EMD simulations in an isobaric ensemble were performed to allow the polymer to swell in the presence of gas molecules for 1 ns. This procedure was repeated 10-15 times, till a constant polymer density (average over last 0.5 ns) in last 3 runs of MD simulation has been achieved, confirming no further swelling of polymer upon gas sorption. The averages over last 3 runs were considered to compute the adsorbed gas concentration. The error in the sorption isotherm was determined from the last 3 GCMC runs by dividing them into 6 blocks and. Further, solubility coefficient (S_i) of gas i is evaluated from the sorption isotherm, following:

$$S_i=\frac{c}{p_i} \tag{3-7}$$

where c is the amount of gas absorbed in the polymer at its partial pressure p_i.

3.3.2 Diffusion coefficients

To describe the gas diffusion in a polymer membrane, self, corrected and transport diffusivities are computed using the procedure described below.

Self-Diffusivity: The self-diffusivity, D_s, describes the motion of individual, tagged particles, and can be obtained from average molecular displacements with the aid of the Einstein relation in the

Fickian regime, where the mean square displacement (MSD) varies linearly with the time (t) over sufficiently long-time scales following:

$$D_s = \lim_{t\to\infty} \frac{1}{6t} < | \vec{r}_i(t) - \vec{r}_i(0) |^2 >_i \tag{3-8}$$

where $r_i(t)$ is center of mass position vector of molecule i at time t.

Corrected-Diffusivity: The corrected diffusivity, D_0, describes the collective motion of all adsorbed molecules, and can be computed from EMD simulations using an Einstein relationship similar to eq 3-8, based on the center of mass (COM) motion of all adsorbed molecules, following:

$$D_0 = \frac{1}{6N} \lim_{t\to\infty} \frac{1}{t} < \| \sum_{i=1}^{N} \vec{r}_i(t) - \vec{r}_i(0) \|^2 > \tag{3-9}$$

where $r_i(t)$ is center of mass position vector of molecule i at time t. For pure component diffusion, the MS diffusivity is equal to the corrected diffusivity (D_o).[19]

Transport Diffusivity: The transport diffusivity, D_T, is variously referred to as either the Fickian diffusivity or the chemical diffusivity, and defined in terms of the corrected diffusivity, D_0, following:

$$D_T \approx D_0 \left(\frac{\partial \ln f}{\partial \ln c}\right)_T \tag{3-10}$$

where c represents the gas concentration (gas loading in the polymer), and f its bulk phase fugacity at a given temperature T. The partial derivative in eq 3-10 is defined as the thermodynamic correction factor, and can be obtained from the single component sorption isotherm. By combining the thermodynamic correction factor obtained from GCMC-based isotherms for gas sorption and corrected diffusivity from EMD simulations, the transport diffusivity can be calculated using eq 3-10.

3.4 Membrane performance

Membrane performance for a given gas pair can be determined by computing the gas permeability and perm-selectivity, as defined below:

3.4.1 Permeability

The permeability (P_i) of a gas i in a membrane at a given temperature and pressure can be estimated from its diffusivity (D_i) and solubility (S_i), and is expressed as:

$$P_i = D_i \times S_i \tag{3-11}$$

The permeabilities are expressed in Barrers, where 1 Barrer = $10^{-10}\,\dfrac{cc(stp).cm}{cm^2.s.cmHg}$.

3.4.2 Perm-selectivity

Membranes perm-selectivity (α_{ij}) for a gas pair i, j is defined as the ratio of their individual gas permeability coefficients (P_i, P_j)following:

$$\alpha_{ij} = \frac{P_i}{P_j} = \underbrace{\left(\frac{D_i}{D_j}\right)}_{\substack{\text{diffusivity}\\ \text{selectivity}}} \text{ x } \underbrace{\left(\frac{S_i}{S_j}\right)}_{\substack{\text{solubility}\\ \text{selectivity}}} \qquad (3\text{-}12)$$

3.5 References

1. Flory, P. J., *Statistical mechanics of chain molecules*. reprint ed.; Hanser: 1988; p 432.

2. Martínez, L.; Andrade, R.; Birgin, E. G.; Martínez, J. M., PACKMOL: A package for building initial configurations for molecular dynamics simulations. *J. Comput. Chem.* **2009,** *30* (13), 2157-2164.

3. Li, Y.; Kröger, M.; Liu, W. K., Nanoparticle Geometrical Effect on Structure, Dynamics and Anisotropic Viscosity of Polyethylene Nanocomposites. *Macromolecules* **2012,** *45* (4), 2099-2112.

4. Siepmann, J. I.; Karaborni, S.; Smit, B., Simulating the critical behaviour of complex fluids. *Nature* **1993,** *365* (6444), 330-332.

5. Paul, W.; Yoon, D. Y.; Smith, G. D., An optimized united atom model for simulations of polymethylene melts. *J. Chem. Phys.* **1995,** *103* (4), 1702-1709.

6. Sun, H.; Mumby, S. J.; Maple, J. R.; Hagler, A. T., An ab Initio CFF93 All-Atom Force Field for Polycarbonates. *J. Am. Chem. Soc* **1994,** *116* (7), 2978-2987.

7. Jiang, Q.; Tallury, S. S.; Qiu, Y.; Pasquinelli, M. A., Molecular dynamics simulations of the effect of the volume fraction on unidirectional polyimide–carbon nanotube nanocomposites. *Carbon* **2014,** *67* (Supplement C), 440-448.

8. Zhang, L.; Hu, Z.; Jiang, J., Metal–Organic Framework/Polymer Mixed-Matrix Membranes for H_2/CO_2 Separation: A Fully Atomistic Simulation Study. *J. Phys. Chem. C* **2012,** *116* (36), 19268-19277.

9. Waldman, M.; Hagler, A. T., New combining rules for rare gas van der waals parameters. *J. Comput. Chem.* **1993,** *14* (9), 1077-1084.

10. Harris, J. G.; Yung, K. H., Carbon Dioxide's Liquid-Vapor Coexistence Curve And Critical Properties as Predicted by a Simple Molecular Model. *J. Phys. Chem.* **1995,** *99* (31), 12021-12024.

11. Murthy, C. S.; Singer, K.; Klein, M. L.; McDonald, I. R., Pairwise additive effective potentials for nitrogen. *Mol. Phys.* **1980,** *41* (6), 1387-1399.

12. Sun, Y.; Spellmeyer, D.; Pearlman, D. A.; Kollman, P., Simulation of the solvation free energies for methane, ethane, and propane and corresponding amino acid dipeptides: a critical test of the bond-PMF correction, a new set of hydrocarbon parameters, and the gas phase-water hydrophobicity scale. *J. Am. Chem. Soc.* **1992,** *114* (17), 6798-6801.

13. Plimpton, S., Fast Parallel Algorithms for Short-Range Molecular Dynamics. *J. Comp. Phys.* **1995,** *117* (1), 1-19.

14. Kotelyanskii, M. J.; Hentschke, R., Gibbs-ensemble molecular dynamics: Liquid-gas equilibrium in a Lennard-Jones system. *Phys. Rev. E* **1995,** *51* (5), 5116-5119.

15. Dubbeldam, D.; Calero, S.; Ellis, D. E.; Snurr, R. Q., RASPA: molecular simulation software for adsorption and diffusion in flexible nanoporous materials. *Mol. Simul.* **2016,** *42* (2), 81-101.

16. Purton, J. A.; Crabtree, J. C.; Parker, S. C., DL_MONTE: a general purpose program for parallel Monte Carlo simulation. *Mol Simul.* **2013,** *39* (14-15), 1240-1252.

Chapter 4 Single Component Gas Transport in Polymer Membranes

The content of this chapter is published as:

Ravi C. Dutta and SK. Bhatia, Transport diffusion of light gases in polyethylene using atomistic simulations, *Langmuir*, 33, 936 (2017)

Contributor	Statement of contribution
Ravi C Dutta	Programmed and conducted simulations (100%) Analysis and interpretation of data (80%) Wrote the paper (80%)
Suresh K. Bhatia	Wrote the paper (20%) Analysis and interpretation of data (20%)

4.1 Introduction

Nanoscale understanding of sorption and fluid transport through polymer materials is critical to the design and optimization of several industrial processes for gas filtration and separation. Permeation of gases through a polymer membrane is explained in terms of a solution-diffusion mechanism which involves dissolution of the gas at the high-pressure interface, molecular diffusion of the gas through the polymer film and release of the gas from solution at the low-pressure interface. The effectiveness of the membrane is described by its permeance as well as selectivity. Therefore, gas permeation and separation involves both solubility differences (an equilibrium property) and diffusivity differences (a transport property), and is strongly related to the thermodynamics of the polymer at a given temperature and pressure. Thus, an understanding of fluid sorption and transport is critical to explore the potential applications and possible improvements for a given membrane material.

Transport through porous materials occurs in two modes.[1, 2] The first is transport diffusion which represents the motion of the center of mass of the fluid, and is governed by collective motion of the fluid due to a concentration or chemical potential gradient, while the other is self-diffusion, which characterizes the motion of a single particle at uniform chemical potential. Experimentally, macroscopic methods such as chromatography and frequency response methods measure the motion of the fluid as a whole, and yield the transport diffusivity. On the other hand, self-diffusivity can be extracted from microscopic experimental techniques such as quasi elastic neutron scattering (QENS) and pulse field gradient nuclear magnetic resonance (PFG-NMR) by tracking the displacement of a single molecule over the time. The transport diffusivity or Fickian diffusivity is of great interest in application such as membranes where mass transfer plays a key role, and is defined through the flux (*J*) generated from the concentration (*c*) gradient following:

$$J = -D_t(c)\nabla c \tag{4-1}$$

where D_t is transport diffusivity. In general, both transport and self-diffusion coefficients are functions of concentration, and they are equal only at infinite dilution or zero loading. Due to the presence of positively contributing correlations,[3] transport diffusivities are always higher than self-diffusivity. In extreme cases, the self and transport diffusivities can vary by orders of magnitude.[3-6] Thus, computing transport diffusivity is indispensable for the description of transport across a membrane. The transport behavior of a fluid in a polymer can be explored systematically and accurately with the aid of atomistic simulations, based on a molecular interaction model.

Molecular transport of small molecules through a variety of polymer structures *via.* diffusion has been studied extensively using atomistic simulations.[7-14] Most studies report self-diffusion coefficients predicted using the Einstein relation, finding them to be in agreement, either quantitatively and/or qualitatively, with experimental measurements. However, as discussed above, to describe molecular transport across a membrane, it is the transport diffusivity that is important and this can directly be extracted from non-equilibrium molecular dynamics simulations.[15-17] However, this requires very high forces and is also computationally extensive. A more convenient approach for predicting transport diffusivities of pure components, is that of EMD simulation, proposed by Theodorou et al.[18] Sholl et al. successfully applied this approach to compute the transport diffusivities of the gases in carbon nanotubes,[4-6] metal-organic framework (MOF)[19] and zeolites.[20, 21] They found that at non-zero loading, transport diffusion coefficients are much larger than self-diffusion coefficients. Salles et al.[22] predicted the transport diffusivity of gas molecules in MOF using a combination of QENS-EMD simulations. Liu et al.[23] investigated propane and propylene transport inside single-wall carbon nanotubes of various diameters using EMD simulations, and reported transport diffusivities consistent with literature data. Vegt et al.[11] reported the self-diffusion coefficient by considering single penetrant (CO_2) in PE. However, little work has been done to extract the transport diffusivity of gases in polymers.

On the other hand, performing reliable simulations to predict sorption isotherms of gases in materials such as polymers that undergo significant structural transition upon gas sorption remains challenging, although gas sorption isotherms in rigid porous materials[24, 25] are well explored. Gas sorption in polymers is affected by re-distribution of voids[26] (and channels) through two mechanisms associated with dynamics of the polymer. The free volume in the polymer matrix is continuously redistributed randomly either by generation of new voids or by destruction of voids, or by re-distributing the existing voids due to the movements of the one or more segments of the polymer chain and polymer structural transitions such as swelling/plasticization[27, 28] upon sorption. Most of the earlier reports[26, 29-31] focus on calculation of solubility coefficients either by applying widom particle insertion method or using an osmotic ensemble. However, here we implemented a two-step methodology combining Grand canonical Monte Carlo simulations (GCMC) coupled with NPT (Constant Number of particles, Pressure and Temperature) EMD simulations.

In this chapter pure component MS- diffusivity and sorption isotherms of gases in PE as well as two variants of polyimides (BPDA-APB and 6FDA-durene- PI's) are investigated by considering the structural transitions upon gas sorption in-detail through EMD simulations. Further, an important aspect of this study is the insight into the polymer morphology (structural properties) gained from the analysis of structure-property relations and pore size analysis of the bulk polymer.

4.2 Results and discussions

4.2.1 Polyethylene

<u>Structural Characterization</u>: The 3-dimensional structural characterization of PE polymer membrane provides insight into the simulated sorption isotherms as well as transport properties of the system and is obtained by considering the volume-temperature relations, associated free volume, distribution of free volume elements in the polymer and intermolecular radial distribution functions. Figure 4-1 depicts the structure of the PE polymer membrane at 300 K and 600 K respectively.

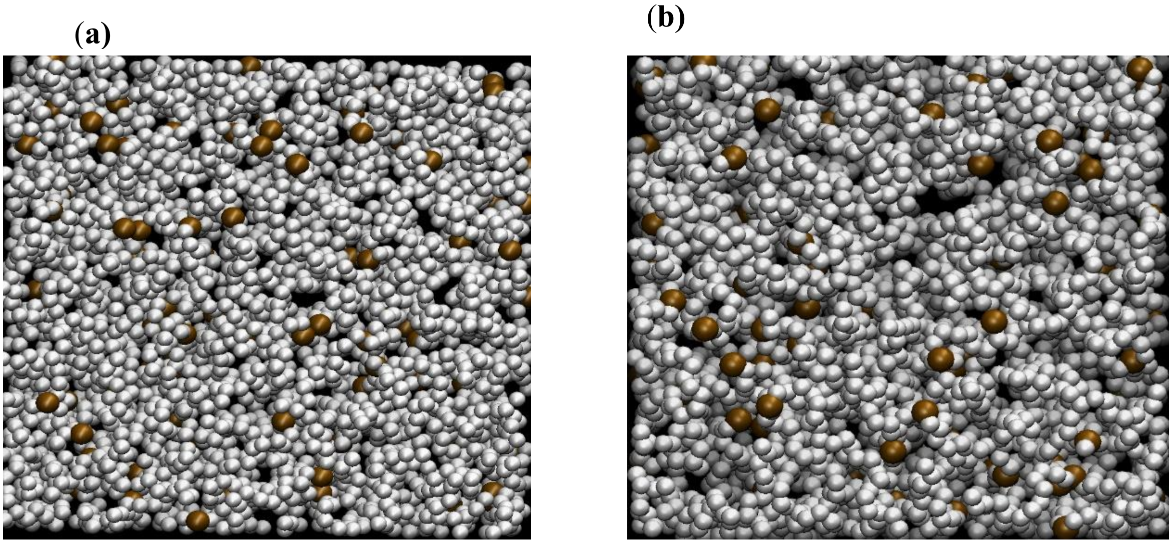

Figure 4-1: Structure of PE polymer matrix at (a) 300 K, and (b) 600 K.

It is observed that density of the polymer decreases linearly with increase in temperature with change in slope at 450 K, the melting point of PE. The calculated thermal expansion coefficient of PE polymer from our simulations is found to be 0.00076 (± 0.00001) K^{-1} (assuming it is independent of temperature), which compares well with the experimental[32] and earlier simulation[11] values of 0.00074 K^{-1} and 0.0008 K^{-1} respectively. We note here that the effect of pressure on the structure of the PE Polymer is found to be negligible up to 20 atm, as shown in Figure 4-2 (b).

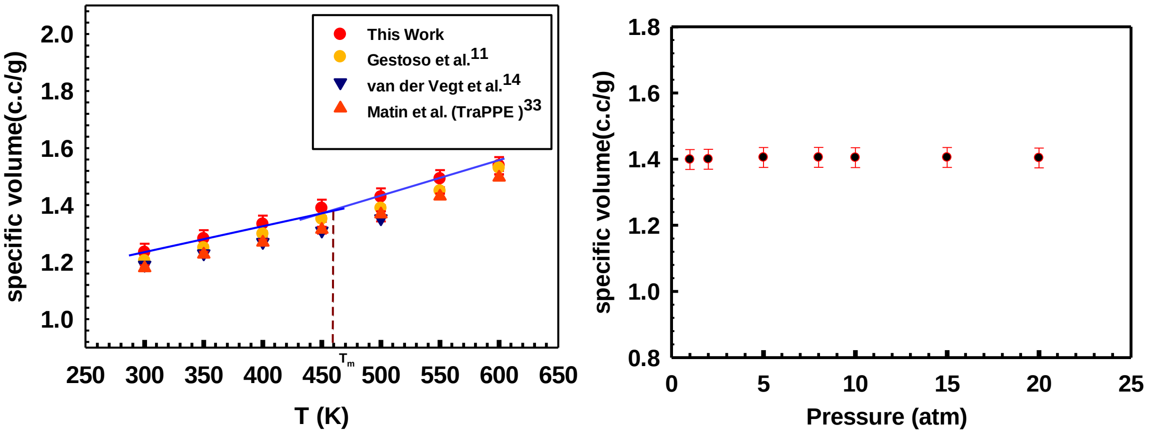

Figure 4-2: (a) Temperature, and (b) Pressure variation of specific volume of PE polymer.

The size of free volume elements in the polymer and accessible volume or free volume (FV) in the PE polymer membrane were determined using the spherical probe geometric approximation technique with a hard sphere probe of diameter 2.64 Å (helium as probe molecule), by considering the different configurations of PE polymer, as discussed in detail elsewhere.[34-36] Figure 4-3 (a) depicts the variation of accessible volume in PE polymer membrane with temperature by considering different configurations. The measured fractional free volume of the PE polymer is approximately 6 (± 0.5), 15 (± 0.5) and 28 (± 1) % at temperature of 300, 450 and 600 K respectively, illustrating the swelling behavior of the polymer with increase in the temperature. It is observed that the accessible volume increases linearly with temperature, but with change in slope at 450 K. Figure 4-3 (b) illustrates the resulting temperature variation of the limiting size of free volume elements in the polymer, the size of the largest spherical probe that can permeate through the structure in polymer. This represents the smallest opening along the free volume element that a molecule needs to cross in order to diffuse through this material. We note here that cavities of 1.5- 3 Å diameter exist in the PE polymer in the temperature range of 300-600 K.

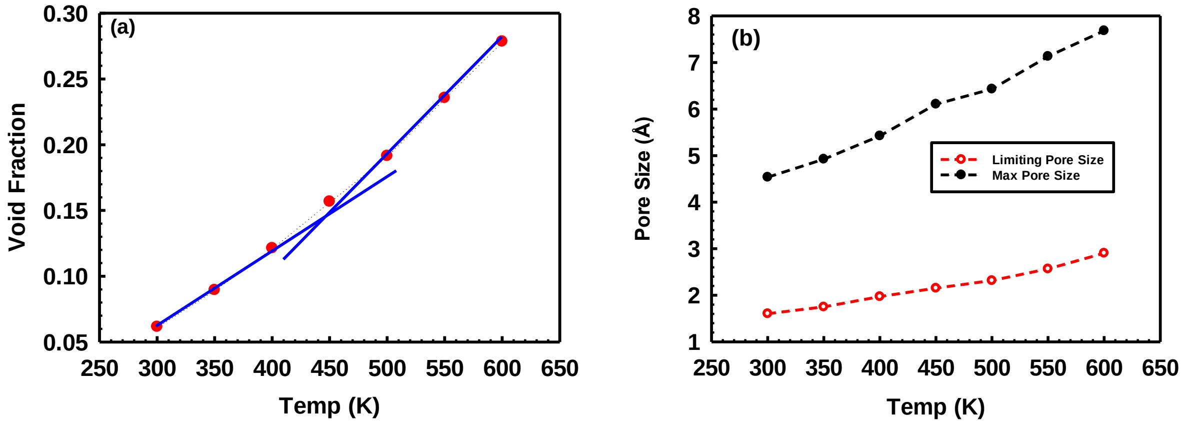

Figure 4-3: (a) Variation of accessible volume in PE with temperature, and (b) maximum and limiting free volume elements in PE. Solid lines along the data points are to emphasize the slope change. Dashed line along the data points is guide to the eye.

<u>*Radial Distribution Function:*</u> To provide insight into the local chain confirmation and packing in the PE polymer membrane, the radial distribution function (RDF), *i.e.* atom-atom pair correlation function $g(r)$ between the CH_2 (C_{PE}) units separated by a distance r, is presented. Figure 4-4 depicts the C_{PE}-C_{PE} intermolecular RDF of PE polymer in the temperature range of 300-600 K. We here note that all kinds of bonded interactions between C_{PE} units [intra-molecular] are ignored while computing the RDF, and hence no peak is observed when $r < 4$ Å. A very slight shoulder at $r = 4$ Å is observed at all temperatures which corresponds to closest contacts between C_{PE}-C_{PE} units. Similar feature has been reported by Boyd et al.[37, 38] at moderate to high temperatures in PE polymer, and it resolves to a peak at very low temperature (= 0 K).

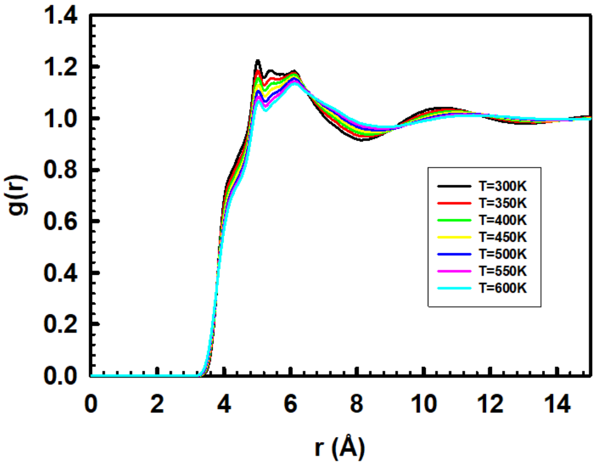

Figure 4-4: C_{PE}-C_{PE} intermolecular radial distribution function of polymer

A second peak, corresponding to average neighbor spacing between the PE polymer chains was found around $r = 5$ Å. Also we note a split in the second peak into two, in contrast to the earlier reports on a similar system,[39, 40] well above the glass transition temperature of PE polymer (> $T = 180$ K) and this split disappears above the melting temperature ($T = 450$ K) of PE polymer. Similar behavior has been reported for other glassy systems,[40] below the melting temperature. However, it is important to note that this feature does not distinguish the glassy and liquid states but the splitting appears gradually as the normal liquid is cooled or compressed to a glassy state and has been discussed thoroughly elsewhere.[41] A third peak has been observed around $r = 6.1$ Å and a broad peak around $r = 11$ Å which presumably corresponds to second and third neighbor chains. An increase in temperature is accompanied by intensity decrease of all the intermolecular peaks suggests that the number of intermolecular contacts decreases with increase in temperature due to the swelling of the polymer with temperature and hence increase in FV in the polymer.

Structural transitions upon gas sorption such as swelling or plasticization in polymer materials alter the sorption kinetics as well as gas transport. Figure 4-5 illustrates the swelling of polymer upon gas sorption in the temperature range of 300-600 K. It is evident that the PE polymer swells upon CO_2, CH_4 and N_2 sorption at all temperatures. It is seen that swelling ratio q, *i.e.* fractional increase in volume due to gas sorption, increases exponentially with increase in temperature for all the gases considered here. The polymer swells least in the presence of CH_4, showing a swelling of 1.5-2.5% in the temperature range of 300-600 K. At lower temperatures in the presence of CO_2 the polymer swells more due to the high solubility of CO_2 in PE polymer, showing a swelling of 1.7-3.0 % in the temperature range of 300-600 K. On the other hand, in the presence of N_2 the PE polymer swells more at higher temperatures displaying a swelling of 1.6-3.5 % in the temperature range of 300-600 K, presumably due to the positive temperature effect of N_2 solubility in the PE polymer network subsequently discussed in detail.

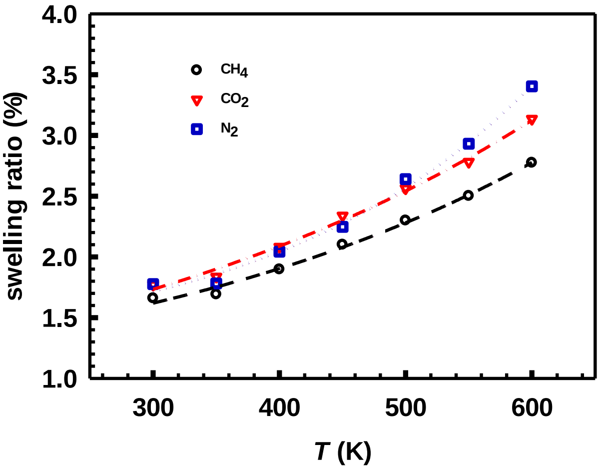

Figure 4-5: Temperature variation of swelling of PE in the presence of gases with temperature.

<u>Gas sorption isotherms and solubility:</u> The sorption behavior of CO_2, CH_4 and N_2 in PE polymer membrane was systematically investigated by exploring the sorption isotherms for each adsorbed gas

as a single component, using GCMC simulations coupled with EMD simulations in the isobaric ensemble as described in section 3.1 of chapter-3, in the temperature range of 300-600 K.

Figure 4-6 (a)-(c) shows the sorption isotherms of CO_2, CH_4 and N_2 in PE polymer matrix respectively, in the temperature range of 300-600 K. At 300 K, it is seen that the CO_2 absorbs strongly while N_2 shows weak absorption in PE, and gas absorption increases with increase in pressure at a given temperature in all the cases. Further, we note that the effect of swelling on the isotherm is significant. The sorption isotherm of each gas considered was fitted using a Dual-mode (DM) sorption model where molecules (i) absorbed in the accessible sites, which is endothermic, and (ii) dissolved in the amorphous polymer matrix, which is exothermic. These modes contribute to the total concentration of the sorbate in the polymer, *C*, of the form:

$$c = k_d p + \frac{C_H^{'} bp}{1 + bp} \tag{4-2}$$

where, c is the total concentration of the sorbate in the polymer, *p* is the pressure, k_d is Henry's law coefficient, $C_H^{'}$ is the Langmuir capacity term, and b is the Langmuir affinity parameter. Further, we note that the sorption isotherms above the melting temperature were fitted using Henry's law model that can be formulated using $C_H^{'} = 0$ in eq (4-2). The dashed lines in Figure 4-6, represent the isotherms fitted using eq (4-2). A similar mechanism was previously reported for sorption of small gas molecules in other polymers.[42-44] It is observed that absorption capacities of CO_2 and CH_4 decrease with increase in temperature. This is due to the significant decrease in gas density with increase in temperature, leading to decreased sorption at higher temperatures.[14] On the other hand, N_2 shows positive correlation of sorption with increase in temperature due to the increase in availability of kinetically closed pores[45]at higher temperatures. A phenomenological explanation for this behavior may be based on a combination of energetic and entropic effects. At lower temperatures significant pore space is inaccessible to gas molecules, while at higher temperatures kinetically closed pores become open and accessible to gas molecules. This occurs because temperature increase results in decrease in polymer density, and therefore increase of the FV accessible to small molecules. Consequently, light gases are able to access more sites and become more soluble with increase in temperature. In order to demonstrate this effect, we tracked the motion (displacement) of gas molecules in a rigid polymer at low and high temperatures. At 300 K, no nitrogen molecule is able to leave the pore space, but only oscillates within the existing FVEs, while at 450 K, N_2 molecules are able to jump out of the regions of local energy minimum to access the pore space as (i) they gain sufficient kinetic energy, and/or (ii) the mouth of the pore opens due to swelling of the polymer at higher temperatures, as shown in Figure 4-7.

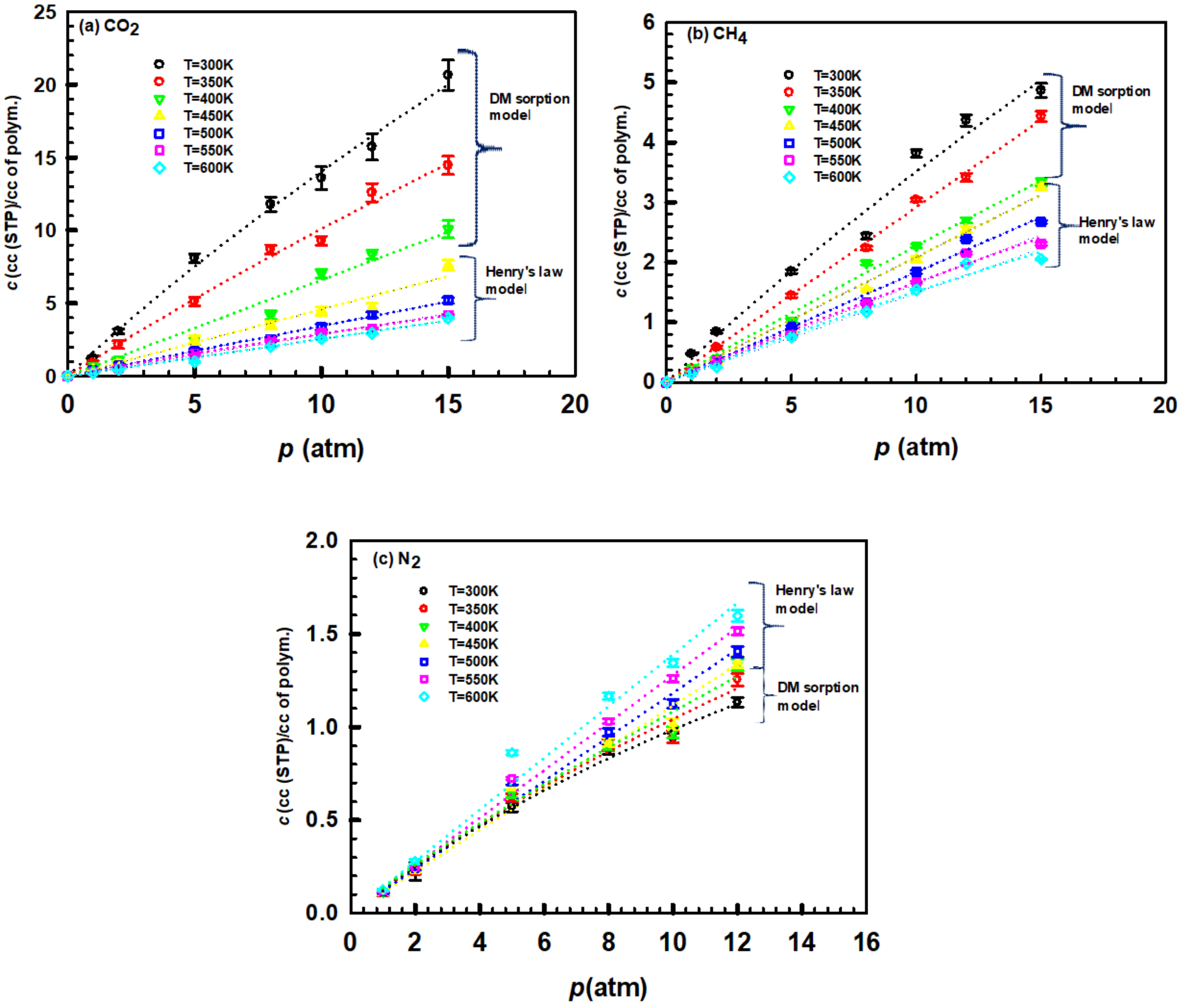

Figure 4-6: Sorption isotherms of (a) CO_2, (b) CH_4, and (c) N_2 in PE at various temperatures. The dashed lines indicate the fitted sorption isotherms using the DM sorption model or Henry's law model.

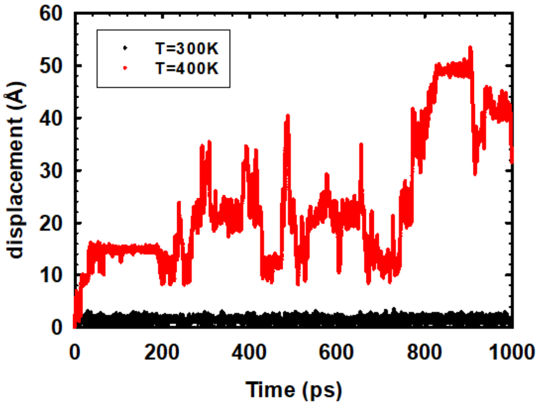

Figure 4-7: Motion of N_2 in rigid polymer at T = 300 K and at T = 450 K.

In the low pressure region, eq (4-2) provides the following Henry law relationship for adsorbed concentration:

$$c = (C_H^{'} b + k_d) * p = S * p \tag{4-3}$$

where *S*, the apparent solubility coefficient in the zero-pressure limit in glassy polymers, represents the ability of the gas to dissolve in the PE polymer matrix and can be computed from DM sorption fitting parameters. It is observed that CO_2 is most soluble while N_2 is least soluble in PE among the gases considered in this study, following the order

$S\,(CO_2) > S\,(CH_4) > S\,(N_2)$

where $S\,(CO_2)$ represents the solubility of CO_2 in the PE polymer matrix. The solubility coefficients predicted from our simulations are qualitatively in good agreement with the previous experiments[46, 47] and simulation results,[14, 48] however, they are quantitatively larger by an order magnitude, as shown in the Table 4-1.

Table 4-1:Solubility coefficients of different gases in PE at 300 K.

Gas	$S\,(\frac{\text{cc}\,(STP)}{\text{cc}\,(polym).atm})$		
	this study	earlier simulations[48]	Expt[46]
N_2	0.1 (± 0.01)	0.08	0.0412
CH_4	0.4 (± 0.1)	0.3	0.203
CO_2	1.4 (± 0.1)	0.55	0.451

This can be attributed to the fact that absolute value of the solubility depends on the crystalline fraction of the polymer which has no capacity to dissolve the gas, as well as on the united atom model (UA) adapted in this study to represent PE polymer structure. However, Bixler et al.[46] showed experientially that, the solubility (k) of semi-crystalline PE follows:

$$k = \alpha k^{*} \tag{4-4}$$

where α is the volume fraction of amorphous material, and k^{*} is solubility constant in a hypothetical completely amorphous PE. Subsequently, Compan et al. [49] showed this relation is approximately valid by computing the solubilities of the gases in semi-crystalline PE. Our simulation predictions of solubility constant correspond to k^{*}, and to compare with experimental results, the value of α is required. This will vary from sample to sample, depending on its processing history as well as the method used to calculate it. Hence, the ratio of solubility coefficients for different gas pairs predicted from our simulations against experimental data at 300 K as well as predictions from earlier simulations is compared in Table.4-2. It is seen that the extracted solubility ratios of different gas pairs from sorption isotherms are in good agreement with experiments as well as earlier simulation results computed using the Widom insertion method. We also note that similar results have been reported for the solubility of O_2 and N_2 in poly-isobutylene polymer,[50] where the UA model overestimated the solubility while the results based on an all atom (AA) model are in close agreement with experiment.

Table 4-2: Solubility ratios for different gas pairs in PE.

Gas Pair	**Solubility ratio**		
	this study	**earlier simulations[48]**	**expt[46]**
$S(CO_2)/S(CH_4)$	3.7 [± 0.2]	1.61	2.22
$S(CO_2)/S(N_2)$	13 [± 0.5]	6.70	10.94
$S(CH_4)/S(N_2)$	3.5 [± 0.2]	4.16	4.93

Figure 4-8 shows the temperature dependence of simulated solubility coefficients for CO_2, CH_4 and N_2 in PE polymer matrix at temperatures from 300 to 600 K. Heats of sorption were calculated from the data presented in Table 2, based on the van't Hoff expression,

$$S = S_0 e^{\frac{-\Delta H_s}{RT}} \tag{4-5}$$

where S_0 is a constant, ΔH_s is apparent heat of solution, R is the gas constant and T is the temperature. It is observed that the solubility of CO_2 and CH_4 decreases with increase in temperature leading to negative heat of solutions. On the other hand, N_2 has positive temperature dependence, with slightly positive heat of solution. Further, we note that the temperature dependence of the solubility constant over the temperature range of 300-600 K, obeys the van't Hoff relation for all the gases in contrast to earlier simulation reports.[11]The computed heats of solutions for CO_2, CH_4 and N_2 are in reasonable agreement with experimental reports[46] as seen in Table 4-3.

Table 4-3: Heats of Solution of various gases in PE.

Gas	Apparent Heats of Solution, $\Delta H_s (kcal / g.mole)$	
	this study	Expt[46]
N_2	0.3 [± 0.05]	0.5
CH_4	-1.23 [± 0.1]	-0.7
CO_2	-1.85 [± 0.1]	-1.3

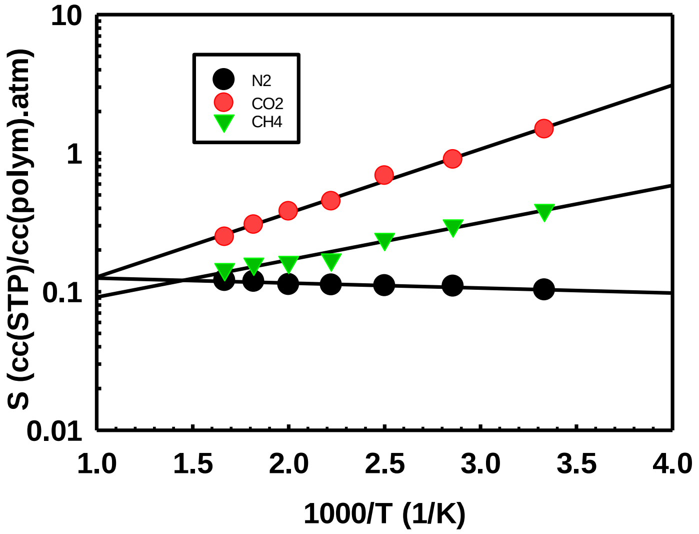

Figure 4-8: Temperature dependence of solubility coefficients of gases in PE.

<u>Gas diffusion:</u> For the purpose of understanding the mechanism of gas diffusion in the PE membrane, the penetrant displacement from its initial position *i.e.* $|r(t)-r(0)|$, where $r(t)$ is penetrant position at

time *t*, is monitored. Figure 4-9 depicts the displacement of CO_2, CH_4 and N_2 in the PE polymer membrane at 300 K. It is seen that gas diffuses through the PE membrane by hopping from one site to another, either by jumping between existing voids or to new voids created by the motion of the polymer chains. To demonstrate this mechanism, the penetrant motion in rigid and flexible polymer chains are therefore determined. It is observed that movements of the polymer chains considerably aid the penetrant motion. Also, it is seen that the penetrant molecules dwell in existing voids, having only oscillatory motions around their equilibrium positions for considerable time before jumping into the neighboring void. The amplitude of oscillations depends on the size of the voids and penetrant. Subsequently, the penetrants do a quick jump into their neighboring voids with a frequency depending on the penetrant's size. Hence, the largest penetrant studied in this work, CH_4, can rarely jump between the voids, and the small penetrant N_2 can jump frequently.

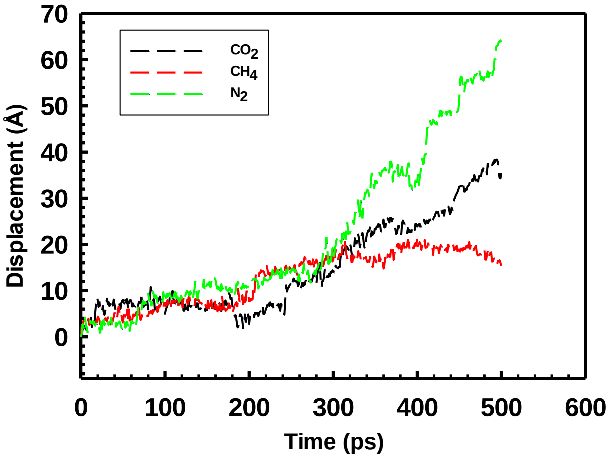

Figure 4-9: Hopping of gas molecules in PE at 300 K.

<u>Self-Diffusion:</u> Figures 4-10 (a)-(c) depict the average mean square displacement of CO_2, CH_4 and N_2 molecules respectively against time (average window size) on a log-log plot. At extremely short times (t < 250 ps), self-diffusion follows ballistic motion (where MSD varies linearly with t^2) followed by normal diffusion over sufficiently long-time scales where the Einstein equation is applicable. The self-diffusion coefficient of the gas molecules has been extracted from the intercept of the MSD *vs*. time plot on a log-log scale in the regime where the slope is approximately unity.

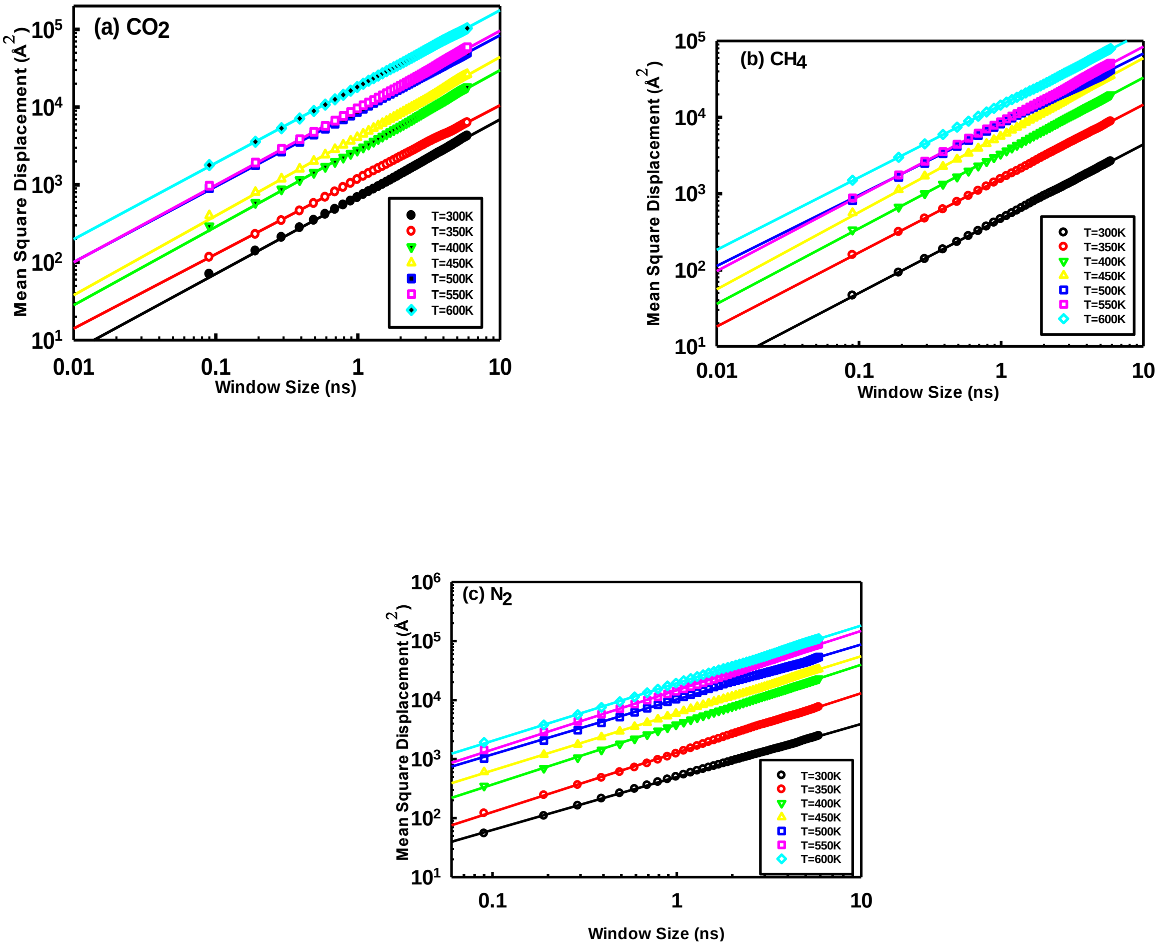

Figure 4-10:log-log plot of mean square displacement of tagged particles (a) CO_2, (b) CH_4, and (c) N_2 *vs*. time (window size average) in PE matrix.

At 300 K, the calculated values of self-diffusion coefficient (D_s) of CO_2, CH_4 and N_2 are 9 (± 0.8) × 10^{-6}, 7 (± 0.5) × 10^{-6} and 8 (± 0.4) × 10^{-6} cm^2/sec respectively, and in agreement with earlier simulation report values of the order 10^{-6} cm^2/sec .[11, 13, 14, 51] On the other hand, predicted self-diffusion coefficients from our simulations are qualitatively in agreement with experimental values of 9.8 × 10^{-5}, 6 × 10^{-5} and 8.3 × 10^{-5} cm^2/sec for CO_2, CH_4 and N_2 respectively[52], while quantitatively being overestimates by an order magnitude. This is because our simulations consider PE as amorphous homogeneous material while it is semi-crystalline. To compare the predicted diffusion coefficients with experimental results, proper correction factor accounting the reduction in diffusion constant due necessity of molecules to bypass crystallites and reduction in chain mobility near the crystals is required. Bixler et al.[52] estimated these impedance factors, assuming the relation,

$$D = {D^*}\big/{\tau\beta} \qquad (4\text{-}6)$$

where D^* is the diffusion constant in completely amorphous PE, τ is a geometric impedance factor accounting for the reduction in diffusion constant to bypass the crystalline fraction and β is the chain immobilization factor in the vicinity of crystallites. This D^* values are qualitatively in agreement with our simulation predictions, while quantitatively over predicted by three-fold, as shown in Table 4-4. Further, the dependence of density of the polymer on chain length and hence proper correction factor is required to compare simulation predictions with experiments.

Table 4-4: Gas diffusion coefficients in amorphous PE at 300 K.

Gas	D^* ($\times 10^6$ cm^2/sec),		
	This study	Earlier simulations[11, 13, 14]	Experimental reports[52]
N_2	8 (± 0.4)	0.98	2.7
CH_4	7 (± 0.5)	0.37, 7	2.14
CO_2	9 (± 0.8)	4, 6	3.02

Corrected-Diffusion: In order to compute corrected diffusivities, the average mean square displacement associated with the motion of the center mass of the gas molecules over multiple independent simulation runs was considered. Figures 4-11 (a)-(c) depict the average mean square displacement of the center of mass of the CO_2, CH_4 and N_2 molecules respectively against time (average window size) on a log-log plot. It is observed that corrected diffusion follows ballistic motion initially ($t < 2$ ns), in contrast to what has been observed in zeolites where corrected diffusion is linear over the whole range although self-diffusion exhibits single file diffusion initially, presumably due to the slow relaxation of PE chains. Also observed is an intermediate region where MSD changes linearly with t^n, with n lying between 0 and 1. At sufficiently long time scales the MSD is linear with time, and the Einstein equation is applicable. Corrected-diffusion coefficients of the gases have been extracted from the intercept upon fitting a straight line with slope = 1 on a log-log plot of MSD *vs.* time. At 300 K, the calculated values of corrected-diffusion coefficient D_0 of CO_2, CH_4 and N_2 are $4.5 (\pm 1) \times 10^{-4}$, $3.5 (\pm 1) \times 10^{-4}$ and $9.0 (\pm 1) \times 10^{-4}$ cm^2/sec respectively. It is observed that the corrected diffusion coefficients are always greater than self-diffusion coefficients by about two orders magnitude. The transport diffusivity was calculated using the corrected diffusivity and thermodynamic factor from the sorption isotherms and is discussed subsequently.

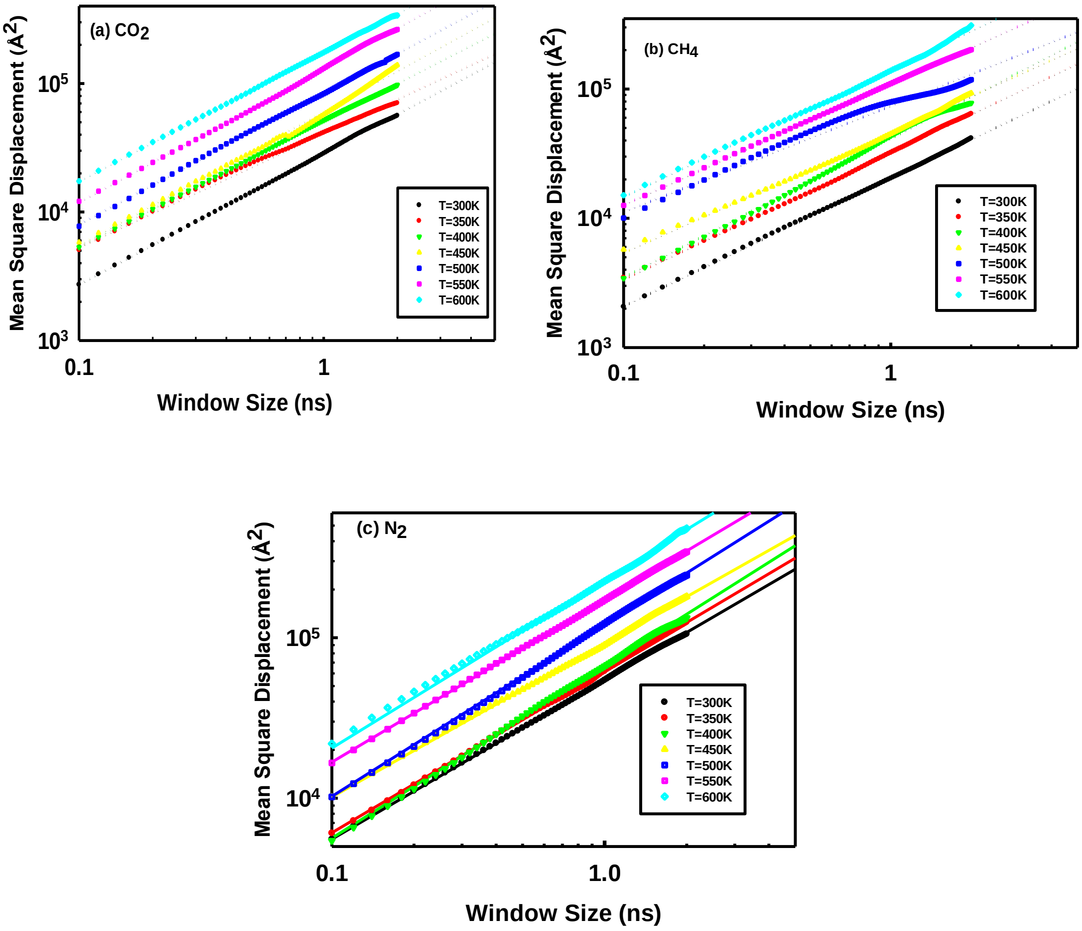

Figure 4-11: Mean Square displacement of center of mass of molecules (a) CO_2, (b) CH_4, and (c) N_2 vs. time (window size average) in PE polymer matrix.

Effect of Temperature: In the literature little agreement on temperature dependence of gas diffusion in PE polymer membrane, with Arrhenius behavior,[52] non-Arrhenius(WLF form)[13]and non-Arrhenius (linear fits with slope change)[11] has been reported. Figures 4-12 (a)-(c), depict the temperature dependence of the self-diffusion coefficients of CO_2, CH_4 and N_2 in PE polymer membrane in the temperature range of 300-600 K. It is seen that the temperature dependence of the self-diffusion coefficients of CO_2, CH_4 and N_2 follow Arrhenius-type behavior. The activation energies for N_2, CO_2 and CH_4 in PE membrane are 20 (± 1), 17 (± 1) and 16 (± 1) kJ / mol respectively, which compares well with literate data 23 kJ / mol for CO_2[11], 20 kJ / mol for CH_4[13] computed from the expression,

$$D = D_0 e^{\frac{-E_D}{RT}} \tag{4-7}$$

where D_0 is a constant, E_D is the apparent activation energy for diffusion, R is the gas constant and T is absolute temperature.

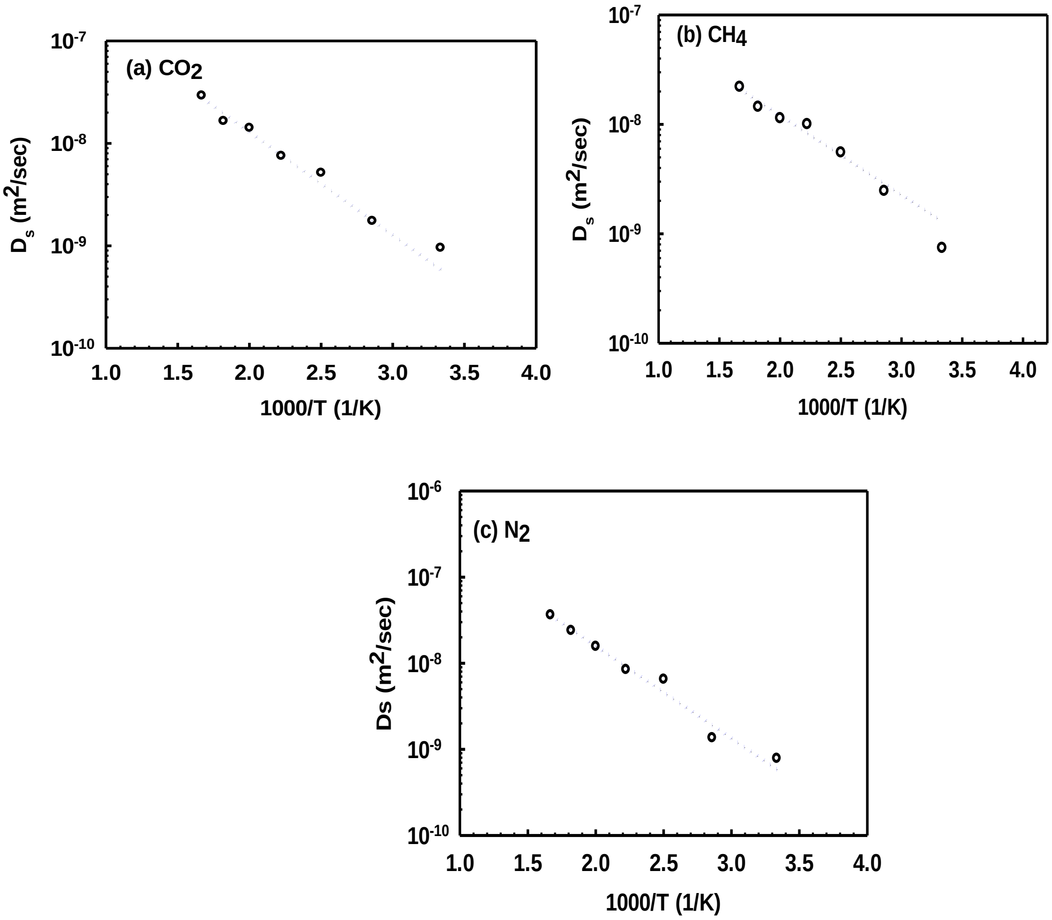

Figure 4-12:Arrhenius plots for the self-diffusion coefficient of (a) CO_2, (b) CH_4, and (c) N_2 in PE polymer membrane. Dashed line represents the fit using eq (4-7)

On the other hand, it is observed that the dependence of logarithm of transport diffusivity (log D_T) on reciprocal temperature for all gas molecules (CO_2, CH_4 and N_2) follows non-Arrhenius behavior as shown in Figure 4-13. It is seen that at 450 K, a change in slope occurs, with different activation energies in the low and high temperature regions. This can be attributed to the change in behavior of the polymer at 450 K, the melting temperature of the polymer, after which larger free volume elements in the polymer exist, leading to higher gas diffusivities. Similar behavior is reported for CH_4 diffusion in PE.[11] The activation energies for N_2, CO_2 and CH_4 in PE membrane are 2 (± 0.5), 8.2 (± 0.8), and 6.3 (± 0.5) kJ/ mol in the low temperature region, and 18.9 (± 1), 16.9 (± 1), and 15.9 (± 1) kJ/ mol in the high temperature region, respectively.

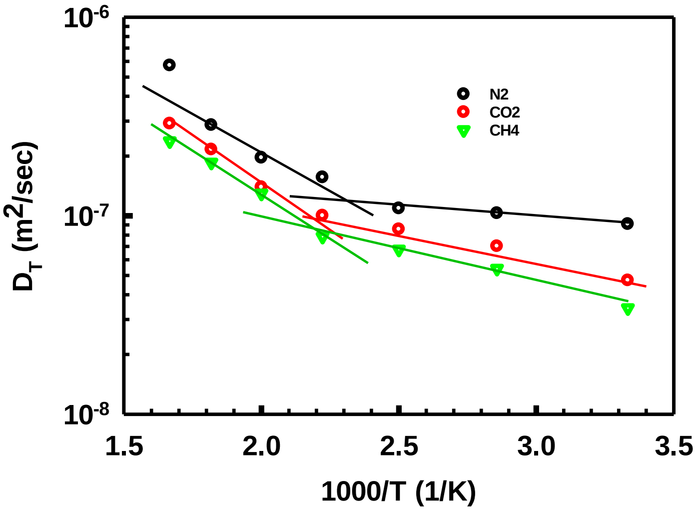

Figure 4-13: Temperature dependence of transport diffusivities of CO_2, CH_4, and N_2 in PE membrane. Solid lines emphasize the slope change.

Effect of Loading: Figure 4-14(a) depicts the concentration dependence of the self-diffusivity of N_2. Due to steric hindrance between diffusing molecules, a negative correlation between self-diffusivity and loading is expected. A moderate decrease in D_s with increase in loading is observed for N_2 while it is independent of loading for CO_2 and CH_4, as shown in Figure 4-15 and 4-16. This behavior is due to our simulations being for moderate pore loadings with respect to saturation capacity as seen in Figure 4-6, and hence the effect of concentration on D_s is weak or independent. Similar behavior has been observed in other nano-porous materials.[19] Figure 4-14(b) depicts the loading dependence of corrected diffusivity of N_2. It is seen that, the corrected diffusivity shows a weak dependence on loading and slightly increases with increase in loading. This is due to D_0 being a collective property, for which the steric hindrance effects are less severe and hence the maximum is observed at saturation capacity.

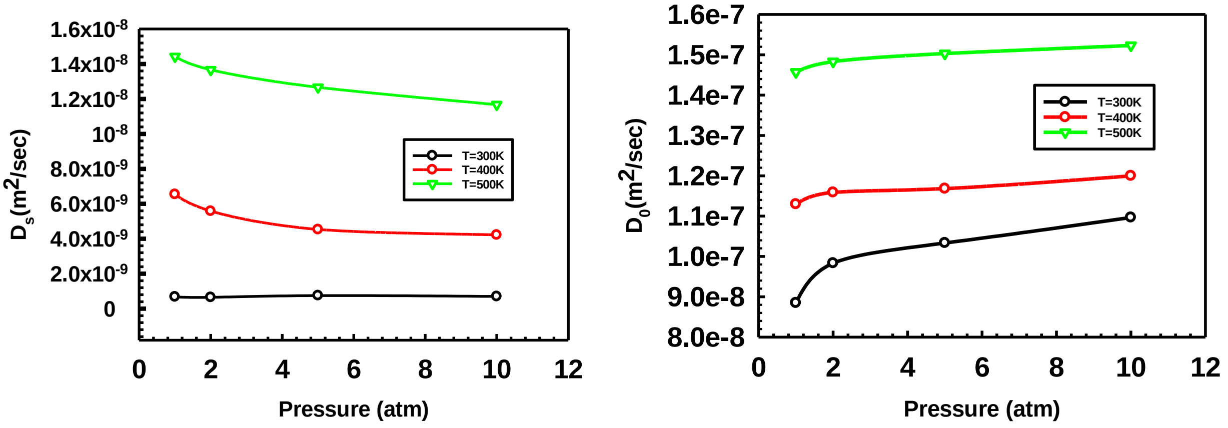

Figure 4-14: Loading dependence of (a) self, and (b) corrected diffusivities of N_2 in PE membrane.

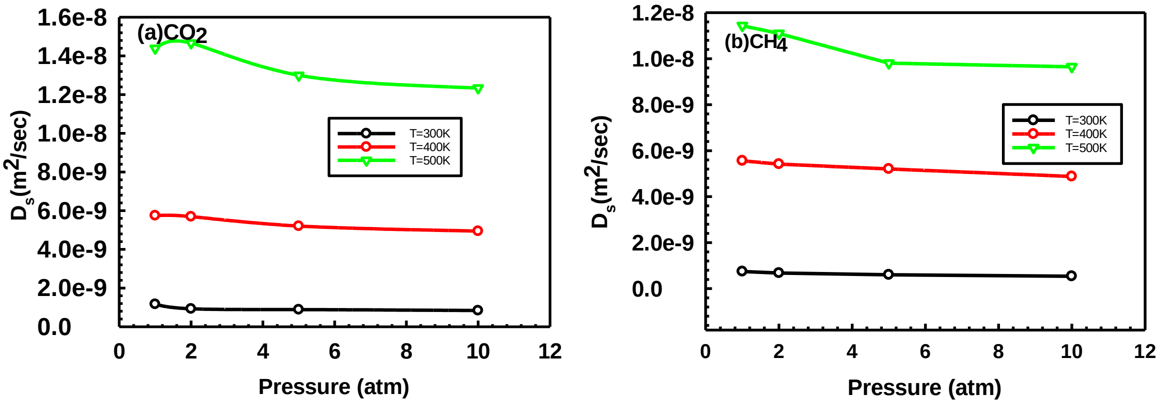

Figure 4-15: Pressure variation of *D*s of (a) CO_2, and (b) CH_4 in PE polymer membrane

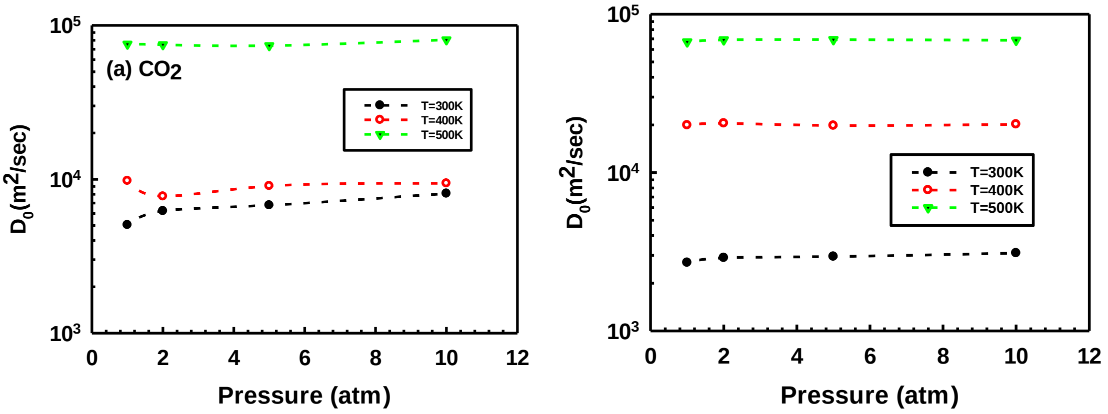

Figure 4-16:Pressure variation of D_0 of (a) CO_2, and (b) CH_4 in PE polymer membrane

4.2.2 BPDA-APB polyimide

Polyimides (PI) are most extensively investigated membrane materials as they exhibit relatively high gas selectivity and permeability. In this section we investigated the gas transport characteristics of BPDA-APB polyimide polymer membrane.

Structure of Bulk Polyimide: The structure of the PI polymer model was characterized by the density−temperature relation, glass transition temperature, distribution of free volume elements (FVE) in the polymer and associated free volume. It is seen that PI Polymer has a density of 1.31 (±0.1) g/cc at 300 K, in agreement with experimental and earlier simulations values of 1.25-1.45 g/cc[53-55] and 1.25-1.27 g/cc[56-58] respectively. Figure 4-17 (a) depicts the structure of the PI polymer membrane at 300 K and 5 atm., and the corresponding radius of gyration of the polymer is found to be 1.5 ((±0.3) nm. Figure 4-17(b) depicts the variation of mass density of bulk PI polymer membrane with temperature. It is observed that density of the PI decreases linearly with increase in temperature with change in slope at 550 (± 25) K, the glass transition temperature of PI.[53, 59] In addition, the accessible volume in the PI polymer membrane was determined using helium as the probe molecule, by considering the different configurations of the PI polymer. We note here that the effect of pressure on the structure of the PI Polymer is found to be negligible up to 15 atm.

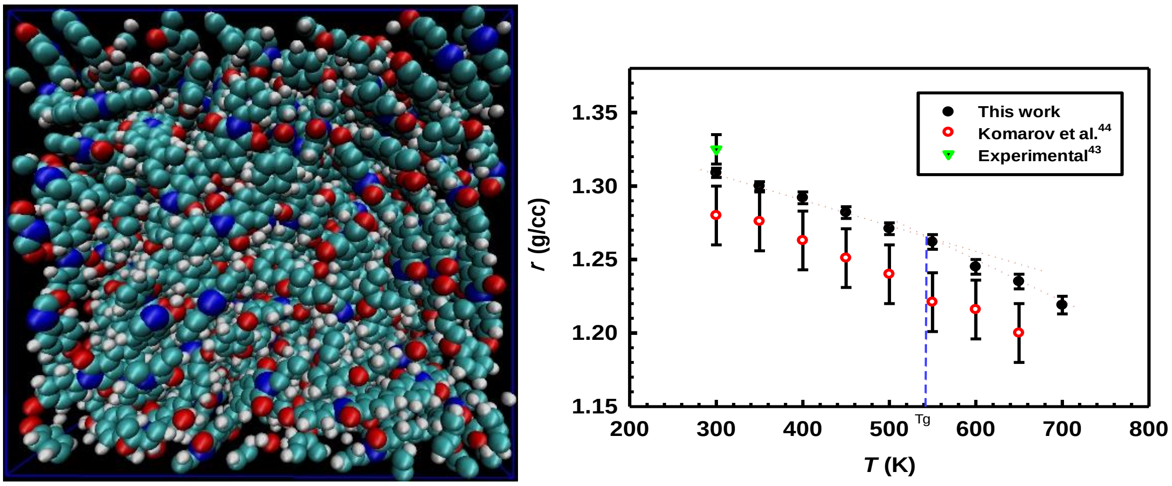

Figure 4-17: Structure of the PI polymer at (a) 300K and 5 atm, and (b) temperature variation of density of PI polymer at 5 atm.

Sorption isotherms of CO_2 and CH_4 in bulk polyimide: The sorption behavior of pure component CO_2 and CH_4 in the bulk PI polymer was systematically investigated by exploring the sorption isotherms for each gas, using the two step procedure considering the polymer structural changes upon gas sorption and described in detail elsewhere.[60] Figure 4-18 (a)-(b) shows the sorption isotherms of CO_2 and CH_4 in the bulk PI polymer respectively, in the temperature range of 300-500 K. It is seen that the CO_2 absorbs strongly while CH_4 shows weak sorption in PI, and gas sorption increases with increase in pressure at a given temperature, while decreasing with increase in temperature. This is due to the significant decrease in gas density with increase in temperature, leading to decreased sorption at higher temperatures.

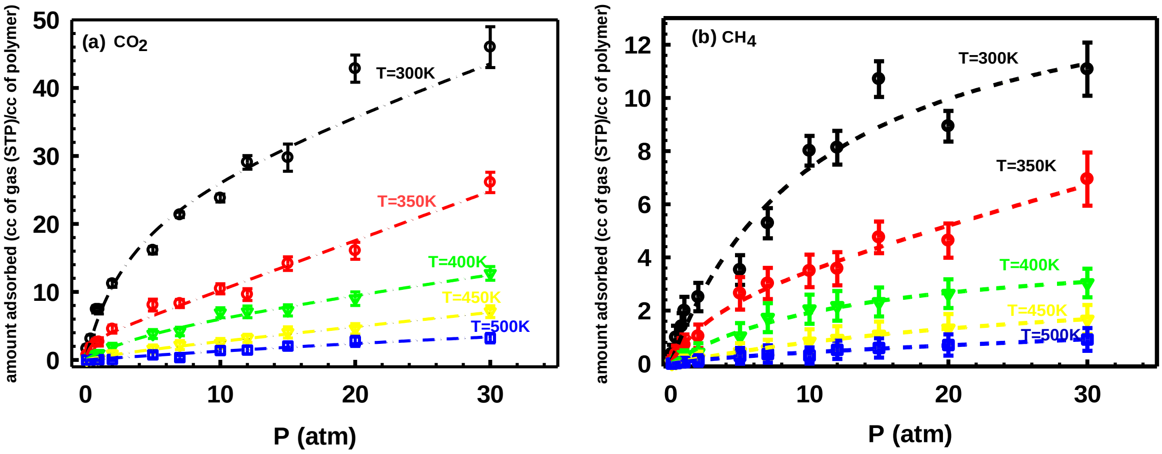

Figure 4-18: Sorption isotherms of (a) CO_2, and (b) CH_4 in PI at various temperatures. The dashed lines indicate the fitted sorption isotherms using the DM sorption model.

Further, we note that the effect of swelling on the isotherm is significant especially at higher pressures and further confirmed by the distribution of free volume elements in the polymer analysis showing greater free volume available at higher pressure, as shown in the Figure 4-19 (a)-(b). Figure 4-19 (c) illustrates loading dependency of the swelling, the fractional increase in volume due to gas sorption in PI at 300K, showing significant swelling for both CO_2 and CH_4. This effect is much more pronounced for CO_2 than CH_4, which may be attributed to the much higher CO_2 sorption capacity of PI.

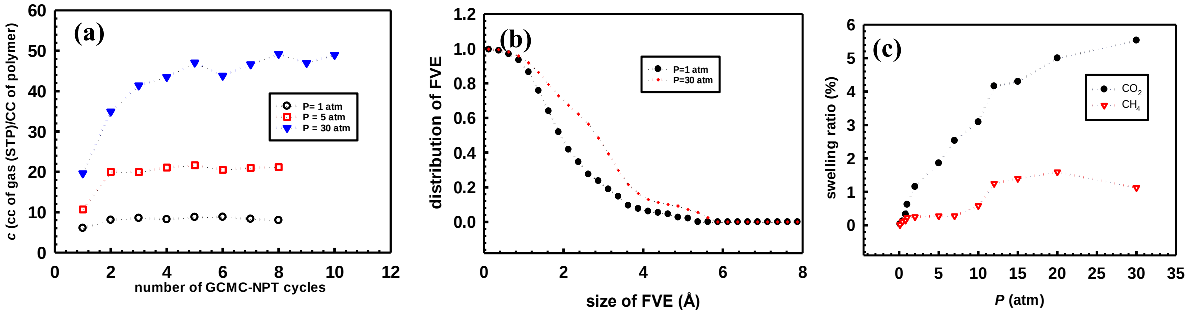

Figure 4-19: (a) Effect of swelling on the gas sorption capacity in PI membrane. CO_2 sorption capacity of PI against the number of GCMC-NPT cycles at *T*= 300K, (b) distribution of free volume elements in the polymer in the presence of CO_2 at *T* =300K, and (c) loading variation of the swelling of PI in the presence of CO_2 and CH_4 at *T* =300K.

The sorption isotherm of each gas considered was fitted using DM sorption model. It seen that the fitting parameters k_1 and k_3 of the DM sorption model from this study are in good agreement with reported values based on fits of experimental isotherms[61, 62] as shown in the Table 4-5.

Table 4-5: Comparison of fitting parameters of DM sorption model with experimental data at T=300 K for sorption in pure PI.

gas	$C_H^{'}$ (cc (STP)/cc)		k_d (cc (STP)/cc. atm)	
	Our simulations	Experimental reports[61, 62]	Our simulations	Experimental reports[61]
CO_2	26.15(±0.3)	25.5-27.5	0.67(±0.3)	1.44
CH_4	15.4064(±0.3)	14.3	0.23 0(±0.05)	0.136

Figure 4-20 shows the temperature dependence of simulated solubility coefficients for CO_2 and CH_4 in the PI polymer at temperatures from 300 to 500 K, calculated using eq (4-3). It is observed that the solubility of CO_2 and CH_4 decreases with increase in temperature. This is due to the decrease in gas sorption capacity with increase in temperature. We note that solubility results based on the all atom model (this study) are in close agreement with experimental reports, while the united atom approach overestimates the gas solubility.[60] It is seen that the temperature dependence of the solubility constant, evaluated as $(C_H^{'}b + k_d)$, obeys the van't Hoff relation. The computed heats of solutions for CO_2 and CH_4 are -17.0 (±3) and -13.5 (±2) kJ/mol in reasonable agreement with experimental values[62] of -15.3 kJ/mol and -11.0 kJ/mol respectively. Further, we note that overall sorption for both the gases is dominated by the Langmuir term $(C_H^{'}b)$, as shown in the Figure 4-21. It is expected that Langmuir part will dominate the gas sorption in the polymers below its glass transition temperature.[54]

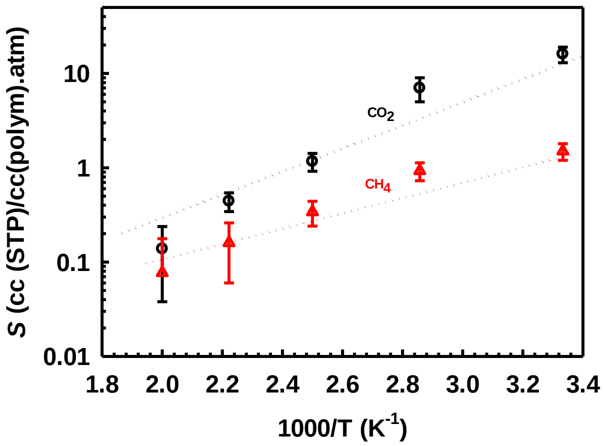

Figure 4-20: Temperature dependence of solubility coefficients in PI.

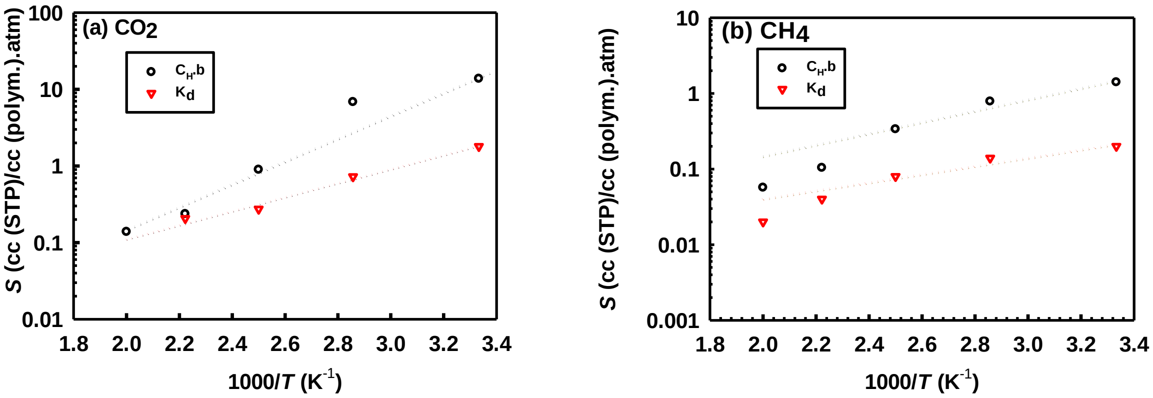

Figure 4-21: Temperature dependence of isotherm parameters for (a) CO_2 and (b) CH_4 in PI.

Diffusion of CO_2 and CH_4 in bulk PI: Figure 4-22 depicts the temperature dependence of the collective-diffusion coefficients of pure component CO_2 and CH_4 in bulk PI in the temperature range of 300-500 K. At 300 K, the calculated values of collective-diffusion coefficient (D_o) of CO_2 and CH_4 are 0.55 (± 1.0) × 10^{-11} and 0.16 (± 0.5) × 10^{-11} m^2/sec, in reasonable agreement with experimental values of 0.36 × 10^{-11} and 0.10 × 10^{-11} m^2/sec respectively[63, 64].

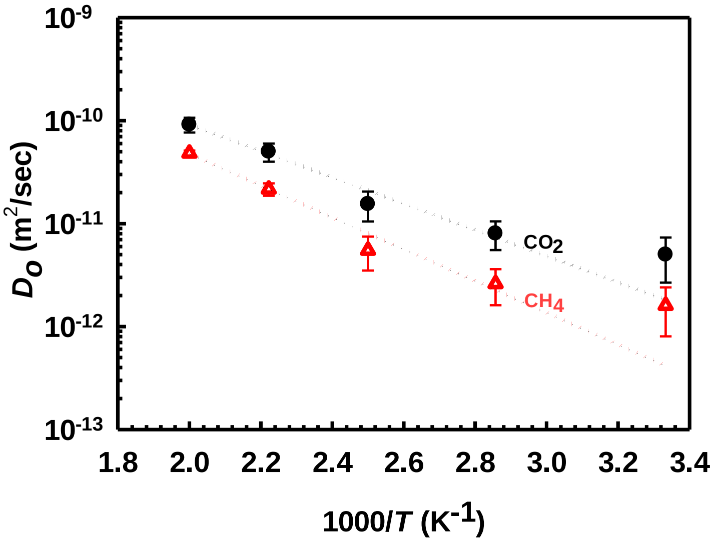

Figure 4-22:Temperature dependence of collective diffusivity of CO_2 and CH_4 in PI membrane

The concentration dependence on the corrected diffusivity of CO_2 and CH_4 in the PI membrane at 300 K shows that the corrected diffusivity has a weak dependence on loading and slightly decreases with increase in loading, as shown in the Figure 4-23. This is due to the availability of very small FVEs in the PI membrane, as a result of which two gas molecules cannot be accommodated in the same FVE, resulting in dominance of molecule-wall interactions over molecule-molecule interactions. In addition, the stronger hindrance to the entry of gas molecules at the pore openings further reduces the importance of intermolecular collisions. A similar observation has been made by Bhatia et al. [65, 66] for the transport of light gases such as CH_4 in narrow nanopores where weak reduction in collective transport coefficient with density increase is reported.

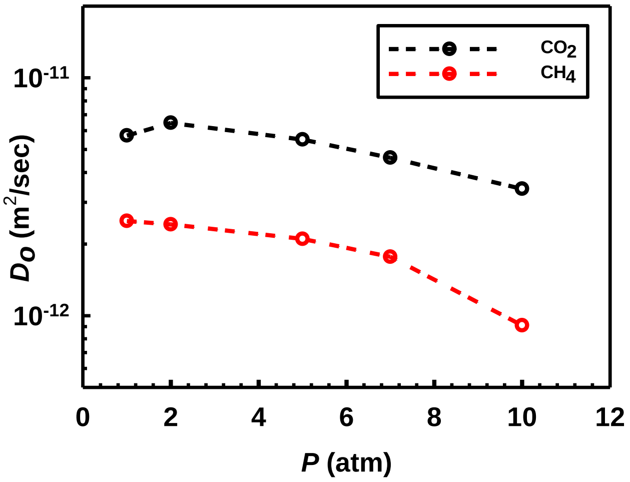

Figure 4-23: Loading dependence of D_o of CO_2 and CH_4 in PI membrane.

Further, it is seen that the temperature dependence of the collective diffusivity of CO_2 and CH_4 follows Arrhenius-type behavior. The activation energies for CO_2 and CH_4 in PI membrane are 25.3 (± 2) and 31.8 (± 3) kJ/mol respectively, computed using eq (4-7).

CO$_2$/CH$_4$ selectivity in bulk PI: Figure 4-24 depicts the temperature dependence of the diffusive, sorption and perm-selectivity of CO$_2$ over CH$_4$ in PI polymer membrane in the temperature range of 300-500 K. At 300 K, the calculated values of diffusive, sorption and perm selectivity of CO$_2$ over CH$_4$ are 3.1 (±0.2), 10.5 (±0.5) and 33.2 (±2), in agreement with experimental values[63, 64, 67] of 2.8-3.7, 9-11 and 30-35 respectively.

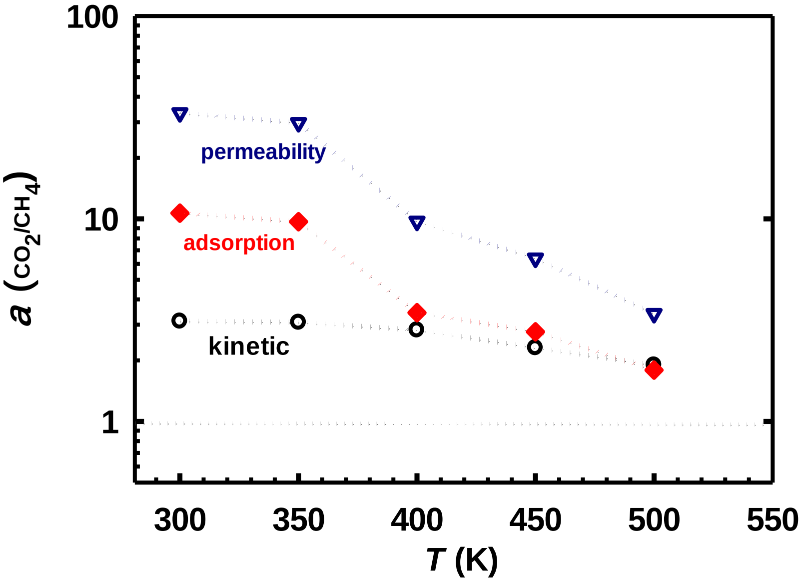

Figure 4-24: Temperature dependence of selectivity of CO$_2$ over CH$_4$ in PI membrane. The gray dotted line depicts selectivity crossover.

It is seen that the PI polymer membrane is selective for CO$_2$ over the temperature range of 300-500 K. Further, we note that CO$_2$ selectivity decreases with increase in temperature. This is due to significant increase in the free volume and chain mobility with increase in temperature, leading to availability of number of large FVEs in the polymer and hence increase in both gas diffusivity and solubility. This effect is more pronounced for the gas with a larger kinetic diameter, CH$_4$ in this case which leads to reduction in CO$_2$ selectivity.

4.2.3 6FDA-durene

We then investigated gas transport characteristics in a commercially used glassy polymeric membrane material, 6FDA-durene PI polymer. The presence of –C(CF$_3$)$_2$– and a bulky methyl group in the polymer backbone contributes to the reduction of local segmental mobility and inhibits the inter chain packing, resulting in a great amount of free volume and thereby good gas separation performance.

Polymer structure Characterization: The ability of the force field to represent 6FDA-durene polymer membrane is illustrated by characterizing the polymer structure using volume-temperature relations, associated free volume and distribution of free volume elements (FVE) in the polymer analysis. Figure 4-25 (a) depicts the temperature dependence of the specific volume ($1/\rho$) of 6FDA-durene polymer at 1 atm pressure. It is seen that 6FDA-durene polymer has a density of 1.34 (± 0.1) g/cc at 300 K, well in agreement with the experimental value of 1.31-1.37 g/cc.[68-70] It is observed that specific volume of the polymer increases linearly with increase in temperature with change in slope at 680 (± 10) K, the glass transition temperature (T_g) of the polymer, which compares well with the experimental value of 683-697 K[68-70] We note here that the effect of pressure on the structure of the polymer is found to be negligible up to 30 atm. The inset of Figure 4-25 (a) depicts the temperature dependence of fractional free volume (FFV) in the polymer, determined using helium as a probe molecule,[34-36, 70] by averaging over several configurations of polymer structure at each temperature. It is seen that FFV of 6FDA-durene polymer increases linearly with increase in temperature, with change in slope at T_g of the polymer, illustrating the swelling behavior of the polymer with increase in the temperature. We note that that 6FDA-durene polymer has a free volume of 7 (±1) % at 300 K, showing a large deviation from the experimental free volume of 18-24 %,[70] estimated using Bondi's group contribution method. This difference arises because the computed free volume neglects the contribution of sites that are not accessible to helium, while Bondi's group contribution method includes these. To confirm this, we determined the FFV of polymer using an imaginary probe of various diameters. It is seen that FFV increases with decrease in probe diameter and reaches an experimental value of ~25 % for a probe diameter of 1 Å, as shown in the Figure 4-25 (b) We further note that a free volume of 6% in 6FDA-durene has been reported using bulk positron annihilation lifetime spectroscopy with sodium probe,[71] in close agreement with predictions of this work.

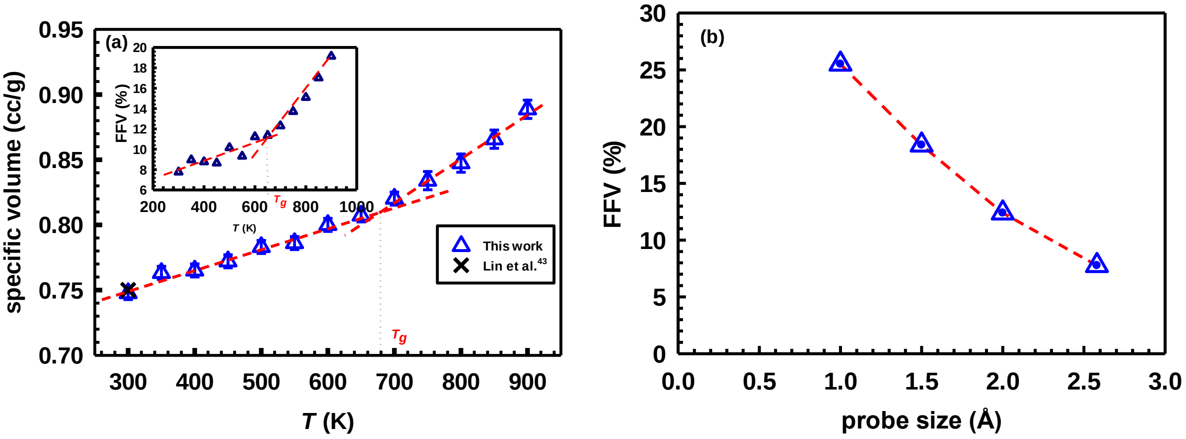

Figure 4-25: (a) Variation of specific volume (inset: fractional free volume) in 6FDA-durene membrane with temperature, and (b) accessible volume with probe diameter at various temperatures.

Figure 4-26 (a) and (b) depicts the variation of accessible volume and size of FVE in the polymer respectively with the diameter of probe at various temperatures in 6FDA-durene polymer membrane. It is seen that FVEs of 3-4 Å diameter exist in the polymer membrane in the temperature range of

300-500 K, and the absence of larger pores even at higher temperatures indicates the availability of more small FVEs with the swelling of the polymer.

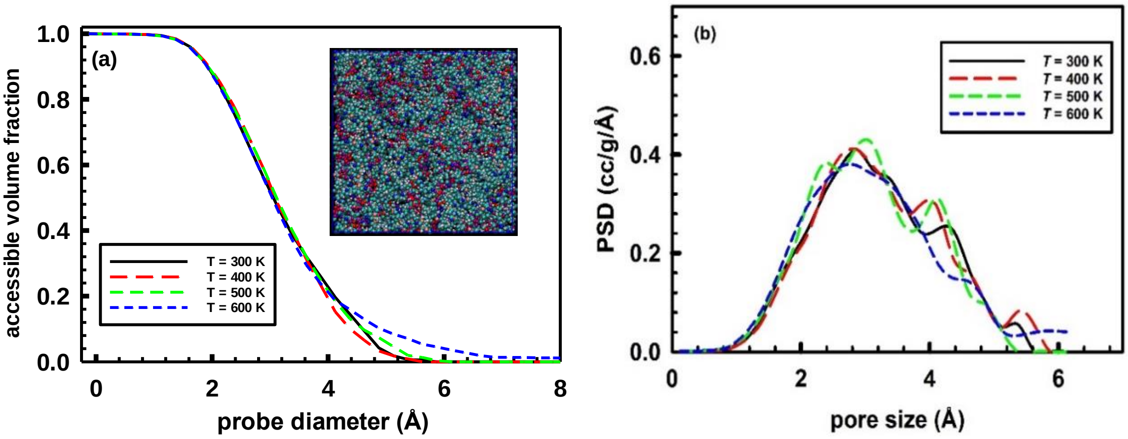

Figure 4-26: Variation of fraction (a) free volume in 6FDA-durene polymer membrane with probe size at 300 K, and (b) comparison of distribution of free volume elements in the polymer at various temperatures.

Pure component gas sorption isotherms: The swelling behavior of 6FDA-durene polymer upon gas sorption and its effect on gas sorption kinetics was systematically investigated by comparing the sorption isotherms for each adsorbed gas as a single component in a polymer, both with and without swelling with gas sorption. A comparison of gas sorption isotherms at 300 K in 6FDA-durene polymer for both cases is shown in the Figure 4-27. It is seen that the swelling behavior of the polymer influences the gas sorption isotherms significantly. Further, the effect of swelling is more pronounced at elevated pressures owing to its high gas sorption capacity. In addition, the effect of swelling on the polymer structure was investigated by computing the distribution of FVEs in the polymer. It is seen that greater free volume and larger FVEs are available at higher pressures, in contrast to the thermally induced swelling due to temperature increase, in which increased availability of small FVEs is seen above.

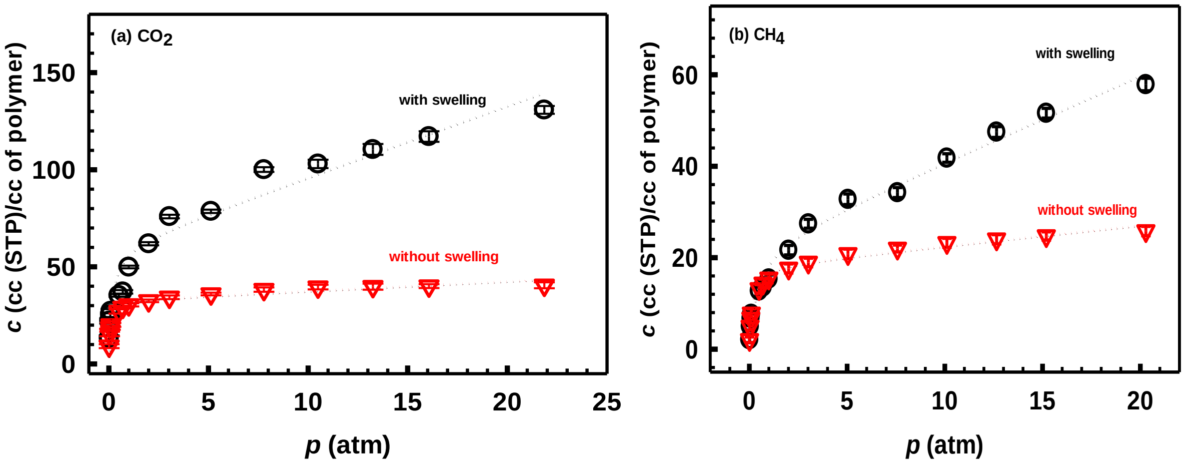

Figure 4-27: Sorption isotherms of (a) CO_2, and (b) CH_4 in 6FDA-durene with and without considering the effect of polymer swelling upon gas sorption at $T = 300$ K.

The sorption isotherm of each gas considered was fitted using a DM sorption model. The fitting parameters $C_H^{'}$, b and k_d of the DM sorption model from this study considering the swelling of the polymer upon gas sorption are provided in the Table 4-6.

Table 4-6: DM sorption model fitting parameters of pure component CO_2 and CH_4 in 6FDA-durene polymer membrane.

DM sorption model parameter	CO_2	CH_4
$C_H^{'}$ (cc (STP)/cc (polym))	60.18 (±6)	22.89 (±2)
b (atm^{-1})	6.08 (±2)	2.46 (±1)
k_d (cc (STP)/cc (polym).atm)	3.645 (±0.5)	1.8593 (±0.2)

Figures 4-28 (a)-(b) depict pure component sorption isotherms of CO_2 and CH_4 in 6FDA-durene polymer membrane respectively considering the swelling upon gas sorption, at temperatures from 300-500 K. Gas sorption isotherms at T =300 K from this study, considering the swelling of the polymer upon the gas sorption, are in good agreement with experiment, as shown in the respective figures. However, the reported gas sorption isotherms in 6FDA-durene polymer membrane from various experimental investigations have significant differences especially for methane, as shown in Figure 4-29 (a)-(b). This can be attributed to the differences in the available free volume (FV) in the membranes. Further, it is seen that the CO_2 absorbs more strongly than CH_4 in 6FDA-durene polymer membrane. The sorption capacity of both the gases decreasing with increase in temperature. However, we note that the parameters are sensitive to the pressure range over which the fitting is done. The sorption isotherm of each gas considered was fitted using DMS model. It is seen that the Langmuir capacity term dominates the overall sorption for both the gases in 6FDA-durene polymer membrane, as expected in glassy polymers.

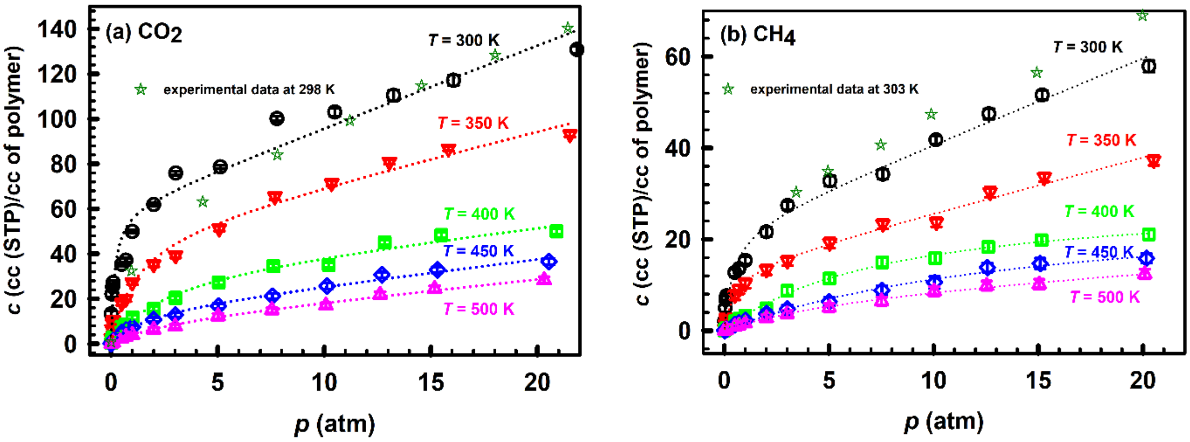

Figure 4-28:Pure component sorption isotherms of (a) CO_2, and (b) CH_4 in 6FDA-durene at various temperatures. The dashed lines indicate the fitted sorption isotherms using the dual-mode sorption model. Experimental data points (symbol-stars) are taken from references [72-75].

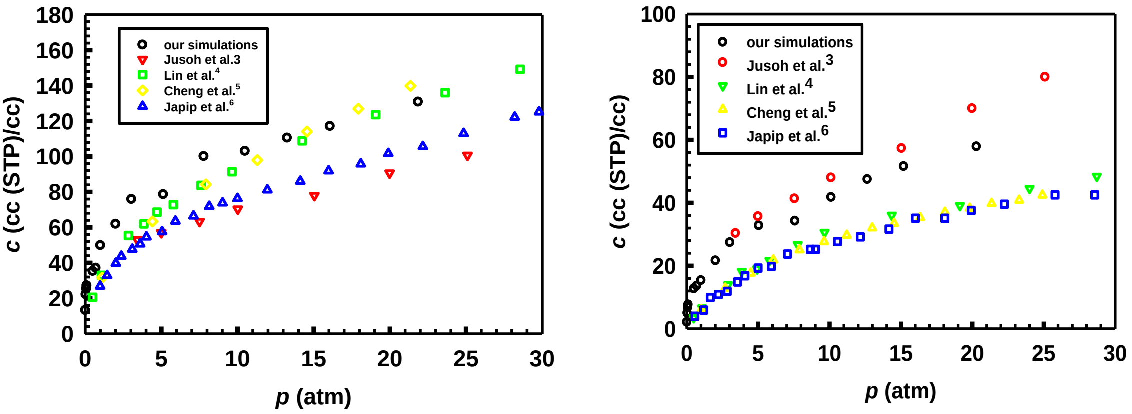

Figure 4-29: Comparison of sorption isotherms of (a) CO_2, and (b) CH_4 in 6FDA-Durene with experimental investigations at $T \approx 300$ K.

Pure-component diffusion: To understand gas diffusion behavior in the 6FDA-durene polymer membrane, corrected diffusion coefficient of gas molecules that corresponds to the MS diffusivity in the pure gas conditions were determined using eq (3-9). Figure 4-30(a) shows the loading dependence of pure component MS diffusivities of CO_2 and CH_4 in the 6FDA-durene membrane at T= 300 K. It is seen that for methane, a moderate increase in diffusivity with increase in loading is observed, while a stronger increase in diffusivity with increase in loading, especially at high loadings, is observed for CO_2. This can be attributed to the plasticization behavior of the polymer at high CO_2 loadings. To investigate this further, the permeability of the gases at various loadings was determined and is depicted in Figure 4-30(b). Good agreement is found between our simulation predictions and experimentally reported gas permeabilities in 6FDA-durene polymer membrane,[60, 66] however, we note that gas permeabilities in 6FDA-durene polymer membrane from various experimental investigations have significant differences.[60, 65-67] In addition, the computed permeability values from this investigation correspond to any given temperature and pressure, while experimental permeabilities are extracted from the pressure gradient across a membrane and hence expected to be higher or lower depending on pressure dependency. It is seen that permeability of methane decreases with increase in loading, as is typical for polymers due to the strong decrease in solubility with pressure, while the permeability of CO_2 decreases up to about 5 atm pressure and then increases with increase in loading. This increase in permeability with increase in pressure has also been observed experimentally[59, 62] at around 5 atm pressure, corresponding to the plasticization pressure of the polymer. Beyond the plasticization pressure, sharp increase in gas diffusivity dominates the effect of decrease in solubility with increase in pressure, leading to increase in permeability with increase in pressure.

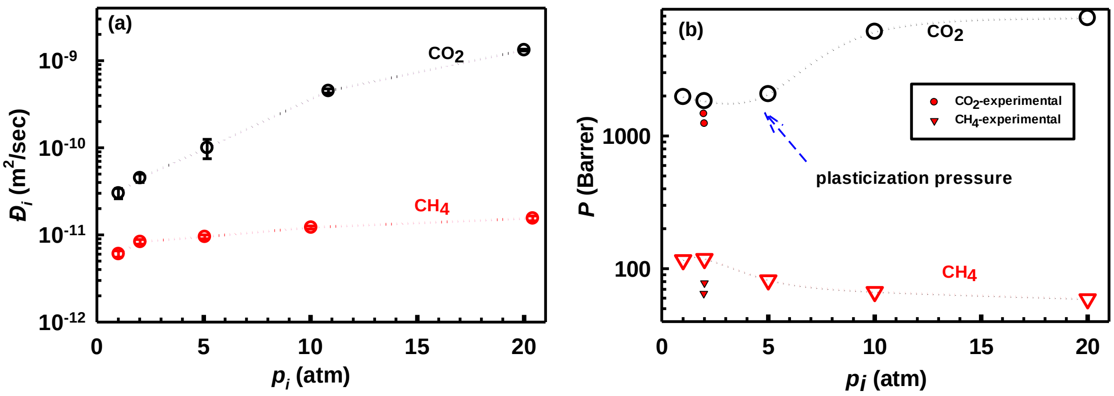

Figure 4-30: Loading dependence of pure component (a) MS diffusivities, and (b) permeability of the gases at *T*=300 K in 6FDA-durene. Open symbols represent simulation results, and the filled symbols are experimental data points.[60, 66] Dotted lines are given as guide for the eye.

We note that while we display the permeability at a given pressure and temperature to illustrate the effect of plasticization, these calculations are not used in the subsequent analysis of membrane permeation. In the latter case the MS equations are integrated over a membrane of given thickness and pressure difference, to predict the membrane performance, while using MS diffusivities evaluated at the local composition.

The structural changes in the polymer membrane due to plasticization can be characterized by investigating the distribution of FVEs in the polymer at various gas loadings using a spherical probe of varying probe diameter through the geometric approximation technique and are depicted in Figure 4-31(a)-(b). An increase in fractional accessible volume for larger probe diameters is seen at high pressures indicating the availability of larger FVEs due to swelling of the polymer upon gas sorption. It is seen that 5-7 Å FVEs are available after swelling in the in the presence of CO_2, while 4-5 Å FVEs are available in the presence of CH_4, as shown in the insets of the respective figures. We note that 3-4 Å FVEs are available in the neat polymer membrane. The greater availability of number of larger FVEs in the presence of CO_2 can be attributed to plasticization behavior of the polymer at elevated pressures. The greater availability of large FVEs at high pressure leads to stronger increase in CO_2 diffusivity with increase in pressure.

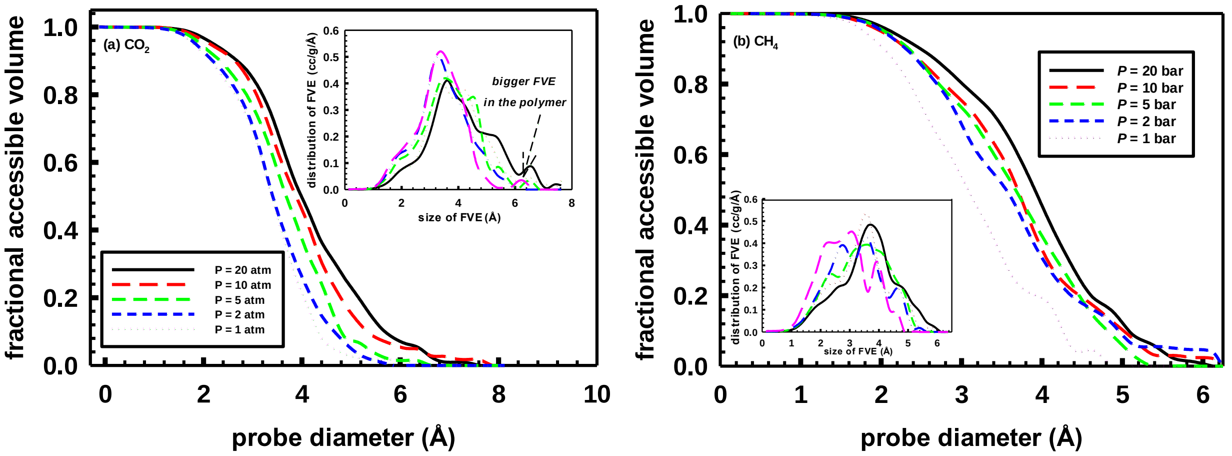

Figure 4-31: Comparison of variation of fractional accessible volume with probe diameter in 6FDA-durene polymer in the presence of (a) CO_2, and (b) CH_4 at various loadings. A comparison distribution of free volume elements in the polymer at various gas loadings is depicted in the respective insets.

Figure 4-32 (a) depicts the temperature dependence of pure component MS diffusivities of CO_2 and CH_4 in a neat 6FDA-durene polymer membrane. The calculated values of MS diffusion coefficient ($Đ_1$) of CO_2 and CH_4 at 300 K are 5 (± 0.5) × 10^{-11} and 0.85 (± 0.1) × 10^{-11} m^2/sec, in good agreement with experimental values of 6.6 × 10^{-11} and 1.25 × 10^{-11} m^2/sec respectively.[66] The activation energies for CO_2 and CH_4 in 6FDA-durene membrane are 5 (± 2) and 10.5 (± 3) kJ/mol respectively, using eq (4-7)

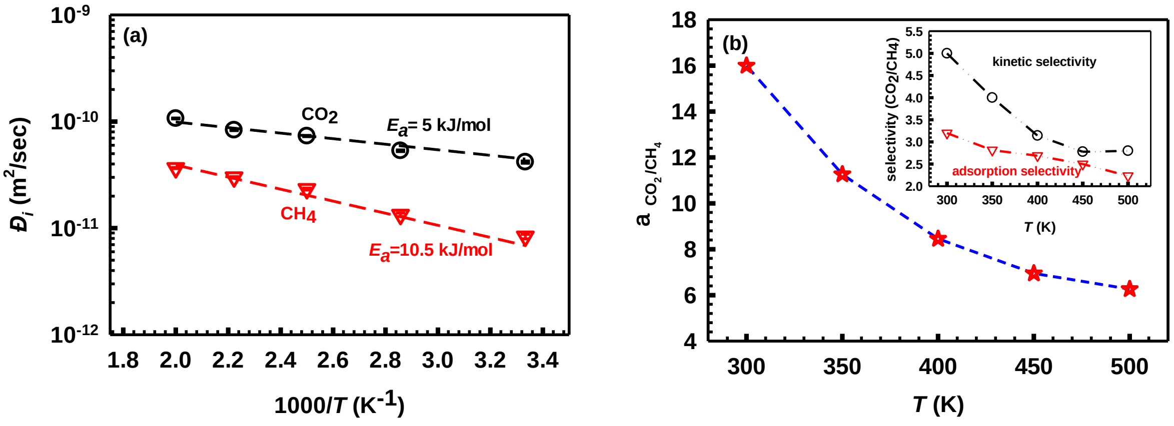

Figure 4-32: (a) Temperature dependence of pure component MS diffusivities of CO_2 and CH_4 in 6FDA-durene membrane, and (b) 6FDA-durene perm-selectivity for CO_2 over CH_4 in in the temperature range of 300-500 K. A comparison of diffusivity and solubility selectivity of CO_2 over CH_4 in 6FDA-durene is depicted in the inset

Figure 4-32 (b) depicts the temperature dependence of 6FDA-durene polymer membranes perm-selectivity for CO_2 over CH_4 in the temperature range of 300-500 K. At 300 K, the calculated values of the diffusive, sorption and perm-selectivity of CO_2 over CH_4 are 5.0, 3.0 and 15, in excellent agreement with experimental values of 5.3, 3.0 and 15.9 respectively.[66] It is seen that 6FDA-durene is selective for CO_2 over the temperature range of 300-500 K and this perm-selectivity decreases with increase in temperature. This decrease in perm-selectivity is due to greater increase in methane diffusivity, this being a lighter and more weakly adsorbing molecule than CO_2, which leads to a steep decrease in diffusivity selectivity with increase in diffusivity selectivity with increase in temperature as shown in the inset of Figure 4-32(b).

4.3 Conclusions

The transport diffusion of CO_2, CH_4 and N_2 at 1 atm in the temperature range of 300-600 K in Polyethylene (PE) polymer matrix has been investigated here, using equilibrium molecular dynamics simulations. The 3-dimensional structure of the PE polymer matrix is visualized by exploring the volume-temperature relations, associated free volume, distribution of free volume elements in the polymer and inter molecular radial distribution function (RDF). A split in the second peak of the RDF has been observed in the glassy region, well above glass transition temperature and below melting point. The swelling behavior of the polymer due to the presence of gas molecules has been investigated at the microscopic level over a wide range of temperatures. Self-diffusivities of CO_2, CH_4 and N_2 in PE are in the order of 10^{-6} cm^2/sec and in good agreement with previous experimental and simulation reports, while the transport diffusivity of the gases is found to be 2 orders magnitude higher. In addition, the transport diffusivity follows non-Arrhenius behavior with temperature while self-diffusivity follows Arrhenius behavior. Also, it is seen that loading has little effect on the self and corrected diffusion coefficients of all the gases in the PE membrane.

Further, we have presented a detailed study of CO_2, CH_4 and N_2 sorption in PE polymer matrix in the temperature range of 300 to 600 K by considering the possible swelling of the polymer and its dynamics. It is found that the isotherm curves for gas sorption in PE are of 'dual-mode sorption' type, a combination of Henry law type dissolution and Langmuir type sorption for all the gases considered in this study. Due to the exothermic nature of the sorption process, the sorption of CO_2 and CH_4 decreases with the increase in temperature with negative heats of sorption. On the other hand, sorption of N_2 increases with increase in temperature, with slightly positive heat of sorption due to the increasing availability of kinetically closed pores at higher temperatures. We find that CO_2 is more soluble, while N_2 is least soluble in PE among the gases considered in this study at all the temperatures, following the order: S (CO_2) > S (CH_4) > S (N_2). Such understanding of gas sorption and transport is helpful to improve the performance of polymer membrane materials such as PE, a key food packaging material.

The transport properties of CO_2 and CH_4 in the temperature range of 300-500 K in two variants of Polyimide (PI) polymer has been investigated here, using equilibrium molecular dynamics simulations. The structure of the PI is visualized by exploring the density-temperature relation. The diffusivities of CO_2 and CH_4 in BPDA PI are of the order of 10^{-12} m^2/sec, and qualitatively as well as quantitatively in good agreement with experimental reports, and it is seen that CO_2 is diffusive selective over CH_4 in neat PI membrane. Further, the diffusivities of CO_2 and CH_4 in in 6FDA-durene polymer membrane are in the order of 10^{-10} -10^{-11} m^2/sec, and in good agreement with experimental reports. It is seen that the corrected diffusivities of the gases increase with increase in loading at 300 K, exhibiting a decrease in methane permeability with increase in pressure, due to swelling reducing sorption, while an increase in CO_2 permeability with increase in pressure occurs above 5 atm, the plasticization pressure of the polymer. In addition, corrected diffusivities of the gases in 6FDA-durene polymer membrane follow Arrhenius behavior with temperature, with diffusivity selectivity for CO_2 being greater than unity at all temperatures.

The gas sorption isotherms in PI were extracted *via* a two-step methodology considering the dynamics and structural transitions in the polymer matrix upon gas sorption. Our results show that the isotherm curves for gas sorption in PI membrane are of ‘dual-mode sorption’ type. It is found that CO_2 is more soluble than CH_4 at all temperatures in a 6FDA-durene polymer membrane, and this solubility decreases with increase in temperature following the van’t Hoff relation.

4.4 References

1. Rincon Bonilla, M.; Bhatia, S. K., Diffusion in Pore Networks: Effective Self-Diffusivity and the Concept of Tortuosity. *J. Phys. Chem. C* **2013,** *117* (7), 3343-3357.

2. Bhatia, S. K.; Nicholson, D., Modeling Self-Diffusion of Simple Fluids in Nanopores. *J. Phys. Chem. B* **2011,** *115* (40), 11700-11711.

3. Beerdsen, E.; Dubbeldam, D.; Smit, B., Understanding Diffusion in Nanoporous Materials. *Phys. Rev. Lett.* **2006,** *96* (4), 044501.

4. Chen, H.; Johnson, J. K.; Sholl, D. S., Transport Diffusion of Gases Is Rapid in Flexible Carbon Nanotubes. *J. Phys. Chem. B* **2006,** *110* (5), 1971-1975.

5. Skoulidas, A. I.; Ackerman, D. M.; Johnson, J. K.; Sholl, D. S., Rapid Transport of Gases in Carbon Nanotubes. *Phys. Rev. Lett.* **2002,** *89* (18), 185901.

6. Chen, H.; Sholl, D. S., Rapid Diffusion of CH4/H2 Mixtures in Single-Walled Carbon Nanotubes. *J. Am. Chem. Soc.* **2004,** *126* (25), 7778-7779.

7. Takeuchi, H.; Okazaki, K., Molecular dynamics simulation of diffusion of simple gas molecules in a short chain polymer. *J. Chem. Phys.* **1990,** *92* (9), 5643-5652.

8. Tamai, Y.; Tanaka, H.; Nakanishi, K., Molecular Simulation of Permeation of Small Penetrants through Membranes. 1. Diffusion Coefficients. *Macromolecules* **1994,** *27* (16), 4498-4508.

9. Müller-Plathe, F.; Rogers, S. C.; van Gunsteren, W. F., Computational evidence for anomalous diffusion of small molecules in amorphous polymers. *Chem. Phys. Lett.* **1992,** *199* (3), 237-243.

10. Mozaffari, F.; Eslami, H.; Moghadasi, J., Molecular dynamics simulation of diffusion and permeation of gases in polystyrene. *Polymer* **2010,** *51* (1), 300-307.

11. van der Vegt, N. F. A., Temperature Dependence of Gas Transport in Polymer Melts: Molecular Dynamics Simulations of CO2 in Polyethylene. *Macromolecules* **2000,** *33* (8), 3153-3160.

12. Faure, F.; Rousseau, B.; Lachet, V.; Ungerer, P., Molecular simulation of the solubility and diffusion of carbon dioxide and hydrogen sulfide in polyethylene melts. *Fluid Phase Equilib.* **2007,** *261* (1–2), 168-175.

13. Pant, P. V. K.; Boyd, R. H., Molecular-dynamics simulation of diffusion of small penetrants in polymers. *Macromolecules* **1993,** *26* (4), 679-686.

14. Gestoso, P.; Karayiannis, N. C., Molecular Simulation of the Effect of Temperature and Architecture on Polyethylene Barrier Properties. *J. Phys. Chem. B* **2008,** *112* (18), 5646-5660.

15. Arya, G.; Chang, H.-C.; Maginn, E. J., A critical comparison of equilibrium, non-equilibrium and boundary-driven molecular dynamics techniques for studying transport in microporous materials. *J. Chem. Phys.* **2001,** *115* (17), 8112-8124.

16. Ford, D. M.; Heffelfinger, G. S., Massively parallel dual control volume grand canonical molecular dynamics with LADERA II. Gradient driven diffusion through polymers. *Mol. Phys.* **1998,** *94* (4), 673-683.

17. Pohl, P. I.; Heffelfinger, G. S., Massively parallel molecular dynamics simulation of gas permeation across porous silica membranes. *J. Membr. Sci.* **1999,** *155* (1), 1-7.

18. Maginn, E. J.; Bell, A. T.; Theodorou, D. N., Transport diffusivity of methane in silicalite from equilibrium and nonequilibrium simulations. *J. Phys. Chem.* **1993,** *97* (16), 4173-4181.

19. Skoulidas, A. I.; Sholl, D. S., Self-Diffusion and Transport Diffusion of Light Gases in Metal-Organic Framework Materials Assessed Using Molecular Dynamics Simulations. *J. Phys. Chem. B* **2005,** *109* (33), 15760-15768.

20. Skoulidas, A. I.; Sholl, D. S., Molecular Dynamics Simulations of Self-Diffusivities, Corrected Diffusivities, and Transport Diffusivities of Light Gases in Four Silica Zeolites To Assess Influences of Pore Shape and Connectivity. *J. Phys. Chem. A* **2003,** *107* (47), 10132-10141.

21. Skoulidas, A. I.; Sholl, D. S., Direct Tests of the Darken Approximation for Molecular Diffusion in Zeolites Using Equilibrium Molecular Dynamics. *J. Phys. Chem. B* **2001,** *105* (16), 3151-3154.

22. Salles, F.; Jobic, H.; Devic, T.; Llewellyn, P. L.; Serre, C.; Férey, G.; Maurin, G., Self and Transport Diffusivity of CO2 in the Metal−Organic Framework MIL-47(V) Explored by Quasi-elastic Neutron Scattering Experiments and Molecular Dynamics Simulations. *ACS Nano* **2010,** *4* (1), 143-152.

23. Liu, H., Transport diffusivity of propane and propylene inside SWNTs from equilibrium molecular dynamics simulations. *Phys. Chem. Chem. Phys.* **2014,** *16* (45), 24697-24703.

24. Bhatia, S. K.; Nicholson, D., Adsorption and Diffusion of Methane in Silica Nanopores: A Comparison of Single-Site and Five-Site Models. *J. Phys. Chem. C* **2012,** *116* (3), 2344-2355.

25. Liu, L.; Nicholson, D.; Bhatia, S. K., Impact of H2O on CO2 Separation from Natural Gas: Comparison of Carbon Nanotubes and Disordered Carbon. *J. Phys. Chem. C* **2015,** *119* (1), 407-419.

26. Cozmuta, I.; Blanco, M.; Goddard, W. A., Gas Sorption and Barrier Properties of Polymeric Membranes from Molecular Dynamics and Monte Carlo Simulations. *J. Phys. Chem. B* **2007,** *111* (12), 3151-3166.

27. Visser, T.; Wessling, M., When Do Sorption-Induced Relaxations in Glassy Polymers Set In? *Macromolecules* **2007,** *40* (14), 4992-5000.

28. Bos, A.; Pünt, I. G. M.; Wessling, M.; Strathmann, H., CO2-induced plasticization phenomena in glassy polymers. *J. Membr. Sci.* **1999,** *155* (1), 67-78.

29. Eslami, H.; Müller-Plathe, F., Molecular Dynamics Simulation of Sorption of Gases in Polystyrene. *Macromolecules* **2007,** *40* (17), 6413-6421.

30. Sarrasin, F.; Memari, P.; Klopffer, M. H.; Lachet, V.; Taravel Condat, C.; Rousseau, B.; Espuche, E., Influence of high pressures on CH4, CO2 and H2S solubility in polyethylene: Experimental and molecular simulation approaches for pure gas and gas mixtures. Modelling of the sorption isotherms. *J. Membr. Sci.* **2015,** *490*, 380-388.

31. Hölck, O.; Böhning, M.; Heuchel, M.; Siegert, M. R.; Hofmann, D., Gas sorption isotherms in swelling glassy polymers—Detailed atomistic simulations. *J. Membr. Sci.* **2013,** *428*, 523-532.

32. Brandrup, J.; Immergut, E. H.; Grulke, E. A., *Polymer handbook*. 4th ed.. ed.; New York : Wiley: New York, 1999.

33. Martin, M. G.; Siepmann, J. I., Transferable Potentials for Phase Equilibria. 1. United-Atom Description of n-Alkanes. *J. Phys. Chem. B* **1998,** *102* (14), 2569-2577.

34. Sarkisov, L.; Harrison, A., Computational structure characterisation tools in application to ordered and disordered porous materials. *Mol. Simul.* **2011,** *37* (15), 1248-1257.

35. Gelb, L. D.; Gubbins, K. E., Pore Size Distributions in Porous Glasses: A Computer Simulation Study. *Langmuir* **1999,** *15* (2), 305-308.

36. Gelb, L. D.; Gubbins, K. E., Characterization of Porous Glasses: Simulation Models, Adsorption Isotherms, and the Brunauer−Emmett−Teller Analysis Method. *Langmuir* **1998,** *14* (8), 2097-2111.

37. Boyd, R. H.; Pant, P. V. K., Simulation of glassy polymethylene starting from the equilibrated liquid. *Macromolecules* **1991,** *24* (14), 4078-4083.

38. Pant, P. V. K.; Han, J.; Smith, G. D.; Boyd, R. H., A molecular dynamics simulation of polyethylene. *J. Chem. Phys.* **1993,** *99* (1), 597-604.

39. Rigby, D.; Roe, R. J., Molecular dynamics simulation of polymer liquid and glass. II. Short range order and orientation correlation. *J. Chem. Phys.* **1988,** *89* (8), 5280-5290.

40. Clarke, J. H. R., Molecular dynamics studies of glass formation in the Lennard-Jones model of argon. *J. Chem. Soc., Faraday Trans. 2* **1979,** *75* (0), 1371-1387.

41. Rahman, A.; Mandell, M. J.; McTague, J. P., Molecular dynamics study of an amorphous Lennard-Jones system at low temperature. *J. Chem. Phys.* **1976,** *64* (4), 1564-1568.

42. Koros, W. J.; Paul, D. R., CO2 sorption in poly(ethylene terephthalate) above and below the glass transition. *J. Polym. Sci. B Polym. Phys.* **1978,** *16* (11), 1947-1963.

43. Hopfenberg, H. B.; Stannett, V., The Diffusion and Sorption of Gases and Vapours in Glassy Polymers. In *The Physics of Glassy Polymers*, Haward, R. N., Ed. Springer Netherlands: Dordrecht, 1973; pp 504-547.

44. Culp, J. T.; Sui, L.; Goodman, A.; Luebke, D., Carbon dioxide (CO2) absorption behavior of mixed matrix polymer composites containing a flexible coordination polymer. *J. Colloid Interface Sci.* **2013,** *393*, 278-285.

45. Nguyen, T. X.; Bhatia, S. K., Determination of Pore Accessibility in Disordered Nanoporous Materials. *J. Phys. Chem. C* **2007,** *111* (5), 2212-2222.

46. Bixler, A. S. M. H. J., Solubility of Gases in Polyethylene. *J. Polym. Sci.* **1961,** *L*, 393-412.

47. Sato, Y.; Fujiwara, K.; Takikawa, T.; Sumarno; Takishima, S.; Masuoka, H., Solubilities and diffusion coefficients of carbon dioxide and nitrogen in polypropylene, high-density polyethylene, and polystyrene under high pressures and temperatures. *Fluid Phase Equilib.* **1999,** *162* (1–2), 261-276.

48. Fukuda, M., Solubilities of small molecules in polyethylene evaluated by a test-particle-insertion method. *J. Chem. Phys.* **2000,** *112* (1), 478-486.

49. Compañ, V.; Del Castillo, L. F.; Hernández, S. I.; López-González, M. M.; Riande, E., On the crystallinity effect on the gas sorption in semicrystalline linear low density polyethylene (LLDPE). *J. Polym. Sci. B Polym. Phys.* **2007,** *45* (14), 1798-1807.

50. Tsolou, G.; Mavrantzas, V. G.; Makrodimitri, Z. A.; Economou, I. G.; Gani, R., Atomistic Simulation of the Sorption of Small Gas Molecules in Polyisobutylene. *Macromolecules* **2008,** *41* (16), 6228-6238.

51. Pant, P. V. K.; Boyd, R. H., Simulation of diffusion of small-molecule penetrants in polymers. *Macromolecules* **1992,** *25* (1), 494-495.

52. Michaels, A. S.; Bixler, H. J., Flow of gases through polyethylene. *J. Polym. Sci.* **1961,** *50* (154), 413-439.

53. Nik, O. G.; Chen, X. Y.; Kaliaguine, S., Amine-functionalized zeolite FAU/EMT-polyimide mixed matrix membranes for CO_2/CH_4 separation. *J. Membr. Sci.* **2011,** *379* (1), 468-478.

54. Barbari, T. A.; Koros, W. J.; Paul, D. R., Gas sorption in polymers based on bisphenol-A. *J. Polym. Sci. B Polym. Phys.* **1988,** *26* (4), 729-744.

55. Shang, X.-y.; Zhu, Z.-k.; Yin, J.; Ma, X.-d., Compatibility of Soluble Polyimide/Silica Hybrids Induced by a Coupling Agent. *Chem. Mater* **2002,** *14* (1), 71-77.

56. Zhang, L.; Hu, Z.; Jiang, J., Metal–Organic Framework/Polymer Mixed-Matrix Membranes for H_2/CO_2 Separation: A Fully Atomistic Simulation Study. *J. Phys. Chem. C* **2012,** *116* (36), 19268-19277.

57. Komarov, P. V.; Chiu, Y.-T.; Chen, S.-M.; Reineker, P., Investigation of Thermal Expansion of Polyimide/SiO2 Nanocomposites by Molecular Dynamics Simulations. *Macromol. Theory Simul* **2010,** *19* (1), 64-73.

58. Heuchel, M.; Hofmann, D., Molecular modelling of polyimide membranes for gas separation. *Desalination* **2002,** *144* (1), 67-72.

59. Lyulin, S. V.; Gurtovenko, A. A.; Larin, S. V.; Nazarychev, V. M.; Lyulin, A. V., Microsecond Atomic-Scale Molecular Dynamics Simulations of Polyimides. *Macromolecules* **2013,** *46* (15), 6357-6363.

60. Dutta, R. C.; Bhatia, S. K., Transport Diffusion of Light Gases in Polyethylene Using Atomistic Simulations. *Langmuir* **2017,** *33* (4), 936-946.

61. Moore, T. T.; Koros, W. J., Gas sorption in polymers, molecular sieves, and mixed matrix membranes. *J. Appl. Polym. Sci.* **2007,** *104* (6), 4053-4059.

62. Scholes, C. A.; Tao, W. X.; Stevens, G. W.; Kentish, S. E., Sorption of methane, nitrogen, carbon dioxide, and water in Matrimid 5218. *J. Appl. Polym. Sci.* **2010,** *117* (4), 2284-2289.

63. Zhao, H.-Y.; Cao, Y.-M.; Ding, X.-L.; Zhou, M.-Q.; Yuan, Q., Effects of cross-linkers with different molecular weights in cross-linked Matrimid 5218 and test temperature on gas transport properties. *J. Membr. Sci.* **2008,** *323* (1), 176-184.

64. Falbo, F.; Brunetti, A.; Barbieri, G.; Drioli, E.; Tasselli, F., CO_2/CH_4 separation by means of Matrimid hollow fibre membranes. *Appl Petrochem Res* **2016,** *6* (4), 439-450.

65. Bhatia, S. K.; Jepps, O.; Nicholson, D., Tractable molecular theory of transport of Lennard-Jones fluids in nanopores. *J. Chem. Phys.* **2004,** *120* (9), 4472-4485.

66. Bhatia, S. K.; Nicholson, D., Anomalous transport in molecularly confined spaces. *J. Chem. Phys.* **2007,** *127* (12), 124701.

67. Ebadi Amooghin, A.; Omidkhah, M.; Kargari, A., Enhanced CO_2 transport properties of membranes by embedding nano-porous zeolite particles into Matrimid 5218 matrix. *RSC Advances* **2015,** *5* (12), 8552-8565.

68. Lin, W.-H.; Vora, R. H.; Chung, T.-S., Gas transport properties of 6FDA-durene/1,4-phenylenediamine (pPDA) copolyimides. *J. Polym. Sci. B Polym. Phys.* **2000,** *38* (21), 2703-2713.

69. Jusoh, N.; Yeong, Y. F.; Lau, K. K.; M. Shariff, A., Enhanced gas separation performance using mixed matrix membranes containing zeolite T and 6FDA-durene polyimide. *J. Membr. Sci.* **2017,** *525*, 175-186.

70. Nafisi, V.; Hägg, M.-B., Gas separation properties of ZIF-8/6FDA-durene diamine mixed matrix membrane. *Separation and Purification Technology* **2014,** *128*, 31-38.

71. Japip, S.; Wang, H.; Xiao, Y.; Shung Chung, T., Highly permeable zeolitic imidazolate framework (ZIF)-71 nano-particles enhanced polyimide membranes for gas separation. *Journal of Membrane Science* **2014,** *467*, 162-174.

72. Jusoh, N.; Yeong, Y. F.; Lau, K. K.; M. Shariff, A., Fabrication of silanated zeolite T/6FDA-durene composite membranes for CO2/CH4 separation. *J. Clean. Prod.* **2017,** *166*, 1043-1058.

73. Lin, R.; Ge, L.; Liu, S.; Rudolph, V.; Zhu, Z., Mixed-Matrix Membranes with Metal–Organic Framework-Decorated CNT Fillers for Efficient CO2 Separation. *ACS Appl. Mater. Interfaces* **2015,** *7* (27), 14750-14757.

74. Cheng, S.-X.; Chung, T.-S.; Wang, R.; Vora, R. H., Gas-sorption properties of 6FDA–durene/1,4-phenylenediamine (pPDA) and 6FDA–durene/1,3-phenylenediamine (mPDA) copolyimides. *J. Appl. Polym. Sci.* **2003,** *90* (8), 2187-2193.

75. Japip, S.; Wang, H.; Xiao, Y.; Shung Chung, T., Highly permeable zeolitic imidazolate framework (ZIF)-71 nano-particles enhanced polyimide membranes for gas separation. *J. Membr. Sci.* **2014,** *467*, 162-174.

Chapter 5 Multi-component Gas Transport in a Polymer Membrane

The content of this chapter is published as:

Ravi C. Dutta and SK. Bhatia, Atomistic Investigation of Mixed-Gas Separation in a Fluorinated Polyimide Membrane, *ACS Appl. Polym. Mater.*, 16,1359 (2019)

Contributor	Statement of contribution
Ravi C Dutta	Programmed and conducted simulations (100%) Analysis and interpretation of data (80%) Wrote the paper (80%)
Suresh K. Bhatia	Wrote the paper (20%) Analysis and interpretation of data (20%)

5.1 Introduction

Screening of membrane materials for a given application is often based on pure component data; however, the performance of a membrane for the separation of a given gas pair in mixed gas conditions can differ significantly from that of pure gas conditions, due to competitive sorption as well as plasticization/swelling behavior of the polymer.[1-6] In addition, the driving force for diffusion of a species in a mixture is not only provided by the gradient of the chemical potential of that particular component, but also by the gradient in the chemical potential of the other components.[7, 8] An understanding of mixture transport is therefore critical to gas separation processes.

The transport behavior of a species in a multicomponent environment can be described using several equivalent mathematical expressions.[7-10] The Onsager formalism, considering chemical potential gradient ($-\nabla\mu$) as driving force, provides a fundamental approach based on irreversible thermodynamics, in which the flux (N_i) is expressed as:

$$N_i = \sum_j L_{ij}(-\nabla\mu_j) \tag{5-1}$$

where L_{ij} is the symmetric matrix of Onsager transport coefficients. An equivalent mathematical expression based on concentration gradient (∇c) as driving force, the generalized Fick's law, can be written as,[8]

$$N_i = \sum_j D_{ij}.(-\nabla c_j) \tag{5-2}$$

where D_{ij} is the multicomponent Fickian diffusion coefficient and can take both positive and negative values. Further, the cross coefficients are typically not equivalent *i.e.* $D_{ij} \neq D_{ji}$. A more convenient approach, often used to represent multicomponent transport in membrane materials, the Maxwell-Stefan (MS) formalism, considers a balance between chemical potential gradient and frictional force experienced by a species *i* with the other species in the mixture, and is expressed as:

$$-\frac{1}{RT}\nabla\mu_i = \sum_{\substack{j=1 \\ j\neq i}}^{n} \frac{x_j(u_i - u_j)}{Đ_{ij}} + \frac{u_i}{Đ_i};\ i = 1, 2, \ldots n; \tag{5-3}$$

where u_i and u_j are the average velocities of species *i* and *j* respectively, *R* is the universal gas constant, and *T* is temperature. $Đ_{ij}$ represents the interaction between species *i* and *j* in the mixture and $Đ_i$ is the MS diffusivity of species *i*. Further, the Onsager reciprocal relations demand

$$Đ_{ij} = Đ_{ji} \tag{5-4}$$

We note that the Fick formulation can be re-written in terms of the Onsager or MS formulations with the help of isotherms relating chemical potential gradients and concentration gradients.[9]

Pure and mixed gas permeation through polymeric membranes has been extensively investigated experimentally. Most of these investigations determine diffusion coefficients of a species by considering the driving force as the concentration gradient of that species only.[1, 3, 11-13] The correlations between the species can be evidenced experimentally from PFG-NMR studies, [14, 15] but this does not provide any quantitative information regarding the exchange coefficients ($Đ_{ij}$). Further, in mixed gas conditions, the matrix of diffusivities depends on the concentrations of all the diffusing species, and its experimental characterization is therefore challenging and not straightforward. On the other hand, atomistic simulations can aid in extracting these correlations and can play an important role as a complement to experiments. Krishna et al.[8, 15-20] extensively investigated mixture diffusion in inorganic membrane materials such as zeolites and found that correlation effects are strong functions of pore concentration, topologies and nature of the mixture. Recently, Krishna[21] analyzed literature experimental data and reported that cross correlations between the diffusing species are extremely significant in polymer membranes. However, there is scant information regarding the correlations between mixture gas molecules, and to the best our knowledge extensive simulations of mixture transport in polymer membrane materials are yet to be reported. In the literature, investigations have been largely devoted to pure component systems.[22-25] While some work on O_2/N_2 mixture diffusion in a 6FDA-6FpDA polyimide membrane has been reported,[26] the analysis is based on a Fickian interpretation of the transient gas uptake using MD, and the binary nature of the transport remains to be addressed.

On the other hand, gas sorption characteristics of glassy polymers in pure and mixed gas conditions has been extensively studied experimentally,[4-6, 27-32] and it has been found that the solubility selectivity is of great importance in determining the overall performance of the membrane. In addition, it has been found that solubility in mixed gas conditions can be significantly different from that in pure gas conditions due to competitive sorption.[4-6] For instance, a decrease in CH_4 sorption without affecting CO_2 sorption has been reported in a PTMSP membrane,[5] while decrease in sorption of both CH_4 and CO_2 in a PIM-1 membrane in mixed gas conditions compared to pure gas conditions has been found.[6] Thus, solubility selectivity in mixed gas conditions is affected not only by competitive sorption but also by the nature of polymer network. Further, to complement experimental investigations, mixture sorption in polymers has been predicted from pure component data,[33, 34] by applying ideal adsorbed solution theory (IAST)[35] that has been reported to be accurate for inorganic membrane materials. However, the validity of the predictions in polymers is unclear due the inherent assumptions on which this theory was developed, such as a rigid host matrix. Additionally, sophisticated techniques such as nonequilibrium thermodynamics of glassy polymers (NET-GP)[36-38] can be applied to determine the sorption characteristics in a glassy polymer in both pure and mixed gas conditions, however, this model requires the knowledge of volume dilation in the glassy polymer matrix upon gas sorption.

On the other hand, interest in the *in-silico* investigations of gas sorption in polymers considering the structural transition upon gas sorption is relatively recent.[39-43] Velioğlu et al. reproduced the plasticization behavior of various polyimides within an order of magnitude by employing sorption-relaxation cycles. Pandiyan et al.[44] studied the sorption and desorption of CO_2 in a variety of fluorinated polyimides, and found significant and homogeneous swelling during the sorption. Hölck et al.[41] studied the sorption behavior of gases in a glassy polymer under conditions leading to maximum and no swelling of the polymer, and proposed a model to describe the gas sorption based on linear combination of the corresponding isotherms, that was in agreement with their experimental results. Further, we note that the accuracy of these predictions depends on the adequacy of the forcefield employed to represent the polymer. It has been found that gas solubility determined through a united atom approach can be an order of magnitude higher than that determined through all-atom model.[45] Further, our recent simulations considering the structural transition and redistribution of voids upon gas sorption in BPDA-APB polyimide[46] offer a more accurate alternative for the single component case, but have yet to be extended for mixtures. Here, GCMC simulations coupled with EMD simulations in an isobaric ensemble is implemented to determine the gas sorption isotherms in mixed gas conditions.

In this chapter, we investigate the mixed gas transport properties of CO_2 and CH_4 in a 6FDA-durene polyimide polymer membrane, by extracting MS diffusivities through EMD simulations. In addition, the membrane performance in practical scenarios is predicted by solving the MS equations for a given membrane thickness and driving force, from the simulation based microscopic diffusivities and sorption characteristics.

5.2 Model system and simulations

5.2.1 MS diffusion coefficients

For a binary mixture, by recasting eq (5-3), the MS equations can be written as,

$$-\frac{c_1}{RT}\nabla\mu_1 = \frac{x_2N_1 - x_1N_2}{Đ_{12}} + \frac{N_1}{Đ_1} \tag{5-5}$$

$$-\frac{c_2}{RT}\nabla\mu_2 = \frac{x_1N_2 - x_2N_1}{Đ_{12}} + \frac{N_2}{Đ_2} \tag{5-6}$$

where c_1 and c_2 are the concentration of species *1* and *2* and x_1 and x_2 are the mole fraction of species *1* and *2* respectively. To compute the mixture MS diffusion coefficients ($Đ_1$, $Đ_2$ and $Đ_{12}$) at any given concentration of both the species it is expedient to first determine Onsager coefficients from EMD simulation, and then use the equivalence of MS formalism and Onsager formalism.[1,7] The matrix of Onsager coefficients [L_{ij}], is readily obtained from EMD simulations, following:[7, 57]

$$L_{ij} = \frac{N_i N_j}{6Vk_B T} \lim_{t\to\infty} \frac{1}{t} < [\vec{r}_i(t) - \vec{r}_i(0)].[\vec{r}_j(t) - \vec{r}_j(0)] > \tag{5-7}$$

where $r_i(t)$ is center of mass position vector of molecule i at time t, V is volume, k_B is Boltzmann constant, N_i is number of molecules of type i and T is temperature. The MS diffusivities are related to Onsager coefficients following:

Upon recasting eq (5-5) and eq (5-6), the MS equations can be re-written as:

$$\nabla(-\mu_1) = \frac{RT}{c_1}\left[\frac{1}{Đ_1} + \frac{x_2}{Đ_{12}}\right]N_1 - \left[\frac{RT}{c_1}.\frac{x_1}{Đ_{12}}\right]N_2 \tag{5-7}$$

$$\nabla(-\mu_2) = \frac{RT}{c_2}\left[\frac{1}{Đ_2} + \frac{x_1}{Đ_{12}}\right]N_2 - \left[\frac{RT}{c_2}.\frac{x_2}{Đ_{12}}\right]N_1 \tag{5-8}$$

Further, the Onsager formalism eq (5-1) for a binary mixture can be written as:

$$N_1 = L_{11}\nabla(-\mu_1) + L_{12}\nabla(-\mu_2) \tag{5-10}$$

$$N_2 = L_{21}\nabla(-\mu_1) + L_{22}\nabla(-\mu_2) \tag{5-11}$$

and upon rearranging eq (5-10) and (5-11):

$$N_1 = \left(\frac{\Delta}{L_{22}}\right)\nabla(-\mu_1) + \left(\frac{L_{12}}{L_{22}}\right)N_2 \tag{5-12}$$

$$\text{where } \Delta = L_{11}L_{22} - L_{12}L_{21} \tag{5-13}$$

Comparing eq (5-7) and (5-12) yields

$$\frac{RT}{c_1}.\frac{x_1}{Đ_{12}}=\left(\frac{L_{12}}{\Delta}\right)=>Đ_{12}=\frac{RT}{c_1}.\frac{x_1.\Delta}{L_{12}} \tag{5-14}$$

$$\frac{RT}{c_1}\left[\frac{1}{Đ_1}+\frac{x_2}{Đ_{12}}\right]=\left(\frac{L_{22}}{\Delta}\right)=>Đ_1=\frac{1}{\frac{L_{22}.c_1}{\Delta.R.T}-\frac{x_2}{Đ_{12}}} \tag{5-15}$$

Similarly,

$$Đ_2=\frac{1}{\frac{L_{11}.c_2}{\Delta.R.T}-\frac{x_1}{Đ_{12}}} \tag{5-16}$$

where $\Delta = L_{11}L_{22} - L_{12}L_{21}$, c_1 is concentration of species 1, c_T is the total gas concentration the polymer *i.e.* $c_T = c_1 + c_2$, and x_1 is mole fraction of specie1, where $x_1 = \frac{c_1}{c_T}$. Thus, the determination of MS diffusivities is exact and does not rely on any empirical relation between mixture and pure component diffusivities.

5.2.2 Membrane modelling:

The actual membrane behavior is predicted by numerically computing the steady state fluxes after a step change in the pressure, by simultaneously solving the ODEs.

$$-\frac{c_1}{P_1}\frac{dP_1}{dz}=\frac{x_2N_1-x_1N_2}{Đ_{12}}+\frac{N_1}{Đ_1} \tag{5-17}$$

$$-\frac{c_2}{P_2}\frac{dP_2}{dz}=\frac{x_1N_2-x_2N_1}{Đ_{12}}+\frac{N_2}{Đ_2} \tag{5-18}$$

$$\nabla.N_i = 0 \qquad \text{where } i=1,2; \tag{5-19}$$

Here the local diffusivities at any position are dependent on the local compositions as determined from simulations. To aid in the integrations the simulation-based MS diffusivities were fitted by an empirical expression, as discussed in Section 3.4. All the calculations were performed on a membrane of finite thickness (δ = 30 µm), with no interfacial mass transfer resistance,[50]and maintaining the downstream at constant partial pressure (p_i =1 atm, i=1,2) with the boundary conditions shown in Figure 5-1. It is assumed that the gas phase, on both upstream and downstream sides of the membrane, consist of an equimolar mixture of CO_2 and CH_4.

Boundary conditions: upstream conditions (at $z = 0$): $p_i = p_0$, $x_1 = x_{1,0}$, $x_2 = x_{2,0}$;

downstream conditions (at $z = \delta$): $p_i = p_\delta$, $x_1 = x_{1,\delta}$, $x_2 = x_{2,\delta}$;

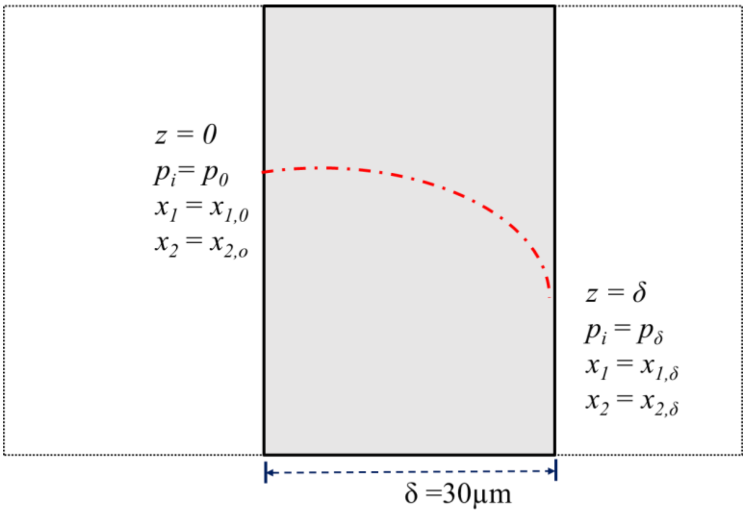

Figure 5-1: Schematic illustration of the 6FDA-durene polymer membrane.

5.3 Results and discussions:

5.3.1 Mixed gas sorption isotherms

The sorption behavior of gases in 6FDA-durene polyimide polymer membrane in mixed gas conditions was systematically investigated by considering an equimolar (1:1) mixture of CO_2 and CH_4. Figure 5-2 depicts the sorption isotherms of an equimolar mixture of CO_2 and CH_4 in 6FDA-durene polymer membrane at 300 K. We note that the individual gas sorption capacity in the mixed gas conditions is lower than the corresponding gas sorption capacity in pure gas conditions at any partial pressure, indicating competitive sorption is inhibiting gas sorption to an extent. This effect is more significant to methane as CO_2 sorption is independent of the presence of methane at lower pressures and has little influence at higher pressures, while methane sorption is significantly influenced by the presence of CO_2 at all pressures investigated in this study. This can be attributed to the preferential sorption of CO_2 in the available Langmuir sites. Since the number of Langmuir sites are fixed, both the gases compete to occupy them and more condensable gases have high affinity for the Langmuir sites. Thus, CO_2 being more condensable than CH_4, occupies most of the Langmuir sites and the presence of CO_2 reduces the sorption of methane.

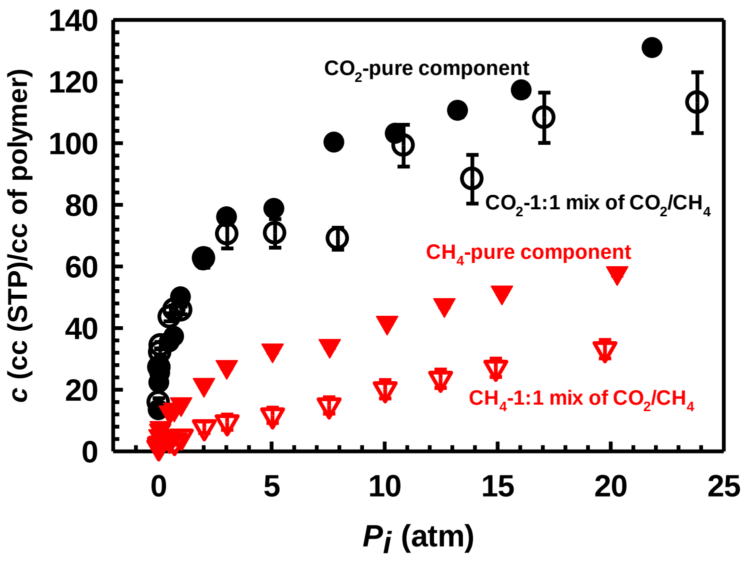

Figure 5-2: A comparison of sorption isotherms of pure component and equimolar mixture of CO_2 and CH_4 in 6FDA-durene at T = 300 K.

Similar plots for sorption isotherms of equimolar mixture of CO_2 and CH_4 in 6FDA-durene polymer membrane in the range 300-500 K, are shown in Figure 5-3. Further, the error bars in Figure 5-3 can be reduced by considering more steps in GCMC simulations; this requires additional computational time but has negligible effect on the mean value reported in this study.

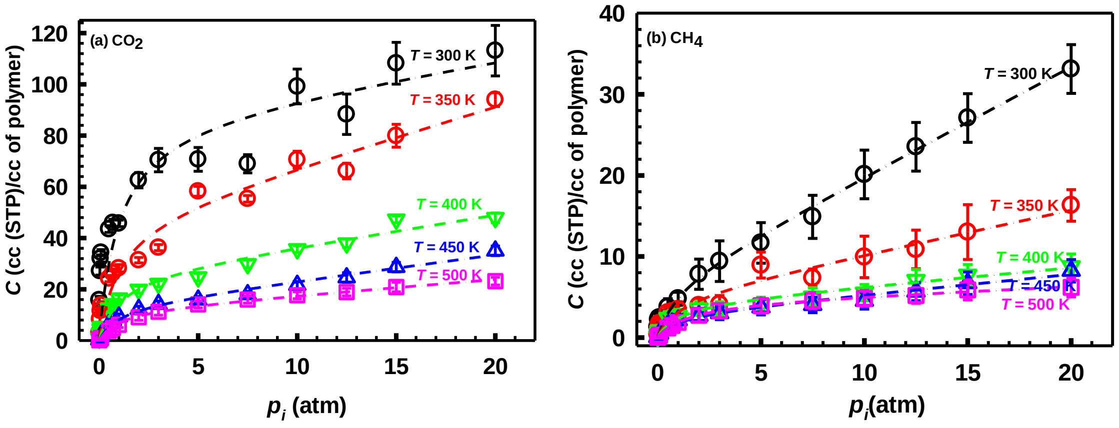

Figure 5-3:Sorption isotherms for equimolar mixture for equimolar CO_2/CH_4 mixture in 6FDA-durene polymer membrane at various temperatures. (a) CO_2, and (b) CH_4.

Figure 5-4 depicts a comparison of the temperature dependence of solubility coefficients under pure and mixed gas conditions for CO_2 and CH_4 in 6FDA-durene polymer membrane at 2 atm pressure. The calculated values of solubility coefficient of CO_2 and CH_4 at 300 K in pure gas conditions are 33 (± 2.0) and 10.9 (± 1.0) cc (STP)/cc (polym).atm, in good agreement with experimental values of 25

(± 3.0) and 8.2 (±1.7) cc (STP)/cc (polym).atm, respectively.[65, 66] The solubility selectivity of CO_2 over CH_4 is found to be 3.0 (±0.2), in excellent agreement with an experimental values of 3.0-3.5.[65, 66] On the other hand, the gas solubility under mixed gas conditions is lower than the corresponding gas solubility in pure gas conditions. The calculated values of solubility coefficient of CO_2 and CH_4 at 300 K in mixed gas conditions are 31 (± 2.0) and 3.9 (± 0.5) cc (STP) / cc (polym). atm, respectively.

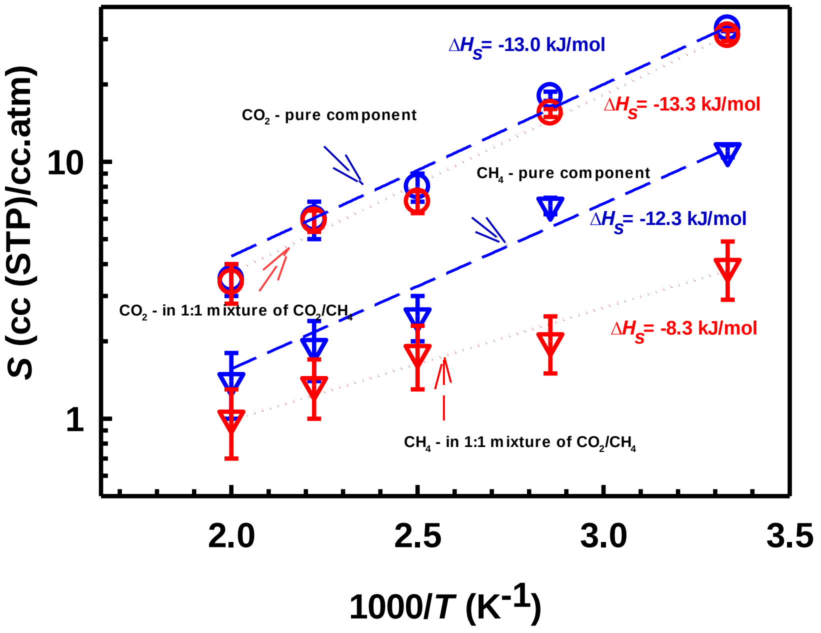

Figure 5-4: Temperature dependence of solubility coefficients of CO_2 and CH_4 in 6FDA-durene at 2 atm pressure in pure and mixed gas conditions.

Here we note that 6FDA-durene membrane solubility selectivity for CO_2 over CH_4 is found to be significantly higher in mixed gas conditions (7.95 (±0.2)) than that of pure gas conditions. This can be attributed to competitive sorption, where a sharp decrease in methane solubility and thus increase in solubility selectivity for CO_2/CH_4 in mixed gas conditions is observed, as shown in Figure 5-5. We note that, gas solubility in mixed gas conditions up to 4.5 times higher than pure gas conditions has also been reported experimentally for CO_2/CH_4 mixtures.[28] In addition, it is seen that gas sorption capacity of the polymer decreases with increase in temperature leading to decrease in gas solubility of both the gases with increase in temperature, following the van't Hoff relation,

$$S = S_0 e^{\frac{-\Delta H_s}{RT}} \tag{5-20}$$

where S_0 is a constant, R is the gas constant, ΔH_s is apparent heat of solution and T is the temperature. Similar values of heat of solution for CO_2 in 6FDA-durene membrane in pure and mixed gas conditions (-13.0 (±1) and -13.3 (±1) kJ/mol respectively) are observed, while a decrease in heat of sorption in mixed gas conditions is observed for methane, due to less effective packing of methane molecules in the presence of CO_2. Further, the narrower, more strongly adsorbing sites are more likely to be filled by CO_2, leaving the predominantly larger sites for CH_4 in the mixed gas. We further note that negative values of ΔH_s demonstrate the exothermic nature of the sorption process.

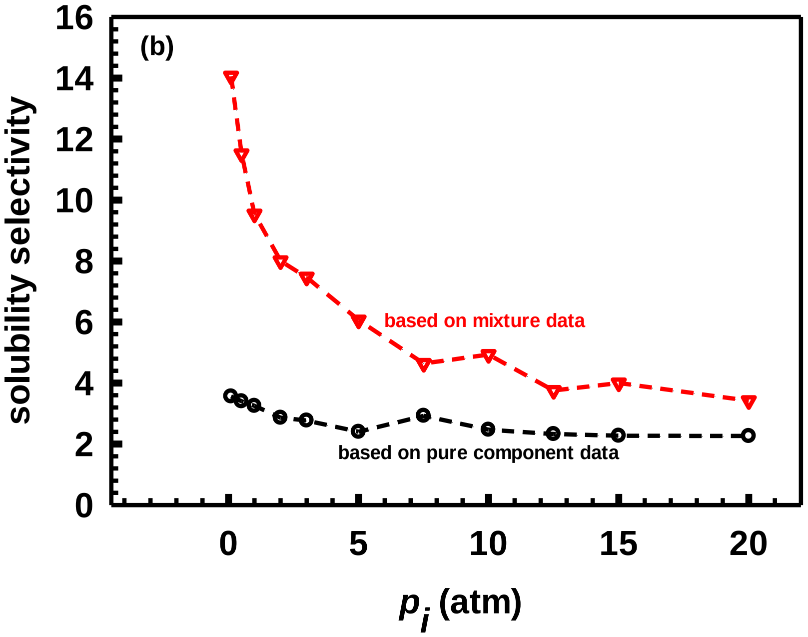

Figure 5-5:A comparison of solubility selectivity of pure component and equimolar mixture of CO_2 and CH_4 in 6FDA-durene at T = 300 K. Dotted lines are given as guide for the eye.

5.3.2 Comparison of simulated sorption isotherms with IAST predictions

The sorption behavior of gases in mixed gas conditions can be estimated from pure component sorption data using ideal adsorption solution theory (IAST) or DMS model for mixed gases. We note that parameters b_1 and b_2 are based on pure component sorption data to predict mixed gas sorption in accordance with the DMS model for pure component data. Further, we have used these fitting parameters to solve the IAST model equations, and the resulting mole fraction of gas molecules in the adsorbed phase is depicted in Figure 5-7 (a). A comparison of simulated sorption isotherms of an equimolar mixture of CO_2, and CH_4 in 6FDA-durene polymer membrane at 300 K with the predictions of both IAST and DMS model for mixed gases is depicted in Figure 5-6 (a) and (b), respectively. It is seen that for the more strongly absorbed CO_2 the predictions of both IAST and the DMS model for mixed gases are consistent with the simulation results, while significantly large deviation between the theories and simulation results is observed for methane. This is because the swelling of the polymer in mixed gas conditions is similar to that in the presence of pure CO_2, this being the more dominant species. While IAST under predicts, the DMS model for mixed gases over predicts the sorption of methane in mixed gas conditions compared to the simulation results. On the other hand, in a recent investigation by Rizzuto et al.[31] good agreement between GCMC simulations and IAST predictions is reported for the sorption of CO_2/N_2 mixtures in thermally rearranged polybenzolxazole, for which much less swelling is expected. The discrepancy with simulation for methane underscores the importance of accounting for structural changes in the polymer due to the presence of partner species, i.e. CO_2 in this case; since the system violates the hypothesis on which these theories were developed, that the adsorbing framework is inert from a thermodynamic point of view. Thus, it is seen that IAST calculations over predict the solubility selectivity of a polymer membrane, while DMS for mixed gases under predicts the solubility selectivity of a polymer membrane, in mixed gas conditions, as shown in Figure 5-7 (b). Further, we note that the error involved in the IAST predictions for methane sorption in 6FDA-durene membrane in mixed gas conditions is as high as 50%, compared to our simulation predictions, as depicted in Figure 5-7 (c).

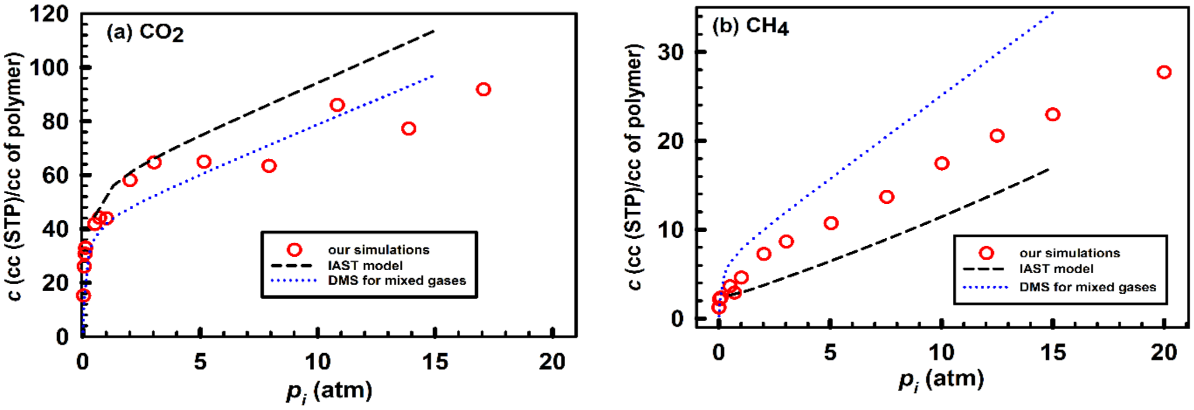

Figure 5-6:Comparison of simulated sorption isotherms of equimolar mixture (a) CO_2, and (b) CH_4 in 6FDA-durene at T = 300 K with the predictions of IAST and DMS model for mixed gases.

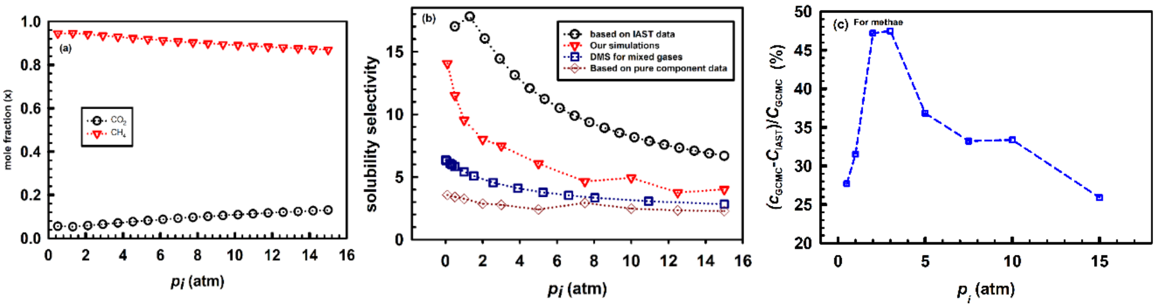

Figure 5-7:Pressure variation of (a) mole fraction of CO_2 and CH_4 in the adsorbed phased, in mixed gas conditions, based on IAST calculations, (b) comparison of solubility selectivity of equimolar mixture of CO_2 and CH_4 in 6FDA-durene membrane at T = 300 K, and (c) error involved in IAST

predictions for methane sorption in 6FDA-durene membrane, in mixed gas conditions. Dotted lines are given as guide for the eye.

5.3.3 Determination of Onsager coefficients

To investigate the diffusion behavior of gases in mixed gas conditions, Onsager coefficients of an equimolar mixture of CO_2/CH_4 were determined using eq (5-7). Figure 5-8 (a) depicts the variation of Onsager coefficients with pressure in a 6FDA-durene polymer membrane at 300 K. It is seen that the diagonal Onsager coefficients L_{12} (= L_{21}) are much smaller than L_{11}, but comparable to L_{22} at low pressures, while the diagonal and off diagonal elements of matrix [L] are of the same order at high pressures. Figure 5-8 (b) depicts the variation of Onsager coefficients with temperature in the 6FDA-durene polymer membrane at a total pressure of 4 atm. It is seen that the diagonal Onsager coefficients L_{12} (= L_{21}) and L_{22} are quite similar to each other at all temperatures while L_{11} is an order of magnitude higher than L_{12} at low temperatures, and of the same order at high temperatures. Further, the influence of these correlations on each of the species cannot be determined from the Onsager coefficients, as these correlations influence all elements in the Onsager coefficients matrix.[9] However, the extent of coupling between the diffusing species can be determined from the Onsager coefficients.

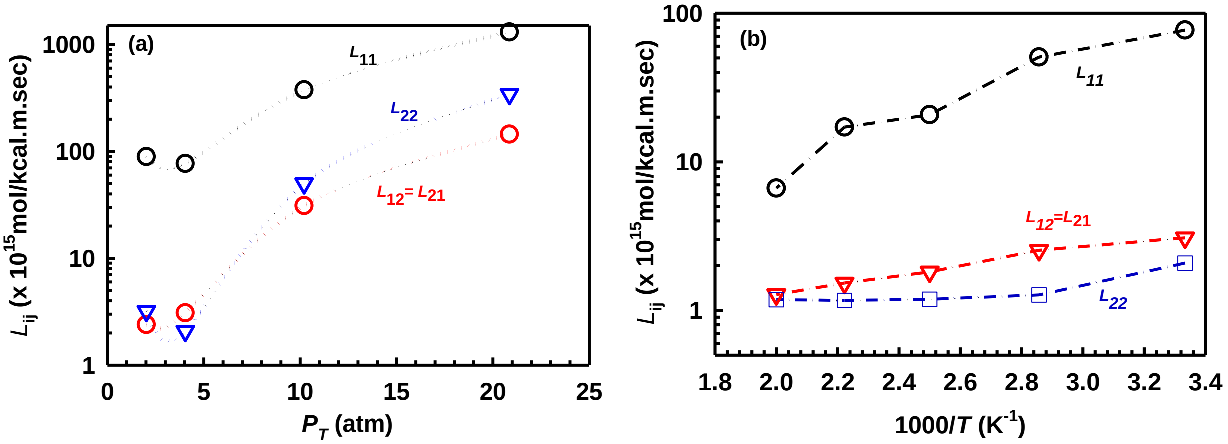

Figure 5-8:Variation of Onsager coefficients of an equimolar mixture of CO_2/CH_4 in 6FDA-durene membrane with (a) pressure at T = 300 K, and (b) with temperature at p_T=4 atm

The extent of coupling can be determined by computing an interaction parameter (λ), following:

$$\lambda = \frac{L_{12}}{\sqrt{L_{11} \cdot L_{22}}} \tag{5-21}$$

Strong correlation between the diffusing species results in $L_{12} = \sqrt{L_{11}L_{22}}$, with $\lambda = 1$. On the other hand, weak correlation between the diffusing species, corresponding to L12 → 0, results in $\lambda = 0$. In all other cases with finite correlations, depending on loading and nature of the adsorbate and adsorbent, λ takes a value between 0 and 1.18 It is seen that the well known relation between Onsager coefficients, $L_{12} = \sqrt{L_{11}L_{22}}$, does not hold for the equimolar mixture of CO_2 and CH_4 in 6FDA –durene polymer membrane, as depicted in Figure 5-9 (a), indicating the presence of weak or finite correlations between the diffusing species in the polymer membrane. Similar behavior is also observed in MFI zeolite that has 3-dimensional pore network with finite exchange correlations.[16] We note that that the Onsager coefficients always satisfy the relation $L_{11}L_{22} > L_{12}L_{21}$,[70] indicating the computed MS diffusivities from Onsager coefficients will only have a positive value. Figure 5-9 (b) depicts the variation of λ with temperature. At 300 K, the λ value is found to be 0.25, indicating the presence of finite correlation between the diffusing species in the polymer membrane, and this interaction parameter increases with increase in temperature, due to increase in CH4 mole fraction and gas diffusivity with temperature arising from the swelling behavior of the polymer. An initial increase in λ with increase in pressure is observed, followed by slight decrease with increase in pressure after 5 atm, as depicted in the inset of Figure 5-9 (b). It is expected that the degree of correlation between the species increases with increase in loading;[14] however, we note that the more fraction of the gases in the polymer membrane may decrease or increase with pressure, and that influences the behavior of λ with pressure.

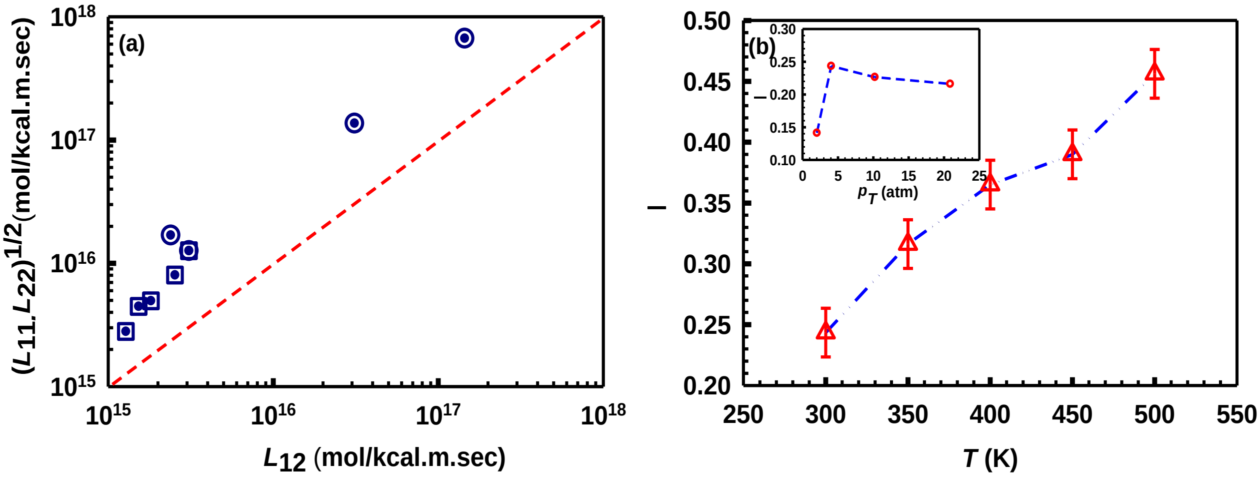

Figure 5-9: (a) Comparison between L_{12} and   in 6FDA-durene polymer, and (b) variation of interaction with parameter (λ) with temperature. Variation of (λ) with pressure at T =300K is shown in the inset.

5.3.4 Determination of MS diffusivities

The above findings indicate that gas diffusion behavior in the mixture can be different to that of the pure components due to the finite correlations that exists between the diffusing species; however, the effect of this correlation on individual species is unclear. The general understanding is that these correlations decrease the mobility of more mobile species and increase the diffusivity of slower species. To investigate this correlation effect on each of the species, the MS diffusivities were determined using eq (14)-(16), with the required Onsager coefficients obtained from our molecular dynamics simulations, following eq (5-7). Figure 5-10 (a) depicts the loading dependency of the MS diffusivities of an equimolar CO_2/CH_4 mixture. It is interesting to note that at high pressures 6FDA-durene membrane is diffusive selective for methane, in contrast to pure gas conditions where this membrane is diffusive selective for CO_2 at all pressures studied in this work at T= 300 K. This is because, at high pressures, the availability of larger FVEs in the polymer promotes methane diffusion, this being a lighter and more weakly adsorbed molecule. We note that similar behavior where membrane is diffusive selective for CO_2 in pure gas conditions, but selective for methane in mixed gas conditions has been observed experimentally in a poly(ethylene oxide) based multi-block copolymer membrane.[11] Further, significant increase in CH_4 diffusivity due to CO_2-induced plasticization has been experimentally reported in Nafion[25] and poly(dimethylsiloxane) [10] membranes. It is seen that $Đ_1$, $Đ_2$ and $Đ_{12}$ are of the same order, further confirming the presence of finite degree of correlations between the diffusing species. Further, the degree of correlation is defined as $\frac{Đ_i}{Đ_{ij}}$, and $\frac{Đ_i}{Đ_{ij}}$ <<1 and $\frac{Đ_i}{Đ_{ij}}$ >>1 are the two limiting scenarios that represent very weak and strong correlations between the diffusing species, respectively. For CO_2, the degree of correlation, decreases with pressure, while it increases with pressure for CH_4 as shown the inset of Figure 5-10 (a). This is due to the fact that correlation effects are more significant to the more mobile species than for the slower species as the latter vacates the sites less frequently. Figure 5-10 (b) depicts the temperature dependency of MS diffusivities of an equimolar mixture of CO_2 and CH_4. It is seen that membrane is diffusive selective for CO_2 over CH_4 at all temperatures. Further, the degree of correlation for both the gases increases with increase in temperature, and this can be attributed to increase in CH_4 mole fraction in the mixture with temperature as shown in Figure 5-11. Further, the swelling behavior of the polymer with temperature can lead to opening up of the pore mouths, resulting in gas-gas interactions increasing in significance compared to gas-polymer interactions. Further, it is seen that $Đ_1$, $Đ_2$ and $Đ_{12}$ increase with increase in temperature following Arrhenius type behavior, with activation energies 4.9 (± 1), 7.1 (± 2) and 3.7 (± 0.5) kJ/mol, respectively. We note that CO_2 has the same activation energy in pure and mixed gas conditions, while a decrease in activation energy is observed for methane in mixed gas condition. This can be attributed to the availability of larger FVEs in the polymer in mixed gas conditions, leading to increase in methane diffusivity compared to the pure component value at low temperatures. As expected, the values of the degree of correlation for CO_2 are larger than those for methane as shown in inset of Figure 5-10 (b), due to the smaller size of the former.

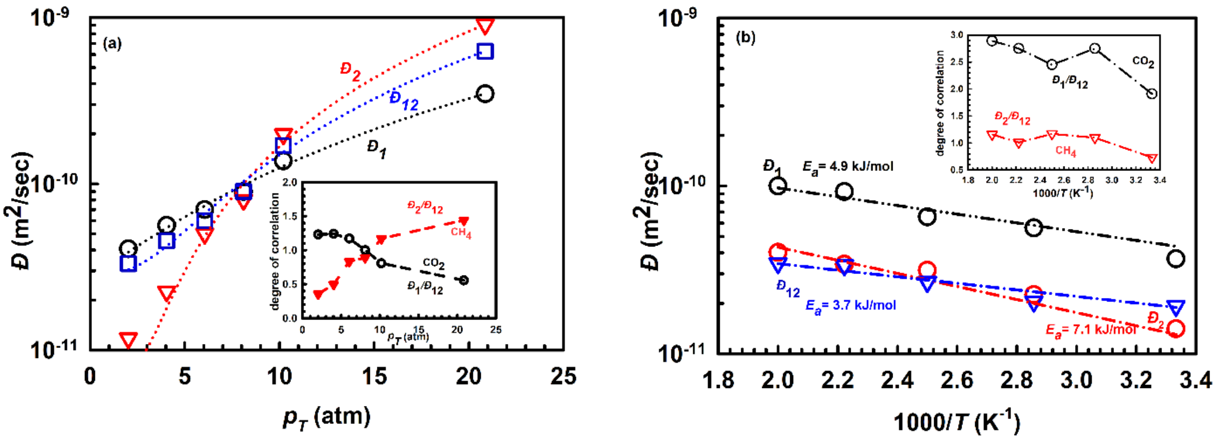

Figure 5-10: Variation of MS diffusivities in an equimolar mixture of CO2/CH4 in 6FDA-durene with (a) pressure at T = 300 K, and (b) with temperature at $p_i = 2$ atm.

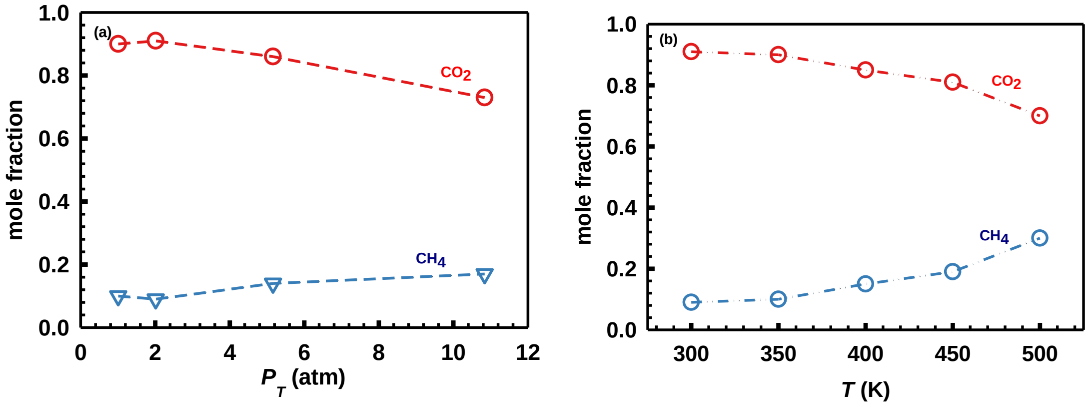

Figure 5-11: Variation of mole fraction of CO2 and CH4 in mixture with (a) pressure, and (b) temperature.

5.3.5 Determination of molar flux across a membrane

To understand the gas separation characteristics of a 6FDA-durene membrane in practical scenarios, from our EMD data, we determined the molar fluxes across the membrane by solving MS equations for a given membrane thickness considering the pressure gradient as driving force. In these calculations we assumed an equimolar mixture on both the feed and permeate sides, and the flow was driven by a pressure difference. Further, to solve the MS equations in mixed gas conditions, the reported MS diffusivities ($Đ_1$, $Đ_2$ and $Đ_{12}$) were fit to an empirical equation as a function of partial pressures using a polynomial of the form,

$$Đ_i = a_0 + a_1 p_i + a_2 p_j + a_3 p_i p_j \tag{5-22}$$

This simplified method was chosen as the diffusivities have been determined from simulation as a function of pressure for an equimolar bulk mixture. This estimation of diffusivities is somewhat approximate as the individual pseudo-bulk partial pressures do not remain equal throughout the membrane; however, our calculations showed the difference in partial pressures to be small. Figure 5-12 depicts the pressure profiles of CO_2 and CH_4 in the membrane for various feed pressures.

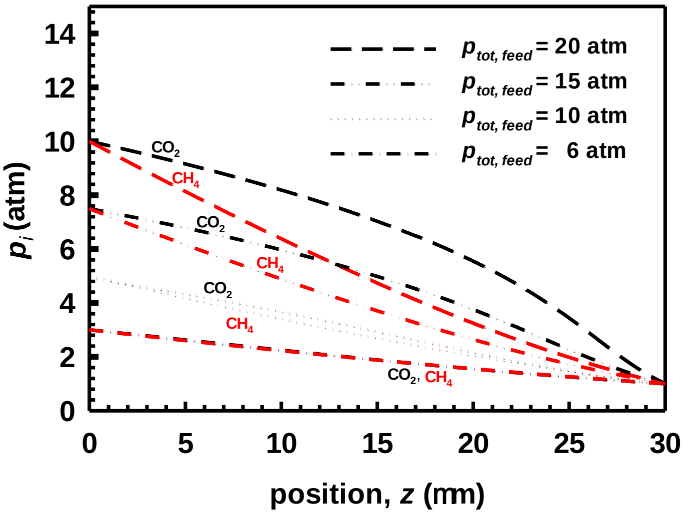

Figure 5-12:Variation of partial pressure of CO_2 and CH_4 in the membrane with position.

It is seen that the partial of pressure of the both the gases are equal at any point of the membrane up to a total pressure of 10 atm, for which use of the diffusion and sorption data determined from our simulations for an equimolar mixture is exact. However, at very high feed pressure, the partial pressures of both the gases can vary up to 30%, and more accurate calculations would entail simulations covering a range of gas mixture compositions.[71,72] For the present purpose, where we are seeking the trend of the selectivity with feed pressure the simplified method adopted suffices. Figure 5-13 depicts the predicted variation of membranes perm-selectivity for CO_2 over CH_4 with feed gas pressure in an equimolar mixture, as well as the corresponding results for the case of pure gas conditions. In mixed-gas conditions, membranes perm-selectivity for CO_2 decreases with increase in feed gas pressure, in contrast to that for pure gas conditions, where an increase in perm-selectivity with increase in feed gas pressure is observed. This can be attributed to the availability of larger FVEs in the polymer membrane due to its swelling behavior which is substantial in the presence of CO_2, leading to an increase in methane diffusivity, this being a lighter and weakly adsorbing molecule. This decrease in perm-selectivity in mixed gas conditions with increase feed gas pressure, as opposed to pure gas conditions, due to plasticization has also been observed experimentally in other polymer membranes. Further, we note that the discrepancy in the perm-selectivity's are evident even below the plasticization pressure, however, this discrepancy is significant after the plasticization pressure. This can be attributed to increase in the membrane's solubility selectivity due to competitive sorption being offset by decrease in diffusivity selectivity due to swelling of the polymer in the presence of CO_2, resulting in an increase in CH_4 diffusivity – thereby decreasing the perm-selectivity of the membrane in mixed gas conditions. The predicted molar fluxes of the gases in pure and mixed gas conditions are summarized in Table 5-1.which indicates that the presence of methane has little influence on the CO_2 permeability in mixed gas conditions. The mixed gas CH_4 permeability, however, shows very different behavior compared to their corresponding pure gas permeability. The foregoing results demonstrate that characterizing the membrane performance for a given application based on the pure component data can be deceptive, and a thorough understanding of membrane performance under realistic mixture operating conditions is indispensable.

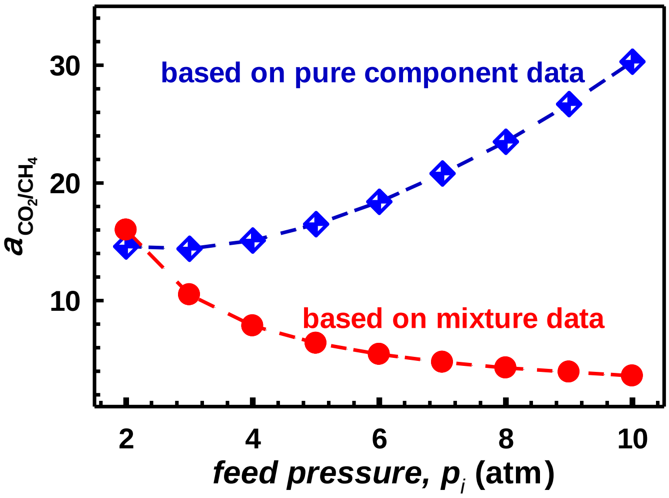

Figure 5-13: Comparison of variation CO_2/CH_4 perm-selectivity with feed pressure in 6FDA-durene polymer membrane, for pure and mixed gas conditions.

Table 5-1: Comparison of molar fluxes of CO_2 and CH_4 in pure and mixed gas conditions with the feed conditions.

$P_{i,feed}$ (atm)	pure gas conditions		mixed gas conditions	
	N_1	N_2	N_1	N_2
	(x 10^{10}moles/m^2. S)	(x 10^{10}moles/m^2. S)	(x 10^{10}moles/m^2. S)	(x 10^{10}moles/m^2. S)
2	21.54	1.48	23.30	1.46
4	55.02	3.63	64.49	8.22
6	99.67	5.41	133.98	24.69
8	165.0	7.03	248.89	58.21
10	258.31	8.53	334.97	92.96

5.4 Conclusions

The Maxwell-Stefan (MS) diffusivities of equimolar mixture of CO_2 and CH_4 in the temperature range of 300-500 K in 6FDA-durene polyimide polymer membrane have been investigated here, using equilibrium molecular dynamics simulations. The swelling behavior of the polymer upon gas sorption has been investigated, and a detailed study of CO_2 and CH_4 sorption in pure as well as mixed gas conditions in 6FDA-durene polymer membrane in the temperature range of 300 to 500 K presented. It is found that CO_2 is more soluble than CH_4 at all temperatures in a 6FDA-durene polymer membrane, and this solubility decreases with increase in temperature following the van't Hoff relation. In mixed gas conditions, a decrease in sorption capacity is observed for both the gases and this effect is more significant for methane, leading to an increase in solubility selectivity of CO_2 over CH_4. It is seen that a 6FDA-durene polymer membrane is selective for CO_2 over CH_4. In addition, the simulated sorption isotherms were compared with the predictions of IAST and dual mode sorption for mixed gases. It is seen that for CO_2 the simulation results are consistent with the predictions of both IAST and the dual mode sorption for mixed gases, while a large deviation between the theories and simulation results is observed for methane. While IAST under-predicts, the dual mode sorption for mixed gases over-predicts the sorption of methane in mixed gas conditions compared to the simulation results. The large discrepancy with simulation underscores the importance of accounting for structural changes in the polymer due to the presence of partner species, when predicting mixed gas isotherms.

Pure component diffusivities of CO_2 and CH_4 in 6FDA-durene polymer membrane are in the order of 10^{-10} -10^{-11} m^2/sec, and in good agreement with experimental reports. It is seen that the corrected diffusivities of the gases increase with increase in loading at 300 K, exhibiting a decrease in methane permeability with increase in pressure, due to swelling reducing sorption, while an increase in CO_2 permeability with increase in pressure occurs above 5 atm, the plasticization pressure of the polymer. In addition, corrected diffusivities of the gases in 6FDA-durene polymer membrane follow Arrhenius behavior with temperature, with diffusivity selectivity for CO_2 being greater than unity at all temperatures. The Onsager coefficients indicate that in mixed gas conditions, finite correlation exist between the diffusing species in the polymer membrane, and this correlation increases with increase in temperature. The MS diffusivities in the mixed gas conditions indicate that membrane's diffusivity selectivity for CO_2 is greater than unity at low pressures, while that for CH_4 is greater than unity at high pressures. It is also found that correlation effects are more significant to the more mobile species than for the slower species, and the degree of correlation increases with increase in temperature and is significant for CO_2 transport at all temperatures. An important aspect of this study is the prediction of membrane behavior in practical scenarios, from EMD data, by determining the steady state flux across a membrane resulting from a pressure difference, by numerically solving the MS equations. It was found that increased feed gas pressure in mixed-gas conditions reduces CO_2 perm-selectivity, while an increase in perm-selectivity with increase in feed gas pressure is observed in pure gas conditions. This can be attributed to the availability of larger FVEs in the polymer membrane due to its swelling behavior which is substantial in the presence of CO_2, leading to an increase in methane diffusivity, this being a lighter and more weakly adsorbing molecule.

5.5 References

1. Ribeiro, C. P.; Freeman, B. D.; Paul, D. R., Pure- and mixed-gas carbon dioxide/ethane permeability and diffusivity in a cross-linked poly(ethylene oxide) copolymer. *J. Membr. Sci.* **2011,** *377* (1), 110-123.

2. Tanis, I.; Brown, D.; Neyertz, S.; Heck, R.; Mercier, R.; Vaidya, M.; Ballaguet, J.-P., A comparison of pure and mixed-gas permeation of nitrogen and methane in 6FDA-based polyimides as studied by molecular dynamics simulations. *Comput. Mater. Sci* **2018,** *141*, 243-253.

3. Reijerkerk, S. R.; Nijmeijer, K.; Ribeiro, C. P.; Freeman, B. D.; Wessling, M., On the effects of plasticization in CO2/light gas separation using polymeric solubility selective membranes. *J. Membr. Sci.* **2011,** *367* (1), 33-44.

4. Gemeda, A. E.; De Angelis, M. G.; Du, N.; Li, N.; Guiver, M. D.; Sarti, G. C., Mixed gas sorption in glassy polymeric membranes. III. CO2/CH4 mixtures in a polymer of intrinsic microporosity (PIM-1): Effect of temperature. *J. Membr. Sci.* **2017,** *524*, 746-757.

5. Vopička, O.; De Angelis, M. G.; Sarti, G. C., Mixed gas sorption in glassy polymeric membranes: I. CO2/CH4 and n-C4/CH4 mixtures sorption in poly(1-trimethylsilyl-1-propyne) (PTMSP). *J. Membr. Sci.* **2014,** *449*, 97-108.

6. Vopička, O.; De Angelis, M. G.; Du, N.; Li, N.; Guiver, M. D.; Sarti, G. C., Mixed gas sorption in glassy polymeric membranes: II. CO2/CH4 mixtures in a polymer of intrinsic microporosity (PIM-1). *Journal of Membrane Science* **2014,** *459*, 264-276.

7. Sholl, D. S., Understanding Macroscopic Diffusion of Adsorbed Molecules in Crystalline Nanoporous Materials via Atomistic Simulations. *Acc. Chem. Res.* **2006,** *39* (6), 403-411.

8. Taylor, R.; Krishna, R., *Multicomponent Mass Transfer*. John Wiley & Sons, Inc.: New York, NY, 1993; Vol. 1, p 579.

9. Krishna, R., Describing the Diffusion of Guest Molecules Inside Porous Structures. *J. Phys. Chem. C* **2009,** *113* (46), 19756-19781.

10. Krishna, R.; van den Broeke, L. J. P., The Maxwell-Stefan description of mass transport across zeolite membranes. *Chem Eng J Biochem Eng J* **1995,** *57* (2), 155-162.

11. Raharjo, R. D.; Freeman, B. D.; Paul, D. R.; Sanders, E. S., Pure and mixed gas CH4 and n-C4H10 permeability and diffusivity in poly(1-trimethylsilyl-1-propyne). *Polymer* **2007,** *48* (25), 7329-7344.

12. Raharjo, R. D.; Freeman, B. D.; Paul, D. R.; Sarti, G. C.; Sanders, E. S., Pure and mixed gas CH4 and n-C4H10 permeability and diffusivity in poly(dimethylsiloxane). *J. Membr. Sci.* **2007,** *306* (1), 75-92.

13. Sadrzadeh, M.; Shahidi, K.; Mohammadi, T., Effect of operating parameters on pure and mixed gas permeation properties of a synthesized composite PDMS/PA membrane. *J. Membr. Sci.* **2009,** *342* (1), 327-340.

14. Fernandez, M.; Kärger, J.; Freude, D.; Pampel, A.; van Baten, J. M.; Krishna, R., Mixture diffusion in zeolites studied by MAS PFG NMR and molecular simulation. *Microporous Mesoporous Mater.* **2007,** *105* (1), 124-131.

15. Krishna, R.; van Baten, J. M., Maxwell–Stefan modeling of slowing-down effects in mixed gas permeation across porous membranes. *J. Membr. Sci.* **2011,** *383* (1), 289-300.

16. Krishna, R.; van Baten, J. M., Describing Mixture Diffusion in Microporous Materials under Conditions of Pore Saturation. *J. Phys. Chem. B* **2010,** *114* (26), 11557-11563.

17. Skoulidas, A. I.; Sholl, D. S.; Krishna, R., Correlation Effects in Diffusion of CH4/CF4 Mixtures in MFI Zeolite. A Study Linking MD Simulations with the Maxwell−Stefan Formulation. *Langmuir* **2003,** *19* (19), 7977-7988.

18. Krishna, R.; van Baten, J. M., Diffusion of Alkane Mixtures in Zeolites: Validating the Maxwell−Stefan Formulation Using MD Simulations. *J. Phys. Chem. B* **2005,** *109* (13), 6386-6396.

19. Krishna, R.; van Baten, J. M., Onsager coefficients for binary mixture diffusion in nanopores. *Chem. Eng. Sci.* **2008,** *63* (12), 3120-3140.

20. Krishna, R., Multicomponent surface diffusion of adsorbed species: a description based on the generalized Maxwell—Stefan equations. *Chem. Eng. Sci.* **1990,** *45* (7), 1779-1791.

21. Krishna, R., Using the Maxwell-Stefan formulation for highlighting the influence of interspecies (1−2) friction on binary mixture permeation across microporous and polymeric membranes. *J. Membr. Sci.* **2017,** *540*, 261-276.

22. Anderson, L. R.; Yang, Q.; Ediger, A. M., Comparing gas transport in three polymers via molecular dynamics simulation. *Phys. Chem. Chem. Phys.*, **2018,** *20* (34), 22123-22133.

23. Lock, S. S. M.; Lau, K. K.; Shariff, A. M.; Yeong, Y. F.; Bustam, M. A., Thickness dependent penetrant gas transport properties and separation performance within ultrathin polysulfone membrane: Insights from atomistic molecular simulation. *J. Polym. Sci. Part B: Polym. Phys.* **2018,** *56* (2), 131-158.

24. Müller-Plathe, F.; Rogers, S. C.; van Gunsteren, W. F., Computational evidence for anomalous diffusion of small molecules in amorphous polymers. *Chem. Phys. Lett.* **1992,** *199* (3), 237-243.

25. Ban, S.; Huang, C.; Yuan, X.-Z.; Wang, H., Molecular Simulation of Gas Adsorption, Diffusion, and Permeation in Hydrated Nafion Membranes. *J. Phys. Chem. B* **2011,** *115* (39), 11352-11358.

26. Neyertz, S.; Brown, D., Air Sorption and Separation by Polymer Films at the Molecular Level. *Macromolecules* **2018,** *51* (18), 7077-7092.

27. Sanders, E. S.; Koros, W. J.; Hopfenberg, H. B.; Stannett, V. T., Pure and mixed gas sorption of carbon dioxide and ethylene in poly(methyl methacrylate). *J. Membr. Sci.* **1984,** *18*, 53-74.

28. Sanders, E. S.; Koros, W. J., Sorption of CO2, C2H4, N2O and their binary mixtures in poly(methyl methacrylate). *J. Polym. Sci., Part B: Polym. Phys.* **1986,** *24* (1), 175-188.

29. Mukaddam, M.; Litwiller, E.; Pinnau, I., Pressure-dependent pure- and mixed-gas permeation properties of Nafion®. *J. Membr. Sci.* **2016,** *513*, 140-145.

30. Vopička, O.; De Angelis, M. G.; Du, N.; Li, N.; Guiver, M. D.; Sarti, G. C., Mixed gas sorption in glassy polymeric membranes: II. CO2/CH4 mixtures in a polymer of intrinsic microporosity (PIM-1). *J. Membr. Sci.* **2014,** *459*, 264-276.

31. David, O. C.; Gorri, D.; Urtiaga, A.; Ortiz, I., Mixed gas separation study for the hydrogen recovery from H2/CO/N2/CO2 post combustion mixtures using a Matrimid membrane. *J. Membr. Sci.* **2011,** *378* (1), 359-368.

32. Gleason, K. L.; Smith, Z. P.; Liu, Q.; Paul, D. R.; Freeman, B. D., Pure- and mixed-gas permeation of CO2 and CH4 in thermally rearranged polymers based on 3,3′-dihydroxy-4,4′-diamino-biphenyl (HAB) and 2,2′-bis-(3,4-dicarboxyphenyl) hexafluoropropane dianhydride (6FDA). *J. Membr. Sci.* **2015,** *475*, 204-214.

33. Rizzuto, C.; Caravella, A.; Brunetti, A.; Park, C. H.; Lee, Y. M.; Drioli, E.; Barbieri, G.; Tocci, E., Sorption and Diffusion of CO2/N2 in gas mixture in thermally-rearranged polymeric membranes: A molecular investigation. *J. Memb. Sci.* **2017,** *528*, 135-146.

34. Lu, W.; Yuan, D.; Sculley, J.; Zhao, D.; Krishna, R.; Zhou, H.-C., Sulfonate-Grafted Porous Polymer Networks for Preferential CO2 Adsorption at Low Pressure. *J. Am. Chem. Soc.* **2011,** *133* (45), 18126-18129.

35. Myers, A. L.; Prausnitz, J. M., Thermodynamics of mixed-gas adsorption. *AlChE J.* **1965,** *11* (1), 121-127.

36. Minelli, M.; Campagnoli, S.; De Angelis, M. G.; Doghieri, F.; Sarti, G. C., Predictive Model for the Solubility of Fluid Mixtures in Glassy Polymers. *Macromolecules* **2011,** *44* (12), 4852-4862.

37. Minelli, M.; De Angelis, M. G.; Giacinti Baschetti, M.; Doghieri, F.; Sarti, G. C.; Ribeiro, C. P.; Freeman, B. D., Equation of State Modeling of the Solubility of CO2/C2H6 Mixtures in Cross-Linked Poly(ethylene oxide). *Ind. Eng. Chem. Res.* **2015,** *54* (3), 1142-1152.

38. Ricci, E.; Gemeda, A. E.; Du, N.; Li, N.; De Angelis, M. G.; Guiver, M. D.; Sarti, G. C., Sorption of CO2/CH4 mixtures in TZ-PIM, PIM-1 and PTMSP: Experimental data and NELF-model analysis of competitive sorption and selectivity in mixed gases. *J. Membr. Sci.* **2019,** *585*, 136-149.

39. Larsen, G. S.; Lin, P.; Hart, K. E.; Colina, C. M., Molecular Simulations of PIM-1-like Polymers of Intrinsic Microporosity. *Macromolecules* **2011,** *44* (17), 6944-6951.

40. Rukmani, S. J.; Liyana-Arachchi, T. P.; Hart, K. E.; Colina, C. M., Ionic-Functionalized Polymers of Intrinsic Microporosity for Gas Separation Applications. *Langmuir* **2018,** *34* (13), 3949-3960.

41. Hölck, O.; Böhning, M.; Heuchel, M.; Siegert, M. R.; Hofmann, D., Gas sorption isotherms in swelling glassy polymers—Detailed atomistic simulations. *J. Membr. Sci.* **2013,** *428*, 523-532.

42. Kupgan, G.; Demidov, A. G.; Colina, C. M., Plasticization behavior in polymers of intrinsic microporosity (PIM-1): A simulation study from combined Monte Carlo and molecular dynamics. *J. Membr. Sci.* **2018,** *565*, 95-103.

43. Balçık, M.; Ahunbay, M. G., Prediction of CO2-induced plasticization pressure in polyimides via atomistic simulations. *J. Membr. Sci.* **2018,** *547*, 146-155.

44. Pandiyan, S.; Brown, D.; Neyertz, S.; van der Vegt, N. F. A., Carbon Dioxide Solubility in Three Fluorinated Polyimides Studied by Molecular Dynamics Simulations. *Macromolecules* **2010,** *43* (5), 2605-2621.

45. Dutta, R. C.; Bhatia, S. K., Transport Diffusion of Light Gases in Polyethylene Using Atomistic Simulations. *Langmuir* **2017,** *33* (4), 936-946.

46. Dutta, R. C.; Bhatia, S. K., Structure and Gas Transport at the Polymer–Zeolite Interface: Insights from Molecular Dynamics Simulations. *ACS Appl. Mater. Interfaces* **2018,** *10* (6), 5992-6005.

Chapter 6 Gas Transport in filler materials

The content of this chapter is published as:

Ravi C. Dutta and SK. Bhatia, Interfacial barriers to gas transport in zeolites: distinguishing internal and external resistances, *Phys. Chem. Chem. Phys.*, 20, 26386 (2018)

Contributor	Statement of contribution
Ravi C Dutta	Programmed and conducted simulations (100%) Analysis and interpretation of data (80%) Wrote the paper (80%)
Suresh K. Bhatia	Wrote the paper (20%) Analysis and interpretation of data (20%)

6.1 Introduction

Mass transport resistance that include both intra-crystalline and interfacial resistances, determines the diffusive transport in porous inorganic materials. The drag exerted by the pore network of the membrane on the gas molecules contributes to intra-crystalline resistance, while the interfacial resistance includes entrance and exit barriers that arise from potential energy differences between activated states in the vicinity of the phase boundary due to symmetry breaking at the interface. These interfacial barriers can be distinguished as external fluid phase resistance and internal interfacial barriers. *External fluid phase resistance* exists on the gas side of the phase boundary, and is experienced by gas molecules entering the pore network, in the external boundary layer; on the other hand, *internal interfacial barriers* exist on solid side of the crystal and are due to the asymmetric potential experienced by the gas molecules inside the crystal but near the phase boundary.

For thick enough membranes, the contribution of interfacial barriers can be negligible and intra crystalline resistance determines the overall mass transfer across the membrane. However, the economic success of membrane based large scale industrial gas separations relies on significantly reducing the membrane thickness, and thereby lowering the driving force that is required for gas transport through nanoporous films for a given flux. This has led to the development ultrathin zeolite membranes[1] and mixed matrix membranes (MMM) with nanosize fillers.[2] At this length scale, interfacial barriers that depend on the adsorbent structure, crystal diversity and the potential energy landscape near the surface can be significant, and are detrimental to separation kinetics. The interfacial barriers are therefore an important paradigm in nanoscale separation and transport.

For long, intra-crystalline resistance has been extensively explored, and interest in the contribution from interfacial barriers to the mass transport is relatively recent. The past decade has witnessed substantial progress in understanding the role of interfacial barriers in mass transport both theoretically and experimentally. Experimentally, micro-imaging techniques[3-5] can quantitatively measure these surface barriers in nanoporous materials, and have revealed the presence of an interfacial mass transfer resistance in a variety of zeolites. However, the non-ideal nature of these crystals can influence the measured transport properties in these materials significantly, and it is difficult to experimentally determine the impact of interfacial barriers that are independent of defects. On the other hand, molecular dynamics simulations (MD) using dual control volume grand canonical MD (DCV-GCMD) simulations[6-8] and local equilibrium flux method (LEFM) [7, 9, 10] have been successfully employed to investigate surface barriers in nanoporous materials, and their relative importance in gas transport. However, these simulations are either computationally demanding or can only provide qualitative information about the surface barriers. Kočiřík et al. report large surface resistance, especially on a small zeolite crystal using a micro-dynamic model.[11] Ahunbay et al.[12, 13]

determined the surface barriers to gas permeation in silicalite that are localized at the crystal surface using DCV-GCMD simulations, and found that these barriers can be significant up to a crystal thickness of 1 μm. However, Newsome et al. found that these DCV-GCMD simulations are sensitive to non-isothermal effects in the interfacial region,[7] and reported that contribution of these barriers to gas permeation can be negligible at all practical conditions by applying a local thermostat in the DCV-GCMD simulations as well as through LEFM method.[7, 10] Zimmermann et al.[14, 15] determined the critical membrane thickness below which the influence of surface barriers plays a role in gas transport through extended dynamically corrected transition state theory, by computing self-diffusion coefficients. Sastre et al.[16] performed MD simulations to study the uptake/release behavior of benzene in a finite MFI crystal, showing that pore blockage effects lead to interfacial resistance. Recent work from our laboratory using equilibrium as well as non-equilibrium MD simulations has demonstrated that the effect of interfacial resistance is significant for gas and water transport in carbon nanotubes.[17-19] However, intra crystalline resistance in these investigations includes the contribution of interfacial resistance to gas transport in the crystal. Thus, while it is evident from these studies that there exist interfacial barriers to gas transport at zeolite crystal surfaces, there is no convenient method to clearly distinguish and quantify the interfacial barriers that originate solely from the phase boundary, and to distinguish barriers on the solid and gas sides of the phase boundary.

In this chapter, we apply equilibrium molecular dynamics (EMD) simulations to quantitatively assess the internal interfacial barriers to the permeation of methane in different classes of zeolites in the presence of bulk gas, isolating the barriers on the solid side of the interface. Further, the effect of the presence of dense external media such as polymer on gas permeation in the zeolites is explored. Based on the additivity of resistances inside the zeolite, a mathematical expression relating the adsorbate diffusion coefficient within the zeolite to length of the crystal is derived and validated against the simulation results. In addition, the external fluid phase resistance for gas diffusion is determined and its importance relative to internal interfacial barriers discussed.

6.2 Model and methodology

6.2.1 Model details*:*

Our model system comprises three different classes of all-silica type zeolites: MFI (interconnected network of straight and sinusoidal channels), SAS (comprising large cages connected by narrow windows, with cage to window ratio 2.2) and PON (having small cages connected by narrow windows, with cage to window ratio 1.18) of finite length, with bulk gas regions on either side of the crystal as shown schematically in Figure 6-1 (a).

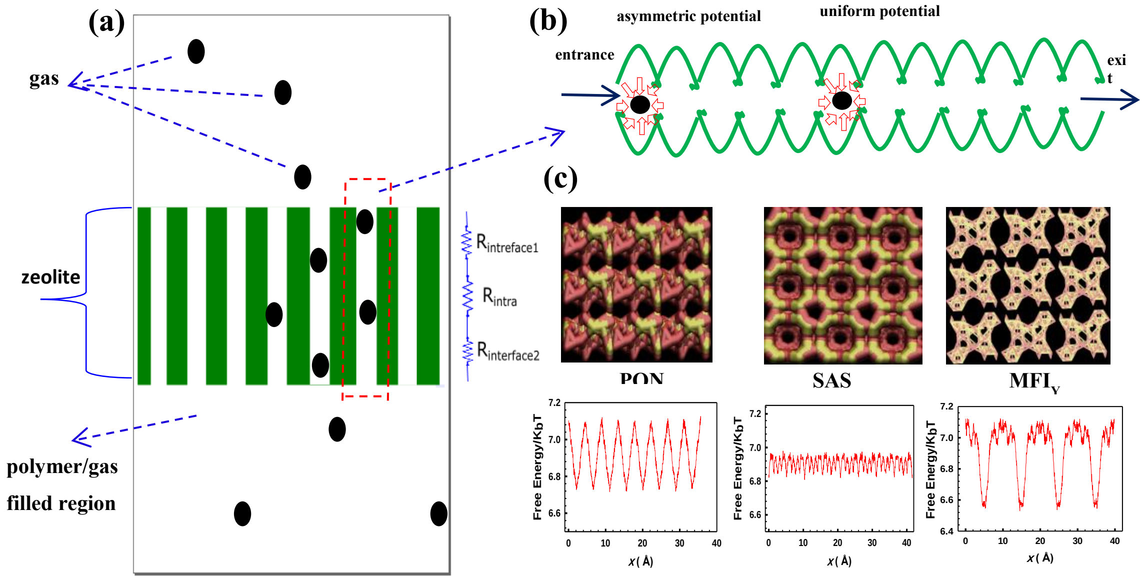

Figure 6-1: Schematic illustration of (a) simulation box, (b) the pore network inside the zeolite and the mean force experienced by the gas molecules at different locations in the pore, and (c) zeolite structures investigated in this study and corresponding free energies in the direction of diffusion.

SAS and PON zeolites comprise one dimensional pores, whereas MFI has three dimensional pores; hence in MFI diffusion along the y-direction is examined owing to the presence of straight channel like pore structure that is considered to be favorable for membrane application. Crystals of finite length were cleaved in the direction of available pores and all the surface silica and oxygen and atoms saturated with -OH and -H groups respectively. This structure was relaxed without modifying the cell dimensions by employing conjugate gradient method using VASP software.[20-22], and the resulting zeolite structure treated as rigid in the entire simulation. We note that gas transport in the zeolite may depend on framework flexibility,[23] which may need further investigation. However, rigid structure representation of zeolite has been shown to be a good approximation when the size of the gas molecule is significantly smaller than the pore aperture of the zeolite,[24-26] which is the case in this investigation.

In order to investigate the effect of surrounding media, SAS unit cells were sandwiched between two (6FDA-durene) polyimide polymer-filled regions by performing EMD simulations in the isothermal-isobaric ensemble, following the procedure discussed in detail elsewhere.[27, 28] This is representative of a mixed matrix membrane with nanosized filler, for which we investigate the effect of surrounding polymer on gas transport in the zeolite. The system is assumed periodic in all three directions. Methane is modeled as a spherically symmetric molecule interacting only with oxygen in the zeolite through the Lennard-Jones (LJ) 12-6 potential, with[29] $\varepsilon_{CH_4-CH_4} = 147.9\ \mathrm{K}$, $\sigma_{CH-CH_4} = 3.73\ \text{Å}$,

$\varepsilon_{zeo-CH_4} = 133.3$ K and $\sigma_{zeo-CH_4} = 3.214$ Å. The flexible polymer chains were described by considering a combination of appropriate bonded and non-bonded interactions with an all atom representation, where all the atoms in the system are defined explicitly based on the polymer consistent force field (PCFF).[30] The non-bonded interactions between polymer, MFI and gas molecules were modelled using a hybrid potential. Lorentz−Berthelot rules were used to obtain the corresponding interaction parameters.

EMD simulations were performed using the LAMMPS[31] package to determine the corrected diffusivities with the Nose′-Hoover thermostat and Berendsen barostat for temperature and pressure control respectively. In all the simulations, a cutoff distance of 1.2 nm was used for potential energy calculations. The Verlet method with a time step of 1 fs was used to integrate the particle equations of motion and periodic boundary conditions were imposed in all three dimensions. The simulations were run for 50 ns in the canonical ensemble with 10 ns allowed for equilibration. The results of several independent runs, each starting from a different initial configuration, were averaged to compute the corrected diffusivity. The standard deviation of the results was calculated by dividing the total simulation run into four equal parts and using it to determine the statistical uncertainties associated with the simulations.

Gas adsorption isotherms in a zeolite crystal of finite length were extracted by performing grand canonical Monte Carlo (GCMC) simulations using the DL_MONTE simulation package,[32] where gas adsorbed in a rigid zeolite of finite length is in phase equilibrium with the ambient gas phase. We emphasize that these adsorption isotherms were evaluated by considering the gas adsorbed within the zeolite region only.

6.2.2 Methodology

Gas diffusion in the zeolite and determination of interfacial resistance: A diffusion coefficient (D_n) of n gas molecules in a zeolite crystal of length L_x is computed by calculating its collective coordinate n, for which the differential form of n is defined as

$$dn = \sum_{i \in zeolite(t)} \frac{dz_i}{L_x} \tag{6-1}$$

where dz_i is displacement of gas molecule i in the z direction during time dt in the zeolite region. The mean square displacement (MSD) of n obeys the Einstein relation following the collective diffusion model,[33]

$$D_n = \frac{< n^2(t) >}{2t} \tag{6-2}$$

and this can be related to the corrected diffusion coefficient (D_o), which describes the collective motion of all adsorbed molecules,[28, 34, 35] as:[27]

$$D_o = \frac{D_n.L_x}{\rho.A_c} = \frac{D_n L_x^2}{< N_{mol} >} \tag{6-3}$$

where $<N_{mol}>$ is the ensemble averaged number of gas molecules in the zeolite of cross-sectional area A_c and ρ is the ensemble averaged molar density. This corrected diffusivity is also known as single component Maxwell-Stefan diffusivity,[35, 36] in the extensively used Maxwell Stefan formulation of mass transport. When analyzed in this way,[27, 33] the calculation of D_o from trajectories in a NVT-EMD simulation (for the whole system including external reservoirs) allows for temporal change in the identity of the molecules within the sub-region of interest (the zeolite). This diffusion coefficient represents the internal transport coefficient within the finite crystal of length L, and excludes the effect of any external resistance on the gas side of the boundary.

Using the diffusion coefficient determined from equilibrium molecular dynamics, as above, the net molar flux of a gas follows the irreversible thermodynamics-based description of the transport,[37]

$$j = -\frac{D_o \rho}{k_B T}\left(\frac{d\mu}{dz}\right) \tag{6-4}$$

where T is the temperature of the system. Assuming there exists a small chemical potential difference across the zeolite, eq (6-4) can be readily applied to the zeolite crystal, and can accordingly written as

$$\Delta\mu = -\frac{jLk_B T}{\rho.D_o} \tag{6-5}$$

We define the total internal transport resistance as $-\Delta\mu / jA_c k_B T$, and note that the total internal resistance for flow through the zeolite must additively comprise that for the two interface regions in the zeolite, i.e. near the entrance and the exit ($R_{interface} = R_{interface1} + R_{interface2}$), and the intra-crystalline resistance (R_{intra}), as shown in Figure 6-1(a). Combining this series resistance concept with eqn (6-5) then leads to

$$\frac{L}{\rho.D_o A_c} = \frac{L}{\rho.D_{o,\infty} A_c} + R_{\text{interface}} \tag{6-6}$$

where $L / A_c \rho D_{o,\infty}$ is the intra-crystalline resistance in the absence of interfaces (i.e. based on the diffusivity $D_{o,\infty}$ in an infinitely long crystal). This provides

$$\left\{ \frac{1}{\rho.D_o} \right\} = \left\{ \frac{1}{\rho.D_{o,\infty}} \right\} + \left\{ \frac{A_c R_{\text{interface}}}{L} \right\} \tag{6-7}$$

In addition, the barrier on the gas side of phase boundary, hereinafter referred to as external fluid phase resistance, is determined by subtracting the internal transport resistance from the overall resistance of the system ($R_{sys} = L_{sys} / A_c \rho_{sys} D_{o,sys}$). Here $D_{o,sys}$ is the corrected diffusivity considering all adsorbed gas molecules (of density ρ_{sys}) in a system of length L_{sys}, including a zeolite region and surrounding bulk gas regions, determined by computing the center of mass (COM) motion of all gas molecules in the z-direction, following the Einstein relationship:

$$D_o = \frac{1}{2N} \lim_{t \to \infty} \frac{1}{t} < \| \sum_{i=1}^{N} z_i(t) - z_i(0) \|^2 > \tag{6-8}$$

where $z_i\,(t)$ is center of mass position vector of molecule *i* at time *t*. This provides

$$R_{external} = \frac{L_{sys}}{A_c \rho_{sys} . D_{o,sys}} - \frac{L}{A_c \rho . D_o} \tag{6-9}$$

We note that overall system resistance (R_{sys}) includes the contribution of external fluid phase resistance ($R_{external}$), interfacial resistance ($R_{interfacial}$) and intra-crystalline resistance (R_{intra}), following

$$R_{sys} = \mathrm{R}_{external} + R_{inetrface} + R_{intra} \tag{6-10}$$

6.2.3 Critical membrane thickness

The critical membrane thickness (δ_{critical}), below which the contribution of interfacial resistance to the gas transport is significant, is determined by computing the fractional contribution of interfacial resistance to the overall resistance in the solid (R_{solid}=$R_{interface}$+R_{intra}), as

$$\delta_{\text{critical}} = \frac{R_{\text{interface}}}{R_{solid}} = 1 - \left\{ \frac{D_o}{D_{o,\infty}} \right\} ; \; 0.25 \tag{6-11}$$

We note that value of δ_{critical} is sensitive to the lower limit (0.25 in this work) for significance of the interfacial resistance. The statistical errors associated with the calculation of D_o (up to 10 %) do not permit the choice of a lower value for this limit. Nevertheless, one expects that when the interfacial resistance is insignificant the total resistance to transport in the solid is dominated by the intra-crystalline resistance (i.e. based on the diffusivity in an infinite crystal), and is proportional to length. Thus the critical length for δ_{critical} of 0.1 would be about 2.5 times larger than that based on δ_{critical} of 0.1.

6.3 Results and discussions

6.3.1 Effect of crystal length on corrected diffusivity

Figure 6-2 depicts the zeolite crystal length variation of the corrected diffusivities of methane at a density of 1 mol/u.c. in MFI_Y, SAS and PON zeolites at 300 K. The corrected diffusivities of methane in an infinite and finite crystal differ greatly, with the former diffusing faster by nearly an order of magnitude, and thus the surface barriers are sufficiently strong to hinder the gas transport rate in an ideal crystal, in agreement with experimental findings of Kärger et al.[38]. The corrected diffusivity of methane in the zeolite increases with increase in crystal length, with $1/\rho.D_o$ varying linearly with $1/L$, following eq (6-7). The slope of the linear plot in Figure 6-2 yields a quantitative value of the interfacial resistance-surface area product, showing that the interfacial barriers to methane transport in PON zeolite are the largest while those in MFI_Y zeolite are smallest, following the order: PON < SAS < MFI_Y. We emphasize that the calculated diffusion coefficients are intra-crystalline gas diffusion coefficients within the zeolite region only, and do not include the effect of any external interfacial resistance.

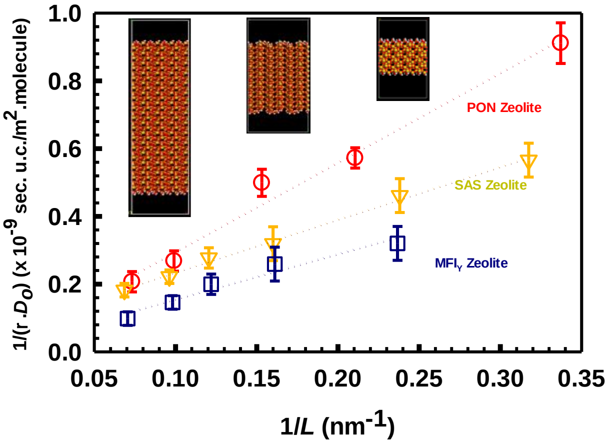

Figure 6-2: Length dependence of CH_4 diffusivity in MFI_Y, SAS and PON zeolites at T=300 K at a loading of ~1 mol/u.c. MFI_Y signifies that the diffusivity corresponds to that in the y direction.

Figure 6-3(a) depicts the variation of corrected diffusivities with zeolite crystal length, for CO_2, CH_4 and H_2 at a density of 1 mol/u.c. in SAS zeolite at 300 K, showing a considerably larger interfacial resistance for the transport of CH_4 and CO_2 compared to that for H_2. The interfacial resistance in SAS zeolite increases steeply with increase in kinetic diameter of the gases due to the strong confining effects of the pore walls when the kinetic diameter of the gas and limiting pore diameter of the zeolite are comparable, as shown in Figure 6-3(b). Further, we note interfacial resistance reaches a finite maximum value when the kinetic diameter of the gas is 70-80 % of the pore limiting pore diameter. This suggests that, interfacial barriers could not influence the selectivity of gases of comparable molecular size.

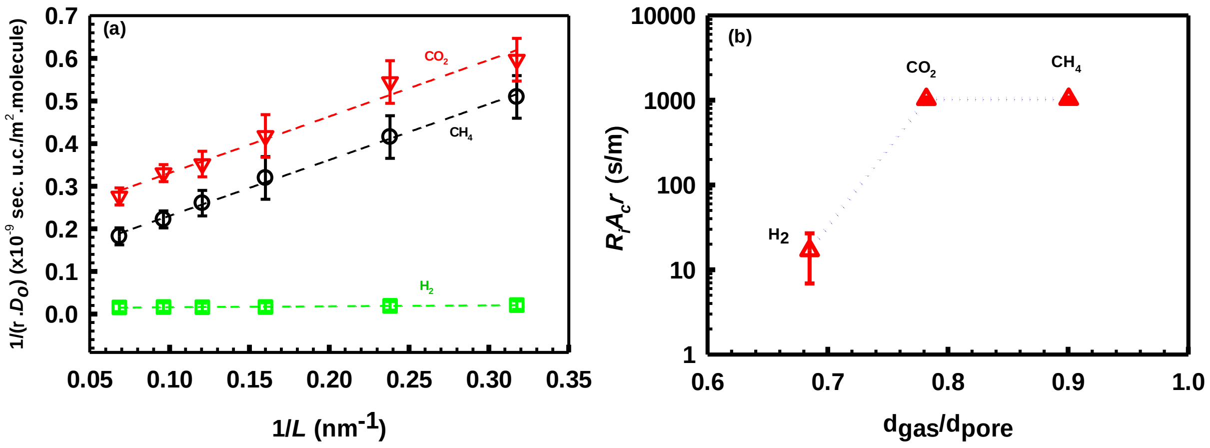

Figure 6-3: Length dependence of gas diffusivities in SAS zeolite at $T = 300$ K at a loading of ~1 mol/u.c, and (b) Variation of interfacial resistance to gas transport with ratio of kinetic diameter of the diffusing species to the limiting pore diameter of zeolite

6.3.2 Effect of loading

Figure 6-4 depicts the loading variation of the interfacial resistance to CH_4 transport in SAS zeolite at 300 K. It is seen that interfacial resistance to methane transport decreases with increase in gas loading in the zeolite, consistent with the earlier simulation predictions.[6] This can be understood by noting that at high gas loadings, gas - gas interactions dominate over gas-zeolite interactions, leading to lower overall momentum loss from gas-solid collision. As a result, the energy barrier due to interfacial resistance can be less significant at higher loadings. This is further supported by increase in corrected diffusivity of methane in SAS zeolite with increase in loading as shown the inset of Figure 6-4.

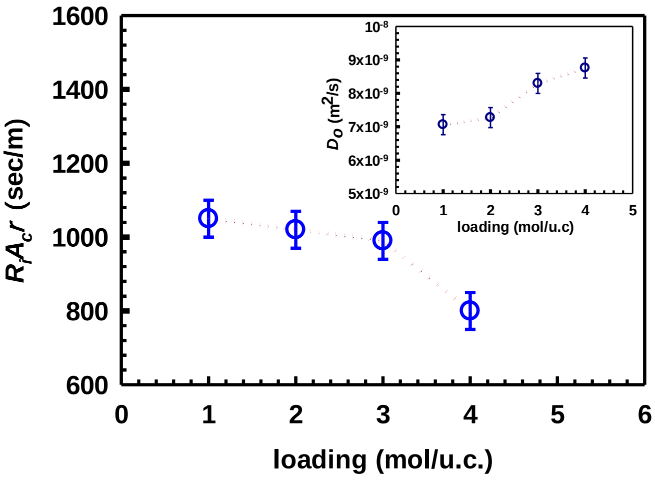

Figure 6-4: Loading dependence of interfacial resistance for CH_4 diffusion in SAS zeolite at T = 300 K. Loading dependence of corrected diffusivity of methane in infinitely long SAS zeolite is depicted in the inset.

6.3.3 Effect of temperature

Figure 6-5(a) depicts the crystal length variation of the corrected diffusivity of methane in SAS zeolite at various temperatures in the range of 300-500K. The slope of $1/\rho.D_o$ *vs.* $1/L$ decreases with increase in temperature, indicating that interfacial barriers are more significant at lower temperature and become less pronounced at higher temperature. This can be understood by noting that the energy barrier due to interfacial resistance can be more easily overcome by gas molecules at higher temperatures due to their high kinetic energy. The inset of Figure 5(a) depicts the temperature variation of intrinsic interfacial resistance in SAS zeolite, following the Arrhenius type relation. Here, we consider the quantity $R_iA_c\rho$ as intrinsic resistance, because resistance is inversely proportional to area. The calculations showed that interfacial barriers have an activation energy of 4.0 (±0.5) kJ/mol, comparable to that of the methane diffusivity in an infinite crystal (3 (±0.5) kJ/mol), suggesting that interfacial resistance and internal collective diffusion proceed by identical elementary mechanisms. Figure 6-5(b) depicts a comparison of fractional interfacial resistance for methane diffusion in SAS zeolites at various lengths in the temperature range of 300-500 K, highlighting the increasing importance of interfacial resistance at lower temperatures compared to that at higher temperatures.

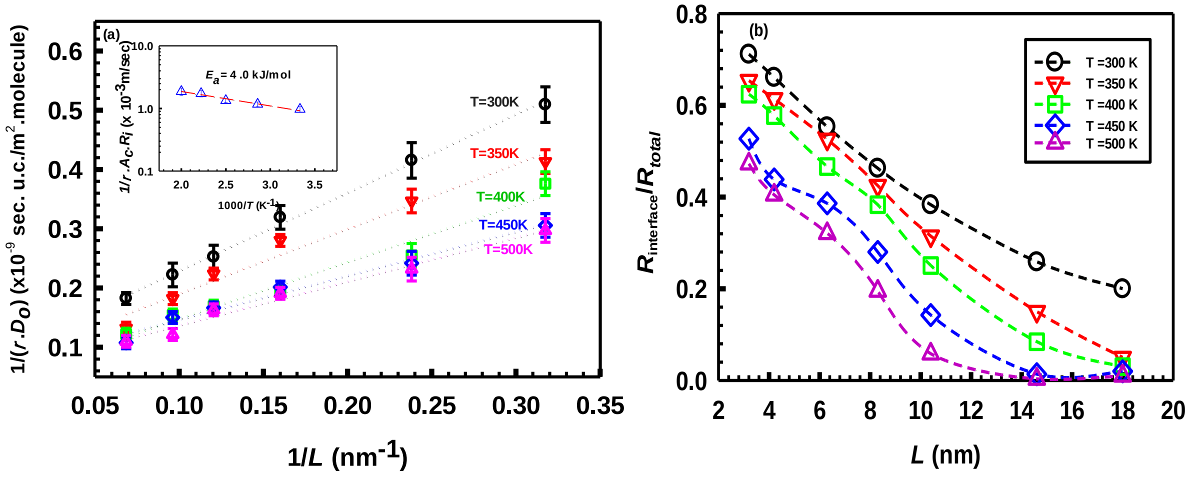

Figure 6-5: Length dependence of methane diffusivity in SAS zeolite, in the temperature range of 300 K to 500 K at a density of ~1 mol/u.c. Temperature dependence of intrinsic interfacial resistance in SAS zeolite is depicted in the inset, and (b) Length dependence of fractional interfacial resistance for CH_4 diffusion in SAS zeolites at various temperatures

The interfacial barrier to gas transport in zeolites has also been investigated when a dense external media such as polymer is present, as occurs in mixed matrix membrane. Figure 6-6(a) depicts a comparison between the effect of surrounding polymer and a bulk gas medium on the variation of corrected internal diffusivity of methane with zeolite crystal length. Our simulations results for methane transport in zeolite SAS having surrounding polymer medium showed different behavior to that of bulk gas, in which interfacial barriers increased when the surrounding medium is polymer. To examine the conditions that lead to this behavior, the corresponding free energies in the zeolite as a function of reaction coordinate in the presence of polymer and bulk gas have been explored and are shown in the Figure 6-7. An internal free energy maximum that exists near the interface corresponding to the interfacial barrier due to the phase boundary is observed in both the cases. However, in the presence of polymer, a free energy minimum exists that corresponds to favorable interaction between polymer and gas compared to that between zeolite and gas, leading to the clustering of molecules close to the polymer surface. This is further evident in inset (i) of Figure 6-6(b), where a density peak near the polymer-zeolite interface is observed that has been extracted by diving the simulation cell into bins of 5 Å each. Figure 6-6(b) depicts the mean square displacement (MSD) of CH_4 in the interface region of the zeolite i.e. first 5 Å from the entrance and exit, in the presence of polymer as well as bulk gas, using eq (6-2), showing considerably larger resistance to gas diffusion when the surrounding medium is polymer compared to that when it is surrounded by bulk gas. Further, this diffusivity is independent of surrounding medium in the region distant from the interface as shown in inset (ii) of Figure 6-6(b).

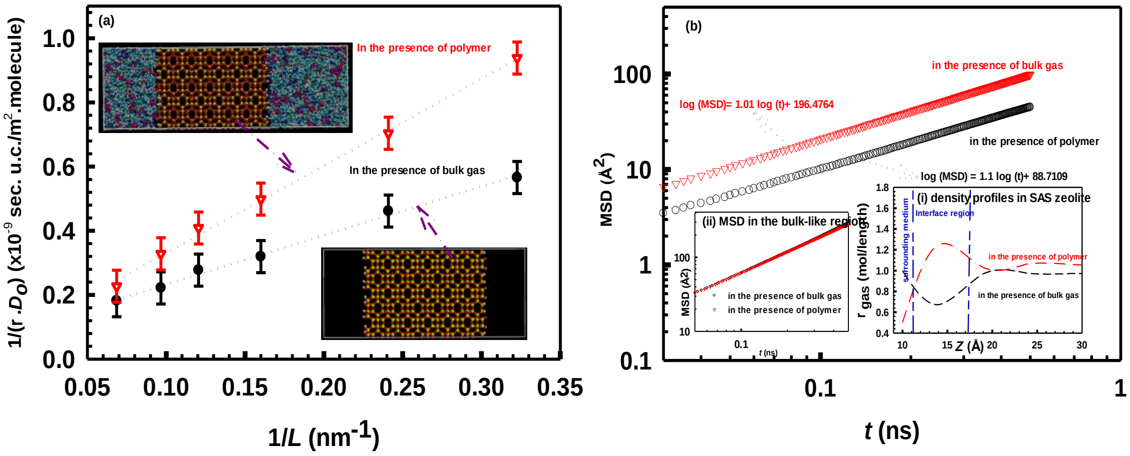

Figure 6-6: (a) Length dependence of CH_4 diffusivity, and (b) Mean square displacement of CH_4 in the interface region of SAS zeolite in the presence of bulk gas and polymer at T= 300 K. In (b) inset (i) shows density profiles of CH_4 gas in SAS zeolite, and inset (ii) shows mean square displacement of CH_4 in the bulk region of SAS zeolite in the presence of bulk gas and polymer at T= 300 K.

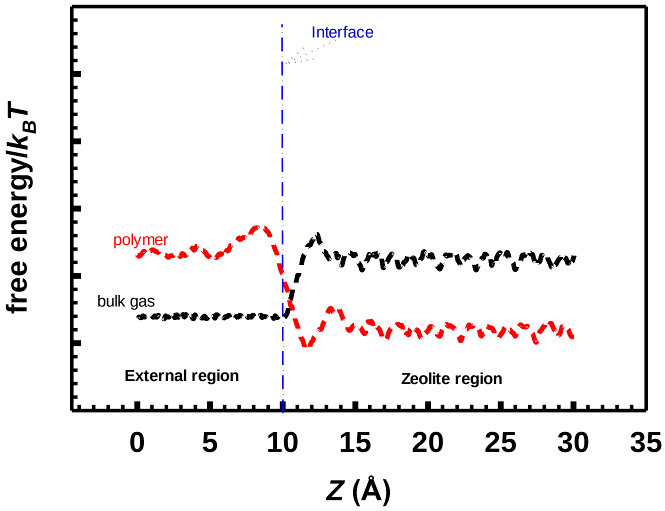

Figure 6-7: Free energy profiles of CH_4 gas in SAS zeolite at T= 300K in the presence of bulk gas and polymer at the loading of ~1 mol/u.c.

Figure 6-8 depicts the internal interfacial resistance to CH_4 transport in a variety of zeolites as determined from eq (6-7). The intrinsic interfacial resistance ($A_cR_{i\rho}$) to methane transport in the PON, SAS and $\mathrm{MFI_Y}$ zeolites is 3300 (±150), 1000 (±50) and 450 (±20) sec/m respectively, despite the fact that all these zeolites have limiting pore dimeter of around 4.5 Å. Thus, it is evident that the intrinsic interfacial resistance depends on the type of pore network in the zeolite. To investigate this behavior further, we calculated their relative interfacial resistance, defined as the ratio of resistances offered by the interface and bulk (having diffusivity of infinitely large crystal) regions, by determining gas diffusivities in the respective regions and found that PON, SAS and MFI zeolites have relative interfacial resistances of 25(±5), 9 (±3) and 5 (±1) respectively. Thus, PON zeolite with the most uniform pore surface, having window and cage diameter ratio of around 1, enhances relative interfacial resistance, which attenuates gas transport, the most. This is consistent with the recent findings of Lang et al.[18] that the transport diffusion coefficient of CH_4 in infinite and finite carbon nanotubes differed by 2 orders of magnitude. Further, we note that other factor including crystal morphology, surface area, pore size,[39] shape[34] and tortuosity[40] can influence these interfacial barriers, which needs further investigation. The inset of Figure 6-8 depicts a direct comparison between the intrinsic interfacial resistance to methane transport when the surrounding medium is bulk gas and polymer in SAS zeolite, demonstrating that the internal interfacial resistance in the presence of dense surrounding medium is twice that in the presence of bulk gas in SAS zeolite.

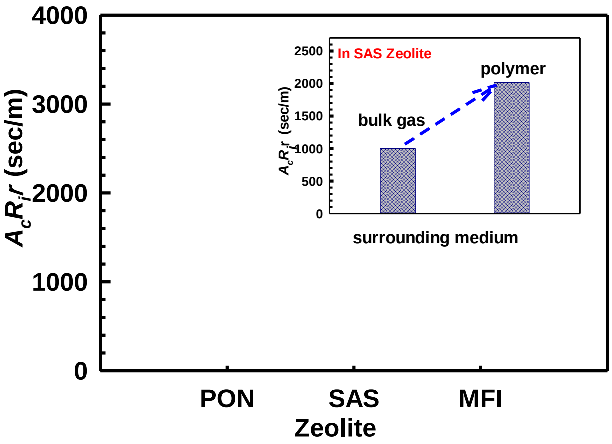

Figure 6-8: Interfacial resistance to methane in zeolites surrounded by bulk gas. A comparison of intrinsic interfacial resistance in SAS zeolite surrounded by bulk gas and polymer is shown in the inset.

Excellent agreement between the estimates of corrected diffusion coefficient in an infinitely long crystal, calculated from the intercept based on a linear plot of $1/\rho D_o$ versus $1/L$ following eq (6-7), and that of intra-crystalline diffusivity obtained by conducting simulations in an infinite crystal, at different temperatures as well as in various zeolites confirming the robustness of the equation, as shown in Figure 6-9.

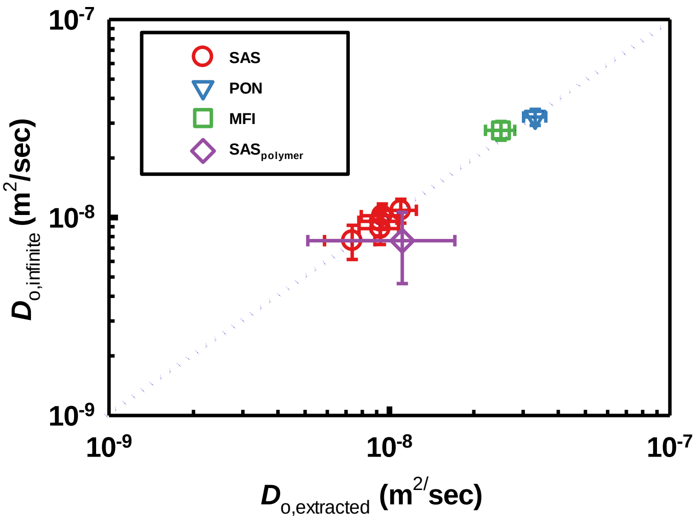

Figure 6-9: Comparison between gas diffusion coefficients in infinite zeolite crystal obtained from eq (6-7), $D_{o,extracted}$ with that directly estimated from simulation, $D_{o,infinite}$.

6.3.4 Internal transport resistance *vs.* External fluid phase resistance

Figure 6-10 (a) depicts a comparison of the transport resistance of the solid and overall system resistance, including internal transport resistance and external fluid phase resistance for methane diffusion in SAS zeolite at various loadings. Close agreement is seen between the estimates of internal transport resistance in the solid (R_{solid}) and overall system resistance (R_{sys}), indicating that the internal transport resistance dominates over external fluid phase resistance. Figure 6-10 (b) depicts a comparison of fractional external fluid phase resistance for methane diffusion in SAS zeolite at various loadings. It is seen that external fluid phase resistance is smaller than the intra-crystalline resistance, and is a maximum of 20-25% of the internal interfacial resistance at any given length of crystal. Further, it is seen that the relative external fluid phase resistance decreases with increase in loading, and goes through a maximum at a length of about 10 nm. These results suggest that the contribution of external fluid phase resistance that exists on the gas side of the interface can be neglected, especially at higher loadings.

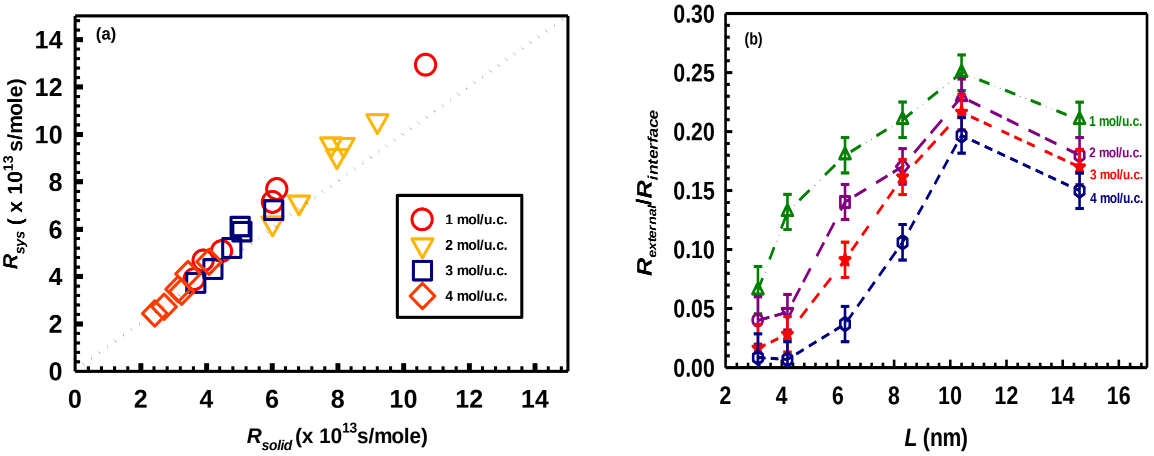

Figure 6-10:(a) Comparison between overall system resistance and total intra-crystalline resistance for methane transport at various loadings in SAS zeolite at T = 300 K, and (b) Length dependence of fractional interfacial resistance for CH_4 diffusion in various zeolites.

6.3.5 Critical membrane thickness ($\delta_{critical}$)

Figure 6-11 depicts a comparison of fractional interfacial resistance for methane diffusion in SAS, PON and MFI$_Y$ zeolites at various lengths. The critical membrane thickness, below which the interfacial barriers are significant, is taken to be that at which the contribution of interfacial resistance to the total resistance is 25%, as in eq (6-11). It is seen that SAS, MFI$_Y$ and PON zeolites, based on methane transport, have a critical membrane thickness of 14 (±2), 65 (±5), and 95 (±5) nm respectively. Thus, the interfacial barriers are significant in the zeolites with uniform pore size, PON zeolite in this case, especially when the size of the pore and gas are comparable. The inset of Figure 6-11 depicts similar results for various gases in SAS zeolite, showing a critical membrane thickness of 3 (±2) , 7 (±1) and 14(±2) nm for H_2, CO_2 and CH_4 transport respectively. The present results would suggest that the critical membrane thickness of zeolites depend on the nature of the pore network as well as size of the diffusing species.

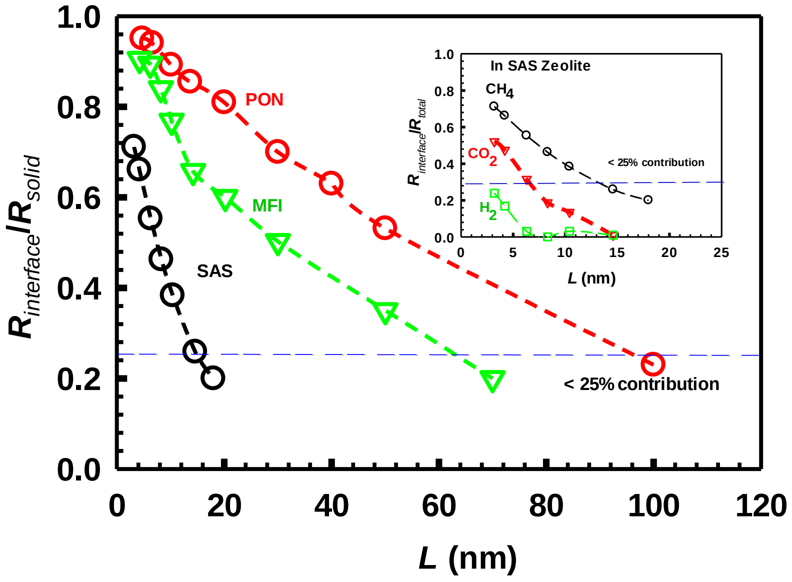

Figure 6-11: Length dependence of fractional interfacial resistance for CH_4 diffusion for various zeolites. A comparison of length dependence of fractional interfacial resistance for various gases in SAS zeolite is depicted in the inset.

6.3.6 Adorption isotherms:

The adsorption behavior of pure component H_2 and CH_4 in SAS zeolite of finite length was systematically investigated by exploring the adsorption isotherms for each gas, by evaluating the concentration of adsorbed gas molecules in the zeolite region only. We emphasize that these isotherms do not include the contribution of gas that is externally adsorbed in the gas region. Figures 6-12 (a) and (b) show a comparison of adsorption isotherms of CH_4 and H_2 in SAS zeolite crystals of various length at T= 300 K. It is seen that the CH_4 adsorption is strongly affected by the crystal length, while H_2 shows a weak dependence on crystal length, and gas adsorption in the zeolite increases with increase in crystal length at a given pressure. This is due to the strong confinement effect experienced by the larger CH_4 molecules having size comparable to the limiting pore dimeter of zeolite, as well as low adsorption capacity of SAS zeolite for the lighter H_2 molecule. The adsorption isotherm of CH_4 and H_2 in SAS zeolite of finite and infinite length was fitted using a Langmuir-mode sorption model of the form:

$$c = \frac{B_{\max}\, P}{K_d + P} \qquad (6\text{-}15)$$

where, C is the total concentration of the sorbate in the polymer and P is the pressure.

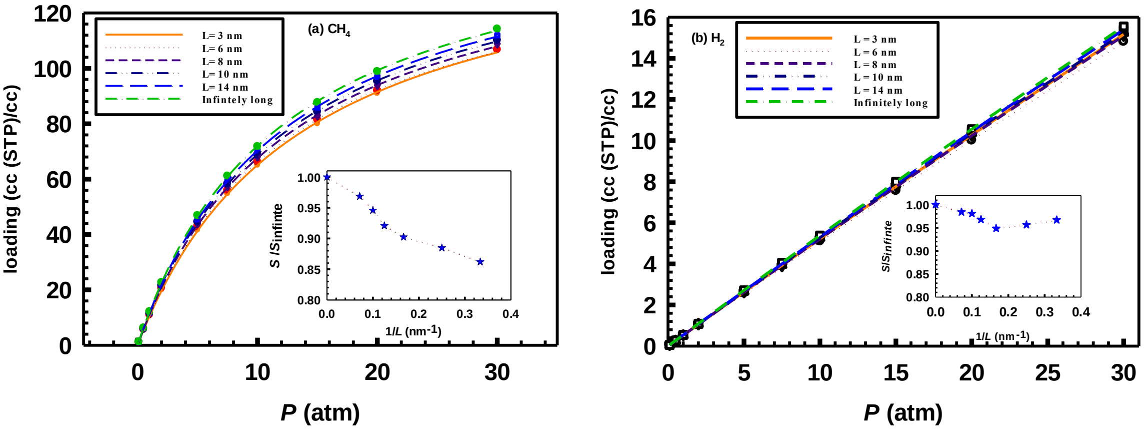

Figure 6-12: Adsorption of isotherms of (a) CH$_4$, and (b) H$_2$ in SAS zeolite of finite length at T=300K. Length dependence of solubility coefficients of these gases in SAS zeolite is depicted as inset in the respective plots.

In the low pressure region, when $K_d >>> P$, eqs (6-12) and (6-15) provide the Henry law relationship for adsorbed concentration:

$$C = (\frac{B_{\max}}{K_d}) * P = S * P \tag{6-16}$$

where S is the apparent solubility coefficient in the zero-pressure limit. We note that the loading at which diffusion coefficients are calculated in this study lies close to this region. The solubility of CH$_4$ and H$_2$ in SAS zeolite is determined by using eq (6-16). The length dependence of fractional solubilities of CH$_4$ and H$_2$ in a finite SAS crystal are depicted in the inset of Figure 6-12 (a) and (b), respectively. It is seen that the fractional solubility of these gases decreases with decrease in crystal length and this effect is more significant for CH$_4$ than for H$_2$.

6.3.7 Performance of zeolite membranes:

Figure 6-13 (a) depicts the crystal length dependence of perm-selectivity of H$_2$ over CH$_4$ in SAS zeolite when the surrounding medium is bulk gas at a loading of 1 molecule per unit cell and T = 300 K. It is seen that selectivity of H$_2$ over CH$_4$ increases with decrease in crystal length. Interestingly, SAS zeolite of infinite length is selective for methane over hydrogen, while the finite zeolite is selective for hydrogen over methane, exhibiting a selectivity cross over at around a crystal thickness of 4 nm. This can be understood by the fact that interfacial barriers considerably attenuate the transport of gases having kinetic diameter comparable to that of limiting pore size of the zeolite, CH$_4$ in this case, thus a larger decrease in the diffusivity of CH$_4$ compared to H$_2$ in the finite zeolites leads to increase in the diffusivity selectivity of H$_2$ over methane, as shown in the inset of Figure 6-13 (a).

Further, we note that diffusivity selectivity of H_2 over CH_4 in the finite crystal is around 2-3 times higher than that of in infinite crystal. In addition, the larger decrease in solubility of CH_4 in a finite crystal compared to that of H_2, further contributes to the increase in selectivity of H_2 over CH_4 in finite crystals. Figure 6-13 (b) compares the performance of finite and infinite SAS crystals with the Robeson upper bound plot.[41] It is seen that the performance of finite zeolites for H_2/CH_4 separation is well above the Robeson plot; nevertheless, the selectivities are too low for practical significance.

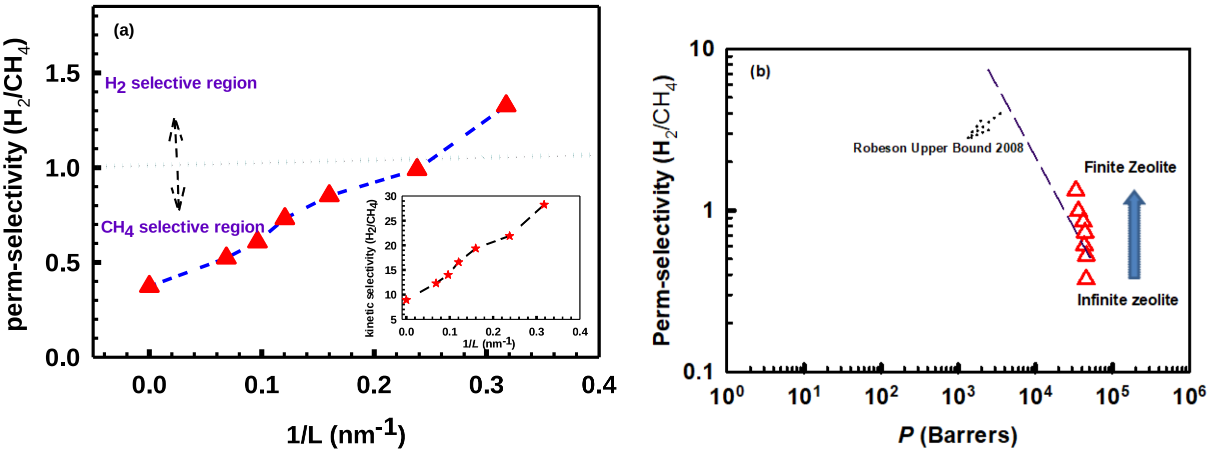

Figure 6-13: Length dependence of perm-selectivity of H_2 over CH_4 in SAS zeolite in the presence of bulk gas at a loading of ~1 mol/u.c. and T =300 K. Inset depicts length dependence of diffusivity selectivity of H_2 over CH_4 in SAS zeolite in the presence of bulk gas at a loading of ~1 mol/u.c. and T =300 K, and (b) Comparison of separation performance of finite and infinite SAS zeolite membranes with Robeson upper bound.

6.4 Conclusions

In summary, we have developed an approach to quantitatively assess the internal interfacial barriers to gas transport, especially in channel-like nanoporous materials. It is evident that the internal interfacial barriers due to the phase boundary contribute significantly to the gas transport resistance at the nanoscale in zeolites, especially when the surface has a uniform morphology as well as when a dense surrounding media such as a polymer is present. It is seen that the external fluid phase resistance that exists on the gas side of the interface is smaller than the internal interfacial resistance by almost an order of magnitude, and therefore can be neglected. Further, the interfacial resistance decreases with increase in temperature following an Arrhenius type relation, having an activation energy comparable to that of the gas diffusivity in an infinite crystal. The critical membrane thickness, below which these interfacial barriers are significant, are found be of the order of 0.01 to 0.1 μm. The contribution of interfacial barriers to gas transport are significantly higher for CH_4 than for H_2, due to its larger kinetic diameter that is comparable to that of the limiting pore diameter of the zeolite, leading to improved H_2/CH_4 diffusivity selectivity in finite crystals. Furthermore, the methane adsorption is hindered in finite crystals of SAS zeolite, while this effect is not significant for H_2. It is seen that small crystals of SAS type zeolite are selective for H_2 over CH_4, while large crystals are selective for CH_4 over H_2.

Our results demonstrate that a series diffusion resistance model, considering the contributions of intra-crystalline and internal interfacial resistance, suffices to explain the transport behavior of gases within nano-porous materials. While we validated this here for a gas in an ideal rigid zeolite, the method should be extendable also to study other nano-porous materials as well as to non-ideal and flexible framework materials. Furthermore, we note that, although this model is extended to study the interfacial resistance in zeolites when the surrounding medium is a polymer, the separation performance of zeolites and overall membrane performance in the presence of polymer is beyond the scope of this investigation and requires further investigation. This method will be useful in considering ways to modify the surface by functionalization in order to reengineer the membrane. On the basis of these insights, it is anticipated that interfacial barriers will be of importance in many of the new generation separation processes based on ultrathin nano-porous membranes.

6.5 References

1. Jeon, M. Y.; Kim, D.; Kumar, P.; Lee, P. S.; Rangnekar, N.; Bai, P.; Shete, M.; Elyassi, B.; Lee, H. S.; Narasimharao, K.; Basahel, S. N.; Al-Thabaiti, S.; Xu, W.; Cho, H. J.; Fetisov, E. O.; Thyagarajan, R.; DeJaco, R. F.; Fan, W.; Mkhoyan, K. A.; Siepmann, J. I.; Tsapatsis, M., Ultra-selective high-flux membranes from directly synthesized zeolite nanosheets. *Nature* **2017,** *543*, 690.

2. Bachman, J. E.; Smith, Z. P.; Li, T.; Xu, T.; Long, J. R., Enhanced ethylene separation and plasticization resistance in polymer membranes incorporating metal–organic framework nanocrystals. *Nat. Mater.* **2016,** *15*, 845.

3. Hibbe, F.; Chmelik, C.; Heinke, L.; Pramanik, S.; Li, J.; Ruthven, D. M.; Tzoulaki, D.; Kärger, J., The Nature of Surface Barriers on Nanoporous Solids Explored by Microimaging of Transient Guest Distributions. *J. Am. Chem. Soc.* **2011,** *133* (9), 2804-2807.

4. Kärger, J., In-depth study of surface resistances in nanoporous materials by microscopic diffusion measurement. *Microporous Mesoporous Mater.* **2014,** *189*, 126-135.

5. Remi, J. C. S.; Lauerer, A.; Chmelik, C.; Vandendael, I.; Terryn, H.; Baron, G. V.; Denayer, J. F. M.; Kärger, J., The role of crystal diversity in understanding mass transfer in nanoporous materials. *Nat. Mater.* **2015,** *15*, 401.

6. Arya, G.; Maginn, E. J.; Chang, H.-C., Effect of the Surface Energy Barrier on Sorbate Diffusion in AlPO4-5. *J. Phys. Chem. B* **2001,** *105* (14), 2725-2735.

7. Newsome, D. A.; Sholl, D. S., Predictive Assessment of Surface Resistances in Zeolite Membranes Using Atomically Detailed Models. *J. Phys. Chem. B* **2005,** *109* (15), 7237-7244.

8. Newsome, D. A.; Sholl, D. S., Molecular Dynamics Simulations of Mass Transfer Resistance in Grain Boundaries of Twinned Zeolite Membranes. *J. Phys. Chem. B* **2006,** *110* (45), 22681-22689.

9. Newsome, D. A.; Sholl, D. S., Influences of Interfacial Resistances on Gas Transport through Carbon Nanotube Membranes. *Nano Lett.* **2006,** *6* (9), 2150-2153.

10. Newsome, D. A.; Sholl, D. S., Atomically detailed simulations of surface resistances to transport of CH_4, CF_4, and C_2H_6 through silicalite membranes. *Microporous Mesoporous Mater.* **2008,** *107* (3), 286-295.

11. Kočiřík, M.; Struve, P.; Fiedler, K.; Bülow, M., A model for the mass-transfer resistance at the surface of zeolite crystals. *J. Chem. Soc., Faraday Trans. 1* **1988,** *84* (9), 3001-3013.

12. Ahunbay, M. G.; Elliott, J. R.; Talu, O., Surface Resistance to Permeation through the Silicalite Single Crystal Membrane: Variation with Permeant. *J. Phys. Chem. B* **2004,** *108* (23), 7801-7808.

13. Ahunbay, M. G.; Elliott, J. R.; Talu, O., Effect of Surface Resistances on the Diffusion of Binary Mixtures in the Silicalite Single Crystal Membrane. *J. Phys. Chem. B* **2005,** *109* (2), 923-929.

14. Zimmermann, N. E. R.; Balaji, S. P.; Keil, F. J., Surface Barriers of Hydrocarbon Transport Triggered by Ideal Zeolite Structures. *J. Phys. Chem. C* **2012,** *116* (5), 3677-3683.

15. Zimmermann, N. E. R.; Smit, B.; Keil, F. J., On the Effects of the External Surface on the Equilibrium Transport in Zeolite Crystals. *J. Phys. Chem. C* **2010,** *114* (1), 300-310.

16. Sastre, G.; Kärger, J.; Ruthven, D. M., Molecular Dynamics Study of Diffusion and Surface Permeation of Benzene in Silicalite. *J. Phys. Chem. C* **2018,** *122* (13), 7217-7225.

17. Glavatskiy, K. S.; Bhatia, S. K., Thermodynamic Resistance to Matter Flow at The Interface of a Porous Membrane. *Langmuir* **2016,** *32* (14), 3400-3411.

18. Liu, L.; Nicholson, D.; Bhatia, S. K., Interfacial Resistance and Length-Dependent Transport Diffusivities in Carbon Nanotubes. *J. Phys. Chem. C* **2016,** *120* (46), 26363-26373.

19. Varanasi, S. R.; Subramanian, Y.; Bhatia, S. K., High Interfacial Barriers at Narrow Carbon Nanotube–Water Interfaces. *Langmuir* **2018,** *34* (27), 8099-8111.

20. Kresse, G.; Furthmüller, J., Efficient iterative schemes for ab initio total-energy calculations using a plane-wave basis set. *Phys. Rev. B* **1996,** *54* (16), 11169-11186.

21. Kresse, G.; Furthmüller, J., Efficiency of ab-initio total energy calculations for metals and semiconductors using a plane-wave basis set. *Comput. Mater. Sci* **1996,** *6* (1), 15-50.

22. Kresse, G.; Hafner, J., Ab initio. *Phys. Rev. B* **1993,** *47* (1), 558-561.

23. Zimmermann, N. E. R.; Jakobtorweihen, S.; Beerdsen, E.; Smit, B.; Keil, F. J., In-Depth Study of the Influence of Host−Framework Flexibility on the Diffusion of Small Gas Molecules in One-Dimensional Zeolitic Pore Systems. *J. Phys. Chem. C* **2007,** *111* (46), 17370-17381.

24. Camp, J. S.; Sholl, D. S., Transition State Theory Methods To Measure Diffusion in Flexible Nanoporous Materials: Application to a Porous Organic Cage Crystal. *J. Phys. Chem. C* **2016,** *120* (2), 1110-1120.

25. C Ford, D.; Dubbeldam, D.; Q Snurr, R., *The Effect of Framework Flexibility on Diffusion of Small Molecules in the Metal-Organic Framework IRMOF-1*. 2009; Vol. 11.

26. Calero Diaz, S., Modeling of Transport and Accessibility in Zeolites. In *Zeolites and Catalysis*.

27. Dutta, R. C.; Bhatia, S. K., Structure and Gas Transport at the Polymer–Zeolite Interface: Insights from Molecular Dynamics Simulations. *ACS Appl. Mater. Interfaces* **2018,** *10* (6), 5992-6005.

28. Dutta, R. C.; Bhatia, S. K., Transport Diffusion of Light Gases in Polyethylene Using Atomistic Simulations. *Langmuir* **2017,** *33* (4), 936-946.

29. Goodbody, S. J.; Watanabe, K.; MacGowan, D.; Walton, J. P. R. B.; Quirke, N., Molecular simulation of methane and butane in silicalite. *J. Chem. Soc. Faraday Trans.* **1991,** *87* (13), 1951-1958.

30. Sun, H.; Mumby, S. J.; Maple, J. R.; Hagler, A. T., An ab Initio CFF93 All-Atom Force Field for Polycarbonates. *J. Am. Chem. Soc.* **1994,** *116* (7), 2978-2987.

31. Plimpton, S., Fast Parallel Algorithms for Short-Range Molecular Dynamics. *J. Comput. Phys.* **1995,** *117* (1), 1-19.

32. Purton, J. A.; Crabtree, J. C.; Parker, S. C., DL_MONTE: a general purpose program for parallel Monte Carlo simulation. *Mol Simul.* **2013,** *39* (14-15), 1240-1252.

33. Zhu, F.; Tajkhorshid, E.; Schulten, K., Collective Diffusion Model for Water Permeation through Microscopic Channels. *Phys. Rev. Lett.* **2004,** *93* (22), 224501.

34. Skoulidas, A. I.; Sholl, D. S., Molecular Dynamics Simulations of Self-Diffusivities, Corrected Diffusivities, and Transport Diffusivities of Light Gases in Four Silica Zeolites To Assess Influences of Pore Shape and Connectivity. *J. Phys. Chem. A* **2003,** *107* (47), 10132-10141.

35. Sholl, D. S., Understanding Macroscopic Diffusion of Adsorbed Molecules in Crystalline Nanoporous Materials via Atomistic Simulations. *Acc. Chem. Res.* **2006,** *39* (6), 403-411.

36. Krishna, R., Multicomponent surface diffusion of adsorbed species: a description based on the generalized Maxwell—Stefan equations. *Chem. Eng. Sci.* **1990,** *45* (7), 1779-1791.

37. Mason, E. A.; Malinauskas, A. P.; Evans, R. B., Flow and Diffusion of Gases in Porous Media. *J. Chem. Phys.* **1967,** *46* (8), 3199-3216.

38. Kärger, J.; Pfeifer, H.; Stallmach, F.; Spindler, H., 129Xe n.m.r. self-diffusion measurements — a novel method to probe diffusional barriers on the external surface of zeolite crystallites. *Zeolites* **1990,** *10* (4), 288-292.

39. Glavatskiy, K. S.; Bhatia, S. K., Effect of pore size on the interfacial resistance of a porous membrane. *J. Membr. Sci.* **2017,** *524*, 738-745.

40. Rincon Bonilla, M.; Bhatia, S. K., Diffusion in Pore Networks: Effective Self-Diffusivity and the Concept of Tortuosity. *J. Phys. Chem. C* **2013,** *117* (7), 3343-3357.

41. Robeson, L. M., The upper bound revisited. *J. Membr. Sci.* **2008,** *320* (1), 390-400.

Chapter 7 Structure and Gas Transport at the Polymer-Zeolite Interface

The content of this chapter is published as:

Ravi C. Dutta and SK. Bhatia, Structure and gas transport at the polymer–zeolite Interface: Insights from molecular dynamics simulations, *ACS Appl. Mater. Interfaces*, 10, 5992 (2018).

Contributor	Statement of contribution
Ravi C Dutta	Programmed and conducted simulations (100%) Analysis and interpretation of data (80%) Wrote the paper (80%)
Suresh K. Bhatia	Wrote the paper (20%) Analysis and interpretation of data (20%)

7.1 Introduction

Mixed matrix membranes (MMMs) have been conventionally prepared by incorporating inorganic fillers such as zeolites,[1] metal organic framework (MOFs)[2, 3] and carbon nanotubes (CNTs)[4] in a continuous polymer matrix. However, the ultimate success of these advanced membranes depends on the material selection and interface defect elimination. Nevertheless, the past decade has witnessed substantial progress both theoretically and experimentally on the selection aspects of these materials for a given application by considering fundamental intrinsic material properties of the individual phases.[5, 6] On the other hand, interface-related problems such as the formation of non-selective voids, rigidified polymer and pore blockage are still challenging. Although the polymer-filler interface occupies only a small fraction of the membrane volume, it appears to effect the MMM performance significantly. Thus, understanding and minimizing interfacial barriers between the polymer and the inorganic filler are therefore critical to the design and optimization of such membranes.

The polymer-filler interface can be of four types depending on the nature of the interaction between the constituents. The first is an ideal interface with properties nearly similar to those of the bulk polymer, which arises when polymer-filler and polymer-polymer interactions are comparable, leading to a homogenous polymer-filler blend. The separation performance of resulting MMM can be superior to the corresponding neat polymer membrane and has traditionally been described by the Maxwell model, although recent work from this laboratory has shown this model to be accurate only at small filler loading below about 20% by volume.[7] Secondly, a weak interaction between the polymer and filler than the polymer and polymer could lead to the formation of non-selective interfacial voids around the filler or 'sieve in a cage' configuration.[8, 9] Such a MMM results in higher permeability with reduction in selectivity, as the gas molecules take the least resistance path offered by the voids. Further, these voids can affect the mechanical integrity of the membrane. The third is formation of rigidified layer of polymer at the interface,[10] due to strongly attractive interaction between the polymer and filler than the polymer and polymer. This polymer in the rigidified layer has more restricted chain motion than in the bulk, which reduces gas permeability. This results in reduction in both permeability and selectivity. The last is plugged sieves, in which the surface pores of the zeolites have been partially blocked by the polymer.[8] This leads to reduction in the gas permeability in the composite system. Thus, the nature of the polymer-filler interface can strongly affect the overall membrane performance. This highlights the importance of design of the polymer-filler interface to achieve better gas separation performance than the corresponding pure polymer membrane.

While much effort has been devoted to the experimental design and fabrication of defect free MMMs for gas transport in the literature, success has been modest. Nair et al.[11] fabricated a defect free MMM comprising sub-micrometer size ZIF-90 and polyimide (PI), demonstrating superior separation performance for CO_2 over CH_4. Kim et al.[12] successfully synthesized a defect free MCM-48 silica/polysulfone MMM, and reported an increase in gas permeability resulting from increase in both solubility and diffusivity without sacrificing selectivity. On the other hand, several investigations have reported the presence of interfacial defects in the MMM, [1, 10, 13] and proposed methods to improve the polymer-filler compatibility. However, direct experimental characterization of the polymer conformation in the presence of inorganic filler is challenging, and indirect measurements such as field emission scanning microscopes(FESEM),[12] small angle neutron scattering (SANS),[14, 15] positron annihilation lifetime spectroscopy(PALS)[16] and differential scanning calorimetry (DSC)[17] are therefore used. Further, the effect of filler size, shape and loading on the structure of the polymer at the interface and thus gas separation performance is not clear, and requires trial and error experimentation. On the other hand, most of the earlier simulation reports based on either atomistic[18] or coarse grained or multiscale modeling[9, 13, 19] simulation approaches have successfully characterized the interface between the filler and the polymer. The results indicate the presence of microscopic void regions[9, 13] or pore blockage[19] or the formation of a rigidified region.[20] Zhang et al.[2] investigated H_2/CO_2 separation performance in a MMM comprising polybenzimidazole (PBI) and zeolitic imidazolateframework-7 (ZIF-7) using equilibrium molecular dynamics (EMD) simulations. They observed that increase in ZIF-7 loading leads to increase in H_2 diffusivity, and attributed this behavior to the presence of interfacial voids between ZIF-7 and PBI. Nevertheless, the issue of the influence of interfacial structure on gas transport remains an open question; and a thorough investigation of gas transport near the interface, including the sorption isotherms considering the structural transitions upon gas sorption in-detail through EMD simulations is required to quantitatively understand MMM behavior, and provide information necessary for the *in silico* design for MMMs.

In this chapter, we investigate the gas transport in a PI-MFI zeolite composite system through EMD simulations. PI's are most extensively investigated membrane materials as they exhibit relatively high gas selectivity and permeability. On the other hand, zeolites display superior CO_2 adsorption due to its higher molecular weight and electrostatic quadrupole moment compared to other light gases. In addition, zeolites such as MFI with three dimensional pore networks offer less restrictive pathways for gas diffusion, and are therefore attractive materials for the gas separation. To the best of our knowledge, this is the first report that explores the microscopic structure of the polymer at the polymer-MFI zeolite interface and its influence on the gas transport in the hybrid MMM system in-detail through EMD simulations. Further, an important aspect of this study is the insight into the gas diffusion at the interface (rigidified region) between the polymer and filler. In addition, we extract the sorption isotherms in PI and the PI-MFI composite system by considering the structural transitions upon gas sorption, implementing a two-step methodology combining Grand canonical Monte Carlo simulations (GCMC) coupled with NPT (Constant Number of particles, Pressure and Temperature) equilibrium molecular dynamics (EMD) simulations.

7.2 Model system and simulations

Our system comprises a MFI zeolite unit cell sandwiched between two PI polymer-filled regions, representing a model MMM, as depicted in Figure 7-1, in which we investigate the interfacial structure of the polymer by considering all the soft matter interactions including different competing interactions, and the sorption and transport of pure component CO_2 and CH_4. The system is assumed periodic in all three directions. In what follows we describe the main elements of the model, and the corresponding interaction potential parameters used in the simulations.

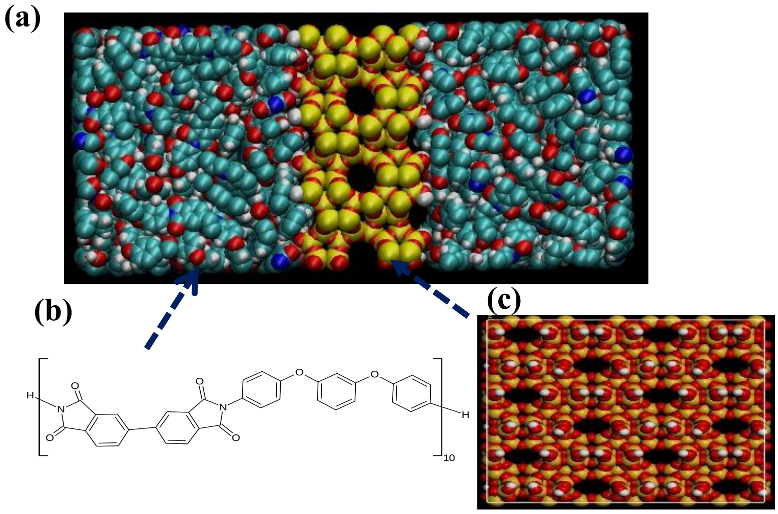

Figure 7-1: Structure of the (a) PI-MFI hybrid system, (b) BPDA-APB polyimide polymer chain, and (c) MFI surface.

7.2.1 Polymer Model

The model polymer system is composed of 15 flexible PI chains, each having 10 monomers of biphenyltetracarboxylic dianhydride (BPDA) and 1,3-bis(4-aminophenoxy)benzene (APB) and was generated by following a self-avoiding random walk technique using Packmol.[21]

7.2.2 The MFI Surface

To model the MFI surface, we considered all-silica-type silicalite (MFI) which consists of interconnected network of straight and sinusoidal channels having two sets of interconnected 10-ring pores of different sizes. Each O-atom in the zeolite was assumed to interact with other atoms in the system through both LJ potential and electrostatic interactions, following

$$U_{ij}^{non-bond} = 4\varepsilon_{ij}\left[\left(\frac{\sigma_{ij}}{r_{ij}}\right)^{12} - \left(\frac{\sigma_{ij}}{r_{ij}}\right)^{6}\right] + \sum_{i,j}\frac{q_i q_j}{r_{ij}} \tag{7-1}$$

while Si-atoms were considered to interact only via electrostatic interactions. Here q_i is the electrostatic charge on site *i*. The Si and O- atoms were assigned partial charges of +2 and -1 respectively. The potential parameters used to represent the MFI surface.[23] A 2 x 2 x 3-unit cell (U.C.) is used to study the gas transport in the MFI system. In the case of the PI-MFI system, the surface in contact with the polymer was cleaved at the (1 0 0) plane, and all the surface oxygen and silica atoms were capped with hydrogen atoms and hydroxyl groups respectively. The resulting structure was relaxed by employing conjugate gradient method without optimizing the cell dimensions using VASP software.[24-26] The structure of the MFI surface after relaxation is shown in Figure 7-1(c). The MFI surface is treated as rigid in the entire simulation.

7.2.3 Methodology

Diffusion coefficient in different regions: The corrected diffusivity, D_o, describes the collective motion of all adsorbed molecules, and its overall value for the entire hybrid system can be computed from EMD simulations using an Einstein relationship, based on the center of mass (COM) motion,[29, 30] following:

$$D_0 = \frac{1}{6N}\lim_{t\to\infty}\frac{1}{t} < \| \sum_{i=1}^{N}\vec{r}_i(t) - \vec{r}_i(0) \|^2 > \tag{7-2}$$

where $r_i(t)$ is center of mass position vector of molecule *i* at time *t*.

In addition to the overall transport coefficient of the system, we extracted the collective diffusion coefficient of gas molecules in different regions, following the method of Zhu et al.[31]. Here, for a given region of length L_x, we calculate a collective coordinate, *n*, defined as

$$dn = \sum_{i\in s(t)}\frac{dz_i}{L_x} \tag{7-3}$$

where dz_i is displacement of gas molecule *i* in the *z* direction during time *dt* in that region. The quantity *n(t)* can be uniquely determined by integrating the above ODE using the stored trajectory data from an EMD run. Gas molecules crossing the channel from one region to the other contribute to *n* by -1 or +1 based on whether they are entering or leaving the region respectively. The mean square displacement (MSD) of *n*, over sufficiently long time obeys the Einstein relation following[31]:

$$D_n = \frac{< n^2(t) >}{2t} \tag{7-4}$$

The net molar flux (j) of any gas close to equilibrium conditions can be related to D_n as:[31]

$$j = \frac{D_n.L_x}{A_c k_B T}\frac{d\mu}{dz} \tag{7-5}$$

where A_c is cross-sectional area of the region of length L_x, k_B is the Boltzmann constant, T is the temperature of the system and μ is chemical potential. More commonly, the net molar flux of a gas is calculated from the irreversible thermodynamics-based description of the transport, considering the chemical potential gradient as the driving force for the mass transport and diffusion of a single component through the system, following the flux model[32-34]

$$j = \frac{D_o\rho}{k_B T}\left(\frac{d\mu}{dz}\right) \tag{7-6}$$

where D_o is collective diffusivity, and ρ is the ensemble averaged mass density. The collective diffusion coefficient D_o can be related D_n , by comparing eq (7-5) and eq (7-6), to yield:

$$D_o = \frac{D_n.L_x}{\rho.A_c} = \frac{D_n L_x^2}{< N_{mol} >} \tag{7-7}$$

Where $<N_{mol}>$is the ensemble averaged number of gas molecules in any given region of length L_x. We note that, for single component systems the corrected diffusivity is proportional to the Maxwell-Stefan (MS) diffusivity.[35]

The above method was used to determine the collective diffusion coefficient in both the MFI and the interfacial region. The latter region could be unequivocally defined based on our simulation results of the polymer structure, which showed its thickness to be 1.2 nm for the chosen PI-MFI zeolite system, as discussed subsequently. As a cross-check of the collective diffusivity values for the different regions determined by the above method, we note that the total resistance for flow through the sandwich must additively comprise that for flow in the zeolite, the two interface regions adjacent to the zeolite and the two bulk polymer regions. To demonstrate this, we appeal to eq (7-6), and for a very small chemical potential difference, the net flux (j) through the overall system of length L, as shown in Figure 7-2, can be accordingly written as

$$j = \frac{D_o\rho}{L}\frac{(f_1 - f_2)}{f} \tag{7-8}$$

where f is fugacity, and $f = f_1 \sim f_2 = \frac{1}{2}(f_1 + f_2)$. Applying eq (7-8) to each region provides

$$\begin{aligned} j &= \frac{D_{o,eff}\rho_{eff}}{L}\frac{(f_1 - f_2)}{f} = \frac{D_{o,b}\rho_b}{L_{b,1}}\frac{(f_1 - f_1^{'})}{f} \\ &= \frac{D_{o,I}\rho_I}{L_{I,1}}\frac{(f^{'}_1 - f_1^{''})}{f} = \frac{D_{o,s}\rho_s}{L_s}\frac{(f^{''}_1 - f_2^{''})}{f} \\ &= \frac{D_{o,I}\rho_I}{L_{I,2}}\frac{(f_2^{''} - f_2^{'})}{f} = \frac{D_{o,b}\rho_b}{L_{b,2}}\frac{(f_2^{'} - f_2)}{f} \end{aligned} \tag{7-9}$$

where $\rho_{eff} = \frac{\rho_b L_{b,1} + \rho_I L_{I,1} + \rho_s L_s + \rho_I L_{I,2} + \rho_b L_{b,2}}{L}$ is the overall density in the system, ρ_b and ρ_I are the mean adsorbate densities in the bulk and interfacial regions of the polymer respectively, and ρ_s is the mean adsorbate density in the MFI, at the same fugacity f. Further, $D_{o,eff}$ is the overall collective transport coefficient of the entire system, while $D_{o,b}$, $D_{o,I}$ and $D_{o,s}$ are the collective diffusivities in the bulk polymer, interfacial region and the zeolite, respectively. Upon rearranging eq (7-9) we obtain

$$\frac{L_{b,1}}{D_{o,b}\rho_b} + \frac{L_{I,1}}{D_{o,I}\rho_I} + \frac{L_s}{D_{o,s}\rho_s} + \frac{L_{I,2}}{D_{o,I}\rho_I} + \frac{L_{b,2}}{D_{o,b}\rho_b} = \frac{L}{D_{o,eff}\rho_{eff}} \tag{7-10}$$

The diffusivity in the interfacial region can then be obtained as

$$D_{o,I} = \frac{\left(L_I \middle/ \rho_I \right)}{\left(\frac{L}{D_{o,eff}\rho_{eff}} - \frac{L_b}{D_{o,b}\rho_b} - \frac{L_s}{D_{o,s}\rho_s} \right)} \tag{7-11}$$

where $L_{b,1} + L_{b,2} = L_b$ and $L_{I,1} + L_{I,2} = L_I$. We note here that since the above analysis is based on a very small fugacity difference, the diffusion coefficients and adsorbate densities in eq (7-11) represent the values at the same fugacity f. Agreement of the value of $D_{o,I}$ using eq (7-11) with that directly calculated for the interfacial region using eq (7-7) from the same EMD run (i.e. at the densities and diffusion coefficients corresponding to the same uniform fugacity or chemical potential) provides confirmation of the results and validity of the methods used here.

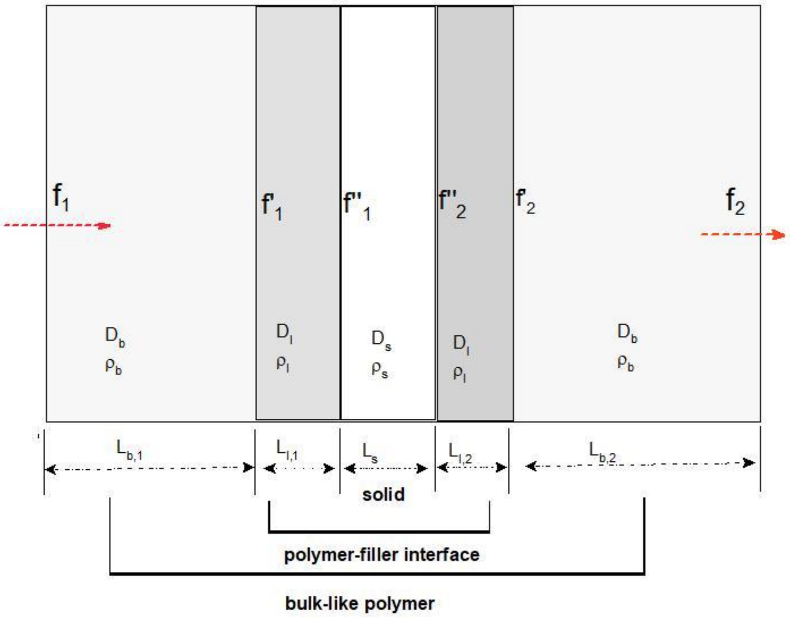

Figure 7-2: Schematic representation of different regions in MMM with the non-ideal interface.

7.3 Results and discussions

7.3.1 Interfacial structure characterization

The structure of the PI in the vicinity of the MFI zeolite was explored by computing the polymer density as a function of distance from the MFI zeolite using a binning procedure, where the simulation cell is divided into narrow bins of 1 Å each in the direction normal to the surface. Figure 7-3 (a) depicts the density of PI as a function of distance from the MFI surface. In Figure 7-3 (a), the region 'S' having zero polymer density represents zeolite MFI. We note here that no polymer penetration into MFI pores is observed. The region 'I' represents the interface between PI and MFI. It is seen that PI shows the layering behavior near the surface with the first layer being 30-40% denser than the bulk polymer, indicating the existence of densified polymer at the interface. We note here that the interface region has thickness around 1.2 nm, including 2-3 layers of the rigidified polymer, before being bulk-like in region 'B'. We also note that no zeolite is included in the interface region. The reported interfacial thickness contrasts with literature reported values of 0.04-0.88 µm,[56, 57] based on empirical fitting of mixed matrix membrane transport data. On the other hand, the above results are consistent with recent findings by Semino et al. that the interface void region is extended up to 9-13 Å.[9, 13] in polymers of intrinsic microporosity in the presence of ZIF-8. Further, the variation of mass density of the PI-MFI system with temperature is shown in the Supporting Information (Figure S9). It is seen that mass density of the PI-MFI system decreases linearly with increase in temperature with change in slope at 600 (± 25) K, corresponding to the glass transition temperature. The increase in glass transition temperature with the incorporation of MFI is consistent with the presence of the rigidified region at the interface.

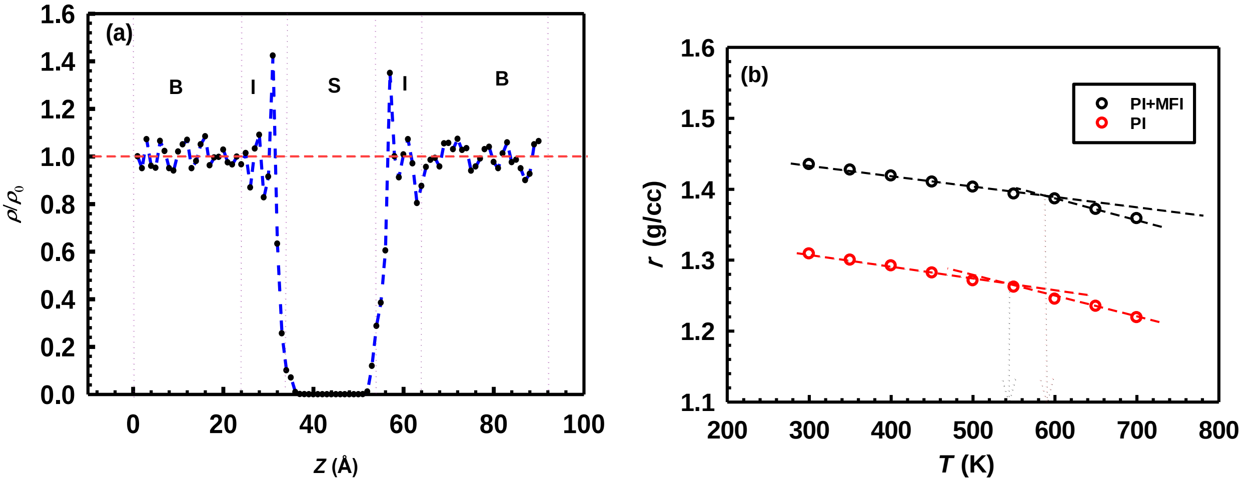

Figure 7-3: (a) Density profile of PI in the PI-MFI composite system at T=300K, (b) Temperature dependence of the density of PI and PI-MFI composite.

In addition, the local chain confirmation of the PI polymer in the bulk and rigidified region has been explored through the radial distribution function (RDF), *i.e.* atom-atom pair correlation function $g(r)$ between the aromatic carbons in PI (C_{arom}- C_{arom} units) separated by a distance r. Figure 7-4(a) depicts the C_{arom}- C_{arom} intermolecular RDF of PI polymer in the bulk and rigidified region at 300 K. A very slight shift towards left for the first two peaks which corresponds to closest contacts between C_{arom}-C_{arom} units in the rigidified region is observed. We note that all the peaks in the rigidified region is accompanied by increase in intensity of the intermolecular peaks. This suggests increase in number of intermolecular contacts in the rigidified region, an additional indication of the existence of the rigidified interfacial region. Further, the distribution of FVEs analysis confirms the absence of free volume elements larger than about 4 Å in the rigidified region as shown in Figure 7-4(b).

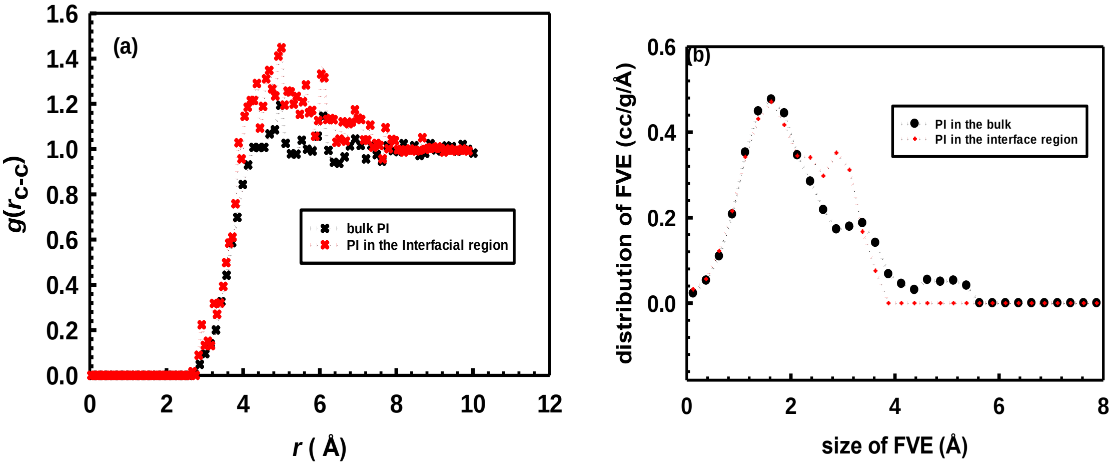

Figure 7-4: (a) C_{arom}−C_{arom} intermolecular RDF of the PI in the bulk and rigidified regions, and (b) cumulative distribution of FVEs in PI in the bulk and rigidified regions at 300K.

7.3.2 Sorption isotherms in PI-MFI composite

It is expected that incorporation of MFI into PI will lead to significant increase in the gas sorption capacity of the composite system compared to the neat polymer, due to the higher gas adsorption capacity of the MFI zeolite. The gas sorption capacity in the PI-MFI composite system is investigated by exploring the gas sorption isotherms using GCMC simulations coupled with EMD simulations in the isobaric ensemble as described in Chapter 3 and elsewhere.[42] Figure 7-5 (a)-(b) shows the sorption isotherms of pure component CO_2 and CH_4 in the PI-MFI composite membrane in the temperature range of 300-500 K. It is seen that the gas absorption is significantly enhanced by the incorporation of MFI zeolite into PI. Further, we note that gas sorption increases with increase in pressure at a given temperature. The sorption isotherm of each gas considered was fitted using a DM sorption model. The dashed lines in Figure 7-5, represent the isotherms fitted using DM sorption model. The fitting parameters of the DM sorption model, $C_H^{'}$ and k_d from this study, are tabulated in Table 7-1 and the solubility coefficients of CO_2 and CH_4 at infinite dilution in the PI membrane, MFI membrane and PI-MFI membrane at 300 K are tabulated in Table 7-2.

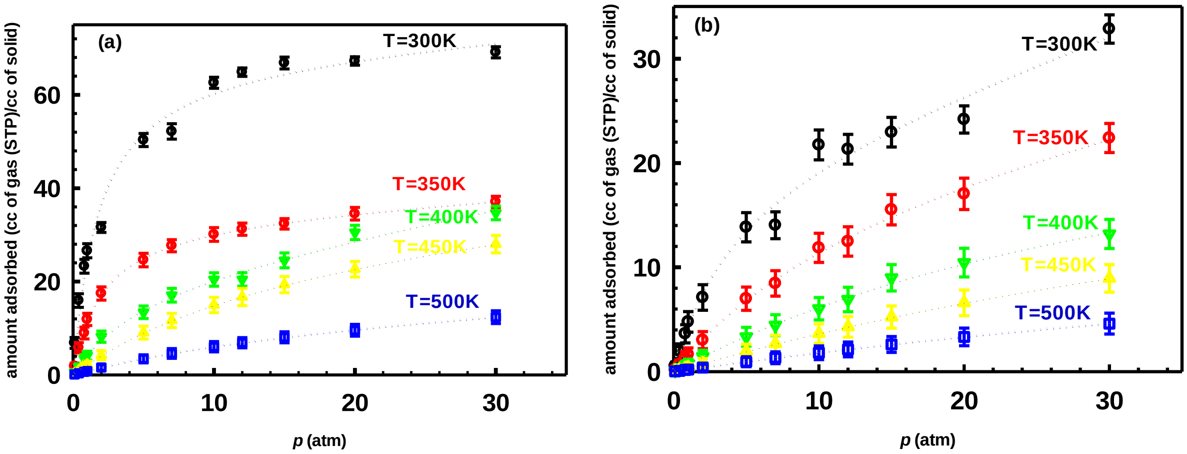

Figure 7-5: Sorption isotherms of (a) CO_2 and (b) CH_4 in PI-MFI composite membrane at various temperatures. The dashed lines indicate the fitted sorption isotherms using the DM sorption model.

Table 7-1: Temperature variation of fitting parameters of the DM sorption model in PI-MFI system.

T (K)	$C_H^{'}$ (cc (STP)/cc.atm)		k_d (cc (STP)/cc.atm)	
	CO_2	CH_4	CO_2	CH_4
300	65.22	4.862	0.21	0.472
350	16.75	1.495	0.18	0.26
400	4.50	0.768	0.56	0.14
450	2.10	0.416	0.24	0.08
500	0.71	0.175	0.138	0.0263

Table 7-2: Comparison of solubility and diffusion coefficients of CO_2 and CH_4 in PI, MFI and PI-MFI composite membranes at 300K.

Membrane	S (cc (STP)/cc.atm)		D_o (m^2/sec)	
	CO_2	CH_4	CO_2	CH_4
PI	16(±1.0)	1.5(±0.5)	$5.5(\pm1.0) \times 10^{-12}$	$1.6(\pm0.5) \times 10^{-12}$
MFI	13(±1.0)	1.2(±0.3)	$2.6(\pm0.8) \times 10^{-9}$	$1.7(\pm0.5) \times 10^{-8}$
PI-MFI	60(±5)	4.8(±0.8)	$3.8(\pm0.8) \times 10^{-12}$	$1.1(\pm0.4) \times 10^{-12}$

Further, we note that the presence of the rigidified layer affects the gas sorption the polymer in the PI-MFI hybrid system. To demonstrate this, we compared the sorption isotherms in PI in the presence of MFI at 300K with those in the neat PI as shown in Figure 7-6 (a)-(b). It is seen that gas sorption capacity of PI in the presence of MFI for both CO_2 and CH_4 is less than that of the neat PI. This is due to presence of the 1.2 nm thick rigidified region near the MFI surface. Further, we note that this effect is more pronounced for CH_4 than CO_2.

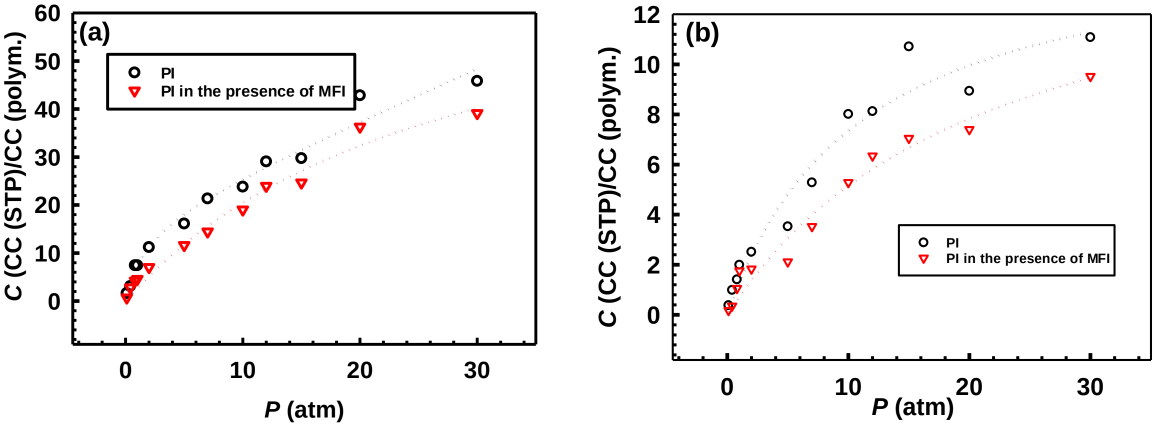

Figure 7-6:Sorption isotherms of (a) CO_2 and (b) CH_4 in PI with and without MFI at 300 K. The dotted lines indicate the fitted sorption isotherms using the DM sorption model.

Figure 7-7 shows the temperature dependence of simulated solubility coefficients for CO_2 and CH_4 in PI-MFI hybrid system at temperatures from 300 to 500 K. It is observed that the solubility of CO_2 and CH_4 significantly increases compared to the neat polymer. Further, it is seen that solubility of the gases decreases with increase in temperature, leading to negative heat of solutions of for CO_2 and CH_4, consistent with the sorption being exothermic. The heats of solutions, computed from eq (17), for CO_2 and CH_4 are -17.8 (±1.5) kJ/mol and -19.6 (±1.2) kJ/mol respectively. Interestingly, the heat of absorption of CH_4 in the composite is larger than that of CO_2, although it is lower in both the neat PI and the MFI. This is due to the greater reduction of CH_4 absorption compared to CO_2 in the rigidified region, and greater opening up of the pore spaces in this region to CH_4 with increase in temperature.

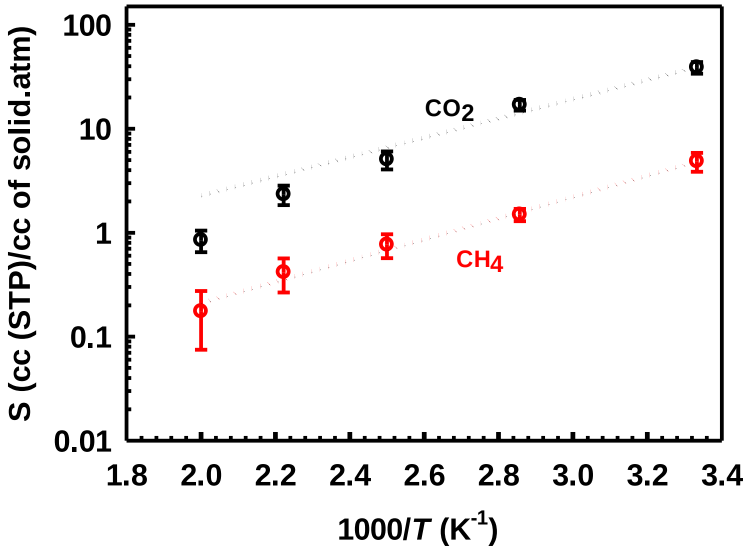

Figure 7-7: Temperature dependence of solubility coefficients in PI-MFI composite system.

7.3.3 Transport of CO_2 and CH_4 in PI-MFI composite system

The diffusion behavior of CO_2 and CH_4 in the PI-MFI membrane was systematically investigated in the direction normal to the surface by computing pure component collective diffusivities of each gas in the temperature range of 300-500 K. At 300 K, the calculated values of D_o in the direction normal to the surface for CO_2 and CH_4 in the PI-MFI hybrid system are 3.8 (± 0.8) × 10^{-12} and 1.1 (± 0.3) × 10^{-12} m^2/sec respectively. Figure 7-8 (a) depicts the temperature dependence of the collective-diffusion coefficients of CO_2 and CH_4 in the composite membrane normal to the surface in the temperature range of 300-500 K. It is seen that the temperature dependence of the collective-diffusion coefficients of CO_2 and CH_4 follow Arrhenius-type behavior, with activation energies of 19.23 (± 3) kJ/mole and 20.95 (± 2) kJ/mole respectively. We note that the overall collective diffusion coefficient for both CO_2 and CH_4 in the PI-MFI hybrid system is lower than that of both the neat polymer and the MFI zeolite, which may be attributed the presence of the rigidified region at the interface. The diffusion coefficients of CO_2 and CH_4 in the PI membrane, MFI membrane and PI-MFI membrane at 300 K are tabulated in the Supporting Information (Table S5). Therefore, to investigate the gas diffusion at the interface, we extracted the gas diffusivities in the rigidified region.

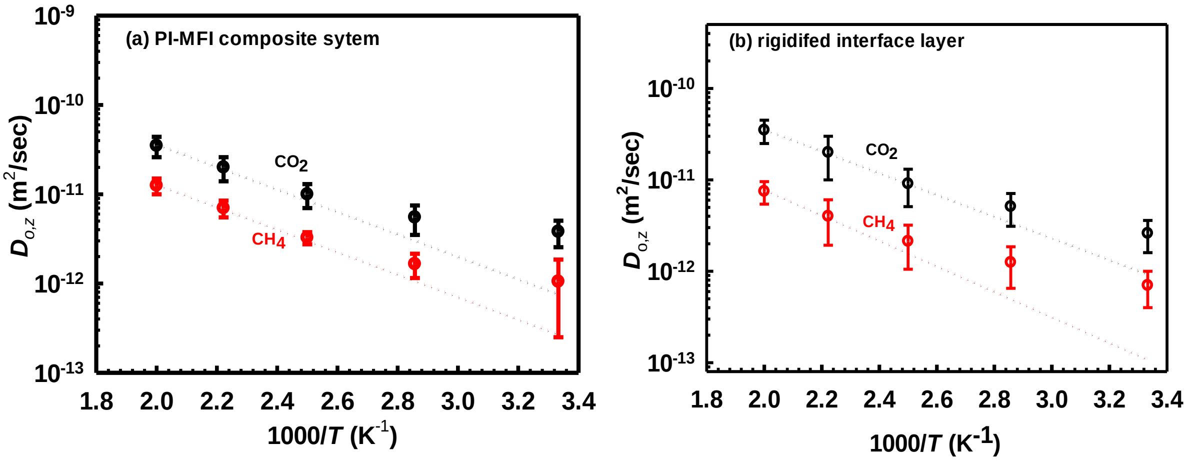

Figure 7-8: Temperature dependence of corrected diffusivities of CO_2 and CH_4 in the a) PI-MFI composite membrane and b) rigidified interfacial layer.

The diffusion behavior of CO_2 and CH_4 in the interface region in the direction normal to the surface was systematically investigated through the collective diffusion model (eqs (7-3) -(7-7)). Figure 7-8 (b) depicts the temperature dependence of the D_o of CO_2 and CH_4 in the interface region between PI and MFI (rigidified region) in the temperature range of 300-500 K, at 5 atm pressure. At 300 K, the calculated values of D_o of CO_2 and CH_4 are 2.75 (± 2) × 10^{-12} and 7.0 (± 2) × 10^{-13} m^2/sec respectively, much lower than the corresponding diffusivities in the neat polymer. Further, a moderate decrease in

D_o with increase in loading is observed for CO_2 and CH_4, as shown in Figure 7-9 (a). We note that gas diffusion at the interface in the xy- direction is slightly higher than the gas diffusion in the z-direction (normal to MFI surface), as shown in Figure 7-9 (b), which is due to the more uniform potential in the xy-direction than that in the z-direction. This suggests that the diffusion in the interface layer is slightly anisotropic. In addition, it is seen that the diffusion in the rigidified interfacial region is an activated process, with the temperature dependence of the collective-diffusion coefficients of CO_2 and CH_4 following Arrhenius-type behavior. The activation energies for CO_2 and CH_4 in the interface region, computed from eq (18), are 21 (± 3) kJ/mole and 19.0 (± 2) kJ/mole respectively.

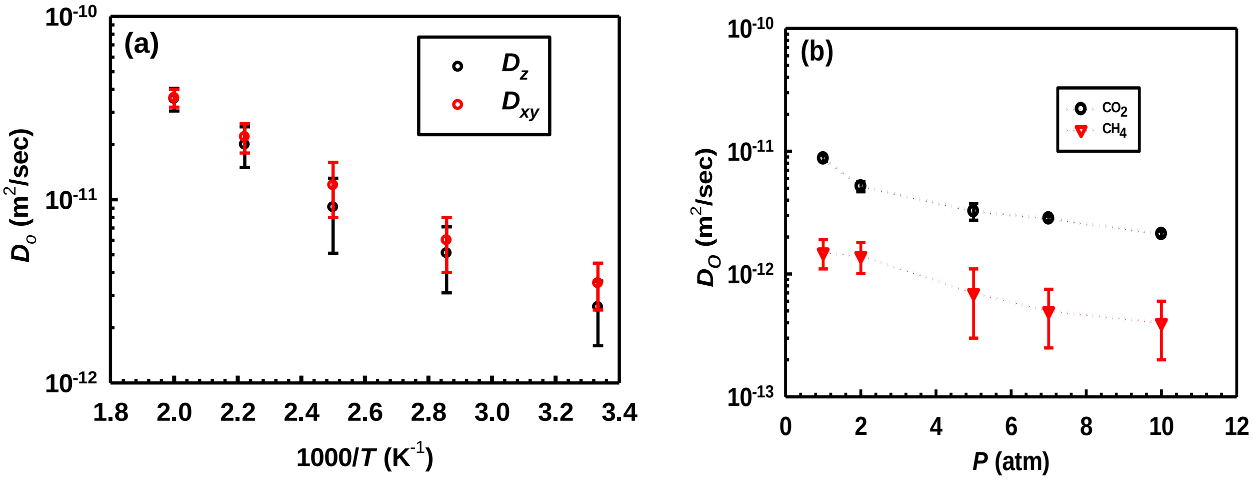

Figure 7-9: Temperature dependence of corrected diffusivities of CO_2 and CH_4 in z and xy- directions in the interfacial region in the PI-MFI hybrid membrane.

To demonstrate accuracy of the extracted diffusion coefficients in the interface region, we computed the gas diffusivities calculated using eq (7-11). Figure 7-10 depicts the comparison of extracted (based on the collective diffusion model in eqs (7-3) -(7-7) and calculated (based on eq (7-7)) interfacial gas diffusivities, showing good agreement between the estimates, confirming consistency of the methods used. This agreement also confirms the additivity of resistances in the zeolite, interfacial layer and the bulk-like polymer region in influencing permeation in the composite, as follows from eq (7-11).

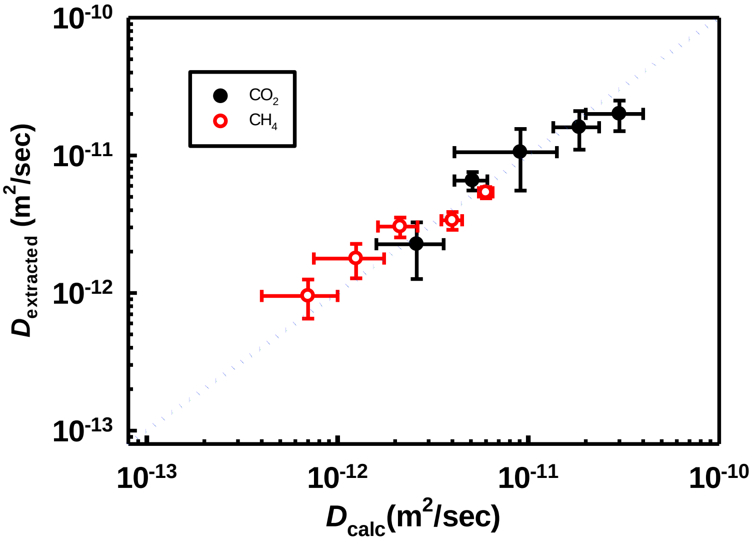

Figure 7-10: Comparison of the calculated (eq (12)) and extracted (eq (8)) diffusion coefficients in the interface region between the PI and MFI in PI-MFI composite membrane.

7.3.4 Effect of zeolite crystal size on interfacial layer properties

Figure 7-11 (a)-(c) depicts the crystal size dependence of the structure of the polymer near the interface and the gas diffusivity in the interface region. We considered crystals of 1, 2 and 4 unit cells size in the z-direction and explored the polymer density profiles. It is seen that the structure of the polymer in the interfacial region is independent of the crystal size, with thickness of the interface around 1.2 nm in all the cases, and the first layer 30-40% denser than the bulk. In addition, we observed that the corrected diffusivity of the gases in the interface region is independent of crystal size, due to the structure of the polymer being independent of the crystal size. However, the gas diffusion in the zeolite may depend on the size of the crystal as well as framework flexibility, which needs further investigation.

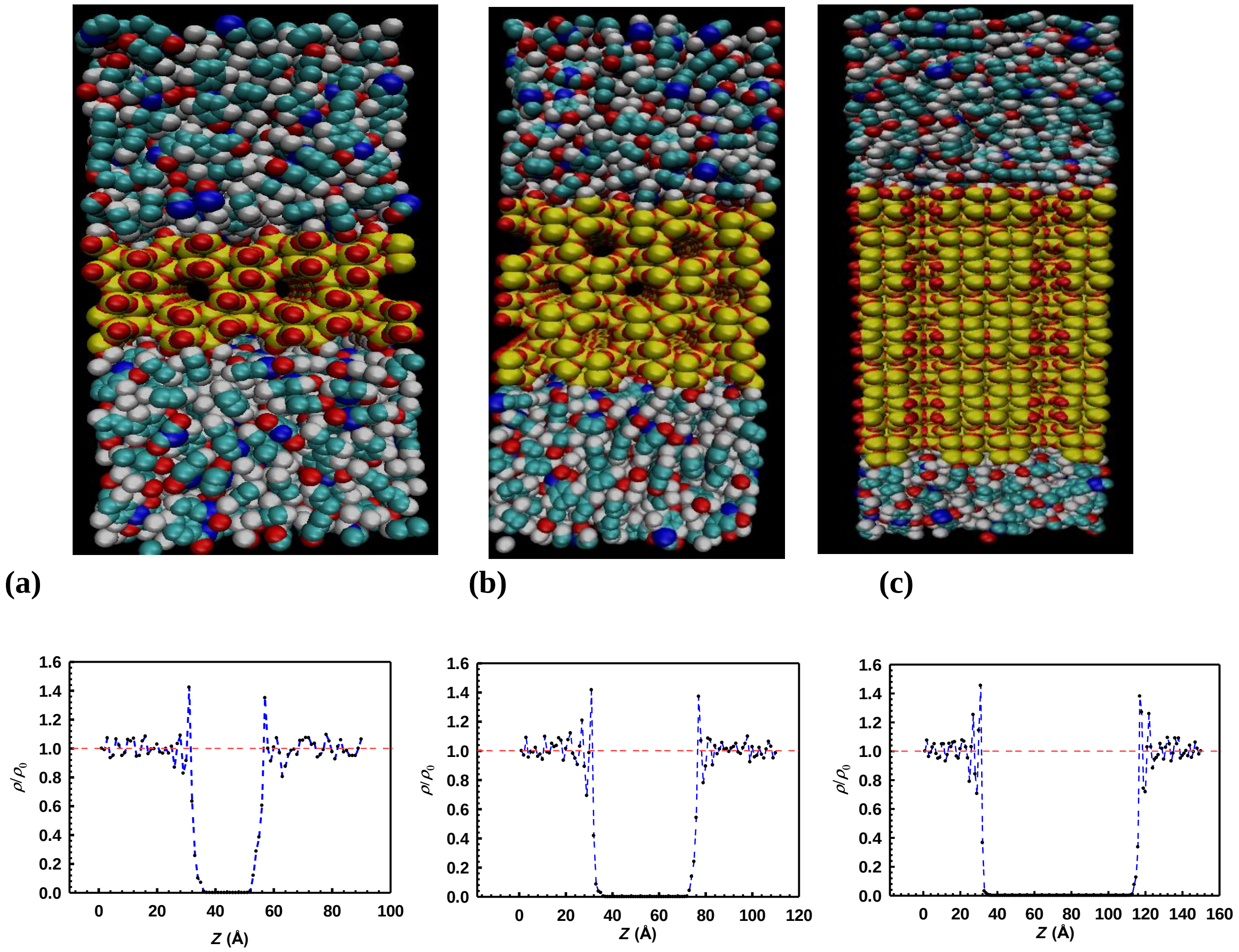

Figure 7-11:Crystal size dependence of the structure of PI in PI+ MFI composite system. (a) 1 U.C. (b) 2 U.C. and (c) 4 U.C.

7.3.5 Separation performance of PI-MFI composite membrane

Figure 7-12 depicts a comparison of the temperature dependence of the diffusivity selectivity of CO_2 over CH_4 in PI, PI-MFI membrane and the rigidified region at the interface between PI and MFI, in the temperature range of 300-500 K. It is seen that PI-MFI system shows higher CO_2/CH_4 diffusivity selectivity than the pure PI membrane system at all temperatures, and at 300 K the calculated diffusivity selectivity of CO_2 over CH_4 in the PI-MFI hybrid membrane is 3.6 (± 0.5), which is 16% higher than the corresponding neat polymer membrane. This selectivity increase in the composite is due to the extra resistance offered in the rigidified region to the gas with larger kinetic diameter, CH_4 in this case. Further, we note that selectivity of CO_2 over CH_4 in the rigidified region is around 30% higher than the pure polymer. It is seen that diffusivity selectivity of CO_2 over CH_4 decreases with increase in temperature for PI-MFI. This may be attributed to the presence of polymer rich phase (75% vol) in PI-MFI system, and similar behavior to that of pure PI is expected. On the other hand, it is seen that diffusivity selectivity of CO_2 over CH_4 increases with increase in temperature in the rigidified region.

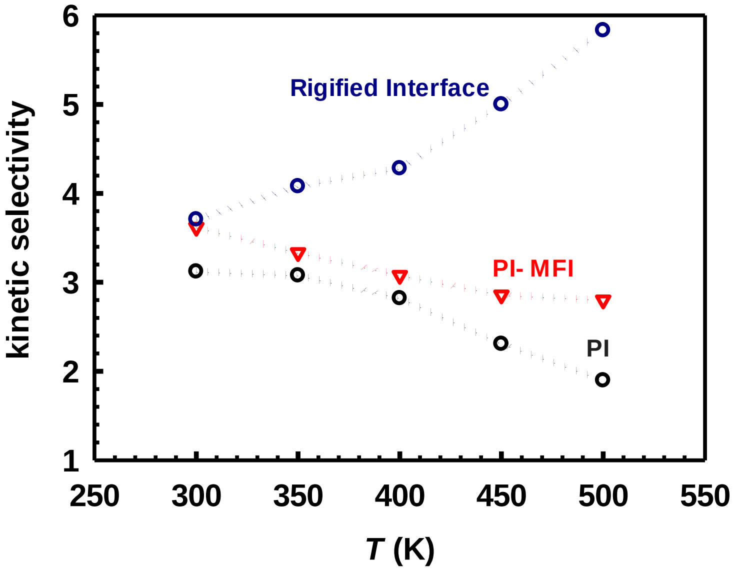

Figure 7-12: Temperature dependence of CO_2/CH_4 diffusivity selectivity in PI, PI-MFI and rigidified interfacial region between PI-MFI.

This is due to the availability of little free volume in the rigidified region, and the polymer structure is consequently less dependent on temperature in this region, as shown in Figure 7-13. Further, it may also be attributed to the greater increase in availability of narrow FVEs in the polymer at higher temperatures that are kinetically closed to the smaller gas molecule, CO_2 in this case, at lower temperatures.[58, 59] Further, we note that selectivity of CO_2 over CH_4 in the rigidified region is around 3 times higher than the pure polymer at 500K.

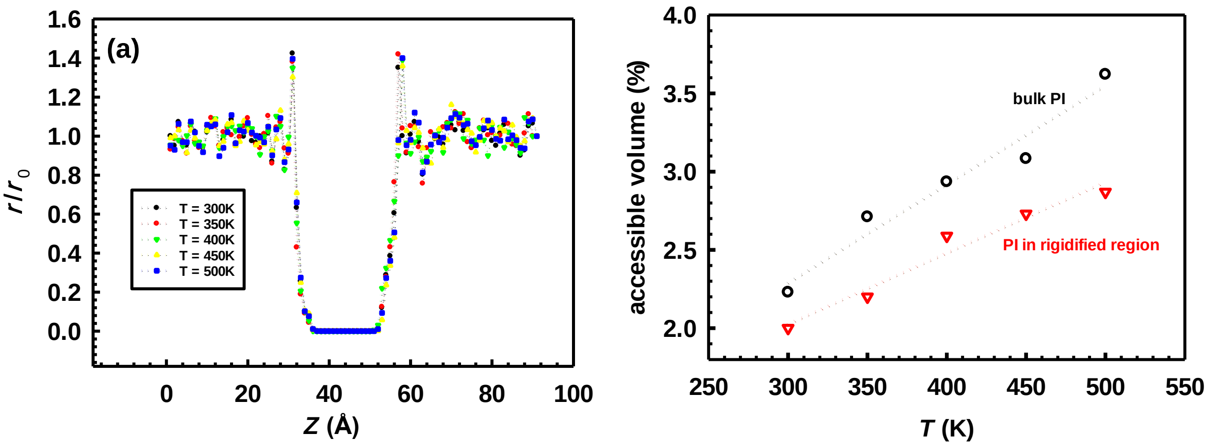

Figure 7-13: Temperature dependence of CO_2/CH_4 diffusivity selectivity in PI, PI-MFI and rigidified interfacial region between PI-MFI.

Figure 7-14 depicts a comparison of the temperature dependence of the diffusivity, solubility and perm- selectivity of CO_2 over CH_4 in PI, PI-MFI membrane and the rigidified region in the temperature range of 300-500 K. At 300 K, the calculated values of diffusivity, solubility and perm-selectivity of CO_2 over CH_4 are 3.6 (±0.3), 15 (±0.6), and 54 (±8.0) respectively. Further, we note incorporation of MFI in PI results in 65% improvement in perm-selectivity for CO_2, which includes around 15% and 50% improvement in the diffusivity and solubility selectivity respectively at 300K.

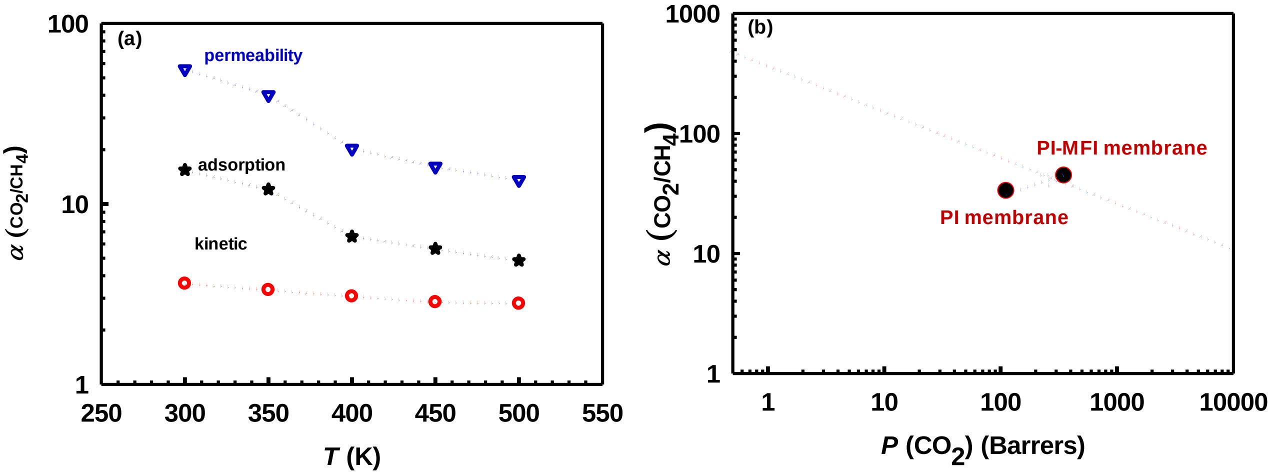

Figure 7-14: (a) Temperature dependence of selectivity of CO_2 in PI-MFI membrane, and (b) comparison of separation performance of the PI and PI-MFI membranes with Robeson upper bound.

The diffusivity, solubility and perm-selectivity of CO_2 over CH_4 in a neat PI polymer and PI-MFI composite membrane at 300 K are compared in Table 7-3, showing the composite PI-MFI membrane to have higher selectivity at this temperature. While Figure 7-14(a) shows that this selectivity decreases with increase in temperature, the PI-MFI composite is nevertheless more selective to CO_2 over CH_4 in the temperature range of 300-500K. Further, we note that this selectivity is higher than that of the neat PI membrane selectivity at all temperatures.

Table 7-3: Selectivity of CO_2 over CH_4 in PI and PI-MFI composite membrane at 300K.

Selectivity	Membrane system	
	PI	PI-MFI composite
Diffusivity	3.1 (±0.2)	3.6(±0.3)
Solubility	10.5 (±0.5)	15(±0.6)
Perm	32.5 (±2)	54(±8.0)

A comparison of permeability against selectivity of PI membrane and PI-MFI membrane at 300 K is shown in Figure 7-14(b). It is seen that incorporation of MFI into PI polymer leads to increase in both permeability and selectivity, exhibiting overall performance slightly above the Robeson upper bound plot.[60] This is due to the larger resistance offered by the rigidified region to CH_4, and the high CO_2 sorption in MFI for CO_2, leading to increase in diffusivity and solubility selectivity for CO_2 in the composite system. On the other hand, decrease in both diffusivity and solubility due to the rigidified interface leads to decrease in gas permeability in the PI. However, the latter is compensated by the increase in solubility and diffusivity by incorporation of MFI in PI, leading to overall increase in CO_2 permeability as shown in the Figure 7-14(b). Further, by exploring strategies to improve the permeability of CO_2 in the composite system such as improving the interface between PI and MFI zeolite, separation performance well above the Robeson upper bound plot[60] should be achievable.

7.4 Conclusions

The transport properties of CO_2 and CH_4 at 5 atm in the temperature range of 300-500 K in a PI-MFI composite membrane system have been investigated using equilibrium molecular dynamics simulations. It is seen that incorporation of MFI zeolite into PI results in the formation of a densified polymer region near the surface having thickness around 1.2 nm, before being bulk-like, contradicting earlier empirical fitting-based suggestions of interfacial thickness of the order of 1 micron in MMMs. Also, it is seen that crystal size has little effect on the polymer structure at the polymer-filler interface. We find that the gas diffusion in the rigidified polymer layer is weakly anisotropic, and is always slower than in the bulk polymer, and offers an extra resistance to gas diffusion, especially for the molecule having larger molecular kinetic diameter, CH_4 in this case. Thus, this rigidified layer improves the diffusivity selectivity of CO_2 over CH_4. Furthermore, the temperature dependence of the collective diffusivity of CO_2 and CH_4 follows Arrhenius behavior in PI, MFI zeolite and PI+MFI hybrid membranes, and at 300 K the calculated diffusivity selectivity of CO_2 over CH_4 is 3.1(±0.2) and 3.6 (±0.3) in the PI and PI-MFI hybrid membrane respectively. The diffusivity selectivity for CO_2 of pure PI and PI-MFI membranes decreases with increase in temperature.

The gas sorption isotherms in a PI-MFI hybrid system were extracted *via* a two-step methodology considering the dynamics and structural transitions in the polymer matrix upon gas sorption. Our results show that the isotherm curves for gas sorption in PI, MFI and PI-MFI hybrid membranes are of ‘dual-mode sorption’ type. It is found that incorporation of MFI into PI improves the solubility selectivity of CO_2 over CH_4, and at 300 K the calculated solubility selectivity of CO_2 over CH_4 is 10.5(±1) and 15 (±1) in the PI and PI-MFI hybrid membrane respectively. It is seen that gas sorption in the polymer phase of the PI-MFI composite is less than that in the pure polymer due to presence of the rigidified region. The solubility selectivity for CO_2 of PI and PI-MFI membranes decrease with increase in temperature. The perm selectivity of PI-MFI and PI membranes for CO_2 are 54 and 32.5 respectively. In conclusion, a significant increase in CO_2 selectivity is observed on incorporation of

MFI into PI without compromising the permeability compared to the neat PI polymer membrane, and this increase is mediated by the high selectivity of the rigidified interfacial layer.

7.5 References

1. Chen, J.-T.; Shih, C.-C.; Fu, Y.-J.; Huang, S.-H.; Hu, C.-C.; Lee, K.-R.; Lai, J.-Y., Zeolite-Filled Porous Mixed Matrix Membranes for Air Separation. Ind. Eng. Chem. Res 2014, 53 (7), 2781-2789.

2. Zhang, L.; Hu, Z.; Jiang, J., Metal–Organic Framework/Polymer Mixed-Matrix Membranes for H2/CO2 Separation: A Fully Atomistic Simulation Study. J. Phys. Chem. C 2012, 116 (36), 19268-19277.

3. Adams, R.; Carson, C.; Ward, J.; Tannenbaum, R.; Koros, W., Metal organic framework mixed matrix membranes for gas separations. Micropor. Mesopor. Mater. 2010, 131 (1-3), 13-20.

4. Zhang, H.; Guo, R.; Hou, J.; Wei, Z.; Li, X., Mixed-Matrix Membranes Containing Carbon Nanotubes Composite with Hydrogel for Efficient CO2 Separation. ACS Appl. Mater. Interfaces 2016, 8 (42), 29044-29051.

5. Mahajan, R.; Koros, W. J., Factors Controlling Successful Formation of Mixed-Matrix Gas Separation Materials. Ind. Eng. Chem. Res 2000, 39 (8), 2692-2696.

6. Adams, R.; Johnson, J. R.; Zhang, C.; Lively, R.; Dai, Y.; Esekhile, O.; Liu, J.; Koros, W. J.; Hoek, E. M. V.; Tarabara, V. V., Mixed-Matrix Membranes. In Encyclopedia of Membrane Science and Technology, John Wiley & Sons, Inc.: 2013.

7. Monsalve-Bravo, G. M.; Bhatia, S. K., Extending effective medium theory to finite size systems: Theory and simulation for permeation in mixed-matrix membranes. J. Membr. Sci. 2017, 531 (Supplement C), 148-159.

8. Moore, T. T.; Koros, W. J., Non-ideal effects in organic–inorganic materials for gas separation membranes. J. Mol. Struct. 2005, 739 (1–3), 87-98.

9. Semino, R.; Ramsahye, N. A.; Ghoufi, A.; Maurin, G., Microscopic Model of the Metal–Organic Framework/Polymer Interface: A First Step toward Understanding the Compatibility in Mixed Matrix Membranes. ACS Appl. Mater. Interfaces 2016, 8 (1), 809-819.

10. Roilo, D.; Patil, P. N.; Brusa, R. S.; Miotello, A.; Aghion, S.; Ferragut, R.; Checchetto, R., Polymer rigidification in graphene based nanocomposites: Gas barrier effects and free volume reduction. Polymer 2017, 121 (Supplement C), 17-25.

11. Bae, T.-H.; Lee, J. S.; Qiu, W.; Koros, W. J.; Jones, C. W.; Nair, S., A High-Performance Gas-Separation Membrane Containing Submicrometer-Sized Metal–Organic Framework Crystals. Angew. Chem 2010, 49 (51), 9863-9866.

12. Kim, S.; Marand, E.; Ida, J.; Guliants, V. V., Polysulfone and Mesoporous Molecular Sieve MCM-48 Mixed Matrix Membranes for Gas Separation. Chem. Mater 2006, 18 (5), 1149-1155.

13. Benzaqui, M.; Semino, R.; Menguy, N.; Carn, F.; Kundu, T.; Guigner, J.-M.; McKeown, N. B.; Msayib, K. J.; Carta, M.; Malpass-Evans, R.; Le Guillouzer, C.; Clet, G.; Ramsahye, N. A.; Serre, C.; Maurin, G.; Steunou, N., Toward an Understanding of the Microstructure and Interfacial Properties of PIMs/ZIF-8 Mixed Matrix Membranes. ACS Appl. Mater. Interfaces 2016, 8 (40), 27311-27321.

14. Tuteja, A.; Duxbury, P. M.; Mackay, M. E., Polymer Chain Swelling Induced by Dispersed Nanoparticles. Phys. Rev. Lett. 2008, 100 (7), 077801.

15. Jouault, N.; Dalmas, F.; Said, S.; Di Cola, E.; Schweins, R.; Jestin, J.; Boué, F., Direct small-angle-neutron-scattering observation of stretched chain conformation in nanocomposites: More insight on polymer contributions in mechanical reinforcement. Phys. Rev. E 2010, 82 (3), 031801.

16. Galizia, M.; De Angelis, M. G.; Messori, M.; Sarti, G. C., Mass Transport in Hybrid PTMSP/Silica Membranes. Ind. Eng. Chem. Res 2014, 53 (22), 9243-9255.

17. Díaz, K.; Garrido, L.; López-González, M.; del Castillo, L. F.; Riande, E., CO2 Transport in Polysulfone Membranes Containing Zeolitic Imidazolate Frameworks As Determined by Permeation and PFG NMR Techniques. Macromolecules 2010, 43 (1), 316-325.

18. Jiang, Q.; Tallury, S. S.; Qiu, Y.; Pasquinelli, M. A., Molecular dynamics simulations of the effect of the volume fraction on unidirectional polyimide–carbon nanotube nanocomposites. Carbon 2014, 67 (Supplement C), 440-448.

19. Semino, R.; Dürholt, J. P.; Schmid, R.; Maurin, G., Multiscale Modeling of the HKUST-1/Poly(vinyl alcohol) Interface: From an Atomistic to a Coarse Graining Approach. J. Phys. Chem. B 2017, 121 (39), 21491-21496.

20. Falkovich, S. G.; Nazarychev, V. M.; Larin, S. V.; Kenny, J. M.; Lyulin, S. V., Mechanical Properties of a Polymer at the Interface Structurally Ordered by Graphene. J. Phys. Chem. C 2016, 120 (12), 6771-6777.

21. Martínez, L.; Andrade, R.; Birgin, E. G.; Martínez, J. M., PACKMOL: A package for building initial configurations for molecular dynamics simulations. J. Comput. Chem. 2009, 30 (13), 2157-2164.

22. Sun, H.; Mumby, S. J.; Maple, J. R.; Hagler, A. T., An ab Initio CFF93 All-Atom Force Field for Polycarbonates. J. Am. Chem. Soc 1994, 116 (7), 2978-2987.

23. Makrodimitris, K.; Papadopoulos, G. K.; Theodorou, D. N., Prediction of Permeation Properties of CO2 and N2 through Silicalite via Molecular Simulations. J. Phys. Chem. B 2001, 105 (4), 777-788.

24. Kresse, G.; Furthmüller, J., Efficient iterative schemes for ab initio total-energy calculations using a plane-wave basis set. Phys. Rev. B 1996, 54 (16), 11169-11186.

25. Kresse, G.; Furthmüller, J., Efficiency of ab-initio total energy calculations for metals and semiconductors using a plane-wave basis set. Comput. Mater. Sci 1996, 6 (1), 15-50.

26. Kresse, G.; Hafner, J., Ab initio. Phys. Rev. B 1993, 47 (1), 558-561.

27. Harris, J. G.; Yung, K. H., Carbon Dioxide's Liquid-Vapor Coexistence Curve And Critical Properties as Predicted by a Simple Molecular Model. J. Phys. Chem. 1995, 99 (31), 12021-12024.

28. Sun, Y.; Spellmeyer, D.; Pearlman, D. A.; Kollman, P., Simulation of the solvation free energies for methane, ethane, and propane and corresponding amino acid dipeptides: a critical test of the bond-PMF correction, a new set of hydrocarbon parameters, and the gas phase-water hydrophobicity scale. J. Am. Chem. Soc. 1992, 114 (17), 6798-6801.

29. Bhatia, S. K.; Bonilla, M. R.; Nicholson, D., Molecular transport in nanopores: a theoretical perspective. Phys. Chem. Chem. Phys 2011, 13 (34), 15350-15383.

30. Sholl, D. S., Understanding Macroscopic Diffusion of Adsorbed Molecules in Crystalline Nanoporous Materials via Atomistic Simulations. Acc. Chem. Res. 2006, 39 (6), 403-411.

31. Zhu, F.; Tajkhorshid, E.; Schulten, K., Collective Diffusion Model for Water Permeation through Microscopic Channels. Phys. Rev. Lett. 2004, 93 (22), 224501.

32. Frentrup, H.; Avendaño, C.; Horsch, M.; Salih, A.; Müller, E. A., Transport diffusivities of fluids in nanopores by non-equilibrium molecular dynamics simulation. Mol Simul. 2012, 38 (7), 540-553.

33. Wang, Y.; LeVan, M. D., Mixture Diffusion in Nanoporous Adsorbents: Equivalence of Fickian and Maxwell−Stefan Approaches. J. Phys. Chem. B 2008, 112 (29), 8600-8604.

34. Mason, E. A.; Malinauskas, A. P.; Evans, R. B., Flow and Diffusion of Gases in Porous Media. J. Chem. Phys. 1967, 46 (8), 3199-3216.

35. Krishna, R., Multicomponent surface diffusion of adsorbed species: a description based on the generalized Maxwell—Stefan equations. Chem. Eng. Sci. 1990, 45 (7), 1779-1791.

36. Nik, O. G.; Chen, X. Y.; Kaliaguine, S., Amine-functionalized zeolite FAU/EMT-polyimide mixed matrix membranes for CO2/CH4 separation. J. Membr. Sci. 2011, 379 (1), 468-478.

37. Barbari, T. A.; Koros, W. J.; Paul, D. R., Gas sorption in polymers based on bisphenol-A. J. Polym. Sci. B Polym. Phys. 1988, 26 (4), 729-744.

38. Shang, X.-y.; Zhu, Z.-k.; Yin, J.; Ma, X.-d., Compatibility of Soluble Polyimide/Silica Hybrids Induced by a Coupling Agent. Chem. Mater 2002, 14 (1), 71-77.

39. Komarov, P. V.; Chiu, Y.-T.; Chen, S.-M.; Reineker, P., Investigation of Thermal Expansion of Polyimide/SiO2 Nanocomposites by Molecular Dynamics Simulations. Macromol. Theory Simul 2010, 19 (1), 64-73.

40. Heuchel, M.; Hofmann, D., Molecular modelling of polyimide membranes for gas separation. Desalination 2002, 144 (1), 67-72.

41. Lyulin, S. V.; Gurtovenko, A. A.; Larin, S. V.; Nazarychev, V. M.; Lyulin, A. V., Microsecond Atomic-Scale Molecular Dynamics Simulations of Polyimides. Macromolecules 2013, 46 (15), 6357-6363.

42. Dutta, R. C.; Bhatia, S. K., Transport Diffusion of Light Gases in Polyethylene Using Atomistic Simulations. Langmuir 2017, 33 (4), 936-946.

43. Moore, T. T.; Koros, W. J., Gas sorption in polymers, molecular sieves, and mixed matrix membranes. J. Appl. Polym. Sci. 2007, 104 (6), 4053-4059.

44. Scholes, C. A.; Tao, W. X.; Stevens, G. W.; Kentish, S. E., Sorption of methane, nitrogen, carbon dioxide, and water in Matrimid 5218. J. Appl. Polym. Sci. 2010, 117 (4), 2284-2289.

45. Zhao, H.-Y.; Cao, Y.-M.; Ding, X.-L.; Zhou, M.-Q.; Yuan, Q., Effects of cross-linkers with different molecular weights in cross-linked Matrimid 5218 and test temperature on gas transport properties. J. Membr. Sci. 2008, 323 (1), 176-184.

46. Falbo, F.; Brunetti, A.; Barbieri, G.; Drioli, E.; Tasselli, F., CO2/CH4 separation by means of Matrimid hollow fibre membranes. Appl Petrochem Res 2016, 6 (4), 439-450.

47. Bhatia, S. K.; Jepps, O.; Nicholson, D., Tractable molecular theory of transport of Lennard-Jones fluids in nanopores. J. Chem. Phys. 2004, 120 (9), 4472-4485.

48. Bhatia, S. K.; Nicholson, D., Anomalous transport in molecularly confined spaces. J. Chem. Phys. 2007, 127 (12), 124701.

49. Ebadi Amooghin, A.; Omidkhah, M.; Kargari, A., Enhanced CO2 transport properties of membranes by embedding nano-porous zeolite particles into Matrimid 5218 matrix. RSC Advances 2015, 5 (12), 8552-8565.

50. Papadopoulos, G. K.; Jobic, H.; Theodorou, D. N., Transport Diffusivity of N2 and CO2 in Silicalite: Coherent Quasielastic Neutron Scattering Measurements and Molecular Dynamics Simulations. J. Phys. Chem. B 2004, 108 (34), 12748-12756.

51. Selassie, D.; Davis, D.; Dahlin, J.; Feise, E.; Haman, G.; Sholl, D. S.; Kohen, D., Atomistic Simulations of CO2 and N2 Diffusion in Silica Zeolites: The Impact of Pore Size and Shape. J. Phys. Chem. C 2008, 112 (42), 16521-16531.

52. Bowen, T. C.; Falconer, J. L.; Noble, R. D.; Skoulidas, A. I.; Sholl, D. S., A Comparison of Atomistic Simulations and Experimental Measurements of Light Gas Permeation through Zeolite Membranes. Ind. Eng. Chem. Res 2002, 41 (6), 1641-1650.

53. Krishna, R.; van Baten, J. M.; García-Pérez, E.; Calero, S., Diffusion of CH4 and CO2 in MFI, CHA and DDR zeolites. Chem. Phys. Lett. 2006, 429 (1), 219-224.

54. García-Pérez, E.; Parra, J. B.; Ania, C. O.; García-Sánchez, A.; van Baten, J. M.; Krishna, R.; Dubbeldam, D.; Calero, S., A computational study of CO2, N2, and CH4 adsorption in zeolites. Adsorption 2007, 13 (5), 469-476.

55. Skoulidas, A. I.; Sholl, D. S., Molecular Dynamics Simulations of Self-Diffusivities, Corrected Diffusivities, and Transport Diffusivities of Light Gases in Four Silica Zeolites To Assess Influences of Pore Shape and Connectivity. J. Phys. Chem. A 2003, 107 (47), 10132-10141.

56. Di Maio, F. P.; Santaniello, A.; Di Renzo, A.; Golemme, G., Description of gas transport in perfluoropolymer/SAPO-34 mixed matrix membranes using four-resistance model. Sep. Purif. Technol. 2017, 185 (Supplement C), 160-174.

57. Moore, T. T.; Mahajan, R.; Vu, D. Q.; Koros, W. J., Hybrid membrane materials comprising organic polymers with rigid dispersed phases. AIChE Journal 2004, 50 (2), 311-321.

58. Nguyen, T. X.; Bhatia, S. K., Determination of Pore Accessibility in Disordered Nanoporous Materials. J. Phys. Chem. C 2007, 111 (5), 2212-2222.

59. Nguyen, T. X.; Jobic, H.; Bhatia, S. K., Microscopic Observation of Kinetic Molecular Sieving of Hydrogen Isotopes in a Nanoporous Material. Phys. Rev. Lett. 2010, 105 (8), 085901.

60. Robeson, L. M., The upper bound revisited. J. Membr. Sci. 2008, 320 (1), 390-400.

Chapter 8 Interfacial Engineering of Polyimide-ZIF-8 Mixed Matrix Membrane

8.1 Introduction

Metal–organic framework (MOF) based mixed matrix membranes (MMM) have received significant attention owing to the organic functionality in their bridging ligands, which can interact well with polymers.[1] This can avoid the presence of non-selective micro-voids, as evident in MMMs having zeolite fillers.[2] The future directions for these new filler materials are very promising, primarily because of the enormous chemical flexibility of their base structures. Theoretically, innumerable MOFs can be fabricated by combining the numerous available linkers and metal ions, to achieve the required pore size and chemical flexibility for a gas separation of interest. Substantial work in this direction has been done and more than 20000 different MOFs structures being reported within the past decade,[1, 3, 4] which can then be used as filler materials in MMMs; consequently, screening and selection of suitable filler -polymer combination for a given application is challenging.

Keskin et al.[5-7] employed atomistic simulations to investigate gas transport characteristics of neat MOF as well as polymer membrane materials, and determined the appropriate MOF/polymer combination for gas separation by predicting the performance of a composite membrane based on the Maxwell model. However, this model has been shown to be accurate only at small filler loading below about 20% by volume.[8] Further, this model assumes ideal interface between filler and polymer, which is often not the case. Several experimental investigations on MOF-based MMMs report the presence of voids at the interface.[9-13] and proposed strategies to promote interfacial compatibility between the polymer and various MOFs. These strategies include the inclusion of interface agents such as ionic liquids (ILs), that serve as wetting agent between the filler and polymer, and show great potential due to their unique properties such nonvolatility, high thermal stability, and good intrinsic solubility for CO_2 gas. For example, Lin et al.[12] observed improved gas separation performance when a MMM is fabricated with IL-decorated HKUST-1 in PI, as the ILs are successful in restricting the formation of nonselective interfacial voids. Vu et al.[11] successfully fabricated a MMM having micron-sized ZIF-67 coated with a thin layer of IL dispersed in PI polymer, leading to significant improvement in CO_2/CH_4 gas separation performance. Further, the most important challenge involved in these membranes are to prevent the aggregation of the particles in the polymer, especially at higher filler loadings.[10] An effective way to obtain well dispersed MOF and restrain agglomeration is by employing “one-pot synthesis” technique, that takes the advantage of using the same solvent for MOF synthesis as well as membrane-casting.[14] However, the direct experimental characterization of the polymer conformation in the presence of inorganic filler is challenging and most of these investigations confirmed the presence of leaky interface based on the MMM performance where gas permeabilities far beyond the limit of what is theoretically predicted by the Maxwell model have been found.

While the current imaging techniques such as field emission scanning microscopes(FESEM),[15] small angle neutron scattering (SANS),[16, 17] positron annihilation lifetime spectroscopy(PALS)[18] broadband dielectric spectroscopy (BDS), small-angle X-ray scattering (SAXS)[19, 20] and differential scanning calorimetry (DSC) [21] allow characterization of structural defects such as pore blockage, polymer rigidification and crystal intergrowth , that of sub-nanometer surface defects is still challenging. Further, the effect of filler size, shape and loading on the structure of the polymer at the interface and thus gas separation performance is not clear and requires trial and error experimentation. On the other hand, many of the earlier simulation reports based on either atomistic[22] or coarse grained or multiscale modeling[23-25] simulation approaches have successfully characterized the interface between the filler and the polymer. The results indicate the presence of microscopic void regions[24, 25] or pore blockage[23] or the formation of a rigidified region.[26]

Recently, Semino et al.[27-29] investigated the compatibility between MOF surface and various polymers using a multi-scale simulation approach by combining Density Functional Theory (DFT) calculations with MD simulations. They found that a micro void region in the vicinity of PIM1-ZIF8 surface, of 9-15 Å width, exists. This is in agreement with an experimental finding that the compatibility between the PIM-1 and ZIF-8 is moderate (REF). In addition, it has been found that larger free volume elements of 6-7 Å radius and a higher free volume are available in the interfacial region. Further, they also developed a CG model that allows the investigation of much larger systems, which can reproduce the salient features of the interface that are in agreement with the findings of atomistic simulations.[28] By applying this methodology they found that poly(vinyl alcohol) polymer penetrates into the open pores of HKUST-1, resulting in surface pore blockage. In addition, Zhang et al.[30] investigated the H_2/CO_2 separation performance of a ZIF-7/ PBI membrane through atomistic simulations and found that H_2 and CO_2 have higher permeabilities in the hybrid membrane than the corresponding neat polymer membrane. Further, an increase in gas solubility with increase in filler loading for both the gases, with little enhancement in H_2 selectivity over CH_4 has been reported. These investigations highlight the capability of atomistic simulations to predict the interfacial morphology of the polymer near a surface as well as gas transport characteristics in a model MMM. However, the influence of interfacial morphology on gas transport characteristics is yet to be investigated.

In this chapter, the structure of 6FDA-durene PI polymer in the vicinity of the ZIF-8 surface is characterized through EMD simulations. Further, an ionic liquid that can be used to promote the compatibility between the polymer and ZIF-8 is identified. In addition, the gas diffusion characteristics of 6FDA-durene/ZIF-8 MMM with and without having IL at the interface are investigated. Furthermore, we extract the sorption isotherms in PI and the PI/ZIF-8 composite system by considering the structural transitions upon gas sorption, implementing a two-step methodology combining Grand canonical Monte Carlo simulations (GCMC) coupled with NPT (Constant Number of particles, Pressure and Temperature) equilibrium molecular dynamics (EMD) simulations.

8.2 Model and methodology

Our system comprises a ZIF-8 surface sandwiched between two 6FDA-durene PI polymer-filled regions, representing a model MMM, in which we investigate the interfacial structure, and the sorption and transport of pure component CO_2 and CH_4. The system is assumed periodic in all three directions. In what follows we describe the main elements of the model, and the corresponding interaction potential parameters used in the simulations.

6FDA-durene: Polymer chains each having 35 monomers of 6FDA-durene (4,4′-(hexafluoroisopropylidene) diphthalic anhydride, 2,3,5,6-tetramethyl-1,4-phenylenediamine), as depicted in Figure 8-1 (a) is considered. Further, bonded and non-bonded interactions of the polymer chains were considered as described in Chapter-3. Further, we note that the partial charges on the atoms of polymer were considered in this chapter. To compute the partial charges on atoms of the polymer, a short polymer chain having 3 monomers is considered. The positions of all atoms of a polymer chain in the system is optimized using Perdew–Burke-Ernzerhof (PBE) function with the projector augmented wave (PAW) method, implemented in VASP[31-33] and the charge density files generated. Then, the net charges on atoms of the polymer are computed using density derived electrostatic and chemical (DDEC6) method, [34, 35] reported to be accurate for the prediction of atomic charges in dense molecular systems, such as DNA.[35] These atomic charges are used in both EMD as well as GCMC simulations.

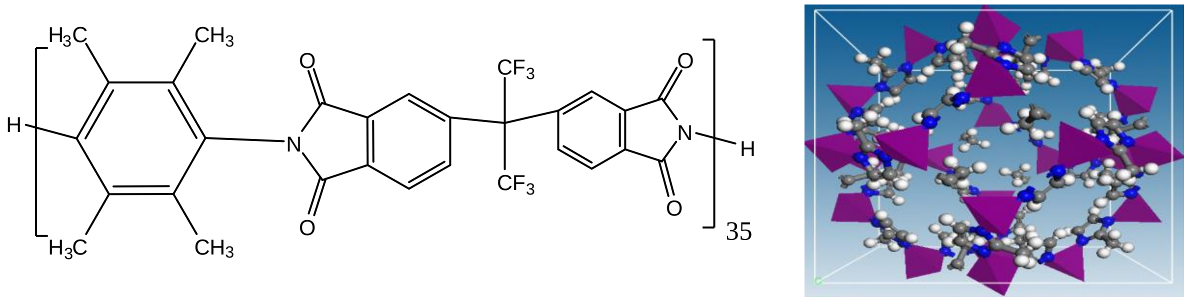
(a) 6FDA-DURENE

(b) ZIF-8

Figure 8-1: Schematic illustration of structure of (a) 6FDA-durene polyimide polymer, and (b) ZIF-8.

ZIF-8 Surface: To model the MOF surface, ZIF-8 which comprises zinc ions coordinated by four imidazolate rings is considered, as shown in the Figure 8-1 (b). We note that ZIF-8 has a pore gate size of 3.4 Å, which is larger than the kinetic diameter of CO_2 (~3.2 Å) as well as smaller than that of methane (~3.8 Å), resulting in good separation performance CO_2 compared to CH_4. The non-bonded van der Waals (vdW) interactions are incorporated using the Lennard–Jones (LJ) potential including the electrostatic interactions of the form:

$$U_{ij}^{non-bond} = 4\varepsilon_{ij}\left[\left(\frac{\sigma_{ij}}{r_{ij}}\right)^{12} - \left(\frac{\sigma_{ij}}{r_{ij}}\right)^{6}\right] + \sum_{i,j}\frac{q_i q_j}{r_{ij}} \tag{8-1}$$

The bonded and non- potential parameters used to represent ZIF-8 are derived on the basis of the AMBER force field as proposed by Zhang et al.[36] This forcefield is successfully employed to investigate the structural as well gas transport characteristics of ZIF-8.[37, 38] A 3 x 3 x 3 unit cell (U.C) with periodic boundary conditions is used to investigate the gas transport characteristics in the neat ZIF-8 membrane system. In the case of the PI/ZIF-8 system, a 2 x 2 x 4 U.C. was considered and the surface in contact with the polymer was cleaved at the (0 0 1) plane, and all the surface atoms were capped with the imidazolate group. The resulting structure was relaxed by employing conjugate gradient method without optimizing the cell dimensions using VASP software.[31-33] The ZIF-8 is treated flexible molecule in the entire simulation.

Ionic Liquid: An ionic liquid, BMIM-BF_4 is considered in this investigation to promote the compatibility between the polymer and ZIF-8 filler. The bonded and non- potential parameters used to represent IL are taken from OPLS/AA forcefield.[39] Further, we note that structure of IL's including the density and radial distribution functions computed from our simulations are well in agreement with the literature report values.[39]

8.3 Results and discussions

8.3.1 Validation of forcefield

The ability of the force field to represent 6FDA-durene polymer membrane is illustrated by characterizing the polymer structure using volume-temperature relations. Figure 8-2(a) depicts the temperature dependence of the specific volume ($1/\rho$) of 6FDA-durene polymer at 1 atm pressure. Our simulation predictions of the density of 6FDA-durene polymer (1.35 (± 0.1) g/cc), are in good agreement with the experimental value of 1.31-1.37 g/cc. A linear increase in specific volume of the polymer with increase in temperature, with change in slope at 710 (± 10) K corresponding to the glass transition temperature (T_g) of the polymer is observed, which compares well with the experimental value of 683-697 K. We note here that pressure has negligible effect on the polymer structure up to 30 atm. Further, the gas- polymer interactions are validated by extracting the gas sorption isotherms

Figure 8-2 (b) depicts the pure component sorption isotherms of CO_2 and CH_4 in 6FDA-durene polymer membrane respectively considering the swelling upon gas absorption, at 300 K, and shows good agreement with experimental data. Further, it is seen that the CO_2 absorbs strongly than CH_4 in 6FDA-durene polymer membrane. The sorption isotherm of each gas considered was fitted using DM sorption model and is shown by the lines in Figure 8-2(b).

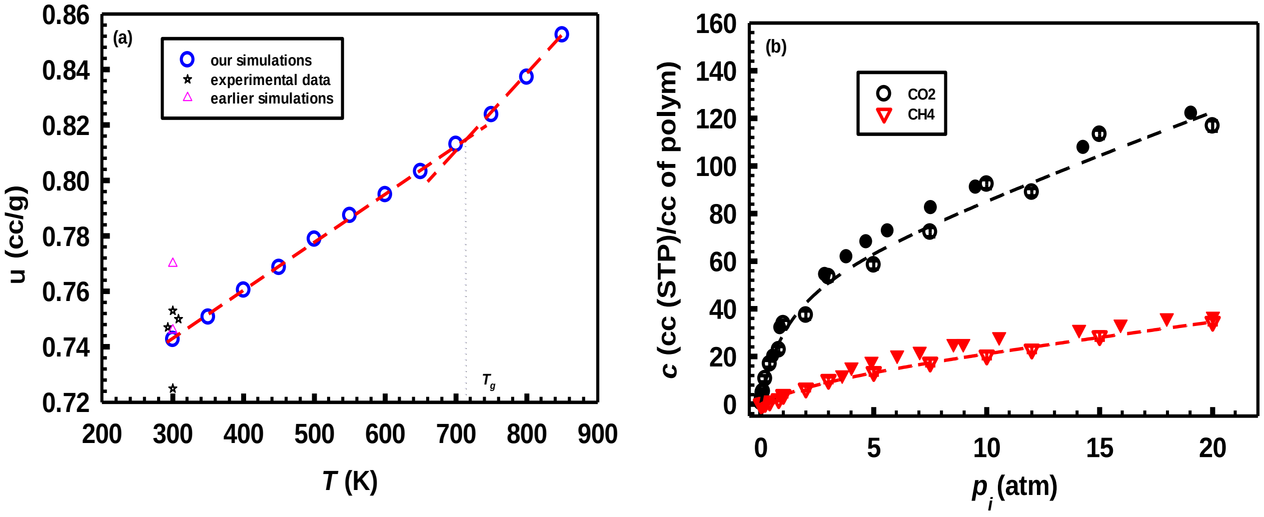

Figure 8-2: (a) Variation of specific volume in 6FDA-durene with temperature, and (b) comparison of computed gas sorption isotherms at 300 K with experimental data (closed symbols) taken from refs. [1,7,40].

8.3.2 Gas diffusion in neat polymer and ZIF-8 membranes

To understand gas diffusion behavior in the neat 6FDA-durene polymer as well as in ZIF-8 membranes, pure component corrected diffusivities were determined by computing the corrected diffusion coefficient of gas molecules by tracking the temporal center-of-mass motion of all the adsorbed species in the membrane. Figure 8-3 (a) shows the loading dependence of pure component MS diffusivities of CO_2 and CH_4 in the 6FDA-durene membrane at T= 300 K. It is seen that for methane, a moderate increase in diffusivity with increase in loading is observed, while a stronger increase in diffusivity with increase in loading, especially at high loadings, is observed for CO_2. This can be attributed to the plasticization behavior of the polymer at high CO_2 loadings. Good agreement is found between our simulation predictions and experimentally reported gas diffusivities in the 6FDA-durene polymer membrane.[41, 42] A similar plot showing the loading dependence of pure component self as well as corrected diffusivities of CO_2 and CH_4 in the ZIF-8 membrane at T= 300 K, is depicted in Figure 3 (b). Weak dependency of gas loading on diffusivities of both the gases in neat ZIF-8 membrane is observed. We note that the flexibility of ZIF-8 is considered while computing the gas adsorption as well as diffusion in ZIF-8. Good agreement is found between our simulation predictions and data from earlier simulations for gas diffusivities in ZIF-8. We note that both neat polymer and ZIF-8 membranes are diffusive selective for CO_2 over CH_4 at all temperatures.

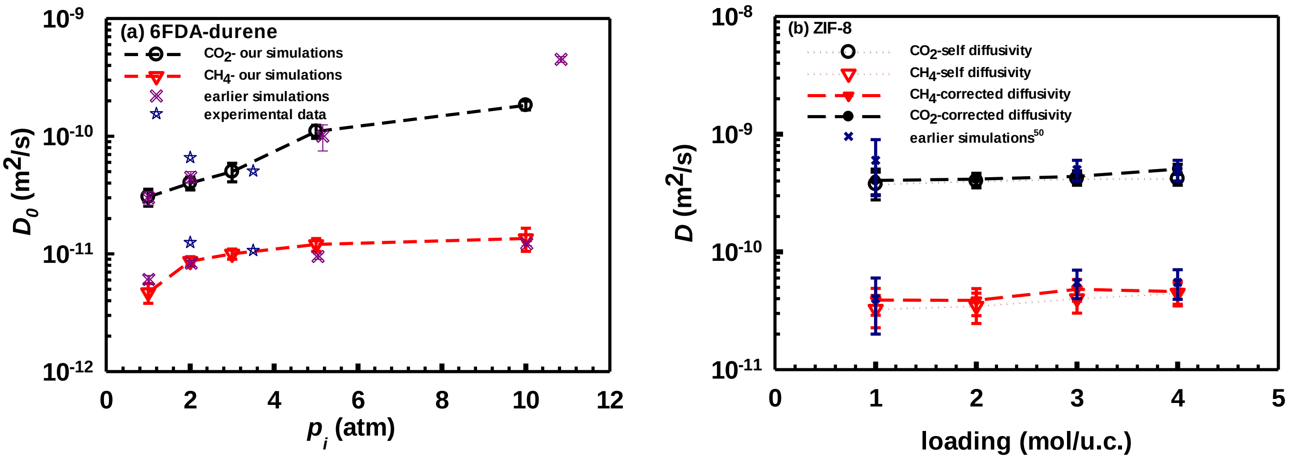

Figure 8-3: Loading dependence of corrected diffusivities of CO_2 and CH_4 in (a) 6FDA-durene PI membrane, and (b) ZIF-8 membrane. Experimental (symbol-stars) and earlier simulation (symbol-cross) data points are taken from refs. [39,41,42].

8.3.3 PI/ZIF-8 composite system

The system comprises a ZIF-8 unit cell sandwiched between two 6FDA-durene PI polymer-filled regions, representing a model MMM, as depicted in Figure 8-4 (a). The system is assumed periodic in all three directions. A magnified view of the polymer/ZIF-8 interface is shown in the inset of Figure 8-4 (a), where sub-nanometer size voids are visually evident. Further, the structure of 6FDA-durene in the vicinity of the ZIF-8 was explored by computing the polymer density as a function of distance from the ZIF-8 surface using a binning procedure, where the simulation cell was divided into narrow bins of 1 Å each in the direction normal to the surface. Figure 8-4(b) depicts the density of PI as well as ZIF-8 as a function of position, normal to the surface in the simulation box. In Figure 8-4 (b), the region having zero polymer density represents the ZIF-8 surface. It is observed that a low-density polymer region exists near the ZIF-8 surface, of thickness around 7 - 10 Å. The reported interfacial region thickness is consistent with recent findings by Semino et al.[29] that the interface void region is extended up to 9-13 Å in polymers of intrinsic micro-porosity in the presence of ZIF-8. We note that no polymer penetration into ZIF-8 pores is observed and no ZIF-8 is included in the calculation of interface region thickness.

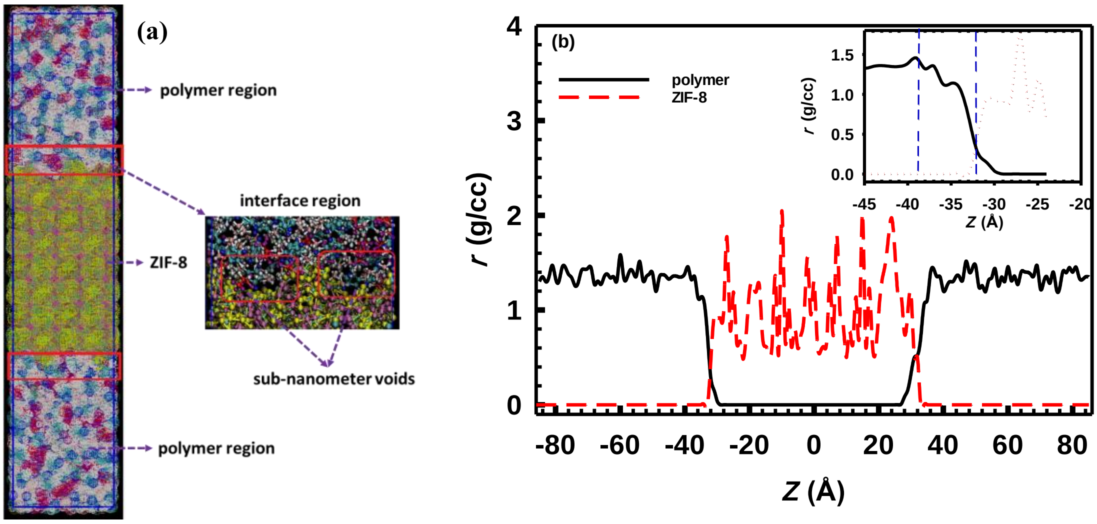

Figure 8-4: (a) Structure of 6FDA-durene in the PI-ZIF-8 composite system, highlighting sub-nanometer voids at the interface, and (b) density profile of PI in the PI-ZIF-8 composite system at 300 K. A magnified view of density profile in the interface region is shown in the inset.

Further, the structure of polymer in the interfacial region as well as in the bulk region is analyzed by computing the distribution of free volume elements (FVE) in the polymer. The presence of larger FVEs of radius 4 – 6 Å in the interfacial region is evident, when compared to bulk region where FVEs smaller than 4 Å radius are present, as shown in Figure 8-5 (a). In addition, the diffusion behavior of CO_2 and CH_4 in the interface region in the direction normal to the surface was systematically investigated through the collective diffusion model, as described in Chapter-7. Figure 8-5(b) depicts the loading dependence of the D_o of CO_2 and CH_4 in the interface region between PI and ZIF-8 (low polymer density region) at 300 K. It is seen that gas diffusivity in the interfacial region is much higher than the corresponding diffusivity in the neat polymer, due to the presence of larger free volume elements in the interfacial region. In addition, the increase in gas diffusivity in the interfacial region is more pronounced for methane than CO_2. This is because the availability of larger free volume elements in the interfacial region promotes methane diffusion, this being a lighter and more weakly adsorbed molecule, as opposed to the neat polymer membrane which offers greater resistance to methane diffusion, which has larger molecular size (kinetically larger molecule than CO_2).

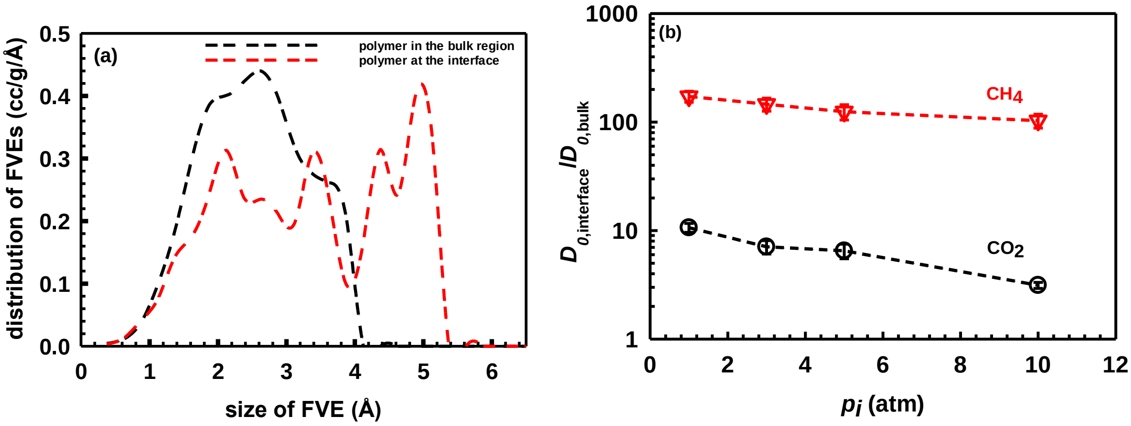

Figure 8-5: (a) Comparison of distribution of FVEs in PI in the bulk and interface region in a PI -ZIF-8 composite system, and (b) Variation of relative gas diffusivity in PI in the interface region with pressure.

8.3.4 Interface engineering of PI/ZIF-8 system with an ionic liquid

To promote interfacial compatibility between the polymer and ZIF-8, we used room temperature ionic liquids (ILs), that serve as wetting agent between the filler and polymer. We note that ILs are successfully employed to improve the polymer -filler interface morphology and demonstrate improved membrane performance especially when separating the mixtures involving CO_2 due to their good intrinsic solubility for CO_2.[11, 12] Here, we identified a suitable IL to fill the voids that exists at the interface between the polymer and ZIF-8, to achieve good compatibility between the polymer and filler. It was seen that 1-Butyl-3-methylimidazolium tetrafluoroborate $[BMIM]^+[BF_4]^-$ has good compatibility with the polymer as well as ZIF-8 and was used as the interface agent to fill the sub-nanometer gaps between the polymer and filler. A schematic illustration of the polymer-ZIF8 system, having an IL at the interface is depicted in Figure 8-6 (a). Further, the structure of the polymer in the vicinity of the ZIF-8, having IL at the interface was explored by computing the density profiles of polymer and IL in the direction normal to the surface. Figure 8-6(b) depicts the density profiles of PI as well as IL, as a function position in the simulation box. In Figure 8-6 (b), the region having zero polymer density represents the ZIF-8 surface, as indicated in the figure. It is seen that the bulk polymer region is followed by an IL region on either side of ZIF-8 surface having density equivalent to bulk density of IL at the given temperature, indicating good compatibility between the IL and polymer as well as ZIF-8. We note that, no void region at the interface is observed. However, IL can penetrate in to the ZIF8, as seen in Figure 8-6(b).

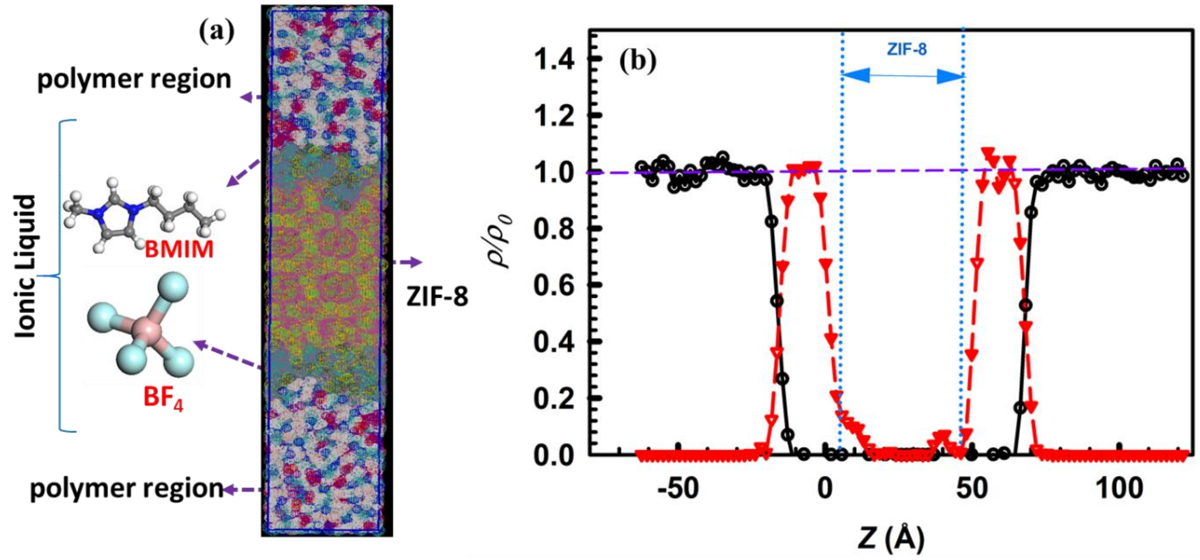

Figure 8-6:(a) Structure of a PI-ZIF-8 MMM having ionic liquid at the interface to improve the compatibility between the polymer and filler phases, and (b) density profile of PI, ZIF-8 and IL in the PI-IL modified ZIF-8 composite membrane system at 300 K.

To explore the gas separation characteristics of MMMs having IL at the interface, the gas sorption isotherms were extracted *via* a two-step methodology considering the dynamics and structural transitions in the polymer matrix upon gas absorption. Figure 8-7 (a) depicts a comparison of the gas sorption isotherms in PI-ZIF-8 MMMs with and without IL at the interface. A decrease in gas absorption capacity for both the gases is observed in a MMM having IL at the interface in contrast to an increase in gas absorption capacity especially for CO_2 in a MMM having IL at the interface, as ILs are demonstrated to have good CO_2 solubility. This is due to sub nanometer voids present at the interface in PI-ZIF-8 MMM act as strong sites. Although, ILs have good intrinsic solubility for CO_2, the former dominates resulting in overall decrease in gas absorption capacity in MMMs having IL at the interface. Further, the pressure dependence of the solubility selectivity of CO_2 over CH_4 in PI, PI-ZIF8 and IL-modified PI-ZIF8 membranes at 300 K is depicted in Figure 8-7(b). No significant change in the solubility selectivity in the neat PI as well as PI-ZIF8 composite membranes is observed at any given pressure. This is attributed to the similar gas sorption capacity of both neat PI and ZIF8 membranes, at any given pressure.

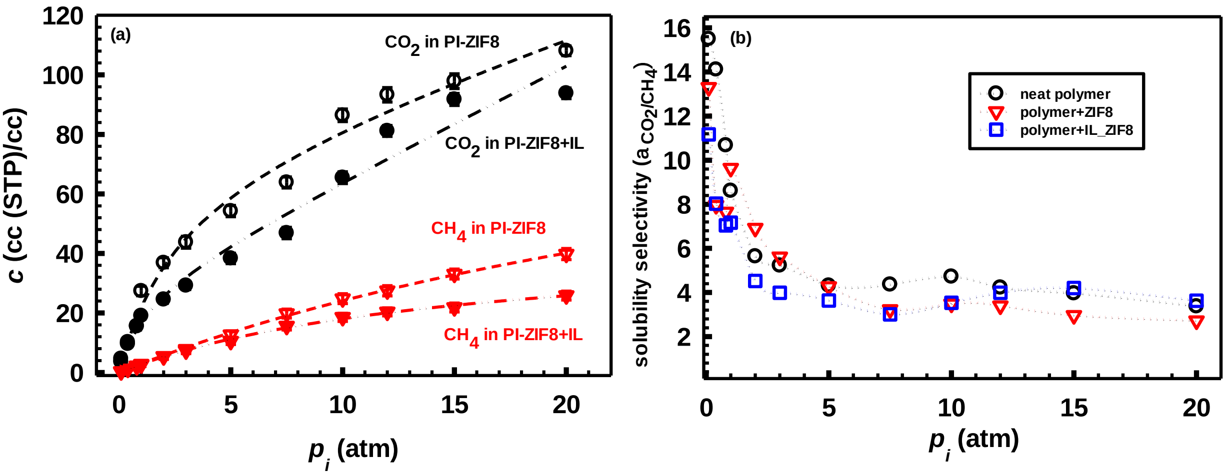

Figure 8-7:A comparison of (a) sorption isotherms, and the (b) solubility selectivity of pure component CO_2 and CH_4 in PI-ZIF8 and PI-IL modified ZIF8 membranes at $T = 300$ K. Dotted lines are given as a guide for the eye.

Further, gas diffusion coefficients of MMMs having IL at the interface at various gas loadings and 300 K were extracted by computing the pure component corrected diffusivities of the gas molecules using EMD simulations. Figure 8-8 (a) depicts a comparison of the corrected diffusion coefficients of CO_2 and CH_4 in a MMM with and without IL at the interface. A decrease in gas diffusion coefficient for both the gases is observed in a MMM having IL at the interface; this effect is more pronounced for methane, as voids present in the PI-ZIF-8 membrane, which are now filled with IL, promote methane diffusivity, as methane is a lighter molecule. This leads to a sharp increase in diffusivity selectivity of CO_2 over methane in a MMM having IL at the interface as depicted in Figure 8-8(b). However, the diffusivity selectivity of neat polymer membrane above 4 atm, the plasticization pressure of the neat polymer, is higher than that of both the composite systems, and is attributed to plasticization resistance of the polymer having inclusion of ZIF-8, which will be discussed subsequently.

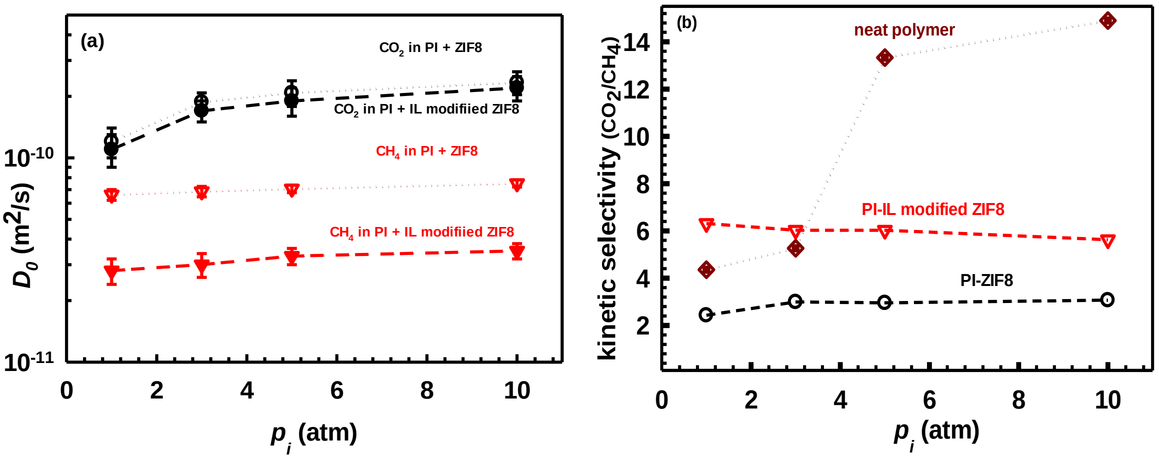

Figure 8-8: Variation of (a) pure-component corrected diffusivities, and (b) diffusivity selectivity of CO_2 and CH_4 in neat PI and PI-IL modified ZIF-8 membranes with pressure at 300 K.

A comparison of CO_2 and CH_4 permeabilities in PI, PI-ZIF-8 and PI-IL modified ZIF-8 membranes with pressure is depicted in Figure 8-9 (a)-(b). Below plasticization pressure of the polymer, a 3-fold increase in CO_2 permeability in a MMM having ZIF-8 in 6FDA-durene PI polymer matrix compared to the neat polymer membrane, at the cost of perm-selectivity is observed, as shown in Figure 9 (c). This further confirms the presence of void region at the interface between polymer and ZIF-8. However, with further inclusion of ionic liquid at the ZIF8 surface, the resulting MMM has higher gas permeability compared to the corresponding neat polymer membrane, but lower than that of the unmodified PI-ZIF-8 membrane, with little improvement in the perm-selectivity.

The permeability of methane in neat 6FDA-durene PI polymer membrane decreases with increase in loading, in all the cases as expected. On the other hand, it is seen that permeability of CO_2 decreases up to about 4 atm pressure and then increases with increase in loading. This increase in permeability with increase in pressure has also been observed experimentally[45, 46] at around 5 atm pressure, corresponding to the plasticization pressure of the polymer. Beyond the plasticization pressure, sharp increase in gas diffusivity dominates the effect of decrease in solubility with increase in pressure, leading to increase in permeability with increase in pressure. Although there exists a weak interaction between the 6FDA-durene polymer and ZIF-8, the resulting membrane interestingly exhibits plasticization resistance even up to 10 atm pressure upon CO_2 absorption. Similar behavior is reported in the HKUST-1-6FDA-DAM MMM system, with no plasticization up to 50 atm pressure, suggesting unusual stability.[13] The authors attributed this behavior to the restricted polymer chain mobility in the presence of surface.

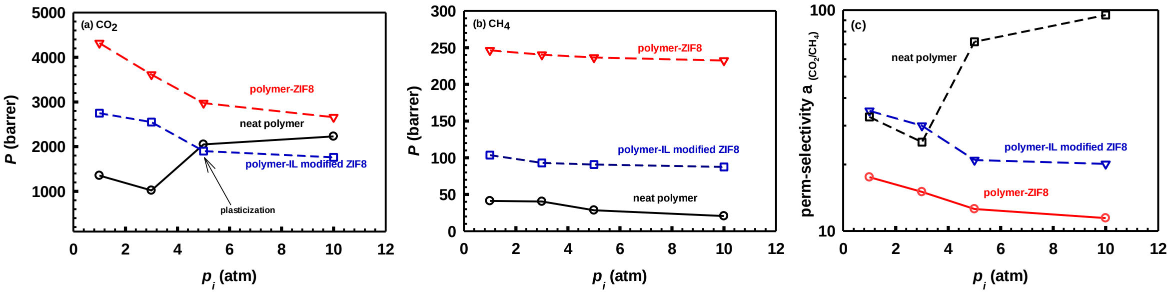

Figure 8-9: Variation of pure-gas (a) CO_2 and (b) CH_4, permeabilities, and (c) CO_2/CH_4 perm-selectivity in neat PI and PI-IL modified ZIF-8 membranes with pressure at 300 K.

To understand this further, the swelling behavior of neat polymer as well as polymer-ZIF-8 composite membranes upon CO_2 sorption was investigated and is depicted in Figure 8-10. The swelling of the polymer in the presence of a gas at any given pressure is computed, following:

$$swelling\ (\%) = \left[\frac{V_{swollen} - V_{unswolloen}}{V_{unswolloen}} \right] x100 \qquad (8\text{-}2)$$

where $V_{swollen}$ and $V_{unswolloen}$ are the polymer volumes in the swollen and initial states respectively. We note that the polymer swelling is only considered in the PI-ZIF-8 composite membrane and compared with swelling of the neat polymer. It is seen that the neat polymer swells to a greater extent than polymer that is physically constrained, as seen in Figure 8-10, where the polymer swelling upon gas sorption in the PI-ZIF-8 composite membrane is always less than the corresponding neat membrane at any given pressure. This is due to the solid surface that reduces the degrees of freedom in which the polymer can swell in the composite membrane, affecting its internal structure. Further, similar behavior is also observed in IL modified ZIF-8 dispersed in 6DA-durene PI polymer membrane. Furthermore, it may be worth noting that the polymer swelling upon gas sorption in a MMM with rigidified polymer layer at the interface can be very different than for the bulk polymer, resulting in completely different gas transport characteristics as predicted from models even with non-ideal effects included, especially at high pressures, which needs further investigation.

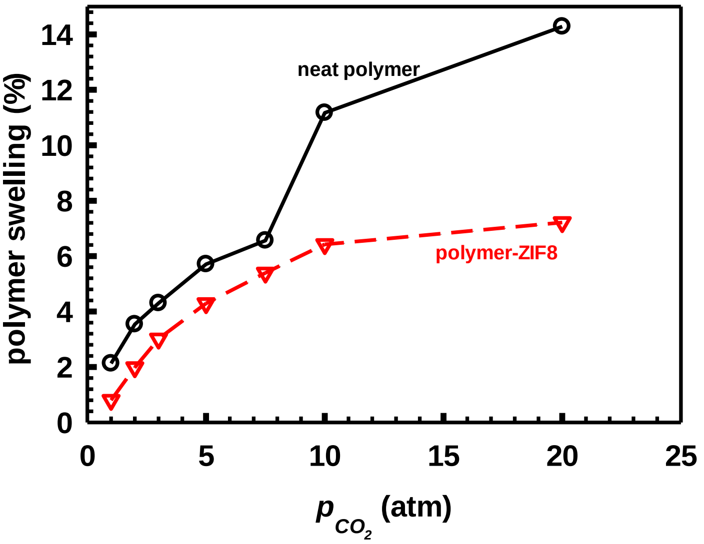

Figure 8-10: Comparison of variation of the swelling of polymer in a neat 6FDA-durene PI and 6FDA-durene-ZIF-8 membranes in the presence of CO_2

8.3.5 Membrane performance

A comparison of permeability against selectivity of 6FDA-durene PI, PI/ZIF-8 and IL modified PI/ZIF-8 membranes at 300 K is shown in Figure 8-11. It is seen that incorporation of ZIF-8 into PI polymer leads to an increase in gas permeability at the cost of selectivity, exhibiting overall performance slightly above the Robeson upper bound plot.[47] This is due to the presence of low polymer density region (void region) near the ZIF8 surface, which promotes methane diffusion over CO_2 diffusion, the former being a lighter molecule. On the other hand, incorporation of IL modified ZIF8 into PI polymer leads to an increase in both gas permeability as well selectivity, exhibiting overall performance well above the Robeson upper bound plot.[47] This can be attributed to the absence of larger voids in the interfacial region which are filled with IL in this case, that act as low resistance paths (leaky interface). However, we note the data presented here assumes gas diffusion through MMM occurs when polymer and ZIF-8 are in series, which is not always the case. Thus, the performance data based on real membrane characteristics can be somewhat different.

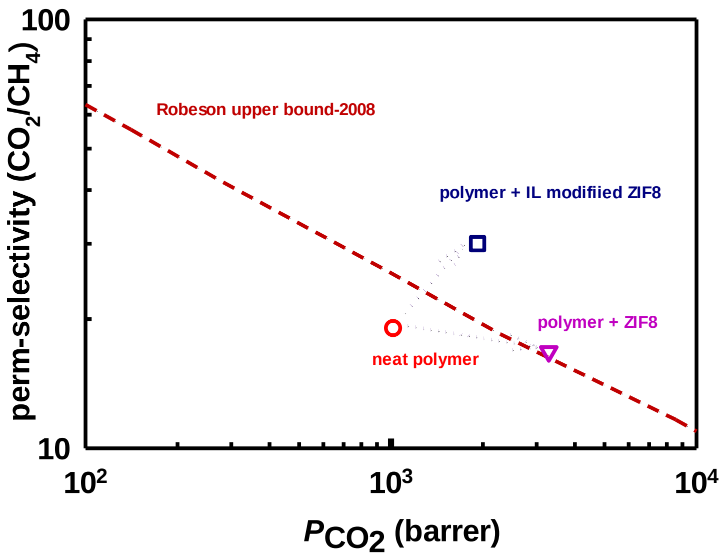

Figure 8-11: The separation performance of neat PI, PI-ZIF-8 and PI-IL modified ZIF-8 membranes with Robeson upper bound at 300 K and 3 atm pressure.

8.4 Conclusions

The transport properties of CO_2 and CH_4 in pure gas conditions in 6FDA-durene PI-ZIF-8 mixed matrix membrane (MMM) are investigated through equilibrium molecular dynamics simulations. It is seen that incorporation of ZIF-8 into PI results in the formation of a low-density polymer region near the surface having thickness around 7-9 Å. In this region, large free volume elements of 4 – 6 Å diameter is present, as opposed to the bulk polymer region where free volume elements of less than 4 Å diameter are present. In the low-density polymer region that exists at the interface, CO_2 diffuses an order of magnitude faster, while methane diffuses 2-orders of magnitude faster than in the bulk polymer. Further, a 3-fold increase in CO_2 permeability in ZIF-8-6FDA-durene MMM compared to the neat polymer membrane, at the cost of perm-selectivity due to the presence of larger voids is observed. Interestingly, in a ZIF-8-6FDA-durene PI MMM, no plasticization is observed for CO_2 up to 10 atm pressure, as opposed to the neat polymer membrane that exhibits plasticization at 4 atm pressure. This is due to the solid surface that reduces the degrees of freedom over which the polymer can swell in the composite membrane, resulting in lower polymer swelling in the composite membrane than in the neat polymer membrane. In addition, to promote the compatibility between the 6FDA-durene polymer and ZIF-8, an ionic liquid (BMIM-BF4), which has favorable interactions with polymer as well as ZIF-8 is identified. The gas diffusion characteristics of 6FDA-durene/ZIF-8 MMM with and without having IL at the interface are investigated.

The gas sorption isotherms in PI and PI-/ZIF-8 (with and without modifying by IL) hybrid systems, were extracted *via* a two-step methodology considering the dynamics and structural transitions in the polymer matrix upon gas absorption. Our results show that the isotherm curves for gas sorption in PI and PI/ZIF-8 hybrid membranes are of ‘dual-mode sorption’ type. It is found that incorporation of ZIF-8 into PI has no significant effect on the solubility selectivity of CO_2 over CH_4 at 300 K. It is seen that voids present near the interface act as strong sorption sites for both the gases, leading to higher gas sorption capacity in the PI-ZIF8 composite membrane than expected. A modest increase in CO_2 solubility selectivity over methane occurs at low pressures, while no significant difference at higher pressures than that of neat polymer is observed. In conclusion, a significant increase in CO_2 permeability is observed on incorporation of IL modified ZIF-8 into PI with little increase in perm-selectivity of the composite membrane compared to the neat PI polymer membrane, leading to a performance well above the Robeson upper bound.

8.5 References

1. Furukawa, H.; Cordova, K. E.; O'Keeffe, M.; Yaghi, O. M., The Chemistry and Applications of Metal-Organic Frameworks. *Science* **2013,** *341*, 1230444.

2. Moore, T. T.; Koros, W. J., Non-ideal effects in organic–inorganic materials for gas separation membranes. *Journal of Molecular Structure* **2005,** *739* (1), 87-98.

3. Allen, F., The Cambridge Structural Database: a quarter of a million crystal structures and rising. *Acta Crystallographica Section B* **2002,** *58* (3 Part 1), 380-388.

4. Qiu, S.; Xue, M.; Zhu, G., Metal–organic framework membranes: from synthesis to separation application. *Chemical Society Reviews* **2014,** *43* (16), 6116-6140.

5. Altintas, C.; Keskin, S., Molecular Simulations of MOF Membranes and Performance Predictions of MOF/Polymer Mixed Matrix Membranes for CO2/CH4 Separations. *ACS Sustainable Chem. Eng.* **2019,** *7* (2), 2739-2750.

6. Erucar, I.; Keskin, S., Computational Methods for MOF/Polymer Membranes. *The Chemical Record* **2016,** *16* (2), 703-718.

7. Yilmaz, G.; Keskin, S., Molecular modeling of MOF and ZIF-filled MMMs for CO2/N2 separations. *J. Membr. Sci.* **2014,** *454*, 407-417.

8. Monsalve-Bravo, G. M.; Bhatia, S. K., Extending effective medium theory to finite size systems: Theory and simulation for permeation in mixed-matrix membranes. *J. Membr. Sci.* **2017,** *531* (Supplement C), 148-159.

9. Bushell, A. F.; Attfield, M. P.; Mason, C. R.; Budd, P. M.; Yampolskii, Y.; Starannikova, L.; Rebrov, A.; Bazzarelli, F.; Bernardo, P.; Carolus Jansen, J.; Lanč, M.; Friess, K.; Shantarovich, V.; Gustov, V.; Isaeva, V., Gas permeation parameters of mixed matrix membranes based on the polymer of intrinsic microporosity PIM-1 and the zeolitic imidazolate framework ZIF-8. *J. Membr. Sci.* **2013,** *427*, 48-62.

10. Ordoñez, M. J. C.; Balkus, K. J.; Ferraris, J. P.; Musselman, I. H., Molecular sieving realized with ZIF-8/Matrimid® mixed-matrix membranes. *J. Membr. Sci.* **2010,** *361* (1), 28-37.

11. Vu, M.-T.; Lin, R.; Diao, H.; Zhu, Z.; Bhatia, S. K.; Smart, S., Effect of ionic liquids (ILs) on MOFs/polymer interfacial enhancement in mixed matrix membranes. *J. Membr. Sci.* **2019,** *587*, 117157.

12. Lin, R.; Ge, L.; Diao, H.; Rudolph, V.; Zhu, Z., Ionic Liquids as the MOFs/Polymer Interfacial Binder for Efficient Membrane Separation. *ACS Appl. Mater. Interfaces* **2016,** *8* (46), 32041-32049.

13. Chi, W. S.; Sundell, B. J.; Zhang, K.; Harrigan, D. J.; Hayden, S. C.; Smith, Z. P., Mixed-Matrix Membranes Formed from Multi-Dimensional Metal–Organic Frameworks for Enhanced Gas Transport and Plasticization Resistance. *ChemSusChem* **2019,** *12* (11), 2355-2360.

14. Seoane, B.; Sebastián, V.; Téllez, C.; Coronas, J., Crystallization in THF: the possibility of one-pot synthesis of mixed matrix membranes containing MOF MIL-68(Al). *CrystEngComm* **2013,** *15* (45), 9483-9490.

15. Kim, S.; Marand, E.; Ida, J.; Guliants, V. V., Polysulfone and Mesoporous Molecular Sieve MCM-48 Mixed Matrix Membranes for Gas Separation. *Chem. Mater* **2006,** *18* (5), 1149-1155.

16. Tuteja, A.; Duxbury, P. M.; Mackay, M. E., Polymer Chain Swelling Induced by Dispersed Nanoparticles. *Phys. Rev. Lett.* **2008,** *100* (7), 077801.

17. Jouault, N.; Dalmas, F.; Said, S.; Di Cola, E.; Schweins, R.; Jestin, J.; Boué, F., Direct small-angle-neutron-scattering observation of stretched chain conformation in nanocomposites: More insight on polymer contributions in mechanical reinforcement. *Phys. Rev. E* **2010,** *82* (3), 031801.

18. Galizia, M.; De Angelis, M. G.; Messori, M.; Sarti, G. C., Mass Transport in Hybrid PTMSP/Silica Membranes. *Ind. Eng. Chem. Res* **2014,** *53* (22), 9243-9255.

19. Holt, A. P.; Griffin, P. J.; Bocharova, V.; Agapov, A. L.; Imel, A. E.; Dadmun, M. D.; Sangoro, J. R.; Sokolov, A. P., Dynamics at the Polymer/Nanoparticle Interface in Poly(2-vinylpyridine)/Silica Nanocomposites. *Macromolecules* **2014,** *47* (5), 1837-1843.

20. Cheng, S.; Carroll, B.; Lu, W.; Fan, F.; Carrillo, J.-M. Y.; Martin, H.; Holt, A. P.; Kang, N.-G.; Bocharova, V.; Mays, J. W.; Sumpter, B. G.; Dadmun, M.; Sokolov, A. P., Interfacial Properties of Polymer Nanocomposites: Role of Chain Rigidity and Dynamic Heterogeneity Length Scale. *Macromolecules* **2017,** *50* (6), 2397-2406.

21. Díaz, K.; Garrido, L.; López-González, M.; del Castillo, L. F.; Riande, E., CO_2 Transport in Polysulfone Membranes Containing Zeolitic Imidazolate Frameworks As Determined by Permeation and PFG NMR Techniques. *Macromolecules* **2010,** *43* (1), 316-325.

22. Jiang, Q.; Tallury, S. S.; Qiu, Y.; Pasquinelli, M. A., Molecular dynamics simulations of the effect of the volume fraction on unidirectional polyimide–carbon nanotube nanocomposites. *Carbon* **2014,** *67* (Supplement C), 440-448.

23. Semino, R.; Dürholt, J. P.; Schmid, R.; Maurin, G., Multiscale Modeling of the HKUST-1/Poly(vinyl alcohol) Interface: From an Atomistic to a Coarse Graining Approach. *J. Phys. Chem. B* **2017,** *121* (39), 21491-21496.

24. Semino, R.; Ramsahye, N. A.; Ghoufi, A.; Maurin, G., Microscopic Model of the Metal–Organic Framework/Polymer Interface: A First Step toward Understanding the Compatibility in Mixed Matrix Membranes. *ACS Appl. Mater. Interfaces* **2016,** *8* (1), 809-819.

25. Benzaqui, M.; Semino, R.; Menguy, N.; Carn, F.; Kundu, T.; Guigner, J.-M.; McKeown, N. B.; Msayib, K. J.; Carta, M.; Malpass-Evans, R.; Le Guillouzer, C.; Clet, G.; Ramsahye, N. A.; Serre, C.; Maurin, G.; Steunou, N., Toward an Understanding of the Microstructure and Interfacial Properties of PIMs/ZIF-8 Mixed Matrix Membranes. *ACS Appl. Mater. Interfaces* **2016,** *8* (40), 27311-27321.

26. Falkovich, S. G.; Nazarychev, V. M.; Larin, S. V.; Kenny, J. M.; Lyulin, S. V., Mechanical Properties of a Polymer at the Interface Structurally Ordered by Graphene. *J. Phys. Chem. C* **2016,** *120* (12), 6771-6777.

27. Semino, R.; Moreton, J. C.; Ramsahye, N. A.; Cohen, S. M.; Maurin, G., Understanding the origins of metal–organic framework/polymer compatibility. *Chemical Science* **2018,** *9* (2), 315-324.

28. Semino, R.; Dürholt, J. P.; Schmid, R.; Maurin, G., Multiscale Modeling of the HKUST-1/Poly(vinyl alcohol) Interface: From an Atomistic to a Coarse Graining Approach. *J. Phys. Chem. C* **2017,** *121* (39), 21491-21496.

29. Semino, R.; Ramsahye, N. A.; Ghoufi, A.; Maurin, G., Microscopic Model of the Metal–Organic Framework/Polymer Interface: A First Step toward Understanding the Compatibility in Mixed Matrix Membranes. *ACS Applied Materials & Interfaces* **2016,** *8* (1), 809-819.

30. Zhang, L.; Hu, Z.; Jiang, J., Metal–Organic Framework/Polymer Mixed-Matrix Membranes for H_2/CO_2 Separation: A Fully Atomistic Simulation Study. *J. Phys. Chem. C* **2012,** *116* (36), 19268-19277.

31. Kresse, G.; Furthmüller, J., Efficient iterative schemes for ab initio total-energy calculations using a plane-wave basis set. *Phys. Rev. B* **1996,** *54* (16), 11169-11186.

32. Kresse, G.; Furthmüller, J., Efficiency of ab-initio total energy calculations for metals and semiconductors using a plane-wave basis set. *Comput. Mater. Sci* **1996,** *6* (1), 15-50.

33. Kresse, G.; Hafner, J., Ab initio. *Phys. Rev. B* **1993,** *47* (1), 558-561.

34. Manz, T. A.; Limas, N. G., Introducing DDEC6 atomic population analysis: part 1. Charge partitioning theory and methodology. *RSC Adv.* **2016,** *6* (53), 47771-47801.

35. Limas, N. G.; Manz, T. A., Introducing DDEC6 atomic population analysis: part 2. Computed results for a wide range of periodic and nonperiodic materials. *RSC Advances* **2016,** *6* (51), 45727-45747.

36. Zhang, L.; Hu, Z.; Jiang, J., Sorption-Induced Structural Transition of Zeolitic Imidazolate Framework-8: A Hybrid Molecular Simulation Study. *Journal of the American Chemical Society* **2013,** *135* (9), 3722-3728.

37. Han, C.; Verploegh, R. J.; Sholl, D. S., Assessing the Impact of Point Defects on Molecular Diffusion in ZIF-8 Using Molecular Simulations. *The Journal of Physical Chemistry Letters* **2018,** *9* (14), 4037-4044.

38. Han, R.; Sholl, D. S., Computational Model and Characterization of Stacking Faults in ZIF-8 Polymorphs. *The Journal of Physical Chemistry C* **2016,** *120* (48), 27380-27388.

39. Doherty, B.; Zhong, X.; Gathiaka, S.; Li, B.; Acevedo, O., Revisiting OPLS Force Field Parameters for Ionic Liquid Simulations. *Journal of Chemical Theory and Computation* **2017,** *13* (12), 6131-6145.

40. Lin, R.; Ge, L.; Liu, S.; Rudolph, V.; Zhu, Z., Mixed-Matrix Membranes with Metal–Organic Framework-Decorated CNT Fillers for Efficient CO2 Separation. *ACS Appl. Mater. Interfaces* **2015,** *7* (27), 14750-14757.

41. An, H.; Lee, A. S.; Kammakakam, I.; Sang Hwang, S.; Kim, J.-H.; Lee, J.-H.; Suk Lee, J., Bromination/debromination-induced thermal crosslinking of 6FDA-Durene for aggressive gas separations. *J. Membr. Sci.* **2018,** *545*, 358-366.

42. Nafisi, V.; Hägg, M.-B., Gas separation properties of ZIF-8/6FDA-durene diamine mixed matrix membrane. *Sep. Purif. Technol.* **2014,** *128*, 31-38.

43. Japip, S.; Wang, H.; Xiao, Y.; Shung Chung, T., Highly permeable zeolitic imidazolate framework (ZIF)-71 nano-particles enhanced polyimide membranes for gas separation. *J. Membr. Sci.* **2014,** *467*, 162-174.

44. Dutta, R. C.; Bhatia, S. K., Atomistic Investigation of Mixed-Gas Separation in a Fluorinated Polyimide Membrane. *ACS Applied Polymer Materials* **2019**.

45. Jusoh, N.; Yeong, Y. F.; Lau, K. K.; M. Shariff, A., Enhanced gas separation performance using mixed matrix membranes containing zeolite T and 6FDA-durene polyimide. *J. Membr. Sci.* **2017,** *525*, 175-186.

46. Jusoh, N.; Yeong, Y. F.; Lau, K. K.; M. Shariff, A., Fabrication of silanated zeolite T/6FDA-durene composite membranes for CO2/CH4 separation. *J. Clean. Prod.* **2017,** *166*, 1043-1058.

47. Robeson, L. M., The upper bound revisited. *J. Membr. Sci.* **2008,** *320* (1), 390-400.

Chapter 9 Conclusions and Perspectives

9.1 Conclusions

This thesis has provided a thorough understanding of polymer structure near a surface for the information necessary to design advanced membrane-based gas separation technologies such as mixed matrix membranes (MMM). Beyond MMMs, understanding of static and dynamic properties of polymers at solid surfaces find use in a host of applications such as thin films or polymer-based composites.

The transport properties of CO_2 and CH_4 in the temperature range of 300-500 K in neat polyimide (PI) polymer membranes has been investigated using equilibrium molecular dynamics simulations. The corrected diffusivities of CO_2 and CH_4 in neat PI membranes are in the order of 10^{-11}-10^{-12} m^2/sec, and qualitatively as well as quantitatively in good agreement with experimental reports. The gas sorption isotherms in neat polymer membranes were extracted *via* a two-step methodology considering the dynamics and structural transitions in the polymer matrix upon gas sorption. Further, analysis of membrane behavior under practical conditions using EMD-based transport coefficients shows that, while the CO_2/CH_4 perm-selectivity increases with an increase in pressure based on pure component data, the trend is opposite for mixture data. Thus, the commonly used approach of screening membrane materials based on pure component data can be misleading, as it overlooks the correlation effects arising from the presence of other species in the mixture.

The analysis of interfacial structure of PI at the surface of a silicalite zeolite indicate the formation of densified polymer layers (rigidified region) near the surface. It is seen that interfacial region thickness, the polymer region that is affected in the presence of the filler before bulk-like behavior of the polymer is attained, is around 1.2 nm, contrary to empirical fits suggesting the existence of an approximately 1 micron thick interface between the polymer and filler. Further, the gas transport properties are determined in the interface region, including the sorption isotherms considering the structural transitions upon gas sorption in detail through EMD simulations. A significant increase in CO_2/CH_4 selectivity as well as gas permeability is observed in the PI-MFI composite membrane compared to that in the pure PI polymer membrane, which is correlated with the high selectivity of the rigidified interfacial layer in the polymer. Thus, while enhancing transport resistance, the rigidified layer is beneficial to membrane selectivity, leading to improved performance based on the Robeson upper bound plot for polymers.

Finally, it is seen that incorporation of ZIF-8 into PI results in formation of sub-nanometer defects near the polymer-filler interface, resulting a 3-fold increase in CO_2 permeability in ZIF-8-6FDA-durene MMM compared to the neat polymer membrane, at the cost of perm-selectivity due to the presence of larger voids is observed. This investigation also included strategies to minimise interfacial defects such as nano-scale voids to promote compatibility between the polymer and filler, so as to achieve the separation performances surpassing the Robeson upper bound limit in the MMMs.

Further, by considering the contributions of intra-crystalline and internal interfacial resistance, this thesis has developed an approach to quantitatively assess the internal interfacial barriers to gas transport, especially in channel-like nanoporous materials. It is found that the internal interfacial barriers due to the phase boundary contribute significantly to the gas transport resistance at the nanoscale in zeolites, especially when the surface has a uniform morphology as well as when a dense surrounding media such as a polymer is present.

9.2 Recommendations

On the basis of these insights, the work in the following directions are anticipated for improved design of new generation separation processes such as MMM and ultra-thin membranes.

Connecting to the multiscale: The present thesis evaluated the gas transport characteristics of the polymer, filler and polymer-filler composite membranes at any given temperature and pressure through EMD simulations, which ignores the practical scenario of pressure gradient that exists across a membrane of given thickness. Thus, direct validation of EMD results with experimental data is not straightforward. Further, that gas diffusion characteristics in the composite membrane are extracted assuming the polymer and filler are in series, which is not always true. Depending on the loading and distribution of filler particles in the membrane, the gas diffusion behaviour in the composite membrane can be very different. A multi-scale simulation approach that combines insights from EMD simulations with macroscopic simulations is necessary to predict the real membrane behaviour which leads to the future study to be more practical and intriguing. Further, an investigating highlighting the effect of size, shape and dynamics of the filler in the polymer matrix is required.

Strategies to improve the compatibility between the polymer and filler: The present investigation highlighted the inclusion of interface wetting agents such as ionic liquids (IL), to promote the compatibility between the filler and polymer. However, the effect of loading of IL on the separation performance of MMM is not fully understood and requires a detailed investigation. Further, a detailed investigation on screening and selection of suitable ILs for a given set of membrane materials as well as application through atomistic simulations can be done. In addition, a study highlighting the effect of presence of different functional groups on polymer and/or on inorganic surface to find a suitable functional group that promote the compatibility between the polymer and filler in the interface region is required.

Screening of the novel filler materials: The present thesis evaluated the structure of polymer near the MFI zeolite as well as ZIF-8, and gas transport characteristics in the resulting MMM. However, a detailed investigation on screening and selection of suitable filler -polymer combination for a given application through atomistic simulations is necessary. Further, state-of-the-art materials such as disordered carbons, [1, 2]and covalent-organic framework (COF) materials[3] considered attractive for various industrial environment and energy related separation processes, can be evaluated for their performance as filler materials to achieve the separation performances surpassing the Robeson upper bound limit in the MMMs.

Interfacial barriers to the gas transport: The present investigation evaluated the contribution of interfacial barriers to gas transport assuming the framework is rigid. However, the flexibility of the framework can significantly influence interfacial barriers, especially when the molecular size of the fluid molecule and available pore size in the membrane are comparable. Further, the contribution of interfacial barriers to gas transport is remarkable when a dense surrounding medium such as polymer is present, requiring detailed investigation to provide the necessary information for the design of MMMs. Furthermore, there remain uncertainties about the influence of pore blockage/constriction, grain boundaries, internal pore blockage and surface functionalization on the interfacial barriers. Work along these lines is yet to be reported, but would appear to be important to explore strategies to manipulate the interfacial barriers to improve the membrane separation performance.

9.3 References

1. Farmahini, A. H.; Opletal, G.; Bhatia, S. K., Structural Modelling of Silicon Carbide-Derived Nanoporous Carbon by Hybrid Reverse Monte Carlo Simulation. *The Journal of Physical Chemistry C* **2013,** *117* (27), 14081-14094.

2. Farmahini, A. H.; Bhatia, S. K., Hybrid Reverse Monte Carlo simulation of amorphous carbon: Distinguishing between competing structures obtained using different modeling protocols. *Carbon* **2015,** *83*, 53-70.

3. Zhang, C.; Wu, B.-H.; Ma, M.-Q.; Wang, Z.; Xu, Z.-K., Ultrathin metal/covalent–organic framework membranes towards ultimate separation. *Chemical Society Reviews* **2019,** *48* (14), 3811-3841.